Tri-Helical Direct Gravure Coating

by

Robert William Hewson

Submitted in accordance with the requirements for the degree of
Doctor of Philosophy

University of Leeds,
Department of Mechanical Engineering

July 2006

The candidate confirms that the work submitted is his own and that appropriate credit has been given where reference has been made to the work of others.

Abstract

Tri-helical, gravure roll coating, operated in reverse mode, is investigated via a combined experimental, theoretical and computational approach.

New experiments were conducted on a pilot coating rig, designed to simulate the industrial process. Flow visualisations reveal the underlying flow structure within the roll-to-web transfer region and highlight when loss of coating stability (streaking) occurs. The latter is found to be influenced by the depth of the tri-helical grooves and the capillary number. Experiments show that as the web-to-roll speed ratio is increased, so too is fluid pickout from the grooves, although the coated film thickness may decrease.

A key feature of the present investigation is the formulation of a novel complementary mathematical model. By starting with a simplified form of the coating process and progressively adding complexity a set of models are developed, first for simple zero pitch angled rectangular grooves then for grooves of arbitrary shape and groove pitch. A further extension to the model is the inclusion of a non-Newtonian model for the fluid (specifically a shear thinning power law formulation). Analysis of the application of shear thinning fluids to the moving substrate is also conducted.

The base model developed is that for rectangular grooves of zero pitch, which takes the form of an analytical solution of the flow equation (a Poisson equation) along a groove. An extension to this model is made by solving the Poisson equation for non-rectangular grooves using the finite element method. Simple meniscus models were applied to make the problem tractable. Agreement between experimental data and predictions from the model is seen to be good for the range of operating conditions considered up to the onset of streaking.

A final extension to the model considers grooves at non-zero pitch angles, representative of the industrial coating process. The limitations of this model, when compared to experimental data are examined and a physical explanation is postulated for the breakdown of the model at steep pitch angles. Under conditions of breakdown, the high pressures within the groove are consistent with the idea that elastohydrodynamics is an important mechanism in the transfer of fluid within the coating bead for discrete cell gravure coating.

Acknowledgements

I would like to express my gratitude to my supervisors Dr N Kapur and Prof P H Gaskell for their support and encouragement throughout my study. Thanks must also go to the other members, both research students and staff, of the Engineering Fluid Mechanics Research group at the University of Leeds for their helpful and interesting discussions, particularly Dr J L Summers for his help with all things computational and Dr M Wilson for interesting discussions of fundamental fluid dynamic problems. Technical assistence in the design, manufacture and assembly of the experimental apparatus was provided by Mr P Banks, Mr L Bellon and Mr K Norris.

Thanks must also go to my fellow students in Mechanical Engineering and to my friends in Leeds for making my time in Leeds so enjoyable. Finally a massive thanks go to my parents and brother for all their support and encouragement during my studies.

The work in this thesis was funded by the Engineering and Physical Sciences Research Council (EPSRC Grant Reference: GR/R70064/01), with additional support from DuPont Teijin Films, for which I am very grateful. Mr A Bates of DuPont Teijin Films provided valuable background information, especially concerning the industrial aspects of gravure roll coating. Thanks are also due to Elementis for providing the rheological additive BenAqua 1000 to enable shear thinning fluids to be explored. Some of the associated computational work was performed on on the White Rose Grid.

Contents

List of Figures

List of Tables

Nomenclature

Note that some of the symbols listed below are defined differently in chapter 3 where they are problem specific, these have been identified with the *(Ch3)* label next to the variable name; local definitions are used in chapter 1.

a, A	Non-dimensional and dimensional groove width respectively
a'	Representative non-dimensional groove width
b, B	Non-dimensional and dimensional groove base width respectivelly
Bo	Roll Bond number ($Bo = \frac{\rho g R_{\text{roll}} A}{\sigma}$)
c	Gap to film thickness ratio obtained from film forming models
c, C (Ch3)	Non-dimensional and dimensional gap to film thickness ratio at the point of film splitting
Ca	Capillary number (based on roll velocity $Ca = \frac{\mu U_{roll}}{\sigma}$)
Ca (Ch3)	Capillary number (based on substrate velocity $Ca = \frac{\mu U_{substrate}}{\sigma}$)
Ca_{FF}	Capillary number used in the BVP solution of the film forming model ($Ca = \frac{\lambda U^n_{\text{substrate}}}{\sigma H^{n-1}_\infty}$)
d, D	Non-dimensional and dimensional web to roll gap respectively
g	Gravitational acceleration ($9.81 m/s^2$)
h	Non-dimensional liquid film thickness
H	Dimensional liquid film thickness
H_∞ (Ch3)	Dimensional final film thickness
h_1	Non-dimensional liquid film thickness on base of groove
h_2	Non-dimensional liquid film thickness on walls of groove
h_3	Non-dimensional liquid film thickness on lands of roll
h_w	Non-dimensional liquid film thickness on web
k	Non-dimensional average groove depth
l, L	Non-dimensional and dimensional groove land width
L (Ch3)	Film thickness measured along the Y direction
n	Shear thinning viscosity power law index
p, P	Non-dimensional and dimensional pressure respectively
q, Q	Non-dimensional and dimensional flux respectively

r, R	Non-dimensional (aspect ratio) and dimensional groove depth respectively
R (Ch3)	Meniscus radius
$r_{\mathrm{roll}}, R_{\mathrm{roll}}$	Non-dimensional and dimensional roll radius respectively
Re	Reynolds number ($Re = \frac{\rho U_{roll} A}{\mu}$)
S	Web to roll speed ratio ($S = \frac{U_{web}}{U_{roll}}$), in the results chapters a positive speed ratio is used to avoid confusion when discussing results ($S = \left\lvert\frac{U_{web}}{U_{roll}}\right\rvert$) [1]
s, S (Ch3)	Dimensional and non-dimensional distance along the free surface respectively
St	Stokes number ($St = \frac{\rho g A R_{\mathrm{roll}}}{\mu U_{roll}}$)
St (Ch3)	Stokes number ($St = \frac{\rho g H_{\infty}}{\mu U_{\mathrm{substrate}}}$)
u, v, w	Non-dimensional cartesian velocity components
U, V, W	Dimensional cartesian velocity components
U, V (Ch3)	Dimensional cartesian velocity components in the X and Y directions respectively
u_l, U_L (Ch3)	Dimensional and non-dimensional velocity of the substrate resolved into the x, X direction respectively
X, Y, Z	Dimensional cartesian coordinates in the groove direction, groove width and groove depth directions
x, y (Ch3)	Non-dimensional cartesian coordinates at tangent and perpendicular to the free surface
X, Y (Ch3)	Dimensional cartesian coordinates at tangent and perpendicular to the free surface
x', y' (Ch3)	Non-dimensional cartesian coordinates aligned with the substrate
X', Y' (Ch3)	Dimensional cartesian coordinates aligned with the substrate
U_{bubble} (Ch3)	Dimensional displaced bubble velocity
$U_{\mathrm{substrate}}$ (Ch3)	Dimensional substrate velocity
β	Web wrap angle
γ	Strain rate tensor
$\dot{\gamma}$	Second invarient of the rate of deformation tensor
η	Generalised viscosity
$\kappa, \boldsymbol{\kappa}$	Non-dimensional and dimensional radius of curvature respectively
λ	Shear thinning viscosity power law consistency factor
μ	Newtonian fluid viscosity
Ψ	Fractional pickout
Φ	Groove helix angle
ρ	Fluid density

σ	Surface tension
τ	Shear stress
θ (Ch3)	Meniscus angle relative the substrate
θ_D, θ_A	Dynamic and static contact angle respectively

---

[1] The convention used for speed ratio is that an increase in speed ratio means a more negative value of $S = \frac{U_{web}}{U_{roll}}$, the same is true when indicating whether speed ratio is high or low, a low speed ratio indicates one that is close to zero while a high speed ratio is one that is far from zero (even though it is in the negative direction).

Acronyms

BVP boundary value problem

DAQ data aquisition

FE finite element

FEM finite element method

FFST finite Fourier sine transform

FSTs Fourier sine transforms

ODE Ordinary differential equation

Chapter 1

Introduction

The application of liquid layers onto solid substrates is a common feature of a wide variety of industrial processes, for which a number of different methods are used. At the heart of all such methods is the displacement of a gas with a liquid phase at the substrate surface which takes place at the "dynamic wetting line", an area of flow which is governed by molecular phenomena. The range of coating methods that have emerged reflects the wide variation in the final requirements of the coated products, which include the film thickness, coating quality and surface properties to name but a few. The variety of coated products produced is vast and includes: packaging material; printed media; photographic film; magnetic media, such as video and audio cassettes; and optical media, such as compact discs; etc. The main driving force behind coating research is the dual requirement for increased coating speed and coating quality, two often conflicting goals.

The global economic importance of coated products is clear; in 1994 the value of the US coating industry alone was worth $20,000,000 per annum, as estimated by the US Department of Commerce [8]. Two commonly occuring coated substrates are polyethylene terephthalate (PET) and polyethylene naphthalate (PEN), running into 750, 000 metric tonnes per year [9], with the largest manufacturer Dupont-Teijin Films responsible for over 300, 000 metric tonnes of production. Despite the decline in demand for video tapes and photographic film, increased demand for film from developing markets (such as China) has generally maintained international volumes [10].

The range of coating methods in common use is illustrated schematically in figure 1.1, some of which are relatively well understood and established - such as reverse roll coating - while others, such as tensioned web coating [11], are still to be investigated in detail. They fall into two broad categories [12] - self metered, where the flux deposited on the web depends on the geometry and operating conditions of the coater as well as the fluid properties (figures 1.1a-b), and pre-metered where the flux is set externally, via a pump for example (figures 1.1c-f). Attention here is focussed on flows most relevant to tri-helical gravure roll coating. Due to its nature of having a continuous fluid domain from the upstream to downstream meniscus it can be argued it has more in common with smooth roll coating than it does with the transient discrete cell form of gravure roll coating, for this reason attention here focusses on both smooth roll and discrete cell gravure roll coating.

This thesis aims to elucudate the physical processes involved tri-helical gravure roll coating. In addition to developing a model able to predict the process performance in terms of the fluid transfer from the roll to the web, the factors influencing the stable coating window are also examined. A combined experimental, analytical and computational approach was taken in order to achieve these goals.

1.1 Roll Coating and Lubrication Flow

A great deal of work on the analysis of roll coating flows owes its origins to lubrication theory, so called because it is used to analyse thin liquid film lubrication between two moving surfaces such as those found in bearings, piston rings or gears. While the emphasis may differ in the case of coating technology compared to tribology application, for example in the case of fixed-rigid roll coating lubrication theory has been used to determine the final liquid film thickness applied to a moving substrate (as opposed to the pressure distribution and load bearing characteristics [13, 14, 15]) - the underlying analysis is essentially the same.

Lubrication theory has been used successfully to model and understand a wide range of coating flows. This includes the analysis of liquid flow over an inclined surface [16, 17, 18], the deposition of thin liquid films onto a moving substrate (see section 1.6), and specific coating flows - such as reservoir-fed roll coating (see section 1.2).

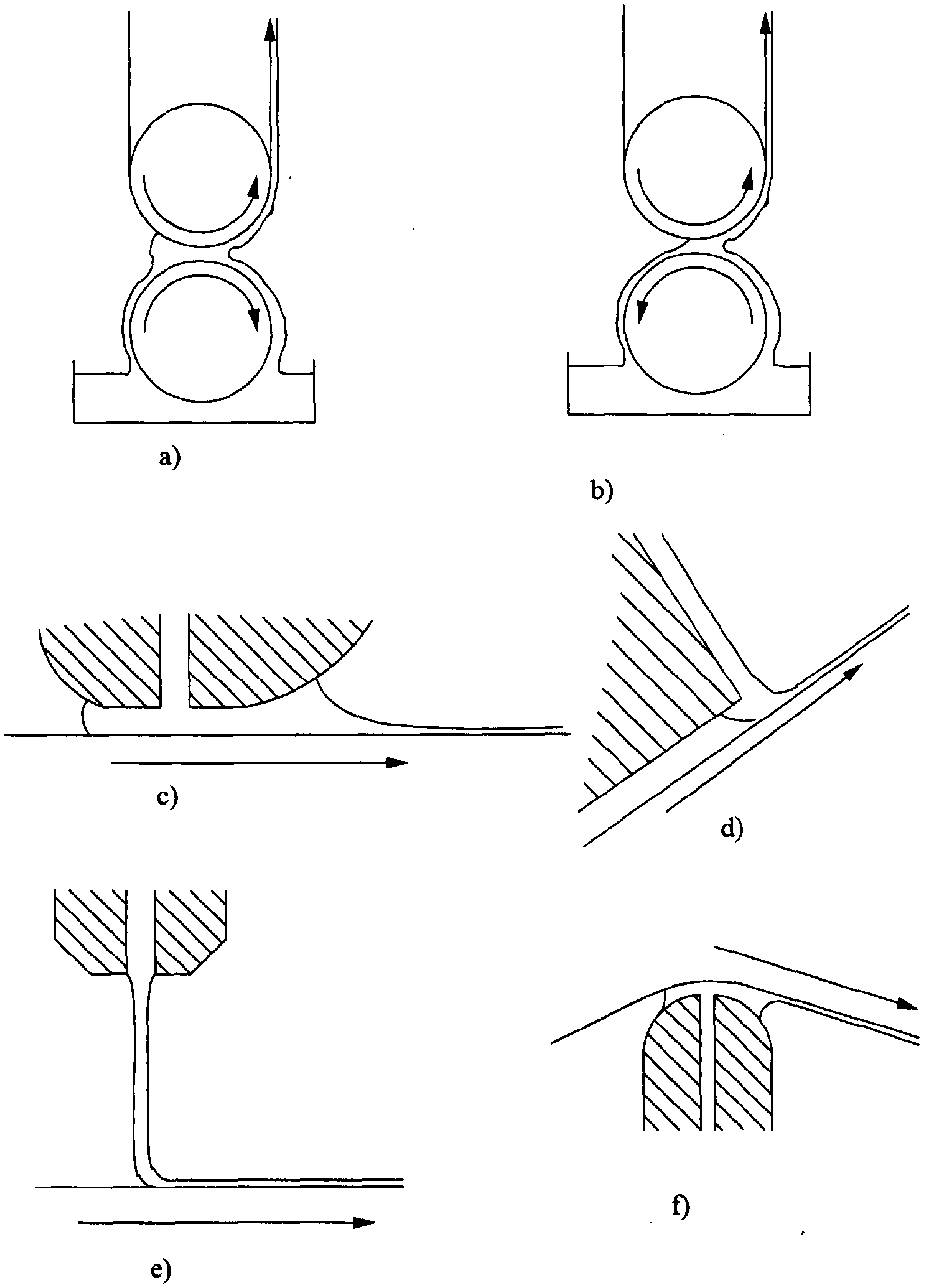

Figure 1.1: Cross-sectional schematics of coating methods in common use: a) forward roll; b) reverse roll; c) slot; d) slide; e) curtain; f) tensioned web.

1.2 Roll Coating

Roll coating is a process whereby a thin layer of liquid is deposited onto a web by means of one or more rotating rolls. The process is self metering as the volume of fluid transfered to the web is controlled by the flow in the small gaps between rolls and/or roll and web. Roll coating can be sub-divided into forward and reverse modes of operation. In the forward mode the two rolls (or roll and web) traverse the coating bead in the same direction, in reverse roll coating the opposite occurs - see figure 1.2.

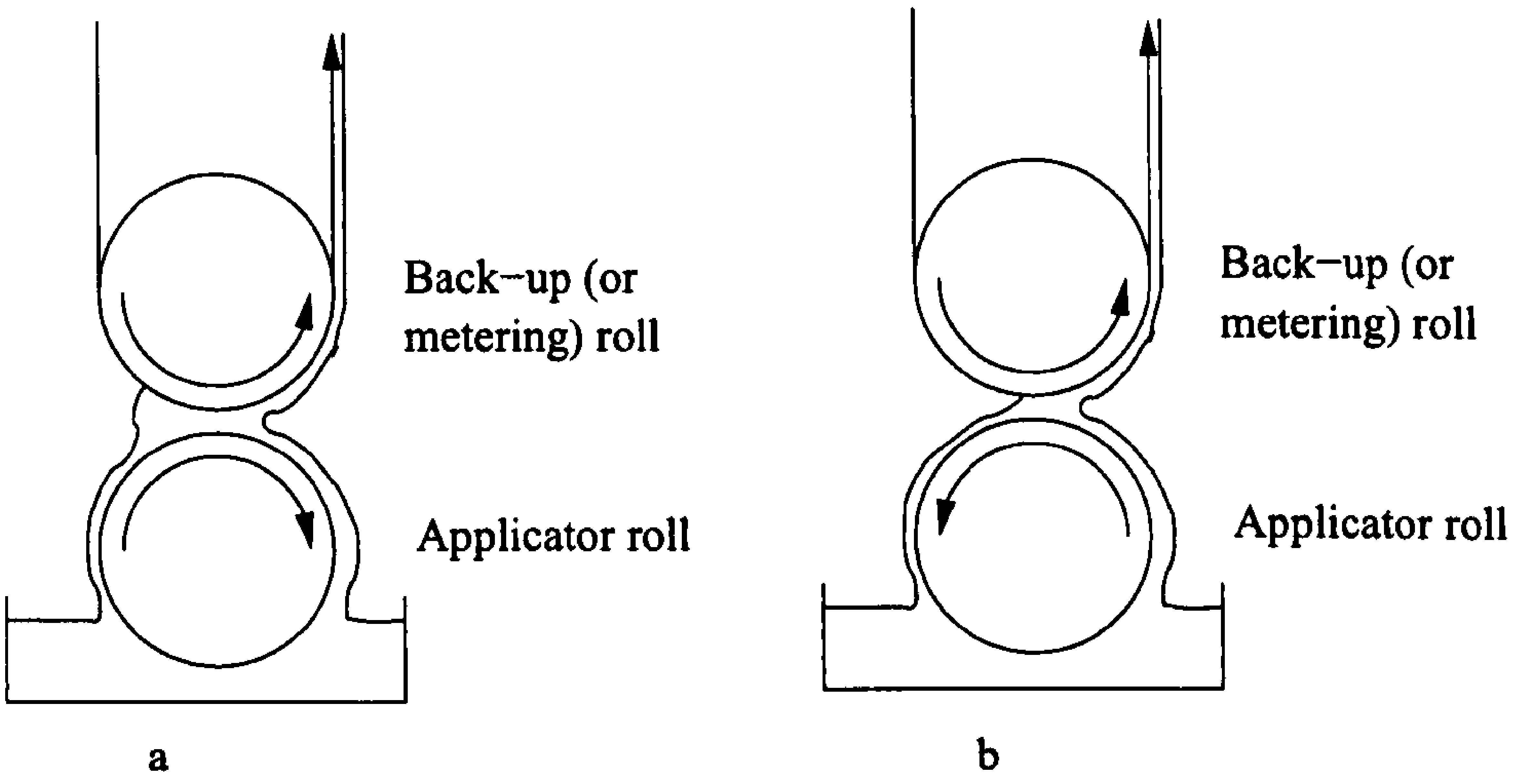

Figure 1.2: Cross-sectional schematic of (a) forward and (b) reverse twin-roll coating.

Metered coating is a form of roll coating in which the substrate is wrapped around a roll and passes through a small gap separating it from a metering roll rotating in the opposite direction which removes (meters) some of the fluid from the web. The fluid dynamics involved are the same as for reverse roll coating. Both forward and reverse roll coating may be operated with a flooded or starved inlet. These definitions correspond to the relative film thickness entering the coating bead compared to the minimum gap between the rolls. When the thickness of the liquid film entering the coating bead is of the same order or greater than the gap a rolling bank of fluid may form and be returned to the coating pool. When the liquid film is significantly thinner than the roll separation the upstream meniscus plays an important part in determining the pressures throughout the coating pool and the behaviour of the coating process in general.

1.2.1 Flooded Forward Roll Coating

One of the earliest applications of Reynolds' lubrication equations [19] to roll coating is that of Banks & Mill [1] who examined forward roll coating using a fully submerged twin roll pair, as shown in figure 1.3.

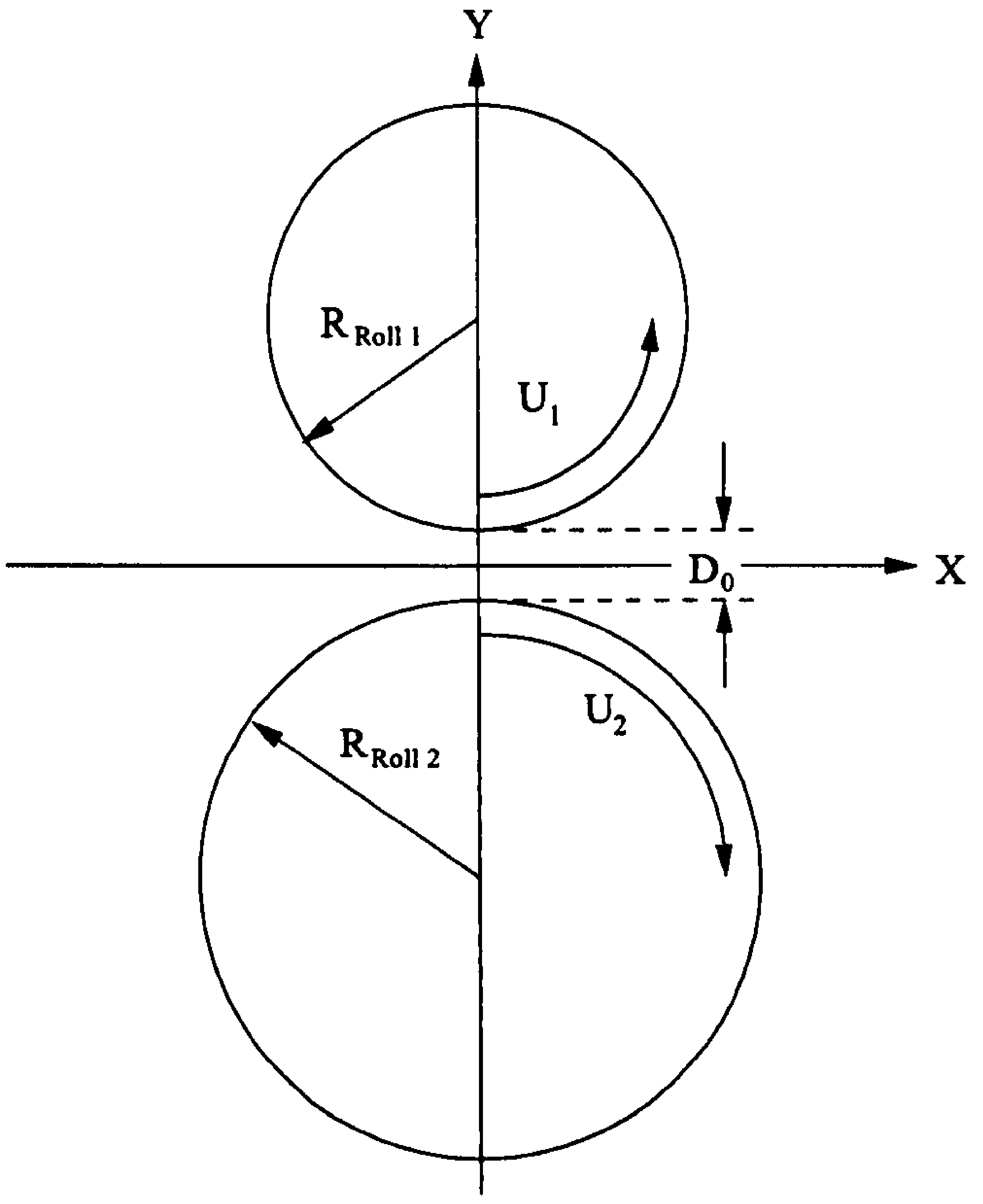

Figure 1.3: Schematic of the twin-roll configuration investigated by Banks and Mill [1]

From the equation describing pressure gradient obtained by Gatcombe [20] the pressure distribution was obtained using the boundary conditions $p = 0$ at $x = \pm\infty$ (the full Sommerfeld condition). Unlike the analysis of Gatcombe a constant viscosity was assumed in the analysis. The resulting pressure distribution has equal but opposite pressures on either side of the nip (location of minimum roll separation) and is given by the following expression:

$$P = -\frac{4\mu U}{D_0^2}\sqrt{2R_{\text{roll}}D_0}\sin\alpha\cos^3\alpha, \tag{1.1}$$

where $\alpha = \frac{X}{\sqrt{2R_{\text{roll}}D_0}}$, $\frac{1}{R_{\text{roll}}} = \frac{1}{R_{\text{roll}\,1}} + \frac{1}{R_{\text{roll}\,2}}$, $U = \frac{U_1+U_2}{2}$, and the symbols are as shown in figure 1.4.

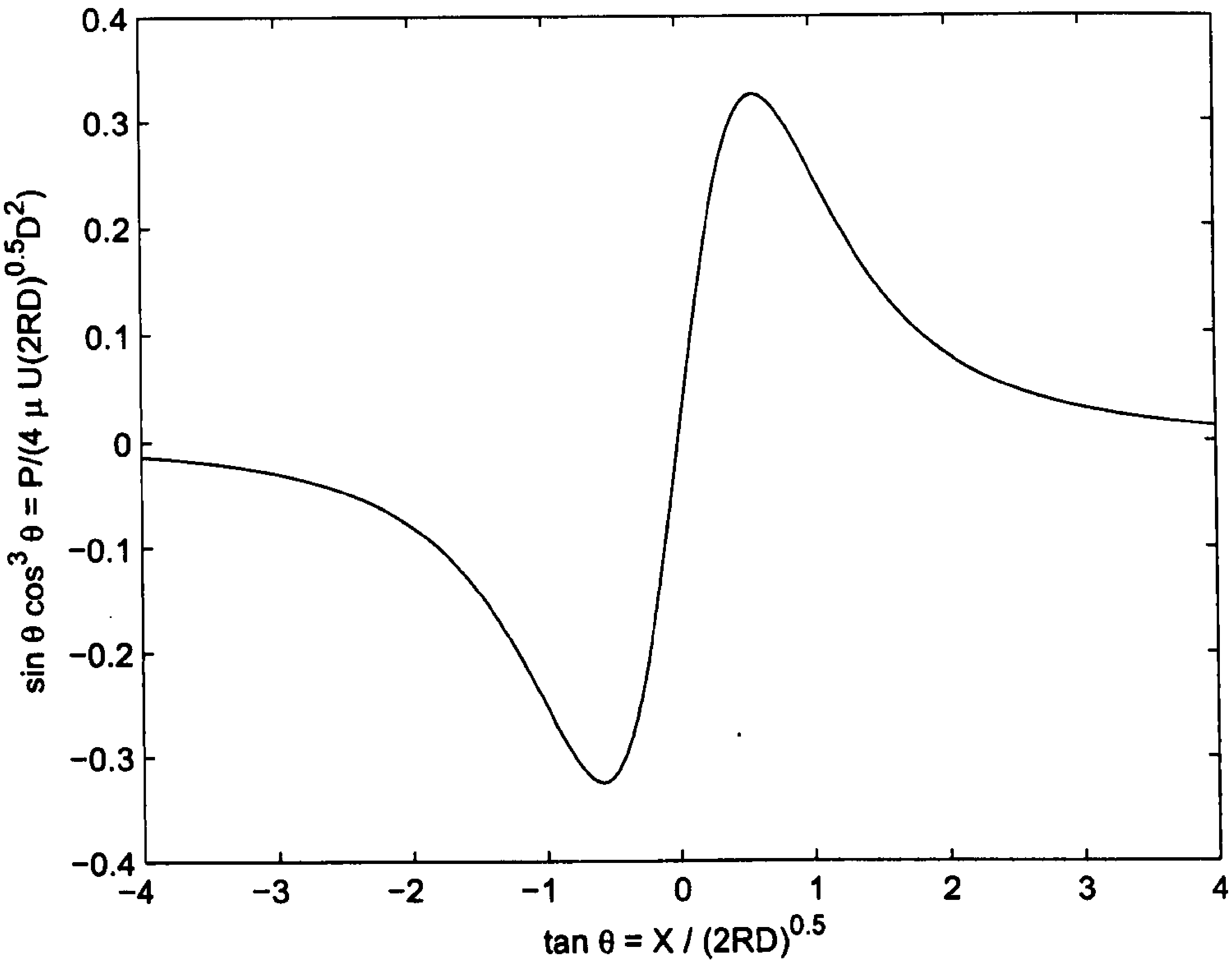

Figure 1.4: Pressure distribution obtained By Banks & Mill [1]

Banks and Mill [1] noted that cavitation may occur if very low pressures arise and if impurities in the fluid, such as dissolved air, are present. Accordingly, the onset of cavitation was also investigated experimentally by them. It is interesting to note that acrylic rollers were used to visualise the flow (an acrylic roll is part of the apparatus used in the course of the experiments described later). A comparison of the factors affecting the magnitude of the minimum pressure and the onset of cavitation were made and it was shown that for their liquid, cavitation occurs at a well-defined pressure.

In a paper by Hopkins [21] the coating of a web emerging from a bath and subsequently being drawn between two moving rollers, as shown in figure 1.5, is modelled. The inlet is flooded and some of the liquid assumed to flow back from the coating nip to the bath.

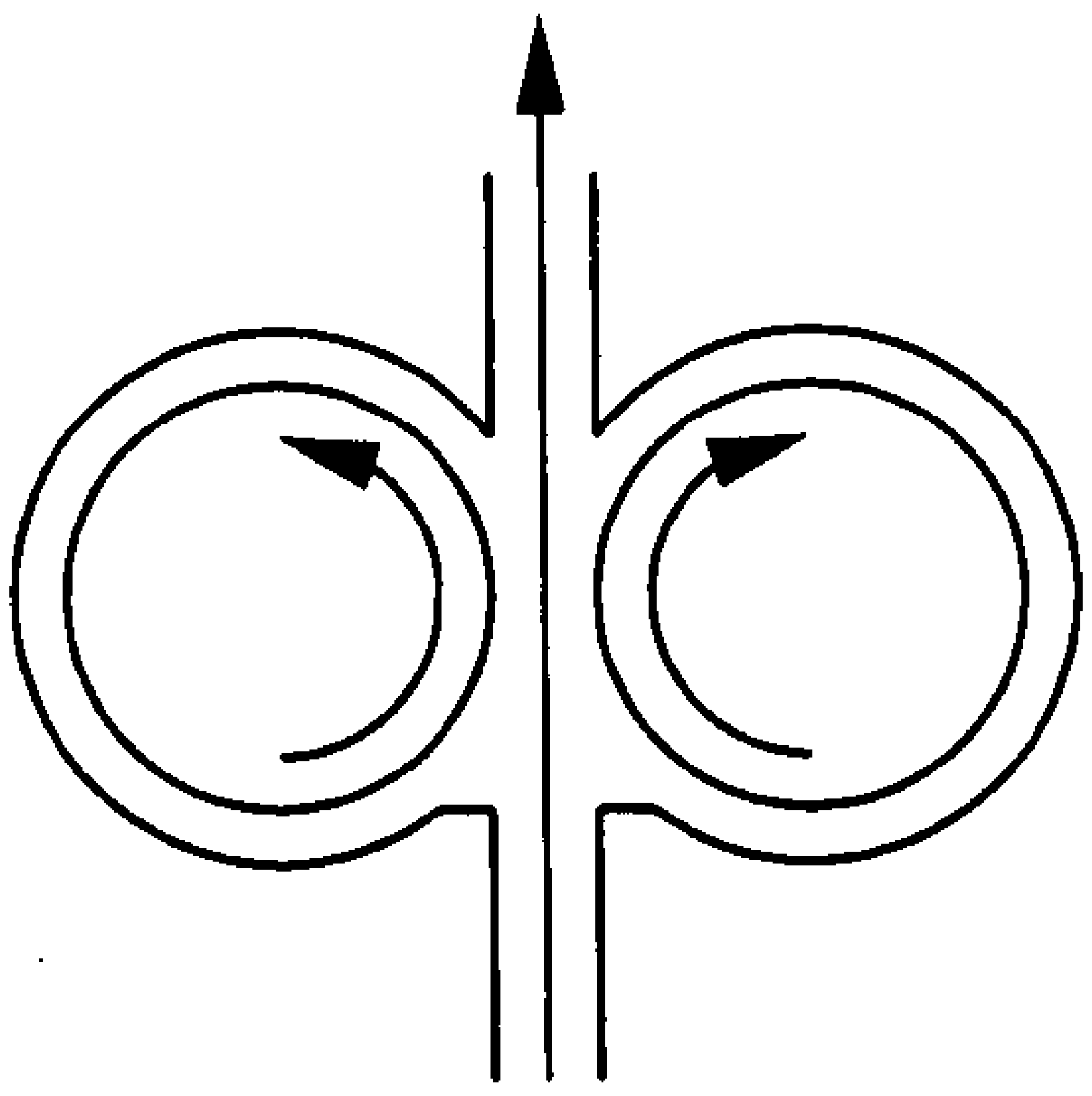

Figure 1.5: Hopkins' web passing between two counter-rotating rollers

The downstream boundary condition is based on the assumption that the fluid divides equally between the roll and the web as they are moving at the same velocity; neglecting surface tension results in predictions for the the film splitting at the stagnation point and the pressure there is given as zero. This allows the average nip velocity to be determined as well as the location of the film split.

The condition where separation occurs at the first stagnation point is now known as the ***"Prandtl-Hopkins"*** condition [22, 21] - a condition, as noted by some authors [23, 24], that is unable to account for recirculation near a meniscus. A critical assessment of the condition is provided by Greener & Middleman [23] where a comparison is made between results obtained using the Prandtl-Hopkins condition and the more thorough Coyne & Elrod equations [6]. Good agreement was found for high capillary number (ratio of viscous to surface tension forces) flows and also between the results obtained using the Prandtl-Hopkins condition and experimental data.

Pitts & Greiller [25] examined the case when two counter rotating rolls are half immersed in a tank of liquid and the fluid is pulled between the rolls (figure 1.6).

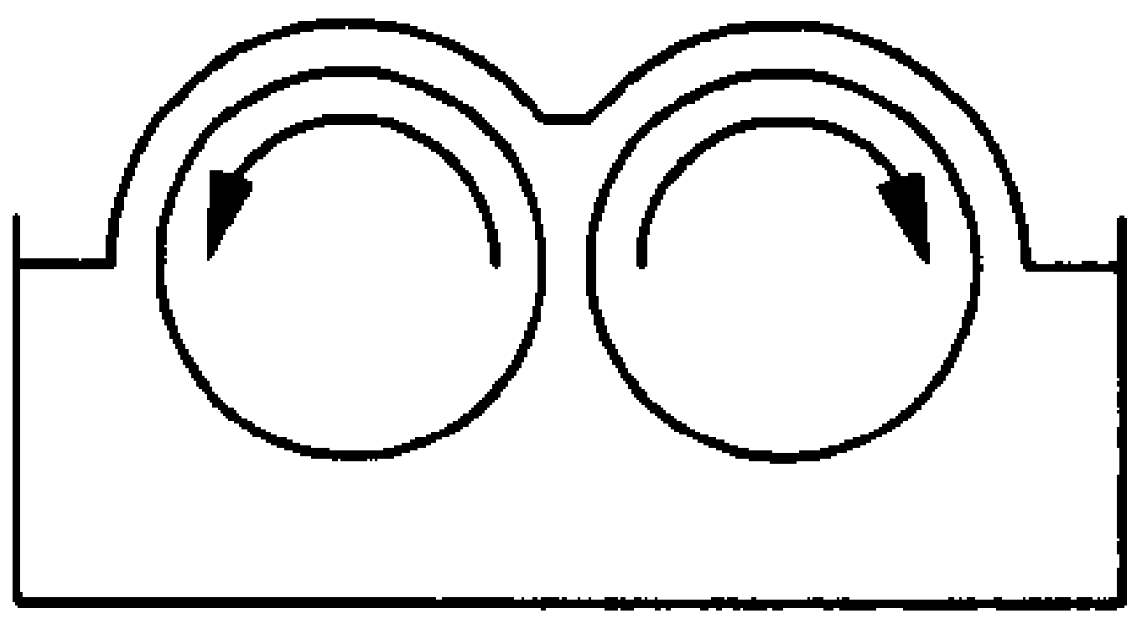

Figure 1.6: Semi-submerged counter rotating rolls

Their paper is divided into two parts, the first investigated stable coating flow by assuming the meniscus is parabolic and solving the biharmonic equation for the surface streamfunction. The importance of the capillary number on the volume flow rate is shown. The second part of the paper examines ribbing (a coating instability) of the interface - this is covered in more detail later in section 1.3.1.

Forward roll coating with rolls having equal peripheral roll speed and radius was examined by Schneider [26] who used the Reynolds condition (also known as the Swift-Steiber condition) [27, 28] as the downstream boundary condition described by:

$$\frac{dP}{dX} = P = 0. \tag{1.2}$$

An upstream zero pressure boundary condition was located at different positions. The effect of its location was examined and found to have negligible influence on film thickness for positions 15° or more from the point of minimum roll-to-roll gap when measured from the centre of one of the rolls.

An experimental investigation of film splitting for a water film between two rotating rolls was made by Hintermaier & White [29]. Linear relationships between film thickness and (i) the roll-roll gap and (ii) the average roll speeds were found. The apparatus used was different to the typical submerged or semi-submerged roller arrangement in that the nip was fed from a V-shaped feeder positioned above the nip. It is highlighted that the combined film thicknesses on the rolls is greater than the nip gap and that there is therefore a favourable pressure gradient at the nip. Their experimental data is compared with corresponding theoretical results obtained from a lubrication approximation of the Navier–Stokes equations.

From 1981 to 1982 three, now widely cited, papers were published on the subject of forward and reverse roll coating by Benkreira, Edwards & Wilkinson [30, 31, 32]. Their forward roll coating configuration is shown schematically in figure 1.7, the top roll, also known as the backing roll, would normally have the web wrapped around it.

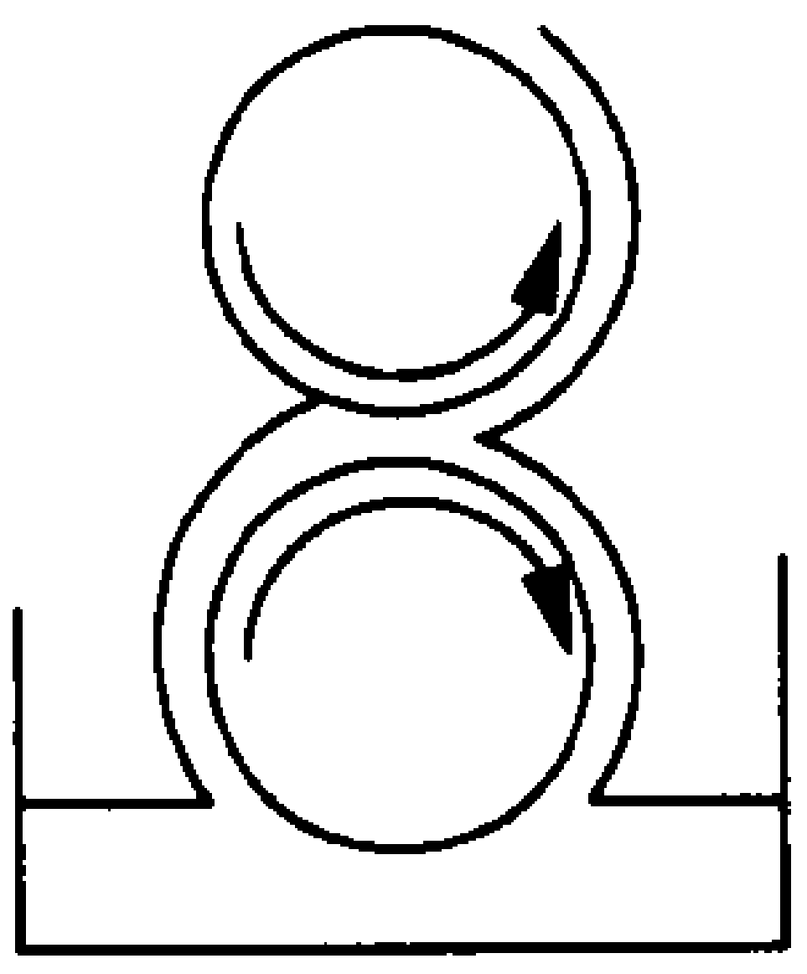

Figure 1.7: Forward roll coating configuration with backing roll

Their second paper [33] carries out a dimensional analysis of the forward and reverse roll problem to predict the main variables determining coating properties. A series of results provide empirical relationships between roll speed ratios and fluxes. Their relationship for the flux passing through the nip of a forward roll coater is:

$$Q_F = 1.31 \left[\frac{1}{2} D_0 \left(U_T + U_B \right) \right], \tag{1.3}$$

where Q_F is the flux per unit length, D_0 is the minimum roll separation (at the nip) and U_T and U_B are the top and bottom roll speeds respectively. The corresponding relationship giving the ratio of flux on the top roller to that on the bottom is:

$$\frac{Q_T}{Q_B} = 0.87 \left(\frac{U_T}{U_B} \right)^{1.65}. \tag{1.4}$$

Note that the constant is not unity due to gravitational effects, as the rolls were arranged one above the other.

An early application of numerical methods to solve the problem of lubrication flow is detailed by Ruschak [4]. In this paper the region around the interface (where the flow is two dimensional in nature) was modelled using a finite element method. The problem was solved by matching pressure gradients and pressures between the finite element solution around the interface and the lubrication solution at the nip.

Two models were developed by Savage [34] using the Reynolds conditions ($p = \frac{dp}{dx} = 0$) and also Prandtl-Hopkins condition ($u = \frac{du}{dx} = 0$) at the meniscus. An explanation of their relevance is provided, and for flows where surface tension is low (high capillary number) it is argued that the Reynolds condition is most relevant.

A paper by Coyle et al. [35] solved the forward roll coating problem using lubrication theory and compared the results with those from a solution of the full Navier–Stokes equations (including surface tension effects) discretised using the finite element method. For both methods the inlet condition was assumed flooded in common with all previous roll coating studies. A comparison between the results obtained showed those from the lubrication analysis to be in good agreement with those found numerically at high capillary numbers only.

As many of the liquids used in coating operations are non-Newtonian a number of authors have attempted to look at the influence of shear thinning and viscoelasticity. Tanner's paper [36] on the flow between two rotating cylinders with equal peripheral speeds for the case of a viscoelastic fluid that obeys the Maxwell law leads to the interesting conclusion that the pressure profile through the nip is qualitatively the same as that for a Newtonian liquid. However, the magnitude of the pressures involved is less in the case of the latter, and this leads to the production of a thinner film for a given load. The inlet boundary condition used was the same as both Gatcombe's and Martin's, in that the inlet pressure is zero; the downstream condition on pressure was that given by the Reynolds condition, that is equation (1.2).

The flow patterns in the coating bead between contra-rotating cylinders (forward mode) was studied by Richardson [37] and Gaskell et al. [38] who examined the effect of the flow rate entering the bead on presence and location of the saddle points and the associated streamline pattern. The starved inlet regime was also examined (see section 1.3) as was the effect of differing roll speed ratios. The stagnation-saddle point was located on the boundary of the recirculating flow on the downstream side at the leading edge of this recirculating region only at equal roll speeds. As the flow entering the coating bead was decreased the downstream stagnation point was observed to move towards the minimum roll gap location.

Benkreira et al. [31] assessed the importance of shear thinning for a liquid whose viscosity follows a power law and concluded that the effect of increasing pseudo-plasticity gives a slight increase in flow through the nip. Coyle et al, [39] also showed, using lubrication theory, a 2-D finite element analysis and experiments that increasing the level of shear thinning leads to an increase in flow through the nip. They also present experimental results for viscoelastic fluids which show how viscoelasticity can drastically alter the flow and greatly decrease the region in which the coating is stable.

1.2.2 Reverse Roll and Metering Roll Coating

Both reverse roll and metering roll coating can be modelled using the same method. With reverse roll coating the back up roll with which the web is in contact, traverses the coating bead in the opposite direction to the applicator roll. In the case of a metering roll it rotates in the opposite direction to the applicator roll, with the fluid that is coated being that which is left on the applicator roll, which is either subsequently transfered to a web or the web is wrapped around the applicator roll itself. Two typical arrangements are shown in figure 1.8.

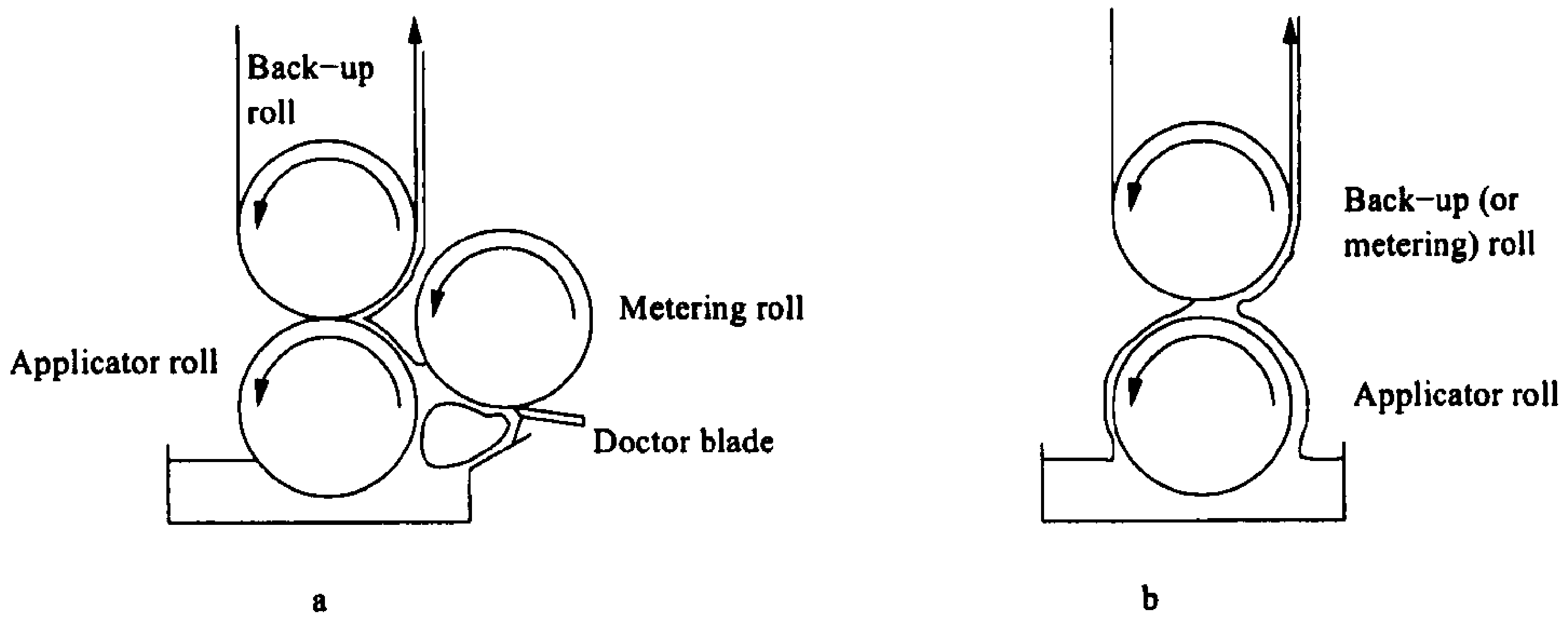

Figure 1.8: Reverse roll coater with (a) metering roll and (b) no metering roll

Reverse roll coating was originally patented by the Champion Coated Paper Company [40] in 1932 (United States Patent Office and in Germany a short time after). Either a doctor blade or a doctor roll is used to meter the fluid onto the applicator roller. It is claimed that the web speed and the fluid properties have "practically no influence on the thickness of the layer". An elastomer covered backing roller is also specified in the construction of the apparatus. However no experimental evidence is provided in the patent application.

Ho & Holland [41] studied reverse roll coating using lubrication theory. Surface tension was not accounted for and the pressure assumed to be atmospheric far downstream of the metering gap and at the point of minimum separation, where the web leaves the backing roll and where the film is assumed to leave the metering roll. The solution is the same as that obtained using the Sommerfeld condition with the pressure going to zero far upstream and downstream (resulting in a zero pressure at the point of minimum separation due to symmetry, which is why this boundary conditions yield the same results). Experimental data appears to agree well with the results obtained theoretically, at least at high speed ratios. Film thickness is shown to decrease linearly with the ratio of metering roll speed to backing roll, and to increase linearly with the gap. The influence of gravity on the results was examined and it was determined that gravitational terms accounted for less than 4% of the pressure terms for the cases studied.

Reverse roll coating was examined experimentally by Benkreira et al [33], illustrated schematically in figure 1.9.

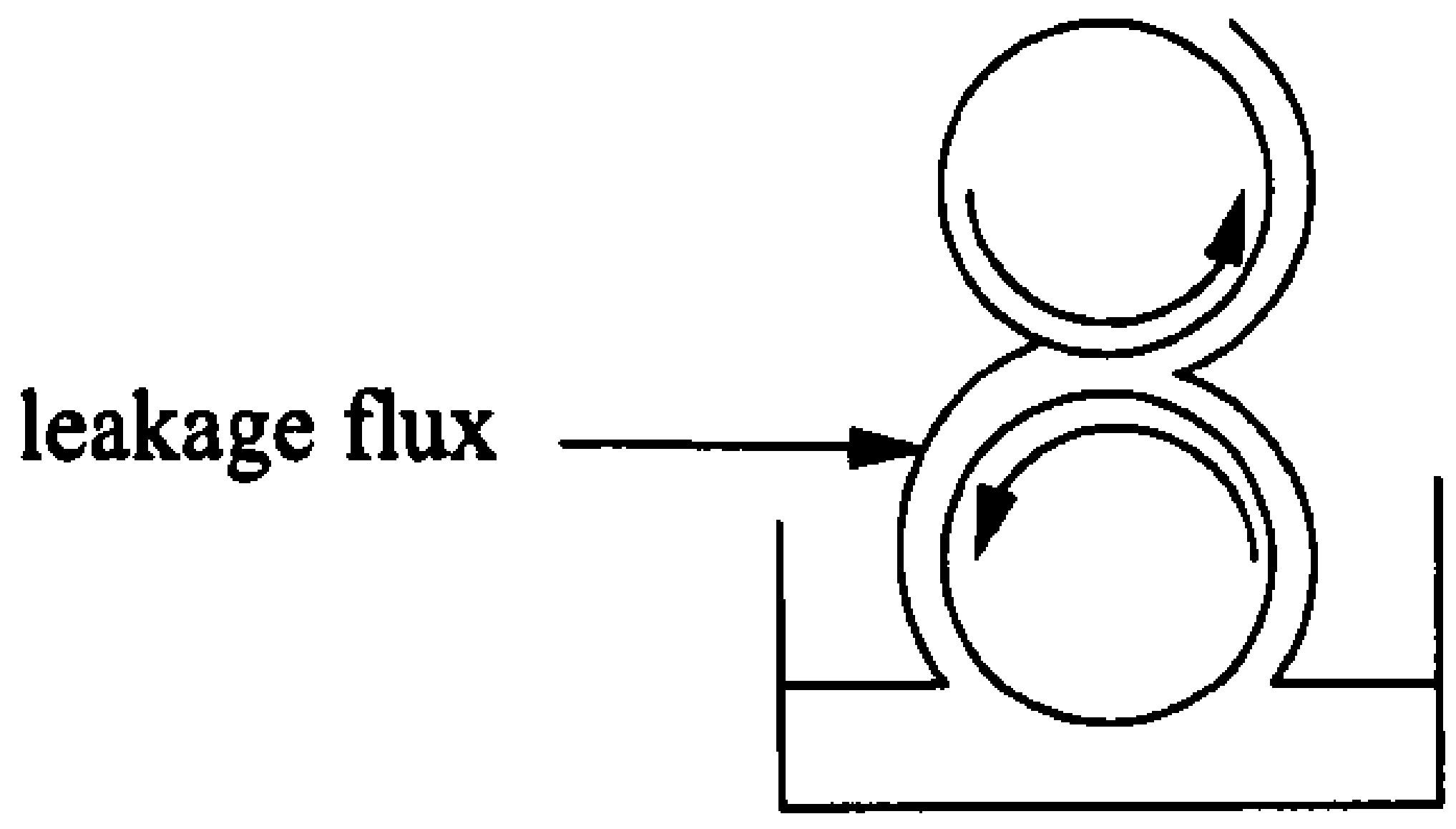

Figure 1.9: Reverse roll coating configuration with backing boll

For the reverse roll case leakage flux, the flux remaining on the applicator roller (also known as the metered flux) is given by the expression:

$$q_L = 0.63h_0\left(u_B - u_T\right). \tag{1.5}$$

In a further paper by Benkreira et al. [32] a mathematical model for reverse roll coating was developed. In this model a method of guessing a flux, fitting a streamline to it and calculating the pressure error is used. Good agreement was found between results from the model and experimental data. It was shown that although the flux has a weak dependence on other factors over the parameter space investigated the results yield the following relationship:

$$\frac{q_L}{h_0\left(u_B - u_T\right)} = 0.62 \pm 2.7\%, \tag{1.6}$$

which is in clear agreement with the empirical relationship given by equation (1.5).

Around the same time as the papers published by Benkreira et al. appeared, Greener & Middleman published a paper on the reverse roll coating of viscous and viscoelastic liquids [42] with rolls horizontally aligned. An easily observable region of circulatory flow upstream of the nip is reported. Despite this two dimensional flow upstream of the nip, the nearly parallel flow in the nip allowed a lubrication model to be developed, with the pressure set to zero far upstream of the nip and the Swift-Stieber condition used downstream of it. Their equation for the dimensionless flux is very similar to that derived by Benkreira et al. (equation (1.5)). Experimental results are in agreement with theory for high speed ratios; however, as speed ratio decreases the theory fails to capture the film thickness trends of the experiments. It was proposed that the reason for the discrepancy is that the two dimensional flow moves closer to that in the nip and therefore influences the flux.

In a paper by Coyle et al [43] the excessive flow rates obtained by Greener & Middleman are attributed to the three dimensional nature of the flow at the ends of the rolls. As the model is based on rolls half submerged the flow through the gap is derived from the difference in film thickness on the applicator roll and that on the metering roll. Therefore for low metering roll speeds there is a large amount of liquid above the nip, some of which escapes at the ends of the rolls, leading to the discrepancy. Gravitational forces were considered to be significant for low metering roll speeds as the hydrostatic head was important and the roller gap to diameter ratio was greater than that of the experiments of Ho & Holland; a hydrodynamic head did not feature in the work of Benkreira et al since the rolls where mounted vertically, thereby reducing the influence of gravity on the flow through the nip.

Using experiments and by obtaining finite element solutions of the Navier–Stokes equations the flow in the metering gap of a reverse roll coater was examined by Coyle et al [44], The streamline patterns generated show that there is a large region of circulatory flow at the upstream side of the nip. A smaller region of circulation was also seen under certain conditions (low capillary numbers) at the downstream side of the nip near the dynamic wetting line. For low speed ratios $\left(\frac{V_m}{V_a}\right)$ the film thickness follows the equations derived by Ho & Holland [41], Greener and Middleman [23] and is similar to that obtained experimentally by Benkreira et al [32]. At higher speed ratios (greater than 0.7) lubrication theory fails to agree with Coyle's computational and experimental results. As the speed ratio increases the film thickness reaches a minimum before increasing again. The reason for this is that the dynamic wetting line can move through the point of minimum separation resulting in the minimum gap the fluid *"sees"* increasing to the gap at the wetting line. Viscoelasticity was found not to be a major factor influencing the flow through the nip.

Reservoir fed reverse roll coating is an important variant of reverse roll coating. A paper by Thompson et al. [45] studies the process experimentally, analytically and computationally. The experimental results show that when the wetting line is far enough downstream of the nip the flow rate increases with reservoir level. Their visualisations and numerical simulations show the flow in the reserviour to be highly re-circulatory. One of the most interesting features of their lubrication model is the incorporation of Shikhmurzaev's [46] theory of hydrodynamic wetting to determine the dynamic contact angle, while the Landau-Levich boundary condition [2, 3] is used to model the meniscus pressure and location.

The case of reverse roll coating with non-Newtonian liquids was considered by Coyle et al. [47]. A modified capillary number based on the average shear viscosity at the nip was used and showed that shear thinning had little influence on film thickness compared to a Newtonian liquid with the same capillary number.

1.3 Meniscus Roll Coating

Meniscus roll coating is similar to the classical flooded form and although used by industry for many years [48] the first experimental investigation of the process was conducted by Malone in 1992 [49]. In his experiments the difference in the flow structure present for flooded and starved inlet (meniscus) roll coating is revealed. Flow visualisation studies for contra-rotating rolls show the existence of two large eddies and a transfer "snake" transferring fluid from one roll the other. Both forward and reverse operating modes were subsequently investigated experimentally by Gaskell et al. [50] who highlighted the fluid transfer jets present for both operating conditions and for differing degrees of inlet starvation.

An analysis of the forward mode of operation is provided by Gaskell et al. [51] using both the finite element method, and lubrication theory together with solutions of the idealised Stokes flow in a rectangular cavity driven by two opposing moving surfaces (at the top and bottom lids of the domain) to simulate the moving rolls. The solution of the Stokes flow for zero flux captures the two eddies observed experimentally; this was confirmed by corresponding finite element solutions. Both the finite element and lubrication models predict entirely sub-ambient pressures within the bead, with the bead pressure distribution becoming more like that of the flooded form of the roll coating process (having a positive pressure at the upstream side of the minimum gap and a negative pressure at the downstream side) as the inlet flux rises. An extensive complementary analysis of the reverse mode of operation is provided by Richardson [37].

A comprehensive analysis of the internal flow structures that can arise in the bead of a twin roll coater operating in forward mode is made by Summers et al [52]. The inlet flux is varied from the flooded regime to that of the starved regime and a combination of lubrication theory and the finite element method is used to show the eddy structures present as well as the upstream and downstream meniscus locations.

1.3.1 Stability

One of the earliest papers detailing the ribbing instability is one by Hoare [53] describing variations in thickness of tin plating. The method employed involved a pinhole source of light producing a reflected pattern on a screen. A similar method was to be used over 50 years later by Coyle et al [54] to visualise the ribbing pattern at the meniscus. A more detailed examination of the ribbing phenomena for forward roll coating was carried out by Chalmers & Hoare [55], in which the gap between the rollers was found to alter the ridge wavelength. It was recognised that increasing the speed of the rolls and the viscosity of the liquid reduced the spacing of the ribs, however, erroneously, the stabilising force was considered to be gravity and there is no mention of the fluid surface tension. Perhaps the earliest paper detailing instabilities in ink based coating is that of Sjodahl [56] where a brief mention of the ribbing instability is made.

Early work by Myers and co-workers [57, 58, 59, 60] focused on experimental methods to visualise film splitting. A novel disc-cone (termed the discone) was used and empirical relationships obtained relating the number of bubbles formed in the cavitating fluid to various parameters such as velocity and viscosity. In the first paper by Miller and Myers [57] the formation of filaments at the downstream meniscus was investigated, where it was found that at high velocities filaments were observed to be present and that the number of filaments increased as the plate and cone velocities increased. Their proposed explanation for this is that small cavities form close to the downstream meniscus and the resultant bubbles grow, and as the gap increases the filaments form.

Pitts & Greiller [25] examined the stability of the films formed on two counter rotating (forward mode) rolls. In their experiments it was shown that the parameter at which ripples (ribs) are first clearly observed is a function of an adapted capillary number, $Ca^{\star}$. Experimental observations led them to conclude that at the critical conditions the following relationship holds:

$$Ca^{\star} \approx 62\frac{h}{R}, \tag{1.7}$$

(where h is the half gap width and R is the roll radius). The theoretical results derived by Pitts & Greiller follow a relationship similar to that of equation (1.7), however their constant of proportionality, around 28, is considerably less than that obtained from experiments. The importance of surface tension was also examined by allowing ether to collect round an otherwise stable meniscus and observing ribs forming due to the consequent reduction in surface tension. By using a small perturbation analysis, stability criteria were obtained to predict the onset of the ribbing instability.

An experimental investigation of ribbing in forward roll coating was made by Mill & South [61], with rollers moving with an equal surface speed and the inlet to the nip flooded. The number of ribs per centimetre was shown to increase with capillary number before remaining constant. An empirical relationship for the onset of ribbing was determined as:

$$Ca = 10.3\left(\frac{2h}{R}\right)^{\frac{3}{4}} = 17.3\left(\frac{h}{R}\right)^{\frac{3}{4}}. \tag{1.8}$$

In a paper by Savage [24] the boundary conditions used to solve the location and pressure of cavities is reviewed. He examined the stability of the cavity-liquid interface to small disturbances and reproduced the important result of Pitts & Greiller, namely:

$$\frac{d}{dx}\left(P + \frac{\sigma}{r}\right) \leq 0 \tag{1.9}$$

Greener et al. [62] undertook experiments to determine the onset of ribbing and it was found that ribbing is first observed under the following conditions:

$$Ca = 7500\left(\frac{h}{R}\right)^{2} \tag{1.10}$$

A comparison is made between the predictions of Pitts & Greiller as well as with theory based on the Coyne & Elrod [6] model and lubrication theory, the conclusions being that neither of these models predict the onset of ribbing with any accuracy.

Using the semi-empirical model arrived at by Benkreira et al. [30] and the cavitation model derived by Coyne & Elrod [6] the operating conditions under which ribbing in forward roll coating becomes apparent was examined by Benkreira et al [63]. From equation (1.9) the pressure gradient is substituted for using lubrication theory and the unknowns (meniscus radius and flux) are provided from one of two coating models. Good agreement is found between the two models. However the use of lubrication theory to determine the pressure gradient at the meniscus may not be valid as the flow close to the meniscus has been shown to be highly two dimensional [25].

Coyle et al. [54] examined the stability of counter rotating (forward) roll coating, using an experimental method of reflecting an oblique light off the meniscus to observe smaller disturbances than otherwise seen with the naked eye. A finite element analysis was also undertaken and led to the discovery of a pair of vortices in each rib which decay rapidly as they move downstream. The onset of instability as predicted by the finite element method showed excellent agreement with the published experimental data of Pitts & Greiller [25], Mill & South [61], Greener et al [62] and Benkreira et al [63]. The work also highlighted that although the various empirical relationships available appear to be in disagreement, when plotted together the data on the whole appears to be similar, to within a reasonable range of scatter. The data recorded using the light reflection method is not in agreement with and the capillary number for the onset of instability is far less than that predicted by the finite element analysis and by previous authors. The explanation for this is that the three dimensional nature of the coating apparatus results in curvature at either end of the roll, producing a standing wave along the meniscus. Using a novel visualisation method of making false ribs out of string and vinyl sheet, Hasegawa and Sorimachi [64] correlated roll capillary number with rib frequency and rib amplitude for two counter-rotating rolls in a variety of conditions.

The stability of reverse roll coating has been examined in less detail. Daniels [65] used lubrication theory and a linear stability analysis to predict the onset of the ribbing instability. He also considered the effect of the additional radius of curvature produced by the ribbing instability and showed that it had a minor effect on the onset of the instability. Coyle et al [44] examined the stability of reverse roll coating and looked at the instabilities on a metered film (the film appearing from the downstream meniscus). At low metering roll speed to applicator roll speeds ribbing was observed, just as it can be present in forward roll coating. As the speed ratio was increased the amplitude of the ribs decreased until the roll surface appeared to be uniform to the naked eye. As the speed ratio was increased further an instability termed the cascade instability (characterised by lines of varying thickness in the direction of the axis of the coating roll) becomes apparent. The reason for this instability is shown in figure 1.10 and is outlined below.

Cascade Instability Mechanism

a) With the contact line past the point of minimum separation the viscous forces result in much of the fluid being transfered to the metering roll.

b) This results in turn in the contact line moving towards the point of minimum separation,

c) and passing though it.

d) The film on the applicator roll now increases as the minimum separation the fluid *"sees"* is reduced. If this increases until the film on the applicator roll contacts the metering roll and refills the gap between the two rolls the cycle begins. However if the film does not completely fill the gap then the contact line can remain stable upstream of the minimum point of separation.

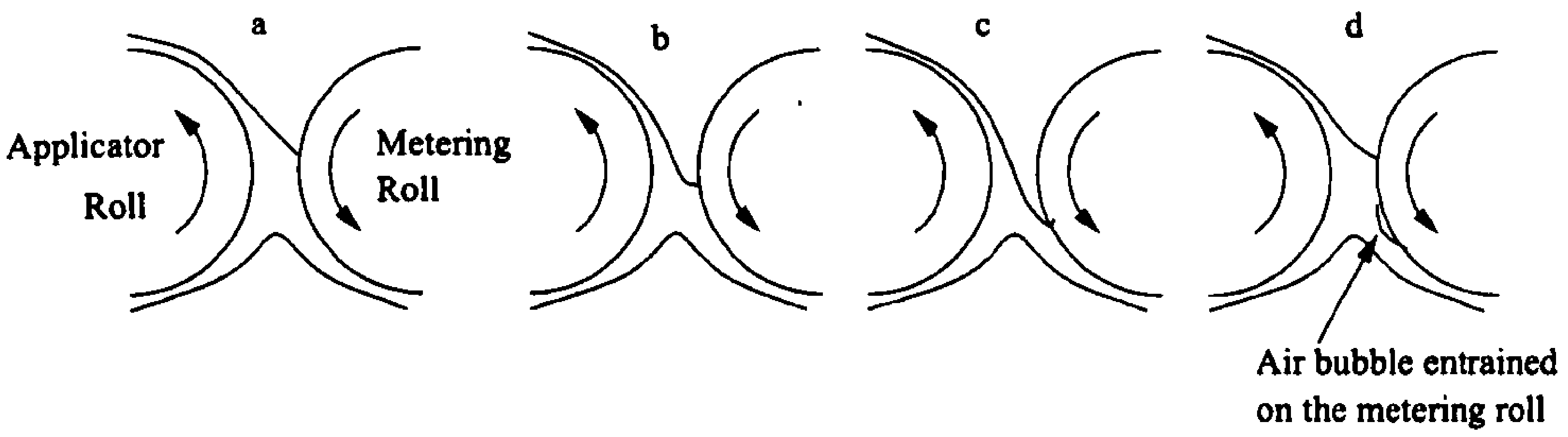

Figure 1.10: Explanation proposed by Coyle et al. for the cascade instability

The bead break instability was first observed in both forward meniscus roll coating by Malone [49]. This instability arises when the continuous liquid bridge between the two rolls breaks. An analysis of this instability was made by Kapur [66] and Gaskell et al. [67] and a criteria for the onset of instability determined.

1.4 Gravure Roll Coating

Gravure, or etched, rolls are used in the manufacture of a vast array of products requiring continuous sheets of material such as paper, plastic or metal foil to be coated with a continuous liquid (typical viscosity $1 - 1500mPas$) at speeds up to 10m/s, producing wet coat film thicknesses in the range 1 to $50\mu m$ [68]. Despite this, there has been little work to explore the fundamental fluid dynamics of the process, nor have any predictive analytical models emerged. The patterned surface of the roll is comprised of either discrete cells or continuous grooves running round the roll surface. Such rolls are manufactured either by knurling against a hard steel master or by using a laser to engrave a ceramic surface coated onto the roll. There is a wide range of patterns available which can be sub-classified as discrete (e.g. quadrangular or laser engraved cells as shown in figures 1.11(a) or 1.11(b)) or continuous (e.g. the tri-helical engraving shown in figure 1.11(c)). Tri-helical grooved rolls have grooves that normally are pitched at 30° to 60° to the roll axis, with the most typical angle being 45° [69, 70].

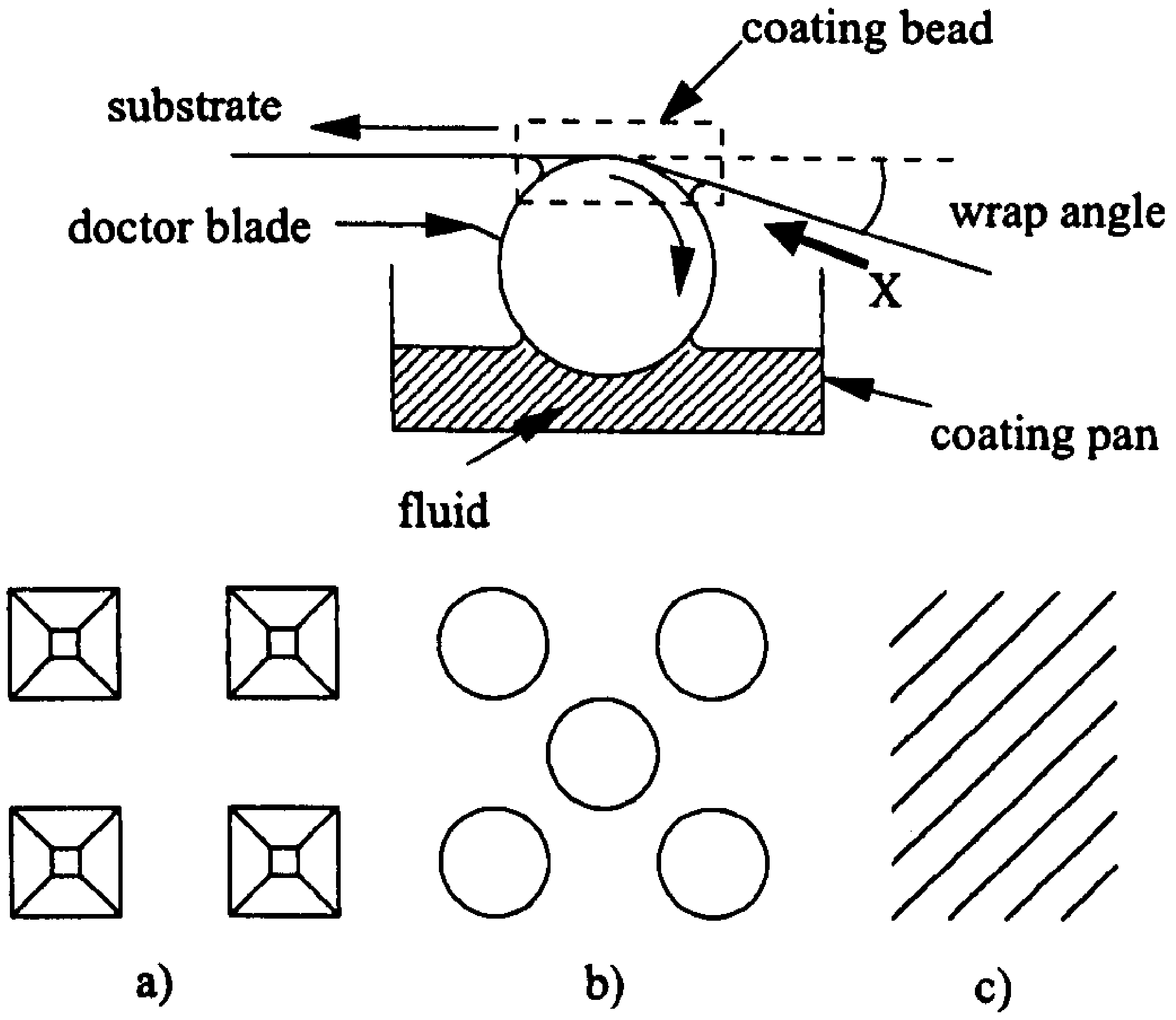

Figure 1.11: Cross sectional schematic of a reverse gravure roll coating arrangement.

The principle of operation is simple, the rotating gravure roll is first coated with an excess of fluid as shown in figure 1.11, either by partially submerging it in a coating pan or using a sealed doctor chamber. Fluid is doctored from the roll surface (lands) using a doctor blade; this ensures the engravings on the roll act as an efficient metering system. A fraction of the fluid is then transferred from the engravings to the web by the action of the latter moving over the roll. Direct gravure roll coating systems can operate in either forward or reverse mode; in the former the web and roll enter and pass through the coating bead (the location at which liquid is transferred from the roll to the substrate) in the same direction, in the latter the roll and web run counter to one another (as in figure 1.11). The reverse mode of operation is the one in most common use due to its generally improved stability of operation [71]. Both the doctoring and transfer mechanisms within the bead affect the final coating.

1.4.1 Roll Doctoring

Direct gravure coating uses a scraper to remove fluid above the roll lands, the properties of which influence the fluid remaining on the roll, as investigated by Patel & Benkreira [72]. Their experimental results show how the change in gap (between roll and blade attachment point) affects the film thickness. They noted that the film thickness increases at a slower rate than the increases in the slot gap. The doctor blade arrangement examined was a trailing doctor blade; reverse angle doctor blades were not considered. Pranckh & Coyle [73] discussed the influence of blade stiffness and loading as well as groove geometry, including that of tri-helically grooved rolls. It was stated that for stiff blades or deep grooves there is little clearance between the blade and land resulting in the fluid being metered almost exclusively by the cell volume. Blade wear and its influence on coating thickness was an area examined in a paper by Hanumanthu [74]. A semi-empirical model based on wear and the relation between the bevel angle and tangent angle of the blade was produced. Again only trailing angle doctor blades were examined.

1.4.2 Forward Gravure Roll Coating

An early paper by Pulkrabek & Munter [75] is one of the first on the subject of gravure roll coating. The paper is concerned with the design of gravure rolls to give a uniform coating (the gravure rollers used were all tri-helical). Two main classifications of non-uniform pickout (i.e. ratio of flux on the web to that entering the coating bead on the roll) are identified, called flashing (when one or more grooves of fluid fail to be picked out) and multiple line pickout (when large uneven ridges of fluid are deposited on the web caused by one or more groove combining at the instance of splitting). To visualise these instabilities very viscous fluids were used. A study was made of how the natural frequency of the fluid, dependent on the thickness of the coat of liquid, affects stability. Matching the groove pitch to the natural frequency of the roll was found to result in stable pickout. It was stated, without any supporting data, that the pickout for a wide range of parameters was about 59%.

Hanumanthu & Scriven [76] compared results of gravure roll coating with those for smooth roll coating and concluded that the transferred film thickness is less for gravure roll coating than for an equivalent volume factor of the knurl on a smooth roll. A comparison is made that shows that qualitatively, the film thickness changes in the same way for both coating methods. The ribbing stability problem was also investigated and a similar conclusion to that made by Pulkrabek & Munter [75] drawn.

Benkreira & Cohu [71] studied forward direct gravure coating experimentally. It was observed that a stable film could only be produced within a narrow window of operating conditions. The same three roll geometries as previously used by Benkreira and Patel [77] were investigated and the stability examined, both air entrainment and ribbing instabilities were observed outside a narrow and complex stable coating window. The film thickness was found to be 15-20% of the equivalent film thickness on the roll (the film thickness on a smooth roll with the same volume as that contained within the gravure cells, V_c) and given by the following equation:

$$H_t = \frac{SV_c}{\beta S^{1.65} + 1}, \tag{1.11}$$

where S is the speed ratio and β is a constant given as being between 2 and 3.

1.4.3 Reverse Gravure Roll Coating

Experiments exploring the film thicknesses produced by reverse direct gravure coating by Benkreira & Patel [77] resulted in an expression for the film thickness (H_t) in terms of cell volume per unit area of surface (V_c) and fractional area of cell opening (A_c):

$$H_t = 0.3\frac{V_c}{A_c}. \tag{1.12}$$

This simple relationship is given to hold for a range of speed ratios, capillary numbers and the three different roll designs used, (quadrangular, tri-helical and pyramidal).

More recently Kapur [78] undertook a parametric study of reverse roll gravure coating where it was shown that cell geometry is an important factor in determining the pickout and therefore film thickness. Film thickness was found to vary linearly with speed ratio below a value of about 1.5 and then remained fairly constant at higher speed ratios. This corresponds to a quadratic relationship between speed ratio and fractional pickout as the speed ratio increases up to $S = 1.5$ before increasing linearly until streaking is observed. An increase in viscosity or a decrease in surface tension was also found to increase the pickout. The geometry of the gravure cells was discovered to have a significant effect on the transfer of fluid, with laser engraved cells producing a greater pickout than mechanically engraved cells. Kapur proposes that this may be due to the smoother profile of the laser engraved cells.

1.4.4 Numerical Models

Rees [79] considered a patterned surface moving beneath a pinned meniscus and developed a three dimensional numerical model; Schwartz et al [80] used a similar method and produced a multi-cell model (a 3D equivelent of that produced by Rees). The numerical results do not completely model the gravure coating process as meniscus curvature and height of the pinned meniscus above the surface are input parameters. However it was shown that increasing the cell size results in greater pickout and that the cell orientation is an important factor. For the same cell size rotating a square cell by 45° greatly increases pickout. A two dimensional extension to the work of Rees and Schwartz et al is made by Powell et al [81]. In their model a web-land height and web velocity is imposed as is a pressure gradient to produce emptying of the rectangular grooves.

Yin & Kumar [82] modelled the flow between a flexible substrate and a patterned surface using the lubrication approximations for two dimensional flow. A simple model for the web was employed with deformation based on the local pressure. The resulting deformation illustrates the importance of elastohydrodynamic lubrication in the discrete cell gravure roll coating process.

1.5 Fluid Rheology

Fluid viscosity is of great importance to coating flows in that it dictates the magnitude of the viscous forces in a system. The viscosity of a fluid relates the strain rate and fluid stress and in its simplest form is a constant coefficient. Many fluids display this Newtonian property including air, water and glycerol. Due to the nature of more complex coating fluids, non-Newtonian viscosities are not uncommon (and perhaps the norm), the most common of these are shear dependent and viscoelastic fluids [83]. Shear dependent fluids (also known as generalized Newtonian fluids) have viscosities dependent on only the local strain rate (for shear dominated flows) and fall into two categories, shear thinning (or "pseudo-plastic") and shear thickening (or "dilatant"). Shear thinning fluids exhibit a decrease in viscosity with increasing shear rate, the reverse is true for shear thickening fluids. Viscoelastic fluids, as the name suggests, exhibit both viscous and elastic properties. These elastic properties may be time-dependent or non-linear and can lead to unusual behaviour, arising from normal stress differences such as the climbing of fluid up a rotating rod [84, 85] and the presence of a convex free surface for a fluid flowing down a tilted trough [86].

1.5.1 Generalised Newtonian Fluids

As coating fluids commonly exhibit shear rate dependent behaviour [69] we examine generalised Newtonian fluids (where shear stresses dominate the flow and time dependence is minimal) in more detail. Most generalised Newtonian fluids are shear thinning in nature and a number of different empirical models exist that describe local viscosity as a function of shear rate. The generalised Newtonian fluid relationship is:

$$\tau_{yx} = -\eta \frac{dU}{dY}, \tag{1.13}$$

where η is a function of $\left|\frac{dU}{dY}\right|$ (τ_{yx} is the shear rate, and $\frac{dU}{dY}$ the strain rate). To extend this definition to arbitrary incompressible flow we have:

$$\tau = -\eta\dot{\gamma}, \tag{1.14}$$

where τ is the fluid stress, $\dot{\gamma}$ is the rate of strain tensor and η is now a function of the magnitude of the second invariant of the rate of strain tensor, $\dot{\gamma}$, which for two dimensional incompressible flow is:

$$\dot{\gamma} = \sqrt{\frac{1}{2}\left(4\left(\frac{dU}{dX}\right)^2 + 2\left(\frac{dU}{dY} + \frac{dV}{dX}\right)^2 + 4\left(\frac{dV}{dY}\right)^2\right)}. \tag{1.15}$$

For generally shearing flows τ is usually referred to as the fluid stress and γ as the strain rate. A number of empiricisms for η exist, perhaps the simplest and most well known of these is the "Power Law" model [87]. This model describes the viscosity as:

$$\eta = \lambda\left|\dot{\gamma}\right|^{n-1}, \tag{1.16}$$

where the two parameters, λ, the power law consistency factor (dimensions Pas^n), and n, the power law index (dimensionless), are fitted to rheometric data. This simple model is most accurate at predicting viscosities at moderate to high shear rates as viscosity tends to infinity when strain rate tends to zero. The measure of shear thinning or thickening in the power law model is the power index, n. For $n < 1$ the fluid is shear thinning, when $n > 1$ the fluid is shear thickening, and when $n = 1$ the fluid is Newtonian and equation (1.16) becomes $\eta = \lambda$.

A number of other generalised Newtonian fluid models exist, the most common are those of Carreau-Yasuda [88, 89], Bingham [90], Ellis [91, 92] and Cross [93]. These more complex models contain a greater number of constants to describe the shear dependent viscosities.

Limitations of Generalised Newtonian Fluid Models

Generalised Newtonian fluid models are generally considered to be valid when the flow is dominated by shear stresses, with minimal normal stresses and time dependency. There are some flow problems that are not dominated by shear stresses to which the generalised Newtonian fluid models have been applied successfully; such flows include free surface flows where shear stresses vanish at the interface and only normal stresses are present [94, 16]. In these cases care must be taken to ensure that the elastic effects of the fluid are unimportant. A measure of the elastic effects is given by the Deborah number [95, 83] which describes the time it takes for the polymers in the fluid to relax compared to the rate at which the flow is deforming them.

1.6 Free Surface Forming

The formation of a thin liquid layer onto a moving substrate is an important aspect of many coating flows. For example, in the industrial process of coating a substrate with a thin liquid film to modify its functionality [8], in thin lubricating flows in bearings or other moving mechanical devices [13], or in the lung [96, 97].

Much work has gone into understanding these processes which depend on a wide range of different operating conditions such as gravity, surface tension, viscous and inertial forces, as described by Quéré [98, 99]. Two major sub-sections of film forming processes are the withdrawal of a solid surface from a pool (figure 1.12a)) and the withdrawal of a surface from a fluid filled gap (figure 1.12b)). For low Weber numbers ($We = \frac{\rho U^2 R}{\sigma}$, where ρ is fluid density, U is withdrawal speed, R is the characteristic length dimension such as tube radius) inertial forces are negligible. Within the visco-inertial regime the film thickness tends to increase due to inertia as described by Quéré [98, 99] and observed by Tallmadge & Stella [100]. These two cases can take many forms, such as the vertical withdrawal of a substrate from a fixed gap, along with a host of different geometries such as the withdrawal of a wire from the fluid reservoir, the coating of a roll surface or the inside of a fluid filled tube as a bubble is forced along its length. We shall focus on the withdrawal of a substrate from a fluid filled gap (figure 1.12b), as it is the geometry most relevant to smooth roll coating geometries and, as will be shown later, to the the tri-helical coating process.

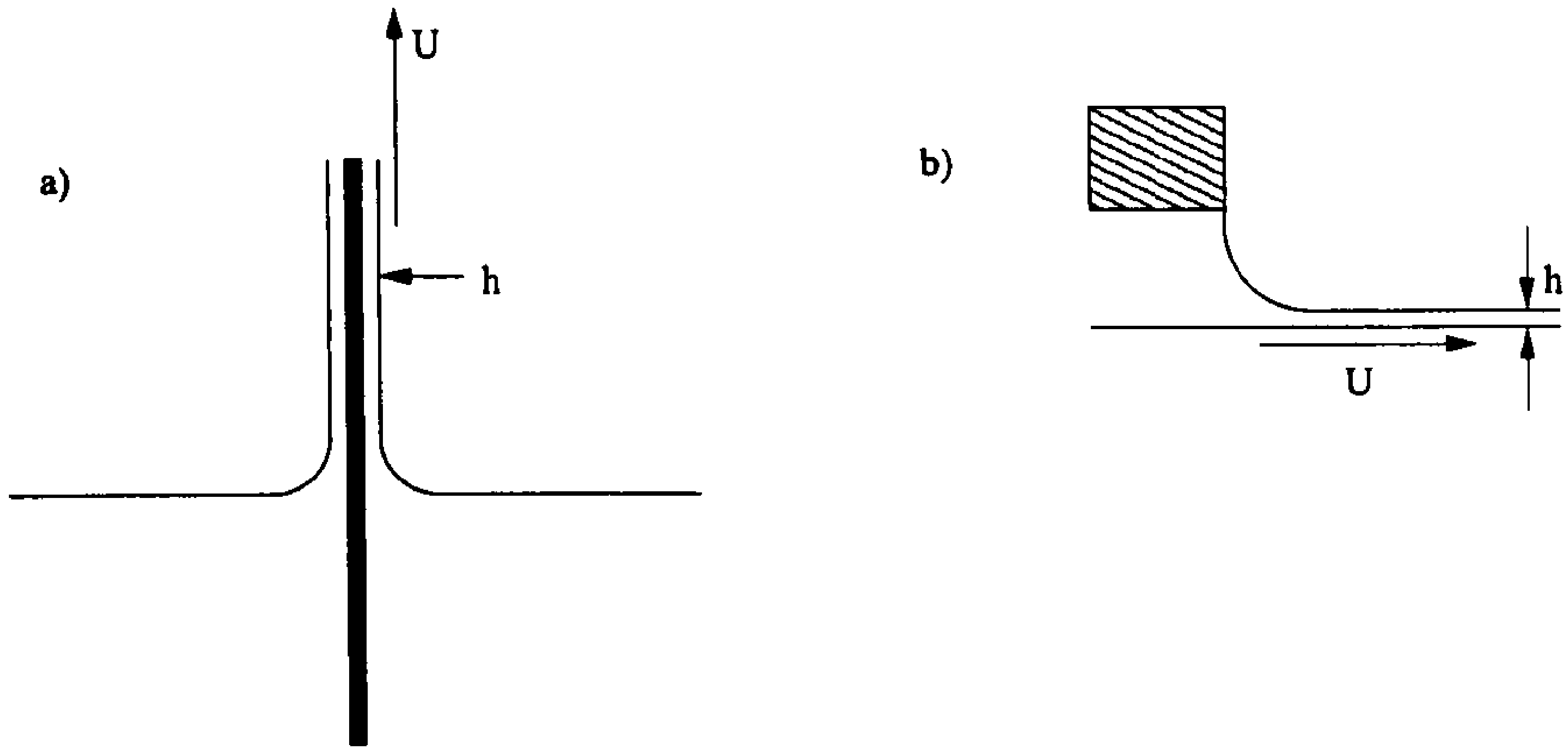

Figure 1.12: Two geometries for fluid coating; a) coating onto a surface being withdrawn from an infinite reservoir; b) coating a substrate emerging from a fluid filled gap.

The problem of withdrawing a plate from an infinite reservoir was first studied experimentally by Goucher & Ward [101] who recognised the importance of capillary number to the liquid film thickness deposited on the moving plate. The earliest theoretical analysis of the withdrawal of a surface from a reservoir is attributed to Landau & Levich [2] who used the method of asymptotic expansion of the meniscus curvature as a function of surface tension, viscous and gravitational forces to obtain the coated film thickness. A similar analysis by Bretherton [3] determined the film thickness on a surface withdrawn from a fluid filled gap. The resulting,now common equation, is given by:

$$H = 1.34 Ca^{\frac{2}{3}} R_{\mathrm{men}}, \tag{1.17}$$

and relates film thickness (H) to the capillary number ($Ca = \left(\frac{\mu V}{\sigma}\right)$, here V is the withdrawal speed, μ is the fluid viscosity and σ is the surface tension) and the meniscus radius, R_{men}. Bretherton's law as described above is used widely and valid for low capillary number flows where $Ca < 0.01$ and a constant meniscus radius is assumed. A summary of this model as derived by Bretherton is given in Appendix A.

Ruschak [4] proposed the following result for higher capillary numbers:

$$H = 0.54Ca^{0.5}R_{\mathrm{men}}. \tag{1.18}$$

However this equation assumes that the meniscus radius is constant, which is only the case when the capillary number is very low (i.e. viscous forces are negligible), this being the basic assumption in the derivation of the Landau-Levich equation. A comparison of Ruschak's equation and the more general Coyne & Elrod equation (detailed below) shows that while the film thickness to gap ratio $\left(\frac{H}{R}\right)$ is captured well by equation (1.18), the radius of curvature of the meniscus as it separates from the gap is not constant as assumed by Ruschak.

Coyne & Elrod [6, 5] derived a set of equations describing the film thickness on a moving surface when drawn out of a flooded gap. They did this by considering the forces acting on the surface of the fluid and by assuming the velocity profile variation tangentially to the surface of the liquid as being quadratic, as is consistent with lubrication assumptions. Under certain conditions (low capillary number, Reynolds number and Stokes number) their model reduces to the Bretherton law [5]. The set of equations are more general than that of the Bretherton law as they permit a variation in curvature along the meniscus. The constants in the quadratic form of the velocity profile are obtained permitting the velocity distribution to be determined and for the associated streamlines to be drawn. The results of the derivation allow the film thickness to be determined as a function of the capillary, Reynolds and Stokes numbers.

The set of equations can be solved relatively easily using the Runge-Kutta or Euler methods, for capillary numbers greater than about 1.1 (with zero Reynolds and Stokes number) where the gap height is 3 times the film thickness. As a stagnation point is encountered at a film height of 3 times the film thickness, a stagnation point and recirculation occur for capillary numbers less than about 1.1; in this region the equations become extremely unstable as noted by Coyne & Elrod. The condition has been used successfully by Greener & Middleman [102], Benkreira et al [63] and Priest et al [13]. Further details of the Coyne and Elrod cavitation model can be found in chapter 3.

1.6.1 Non-Newtonian Film Forming Models

The formation of a fluid obeying the power law onto a plate being withdrawn from a reservoir was analysed by Gutfinger and Tallmadge [103].

Research into the film forming of shear thinning fluids has been examined by Weinstein & Ruschak [17]. In their review of coating flows they examine the work undertaken to study the formation of a shear thinning fluid onto a moving substrate. A semi-empirical equation is deduced and takes a similar form to the Bretherton law in that it relates the final film thickness H_∞ and the meniscus radius of curvature R_{men}, but has an empirically derived constant:

$$H_\infty = \left[K(n)\, R_{\text{men}}\right]^{\frac{3}{2n+1}} \left[\frac{\lambda U_{\text{substrate}}}{\sigma}\right]^{\frac{2}{2n+1}}, \quad \text{where,} \quad K(n) = 2.553e^{-0.65n}, \tag{1.19}$$

where $U_{\text{substrate}}$ is the substrate velocity and $K(n)$ is the empirical function, fitted to data from a finite element analysis. This expression is consistent with the problem of liquid withdrawal from a pool, with $K(n)$ being replaced by a fluid density dependent term as derived analytically by Gutfinger and Tallmadge [103]. Work undertaken by Kamisli & Ryan [7] to solve the film forming problem for power law fluids, using the same approach as Bretherton, ran into problems due to the the slower convergence of the $\frac{d^2h}{dx^2}$ term as $h \to \infty$ (where h is the film thickness and x is the distance along the interface) as the equation describing $\frac{d^3h}{dx^3}$ converges towards zero slower for lower power indices. The equation describing the film formation was shown to be:

$$\frac{d^3h}{dx^3} = \frac{(h-1)^n}{h^{2n+1}}. \tag{1.20}$$

For Newtonian fluids ($n = 1$) equation (1.20) converges like $\frac{1}{h^2} \to 0$ as h tends to infinity. However at the limit of shear thinning ($n = 0$) equation (1.20) converges as $\frac{1}{h} \to 0$, as h tends to infinity. This different rate of convergence is the dominant effect on the results and leads to disagreement with experimental data, as acknowledged by Kamisli & Ryan [7].

1.6.2 Surface Tension Gradient Driven Flow

The presence of surfactants in a coating solution may add complexity to the formation of a liquid film onto a surface. The extraction of a solid surface from a reservoir can lead to a dilution of the surfactant generating a surface tension gradient along the interface, with a high surface tension along the film and a lower surface tension in the reservoir where the surfactant is undiluted. This gradient leads to surface driven flow (Marangoni flow [104, 105]) as reported for the withdrawal of a cylinder from a reservoir by Carroll & Lucassen [106]. Ratulowski & Chang [107] and Park [108] calculated the thickening (increase in film thickness) as being between 1 and $4^{2/3}$ times the calculated inertialess film thickness, depending on the surfactant and concentration. It was assessed by Quéré [98, 99] that for low capillary number the equilibrium value of surface tension is satisfactory, as the difference in surface tension along the withdrawn fluid surface scales like:

$$\frac{\Delta\sigma}{\sigma} = Ca^{\frac{2}{3}}. \tag{1.21}$$

1.6.3 Fluid Wetting Angles

The process of displacing one fluid phase with another (typically a gas phase with a liquid phase) is known as dynamic wetting and occurs in all coating processes. Dynamic wetting is closely related to static wetting, where the surface energies between the different phases describes the contact angle between the fluid phases and the solid substrate. While the physics of static wetting are well developed that of dynamic wetting is less certain.

The static contact angle, θ_S, is defined as the angle the meniscus makes with the solid, as measured through the liquid phase. The static contact angle is related to the surface tensions between the interface of each of the three phases and is given by Young's equation [109]:

$$\sigma \cos\theta_S = \sigma_{SG} - \sigma_{SL}, \tag{1.22}$$

where σ is the liquid-gas surface tension, σ_{SG} is the solid-gas surface tension and σ_{SL} is the solid-liquid surface tension, as shown in figure 1.13.

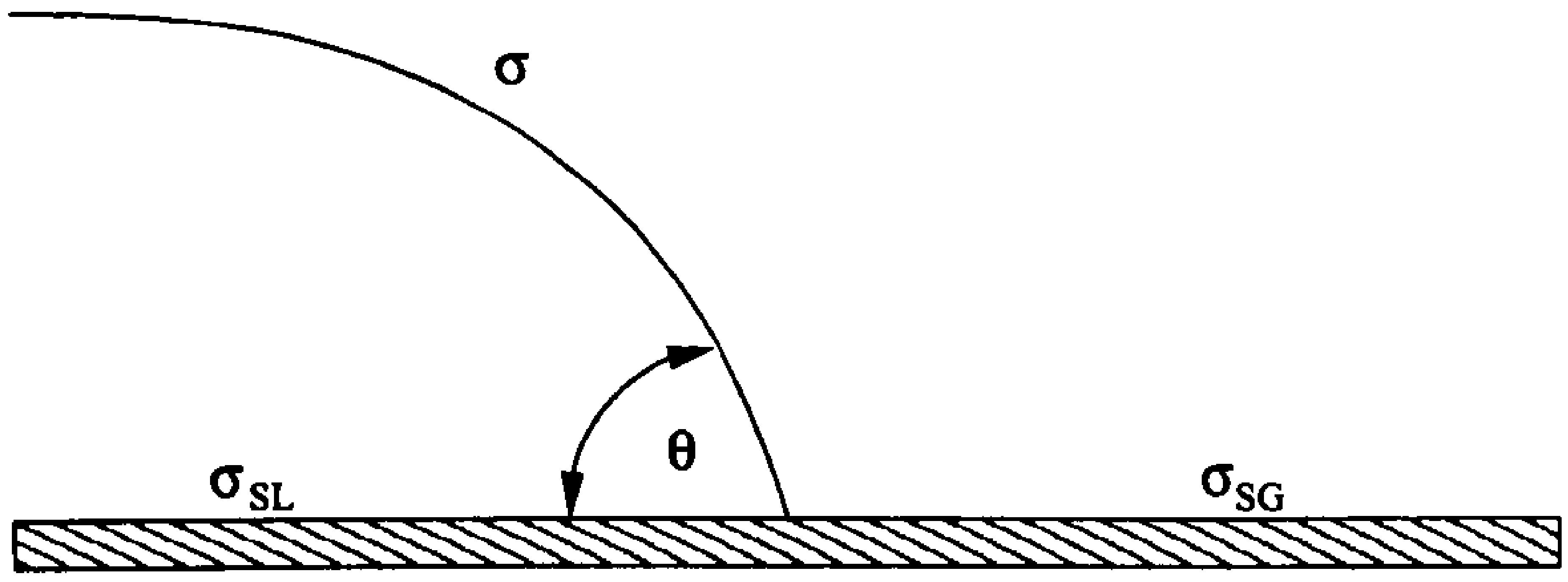

Figure 1.13: Static contact angle and surface tensions.

At a static contact angle of 0° complete wetting occurs and the liquid spontaneously spreads on the solid. Contact angle hysteresis, whereby a range of static contact angles are possible for a given solid/liquid/gas system is often observed and can be attributed to surface roughness or surface heterogeneity, leading to the apparent contact angle when viewed at the macro-scale being different from that observed at the micro-scale and governed by the Young equation. The hysteresis is defined as the difference between the advancing and the receding contact angles, which are the largest angle reached before the wetting line advances and the smallest angle reached before the liquid starts to de-wet the surface, respectively.

A dynamic meniscus is defined as a meniscus that moves with respect to the surface. It has been found that the dynamic contact angle, θ_D, typically differs from the static contact angle [110]. As the speed of the substrate entering a fluid increases then the dynamic contact angle increases beyond the advancing static contact angle. To date no dependable method of theoretically determining the dynamic contact angle has been developed. Two different approaches have been used to model the motion of the dynamic wetting line. The first is the molecular-kinetic theory as detailed by Blake & Haynes [111]. This theory describes the motion of the three phase zone as fluctuating about its mean position (despite the interfacial region being as narrow as 2 angstoms). Both surface tension and viscous forces alter the energy barriers to the displacement moving the interface by setting up a systems that favours the molecular displacements in the direction of wetting. The second method is the hydrodynamic theory in which the meniscus shape is deformed by hydrodynamic forces present at the interface. The singularity arising from the no-slip condition is avoided by truncating the solution from the hydrodynamic forces to molecular scales close to the solid. Several authors have derived the variation in dynamic contact angle with capillary number and determined that θ_D^3 varies linearly with capillary number [112, 113, 114].

A number of authors have experimentally investigated variations in dynamic contact with solid velocity [115, 116, 117], and models developed based on empirical data - all of which confirm that an increase in capillary number leads to an increase in the dynamic contact angle.

1.7 Outline of this Thesis

This thesis examines tri-helical gravure roll coating, which is investigated using a combination of analytical, experimental and computational methods. Chapter 2 describes the experimental apparatus employed, and gives details of the experimental techniques adopted.

Chapter 3 describes the film forming models utilised to describe the coating of a liquid film onto a moving substrate, an important aspect of the coating models developed in subsequent chapters. Coyne & Elrod's film forming model is described including the numerical solution of the stiff set of constituent equations. A new film forming model for shear thinning fluid, obeying the power law, is developed and is used in later chapters for the analysis of the coating of such fluids by means of a limited form of the tri-helical gravure roll coating.

In chapter 4, the first model of tri-helical gravure roll coating for the special case of rectangular grooves and zero groove pitch (i.e. grooves aligned in the direction of web motion), is derived and solved analytically. In chapters 5 and 6 the model is extended to the general case of tri-helical grooves of arbitrary cross sectional geometry with the associated flow equations solved using the finite element method for both Newtonian and shear thinning fluids; for the latter the cross flow component, present in the pitched groove case, is included making the model representative of the industrial coating process.

Chapters 7 compares the zero groove pitch experimental results with those of the analytical predictions from chapter 4 and finite element based predictions from chapter 5. The onset of streaking, a coating defect observed experimentally, is also examined. Chapter 8 compares the predictions of the finite element simulation for non-rectangular grooves at arbitrary groove pitch as well as limited shear thinning zero pitch angle results, against experiment, while chapter 9 uses the validated model to examine the effect of groove geometry and operating conditions on the coating process.

Chapter 10 summarises the main conclusions drawn from the work, and recommends potential avenues for further investigation.

Chapter 2

Experimental Apparatus and Method

The purpose of investigating experimentally a tri-helical gravure roll coater operating in reverse model is to gain a fundamental understanding of the process: (a) by determining the dependence of the film thickness and bead stability on the operating parameters; (b) through visualisation of the coating bead. The latter is critical to identifying valid assumptions to inform the derivation of simplified models of the process and for providing information, such as the position of the web in relation to the lands of the gravure roll, and details concerning the upstream and downstream menisci. The experiments were conducted on a pilot coating rig, carefully designed to encapsulate the essential physics while simulating the industrial coating process.

2.1 Simulation of the Industrial Coating Process

The use of the precision small scale coating apparatus for performing controlled experiments has several advantages over gathering data from industrial coating equipment. These include:

- Cost: non-production time spent using a commercial coating machine designed to run continuously for days at a time can be considerable, making a systematic academic investigation of the process on such apparatus prohibitively expensive.

- Control of geometry: the manufacture of specific groove geometries and associated rolls for use in experiments is cheaper for small scale apparatus, where the coating bead is much more accessible.
- Control of operating conditions: in many industrial processes, coating machines operate over a very narrow range of conditions. On the contrary the experimental apparatus employed was able to span a wide range of operating conditions (albeit at the lower range of operating speeds than encountered in industry).
- Separation of operating variables: the control of individual operating conditions is often not possible in an industrial coating process. For example, some of the coating parameters may be linked - on an extrusion line, the speed and web thickness are frequently linked by the constant flow rate of molten substrate material [118].

In addition, the design of the experimental apparatus was subject to a number of requirements to ensure that clear, consistent and repeatable results could be obtained for well defined or measurable operating parameters. The main experimental requirements were:

- A coating bead that was readily amenable to visualisation, including easy access for light sources to illuminate the bead. The requirement was for visualisation both along the roll axis and from directly above the web, the latter enabled viewing through the transparent plastic substrate of the fluid bead.
- A means to accurately determine the volume of fluid leaving the coating bead attached to the web, allowing accurate measurement of the average fluid film thickness and fractional pickout.
- Efficient removal of excess fluid from the rolls land areas, ensuring that the associated grooves are just full of fluid (i.e. efficient roll doctoring).
- Accurate control of operating conditions such as the web and roll speeds, wrap angle and web tension.
- Accurate measurement of the test fluid properties, namely viscosity and surface tension. Experiments were performed with Newtonian and shear thinning fluids (the latter were characterised by the power law model) in line with corresponding theory developed subsequently.

In addition to the accurate measurement of these parameters, other requirements of the test fluids were (a) that they would not degrade during the course of the experiments and (b) would satisfactorily wet the web.

- Well defined and accurately measurable roll geometries, with minimal roll surface eccentricity.

2.2 Design of the Experimental Rig

The pilot coating apparatus on which the experiments were conducted was commissioned in the 1990's as part of a strategic research initiative between the School of Mechanical Engineering and, what was then ICI Melinex, but has since become part of DuPont Teijin Films, a joint venture by the American DuPont and Japanese Teijin companies. The apparatus (see figure 2.1) was purposely constructed to allow simulation of the full coating process, rather than having to focus exclusively on the roll coating nip [79].

A tensioned web uncoils from one reel to another and passes over the gravure roll, resulting in a truly uncoated web entering the coating bead and reproducing the dynamic wetting line encountered in the industrial process. The apparatus was designed so as to be able to accommodate a range of different coating heads permitting other industrial processes such as curtain, slot and tensioned web coating, in addition to both direct and offset roll coating, to be investigated. The main features of the apparatus are shown in figures 2.1 and 2.2.

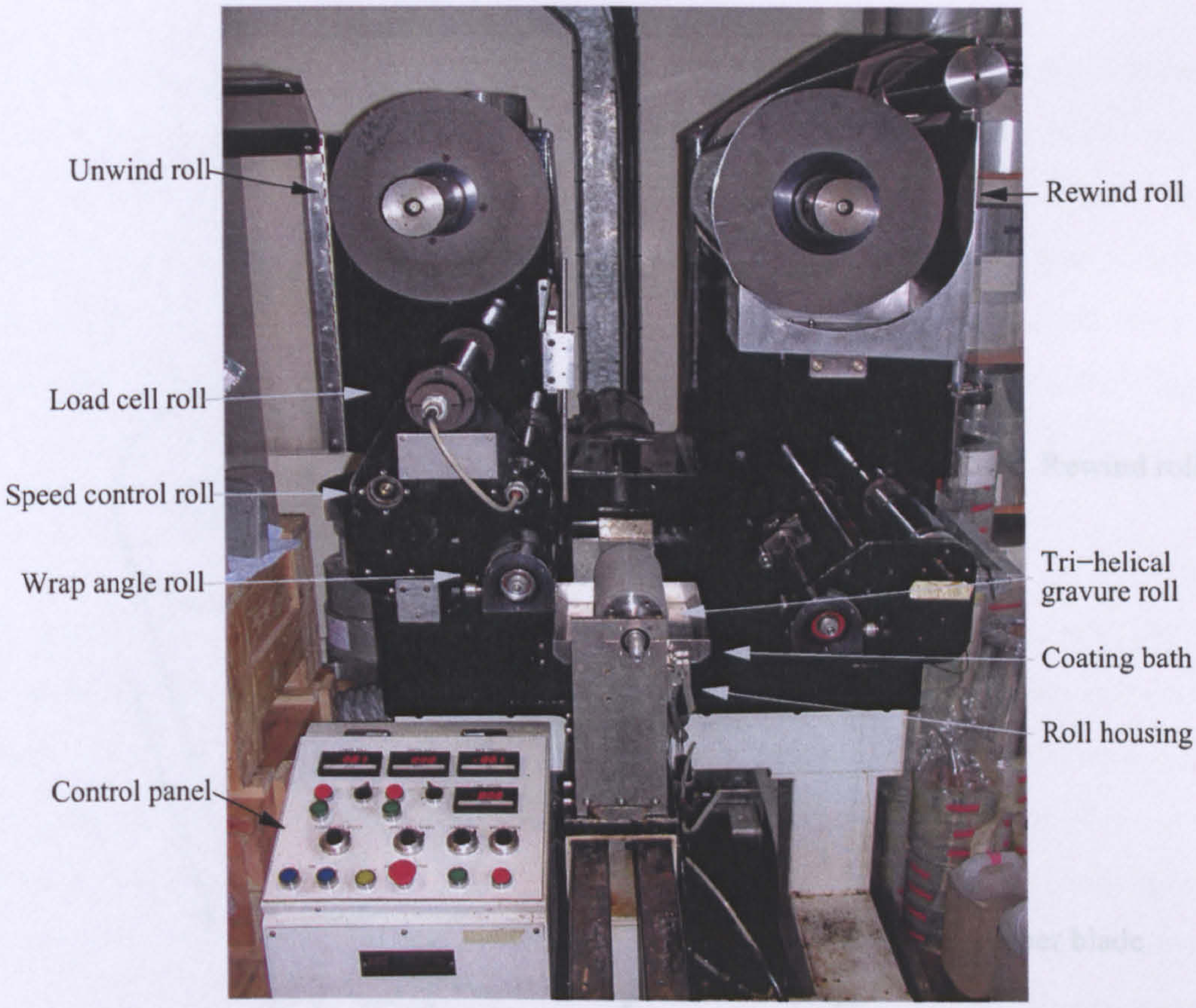

Figure 2.1: Experimental precision coating apparatus as used for the investigation of tri-helical gravure roll coating.

The coating apparatus supports gravure roll coating investigations in both the direct and offset modes, with either a single roll or two rolls mounted one above the other. However, here direct gravure roll coating with a single roll formed the focus of the research and was investigated throughout. Subsequent sections describe the design, installation and operation of the gravure rolls.

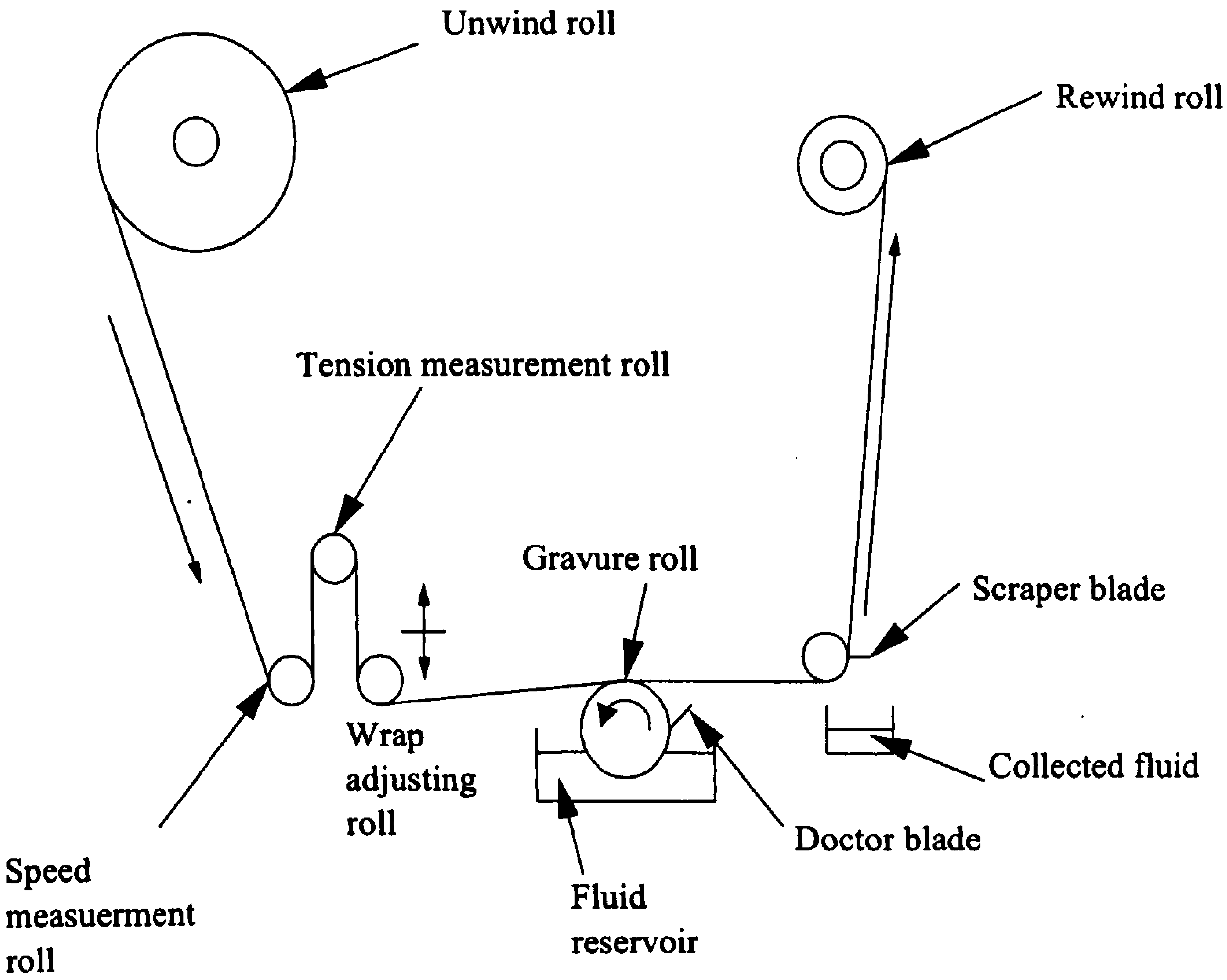

Figure 2.2: Schematic of coating experimental apparatus

2.3 Coating Roll Drive

The roll housing (shown in figure 2.3) was constructed out of $10mm$ thick stainless steel plates, bolted together to form a cradle. The roll shafts were mounted onto this cradle using two sealed bearings (type SKF 6004) located towards the ends of the rolls. The construction of the roll housing from a single block of steel would have been preferential as it would have reduced the potential for run-out tolerances. The rolls were formed from a Perspex sleeve, with the pattern turned into the surface, that was then mounted onto a steel core. Construction of the coating rolls in this way permitted run-out eccentricities to be minimised (the roll design is outlined below) and eccentricity of the roll, if carefully aligned, was found to be less than $0.05mm$.

The gravure roll was supplied with fluid using a simple arrangement where the lower portion of the roll was submerged in a pan of test fluid (typically to a depth of $2cm$), such that as it rotated, it picked up fluid through the action of viscous lifting. Although the level of the fluid in the pan was not tightly controlled, in all cases it provided an excess of fluid on the roll surface. Excess fluid on the lands of the roll was doctored from the surface to ensure that fluid was only contained within the grooves of the roll. Doctoring was performed by a reverse angle doctor blade, made of 220 micron thick Melinex, held against the roll by means of loading the blade with weights suspended from a pulley arrangement. The doctor blade was hinged about one of the rails on which the fluid pan resided and could be used in both the forward and reverse mode of operation, depending on which side of the roller it was positioned. The doctor blade arrangement is illustrated in figures 2.3 and 2.4.

A visual inspection of the grooves, under magnification, was made to ensure that they were *just* full of fluid after being doctored with no fluid observed on the lands of the roll. The influence of doctor blade force was also determined by increasing the mass on the pulley system responsible for holding the doctor blade against the roll; above a minimum mass the coated fluid volume was found to remain constant (as shown for the discrete cell process by Kapur [66]), and it was above this minimum mass ($4kg$) that all experiments were conducted. Doctor blade wear at this loading was not observed during the course of the experiments.

The roll was driven through a 5.72:1 reduction gear box by a five horse power motor which rotated

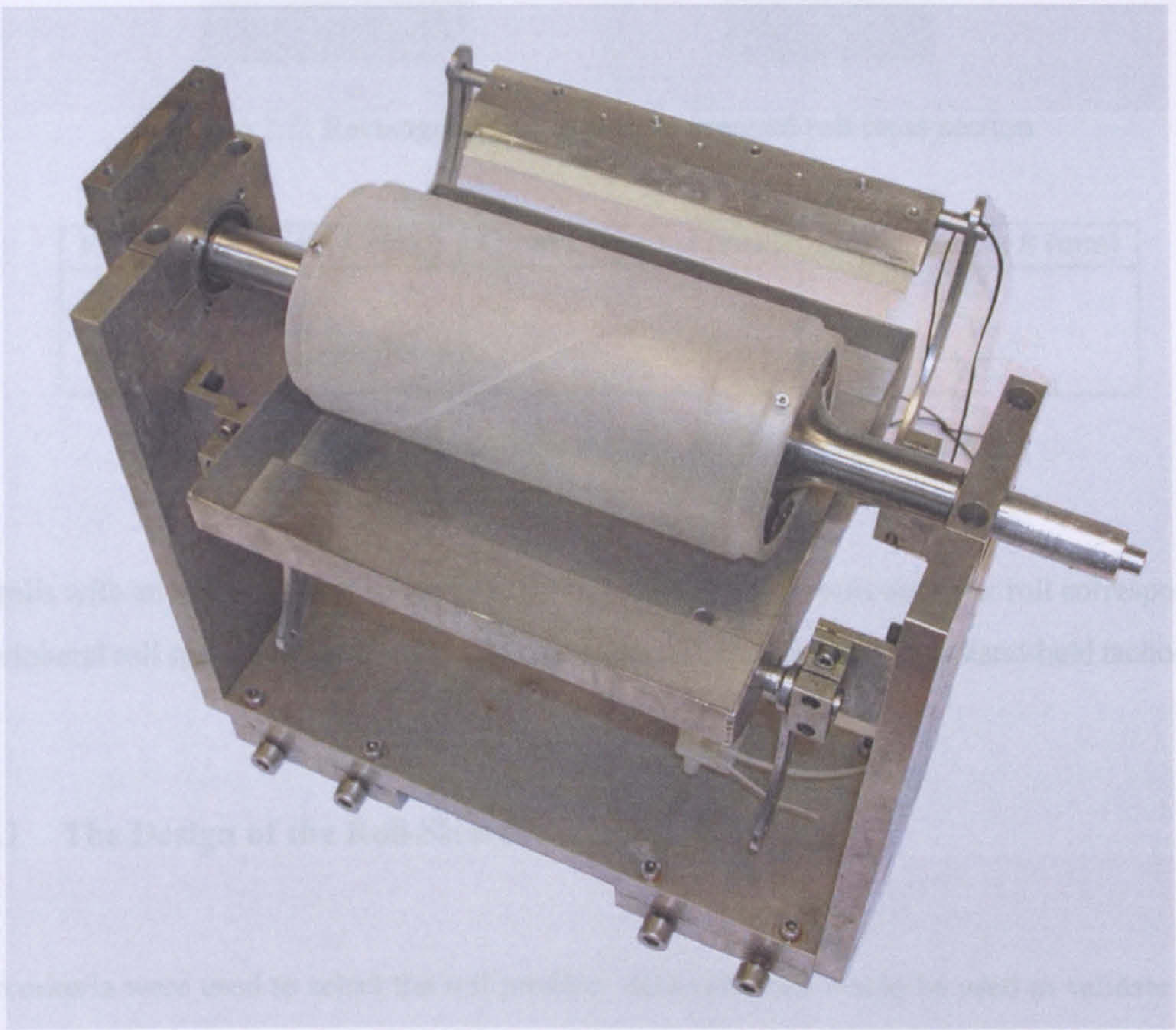

Figure 2.3: Roll mount with roll installed and doctor blade visible

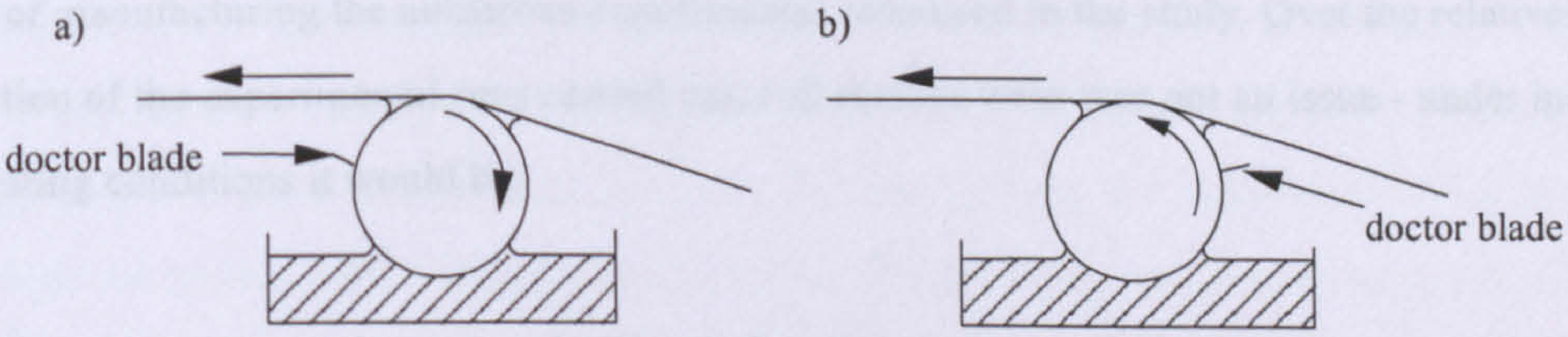

Figure 2.4: Doctor blade position for; a) reverse and b) forward gravure roll coating operations

Figure 2.5: Rectangular and triangular grooved roll cross section

Roll	Land Width L (mm)	Groove Width A (mm)	Groove Depth R (mm)
A1	1	1	0.5
A2	1	1	1
A3	1	1	1.5

Table 2.1: First three large rectangular groove dimensions

the rolls with an angular speed up to $\frac{100}{3} rads^{-1}$, which for a $100mm$ diameter roll corresponds to a peripheral roll speed of $100m/min$. The roll speed was confirmed using a hand-held tachometer.

2.3.1 The Design of the Roll Sleeves

Two criteria were used to select the roll profiles: data collected would be used to validate corresponding mathematical models of the process; the groove geometry had to be such as to allow visualisation of the coating bead. Grooves of rectangular and triangular cross sections were tested, with a range of pitch angles (the angle the groove makes with the plane perpendicular to the roll axis), from 0° to 60° (more precisely 0°, 30°, 45° and 60°), covering those used by industry. The roll sleeves were manufactured from acrylic since it proved easy to machine and facilitated adequate lighting of the fluid bead. The use of acrylic sleeves also simplified and reduced the cost of manufacturing the numerous experimental rolls used in the study. Over the relatively short duration of the experimental runs carried out, roll surface wear was not an issue - under industrial operating conditions it would be.

The first three rectangular grooved rolls employed experimentally had groove dimensions of the order of $1mm$ (see figure 2.5 and table 2.1). Although these dimensions are relatively large by industrial standards, they were specifically designed for flow visualisation purposes.

Roll	Land Width L (mm)	Groove Width A (mm)	Groove Depth R (mm)
B1	0.53	0.47	0.18
B2	0.54	0.46	0.07
B3	0.54	0.47	0.35
B4	0.53	0.47	0.30

Table 2.2: Revised rectangular smaller groove dimensions

Roll	Land Width L (mm)	Groove Width A (mm)	Groove Depth R (mm)
C1	0.20	0.80	0.39
C2	0.29	0.71	0.516
C3	0.18	0.82	0.6

Table 2.3: Triangular groove dimensions (all grooves isosceles triangles)

Tests with these rollers revealed incomplete filling of the grooves after doctoring, the reason could have been the effect of the doctor blade deforming into the large grooves, although a more likely explanation is that in large grooves gravitational forces play a more important role in determining the flow within them compared to viscous forces. The ratio of these forces can be written as the Stokes number, a non-dimensional parameter used to characterise the relative importance of gravitational to viscous forces:

$$St = \frac{\rho g H^2}{\mu U}, \tag{2.1}$$

where ρ is the fluid density, g is the acceleration due to gravity, H, a the characteristic length (in this case groove width), μ the fluid viscosity and U the characteristic velocity (roll velocity). From equation (2.1) it can be seen that halving the groove width reduces the effect of gravitational forces by a factor of 4.

Rolls with smaller grooves were subsequently manufactured, the dimensions of which are given in Table 2.2. As well as rectangular grooves, a series of triangular grooved rolls were also manufactured - see Table 2.3 for the corresponding dimensions. The dimensions for both rectangular and triangular grooves, at non-zero pitch angle, are provided in Table 2.4. Groove pitch Φ is defined as the angle the groove makes with the web direction of travel (plane perpendicular to the roll axis).

Roll	Type	Land Width L (mm)	Groove Width A (mm)	Groove Depth R (mm)	Groove angle Φ
D1	Rectangular	0.50	0.50	0.4	30°
D2	Rectangular	0.50	0.50	0.4	45°
D3	Rectangular	0.60	0.40	0.4	60°
E1	Triangular	0.25	0.33	0.30	30°
E2	Triangular	0.14	0.57	0.30	45°
E3	Triangular	0.29	0.79	0.30	60°

Table 2.4: Angled groove dimensions for rectangular and triangular groove cross sections

2.3.2 Manufacture of the Roll Sleeves

The production of grooved sleeves was carried out using two different manufacturing techniques. The first involved using a CNC lathe for pitch angles of 0° which ensured that the grooves were cut with consistent dimensions. The process involved skimming the rolls, to ensure a truly cylindrical outer surface, before the grooves were turned into the surface using a cutting tool of an appropriate profile. Both stages were performed without the sleeve being removed from the mandrel, thus ensuring grooves of constant cross section and depth. A dwell function was also used in the turning process to ensure that swarf was fully removed from the grooves, producing a clean finish.

For the production of sleeves with a non-zero pitch angle, a different manufacturing technique was required. This is because the transverse travel speed of the cutting tool would need to be of the same order as the peripheral roll speed - clearly an impractical way of cutting clear grooves. Instead, a 4-axis milling machine (XYZ Vulcan 610 Machining Centre with a 4th axis fitted) was used to manufacture pitched-groove sleeves. The machine had an encoder resolution of $2\mu m$, with a realistic maintainable accuracy of around $5\mu m$ [119]. As with the turning process described above, the surfaces of the rolls with spiral grooves were machined to ensure roll land-groove concentricity. As the device used to manufacture these grooves was a milling machine the roll surface was finished with a end milling tool. This raised the potential for the surface profile to vary as the tool base was slightly concave. This problem was reduced by offsetting the tool from the roll center line. The resulting surface appeared free from variations in geometry, confirmed by groove measurements at various locations once the manufacturing process was complete.

The dimensions of the triangular grooves were measured using a talysurf stylus. The abrupt step

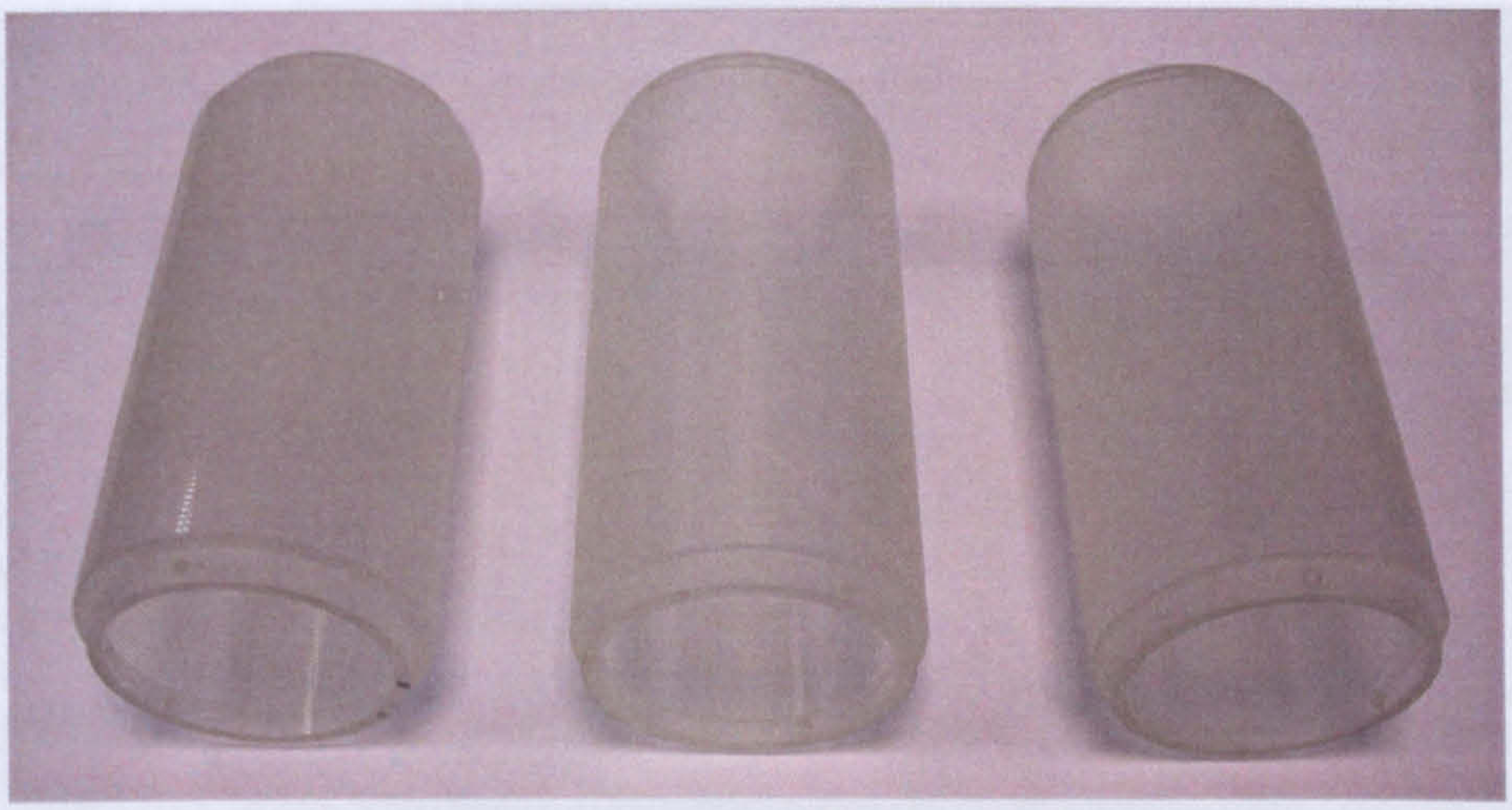

Figure 2.6: Three of the acrylic sleeves used in the experiments

associated with rectangular grooves meant that only the groove depth could be measured in this way by moving the stylus from the roll land to the base, as the stylus was unable to move from the base to the land. Consequently, a different method was required to measure the dimensions of these grooves and verify the cleanness of cut and consistency of cross section. This was achieved by taking a mould of the surface of the roll and using a thin slice of the mould to examine its dimension using an optical projector. The latter was also used to measure the groove widths directly by positioning the roll under the microscope. A combination of these two techniques was used to confirm the dimensions of the rectangular grooves.

The methods of measuring groove dimension also confirmed the finish of both triangular and rectangular grooves and that they were clean and smooth. Photographs of three of the acrylic sleeves used in the experiments is provided in figure 2.6.

The acrylic sleeves (of ID $80mm$) were mounted on a steel roller of diameter $79mm$, i.e. $1mm$ less than that of the sleeve's internal diameter. This allowed grub screws, located at the ends of the sleeve, to be used to minimised roll run-out, and, compensated for lack of concentricity between outer and inner sleeve diameters. The arrangement is shown in figures 2.7 and 2.8.

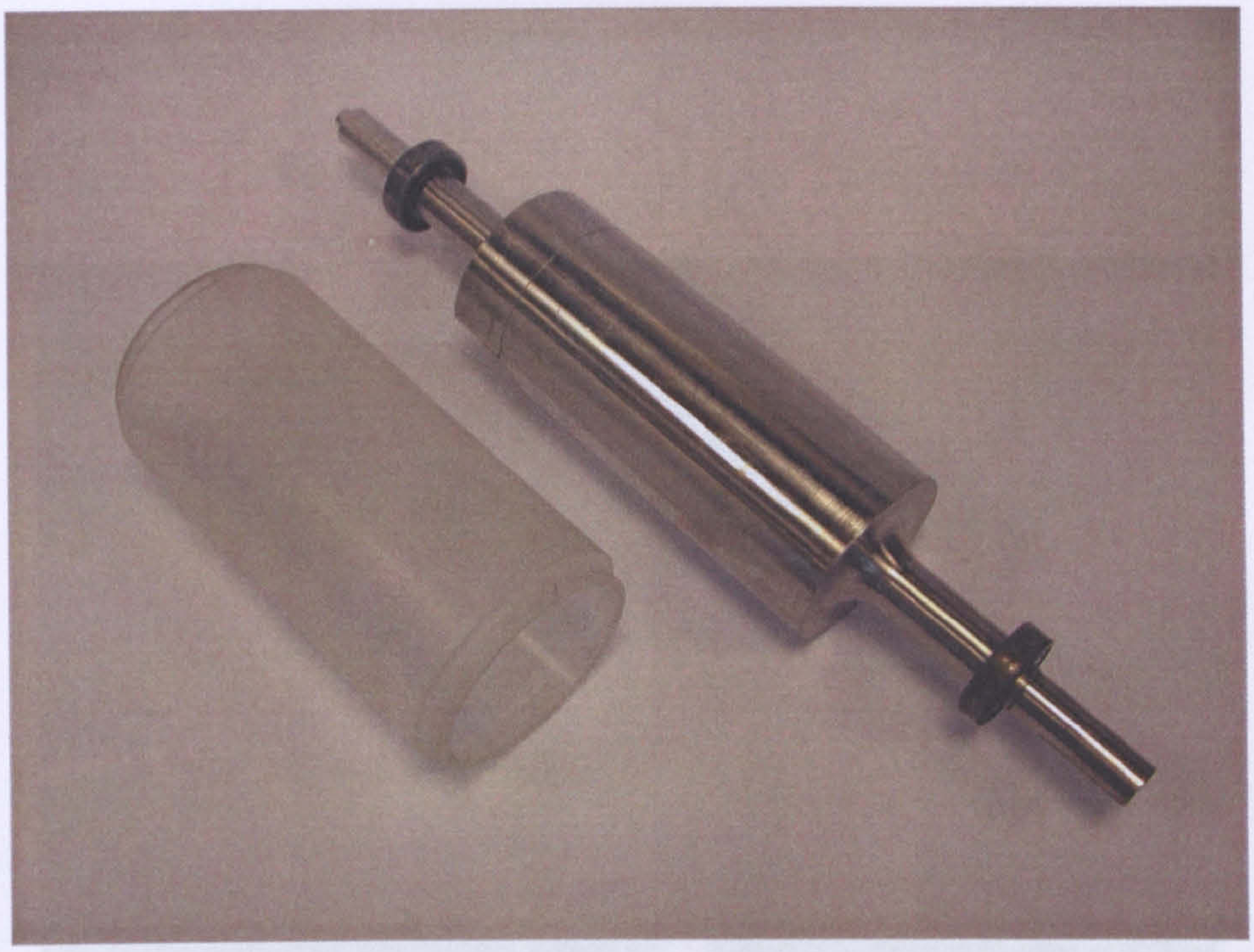

Figure 2.7: Roll and sleeve arrangement

2.4 Web Drive

The web material used in the experiments was uncoated $23\mu m$ thick PET, a common industrial substrate. It came in $2000m$ rolls, with each roll weighing just over $8kg$. The web handling equipment fed the web over the gravure roll at a constant speed, ranging from $0 \rightarrow 75m/min$. The speed of the web and roll were verified by running them against a handheld tachometer.

Web tension was measured by running the web over a roll mounted on a set of load cells. The web was driven by two motors, one for the offwind and the other for the rewind roll. A further roll was mounted on an eccentric journal, in the path of the web, allowing adjustment of the wrap angle, this is illustrated in figure 2.9.

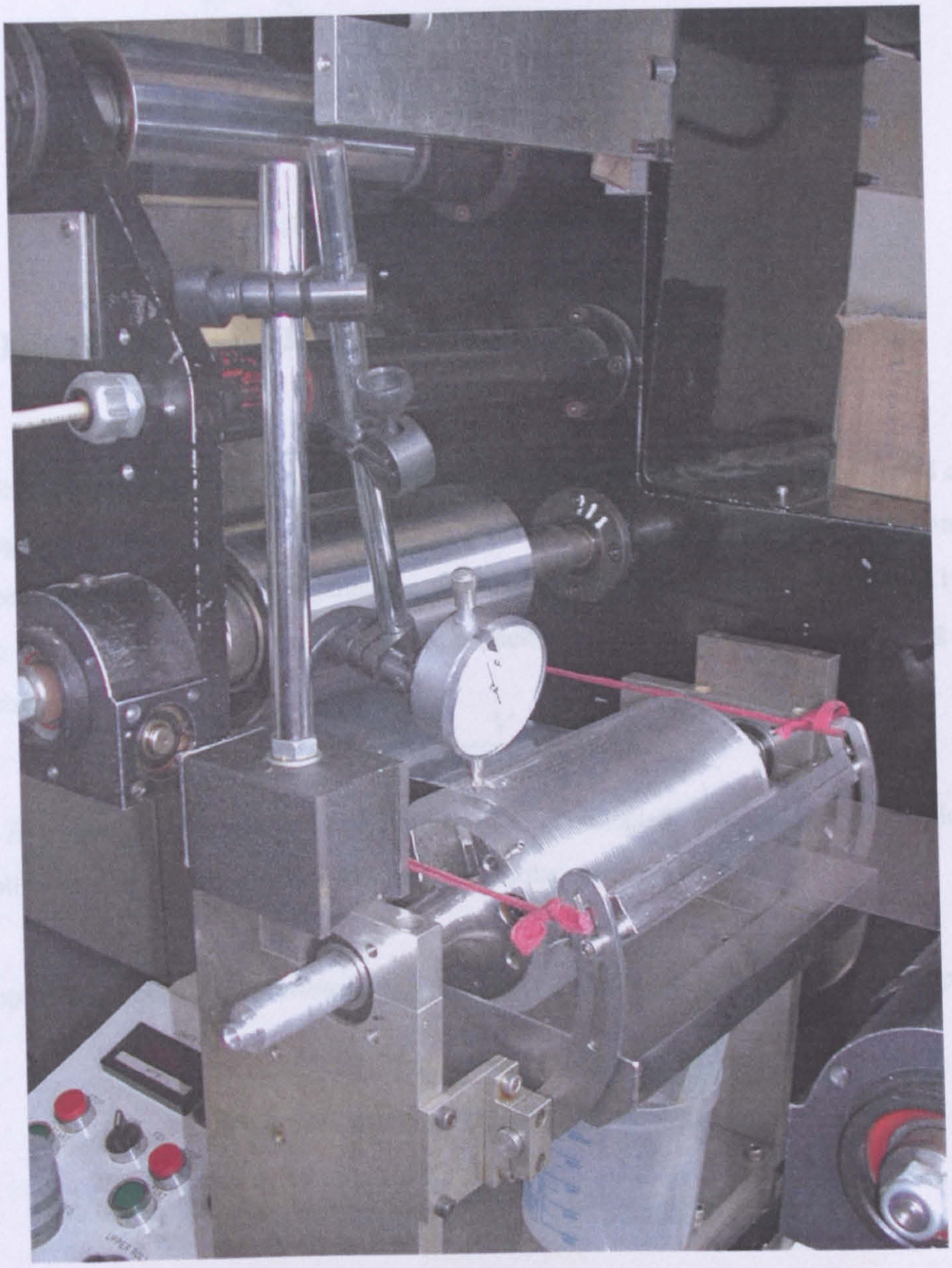

Figure 2.8: Roll alignment

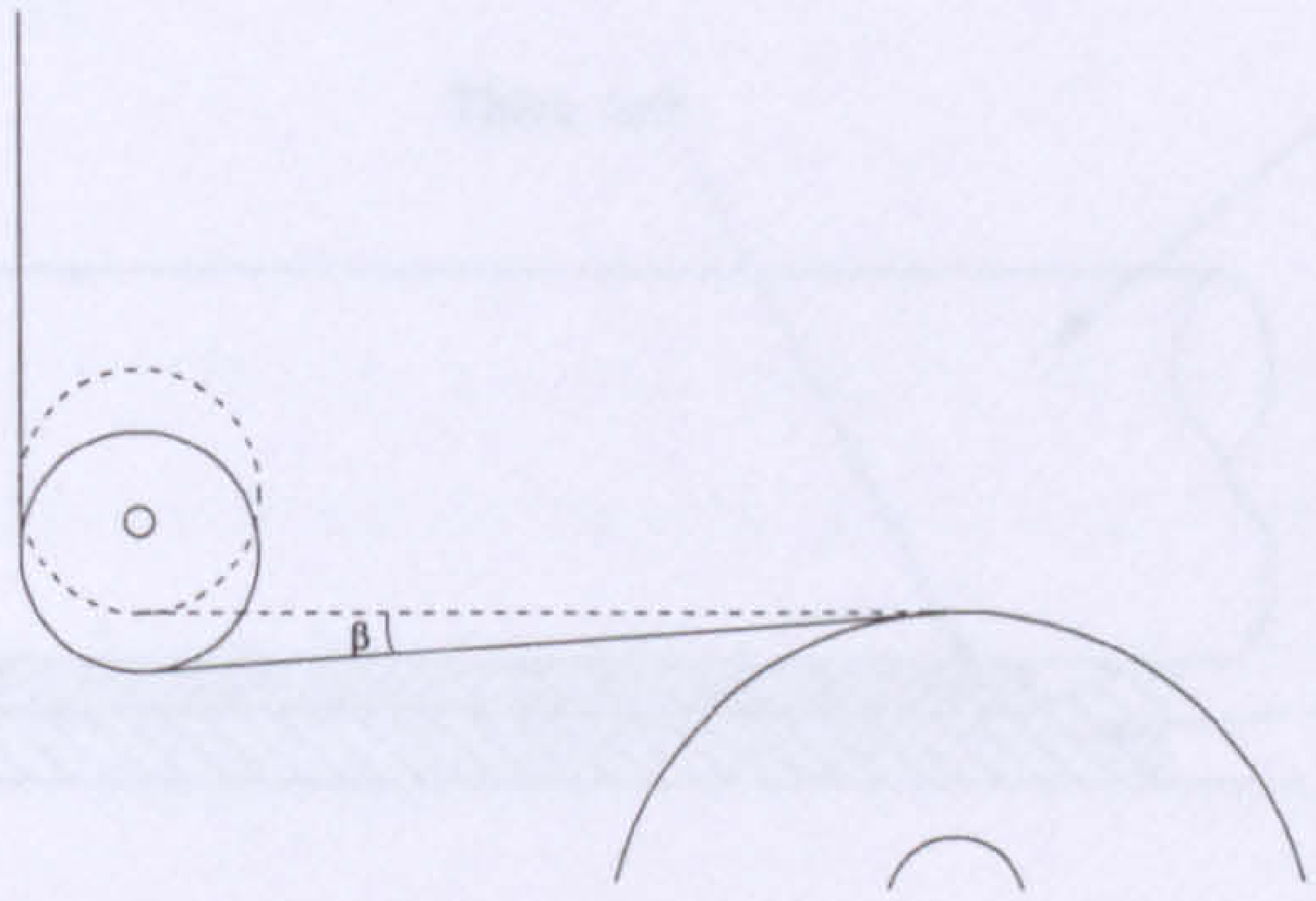

Figure 2.9: Eccentric wrap angle roll

2.5 Film Thickness, Flux and Pickout Measurements

The web, on leaving the coating bead, was scraped with a rubber blade for a fixed period of time allowing both the flux and film thickness to be determined. A windscreen wiper blade installed in a steel clamp and held tightly against the web was used for this purpose, see figure 2.10. The volume of fluid was then measured and the film thickness determined from the following simple relationship:

$$H = \frac{V}{TLU_{web}}, \tag{2.2}$$

where H is the film thickness, V is the volume of fluid collected, T is the time over which fluid was collected, L is the width of the web and U_{web} is the speed of the web.

The approach has been used previously to great effect by Malone [49], Innes [120] and Kapur [66].

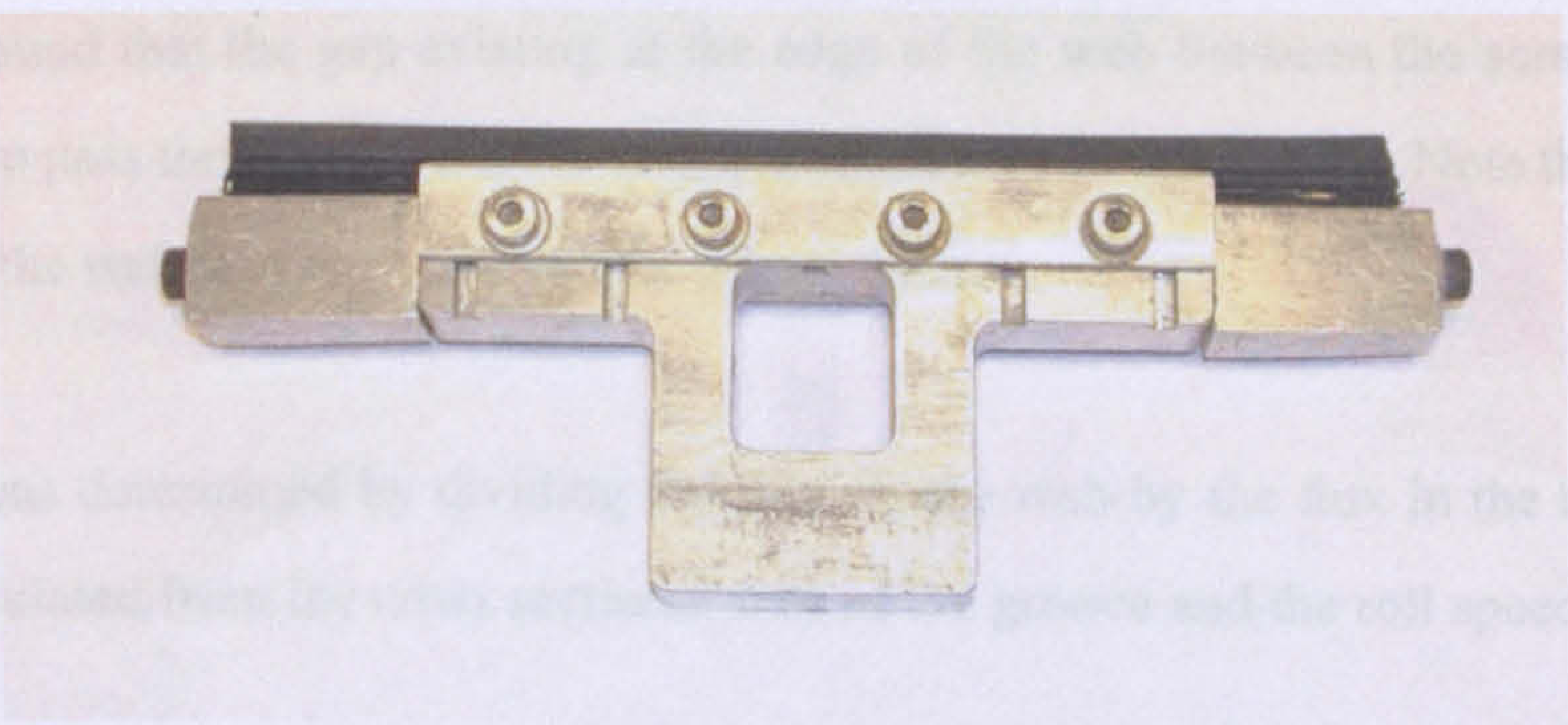

Figure 2.10: Scraping blade used remove fluid from the coated web

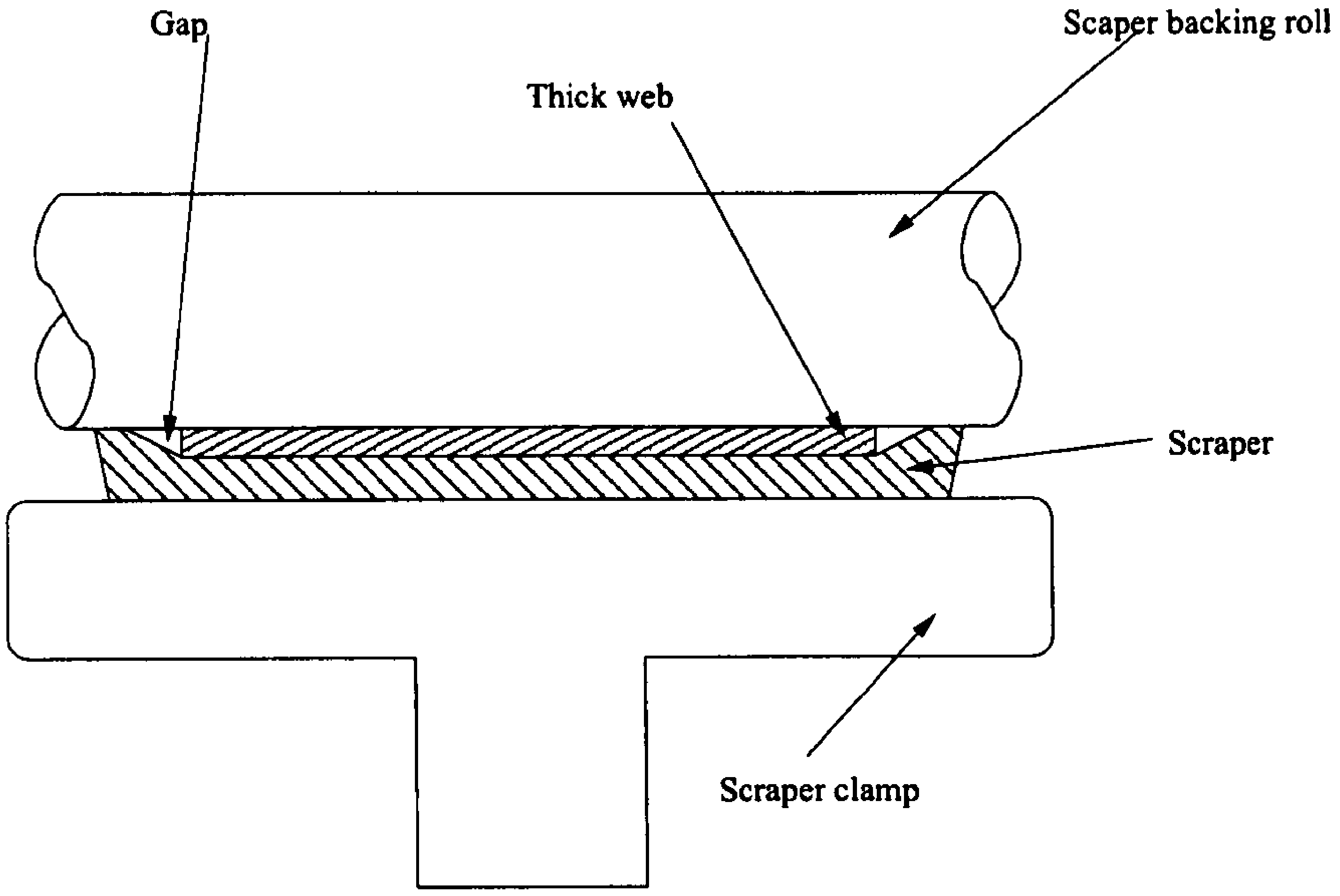

Figure 2.11: Schematic illustrating the gap at the edge of thick webs during scraping and the propensity for liquid to pass through.

With regard to accuracy, Malone estimated the residual film thickness remaining on the web after scraping to be of the order of $2\mu m$. Innes used a double scraper and estimated a residual film thickness of $0.5\mu m$; while Kapur determined that with a properly aligned scraper the residual film thickness remaining on the web was around $0.1\mu m$. Since the film thicknesses produced here are much greater than those in Kapur's investigation, due to the larger roll groove dimensions, it is reasonable to assume that errors from the presence of a residual film after scraping are negligible. Correct alignment of the doctor blade was verified by holding absorbent paper against the web downstream of the scraper; in all cases the fluid absorbed from the web was found to be negligible. One reason for using the thinnest web available ($23\mu m$ thick) was that it aided scraping efficiency since it was found that the gap existing at the edge of the web between the scraper and the roll allowed fluid to pass through for thicker webs, as illustrated in figure 2.11. Note that residual fluid at the edge of the web was not observed for $23\mu m$ webs.

The pickout was determined by dividing the flux on the web by the flux in the roll grooves, the latter was calculated from the cross sectional area of the groove and the roll speed.

2.6 Coating Fluids

Gravure roll coating is generally used for the coating of low viscosity fluids. However as the coating speeds encountered in industry are typically greater than those achievable using the experimental coating apparatus, fluids with a range of viscosities were examined in order to cover as wide a range of capillary number as possible.

The bulk of the test fluids used in the experiments were mixtures of glycerol and water plus a small volume of surfactant (lodyne) to reduce surface tension and improve wettability. These test fluids were chosen for their intrinsic Newtonian behaviour, thus permitting comparisons to be made with the models described later in the thesis. Typical water-glycerol mixtures were in the range $20 : 80$ to $60 : 40$ (by volume) resulting in viscosities in the range of 0.002 to $0.009 Pas$. Surface tension was adjusted using a small quantity of surfactant ($2 - 3ml$ per $5l$), resulting in surface tensions of $0.035 N/m$ as measured using a DuNouy ring.

The shear thinning fluids used obeyed the power law model, these fluids were mixtures of water and BenAqua1000 (around 0.05% to 0.1% by mass), a water soluble polymer derived from a natural polysaccharide; again to adjust surface tension and ensure wetting of the web a small volume of surfactant (lodyne) was added. The test fluids were in use for less than one month of being mixed, over which period they did not record a measurable change in fluid properties. Specific fluid properties are reported along with the test conditions in the appropriate chapters.

Described below are the methods used to characterise these fluids.

2.6.1 Determining Fluid Properties

Viscosity Measurements

Fluid viscosity was measured using a controlled stress Bohlin rheometer (Bohlin CV0-120) as shown in figure 2.12. This rheometer has two surfaces, one held stationary, and a second located

Figure 2.12: Bohlin CV0-120 rheometer

directly above that can rotate. The principle of operation is simple. The rheometer applies a torque to the top plate and the resulting displacement is measured to determine the rate of strain, which in turn can be used to calculate the fluid viscosity. An active control loop allows the strain rate to be specified. A wide range of geometries can be used to measure the viscosity of test fluids, these include parallel plates, a cone and plate and more elaborate arrangements such as cup and bob and double gap geometries, as illustrated in figure 2.13 . In this study a cone and plate geometry was used; the linear variation in the gap with distance from the center of the cone increases giving a constant shear rate over the entire geometry. This provides better defined test conditions than, for example, parallel plates between which the shear rate varies. The maximum shear rate viscosity measured was dependent on the point where fluid was lost from the gap due to centrifugal forces,

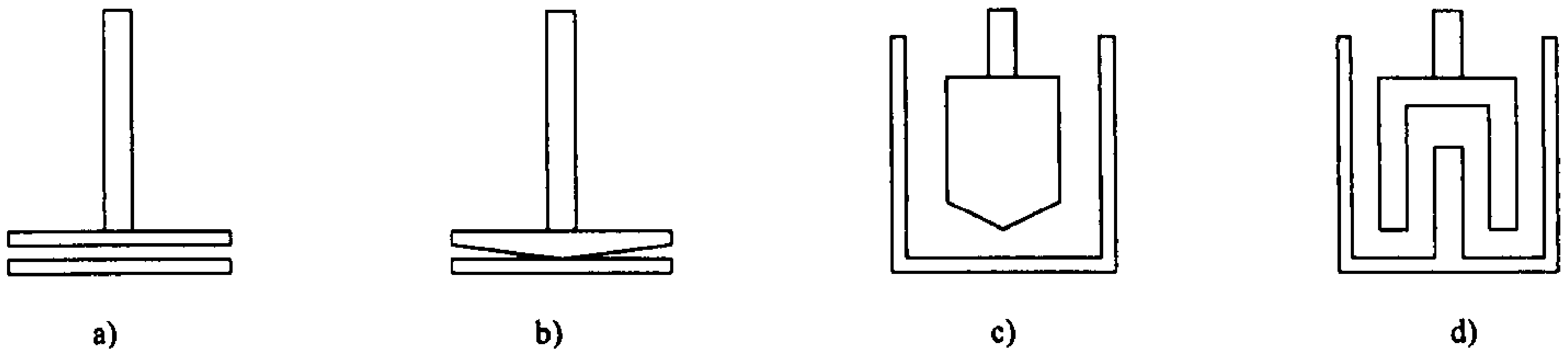

Figure 2.13: Different rheometry measurement geometries: a) parallel plate; b) cone and plates; c) cup and bob; d) double gap

all viscosity measurements were undertaken at 20°C.

Surface Tension Measurements

The surface tension of the test fluids was measured by a White tensiometer and platinum du Nouy ring, see figure 2.14. This involves using a torsion balance to measure the force required to lift a $10mm$ diameter platinum du Nouy ring off the surface of a volume of test fluid. Prior to use the ring and fluid reservoir was cleaned with distilled water in an ultrasonic bath.

Static Contact Angle Measurements

The other fluid parameter required is the static contact angle. This parameter is used in the subsequent models of the process since a dynamic contact angle (as there is for all coating processes where one phase is displaced by another) exists at the upstream meniscus, where the web enters the coating bead. An empirical model is used to related the dynamic contact angle to the static contact angle. The latter was measured by placing a drop of fluid onto the plastic web material, increasing its volume using a syringe and then measuring the static contact angle under a microscope.

2.6.2 Fluid Properties

The properties of the test fluids examined as given in table 2.5 (the raw viscosity data can be found in Appendix G). Figure 2.15 shows the fitting of the power law to the rheometric data of fluids E

Figure 2.14: White tensiometer, with inset picture of platinum du Nouy ring.

Fluid	Viscosity (Pas)	Surface Tension (N/m)	Static Contact Angle ($degrees$)	Power Index	Consistency Factor Pas^n
A	0.0055	0.0369	94.54	-	-
B	0.0076	0.0310	18.00	-	-
C	0.0075	0.0369	94.55	-	-
D	0.0073	0.0360	74.33	-	-
E	-	0.0408	60.96	0.0555	0.750
F	-	0.0260	64.52	0.0065	0.843

Table 2.5: Properties of test fluids

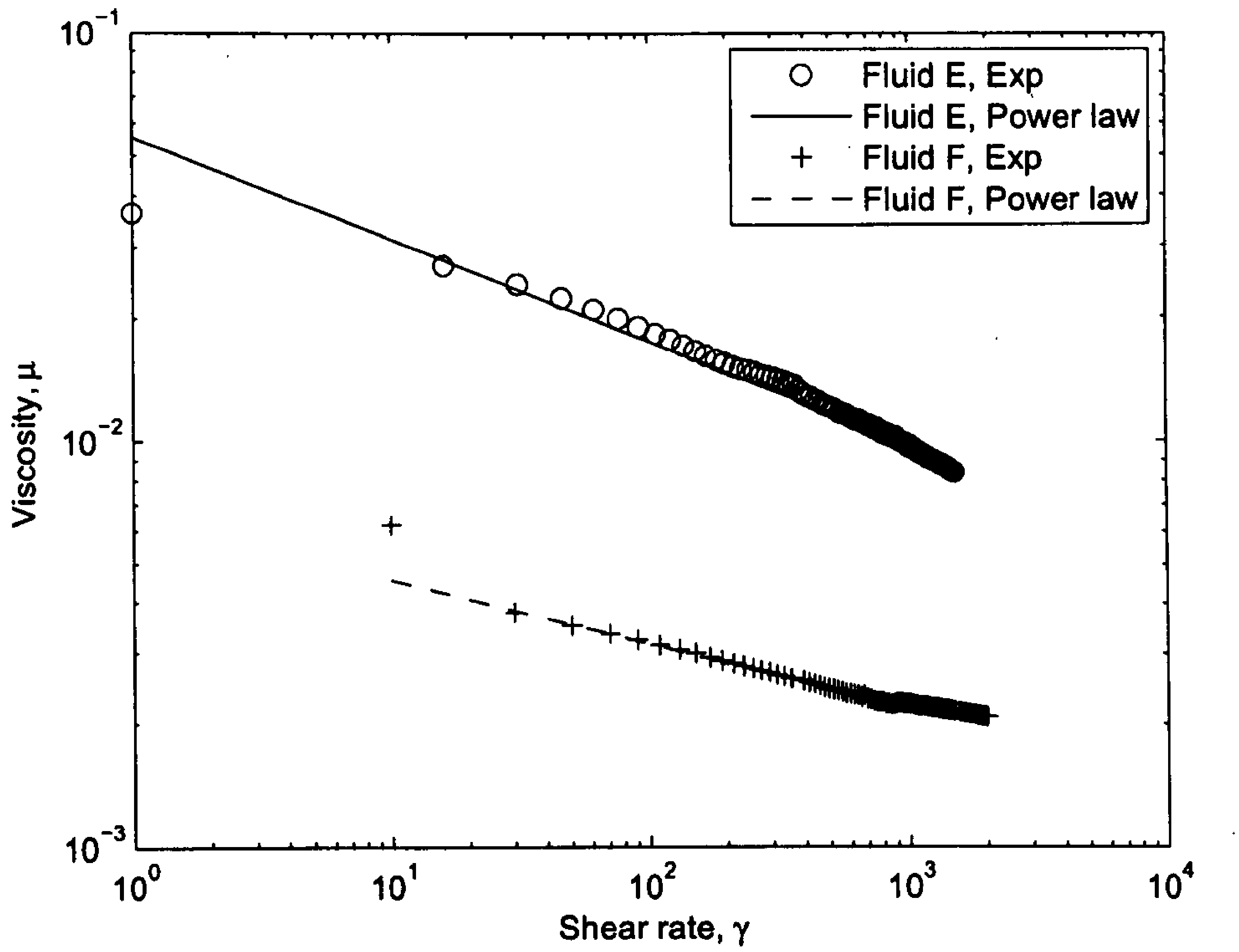

Figure 2.15: Rheometric data for the two shear thinning fluids E and F.

and F.

2.7 Bead Visualisation

The purpose of the visualisation studies was threefold:

- To determine the geometry of the coating bead, in particular the position of the web relative to the roll surface. Confirming the geometry is important, since it underpins the coating models derived subsequently.
- To gain an understanding of the characteristic flow patterns generated within the coating bead.
- To determine the location of the menisci for a variety of coating configurations for comparison with predicted meniscus locations.

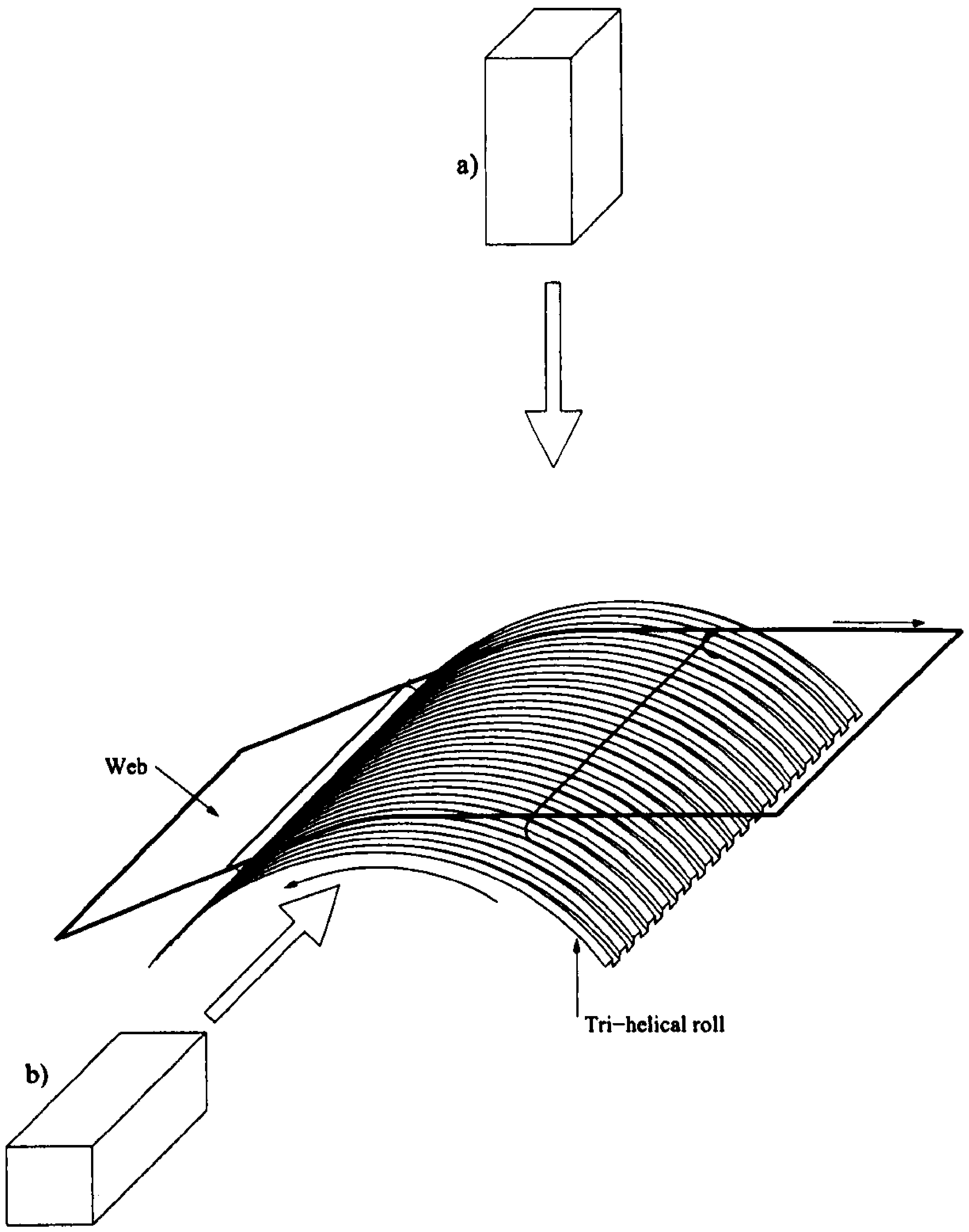

Figure 2.16: Camera mounting positions: a) top view of meniscus; b) side view of meniscus

Two different camera positions were used in the study as illustrated in figures 2.16, mounted either directly above the coating bead with the line of sight directly downwards (location (a)) or with the line of sight aligned along the roll axis (location (b)). The former was used to determine the locations of the upstream and downstream menisci; the latter for flow visualisation and verification of web-to-roll contact.

The camera used was a monochrome CCTV camera. The coating bead was illuminated by means of a halogen light source with two fibre optic light guides. For the images taken along the roll axis (location (b)) the light guides were used to brightly illuminate a white background providing a diffuse illumination of the coating bead and contrast for the flow visualisation studies. Due to the long and thin domain occupied by the coating bead it was difficult to maintain resolution in both directions. Short movies were recorded on a super VHS video recorder connected to a monitor to check focus and image quality. Selected frames of the movie sequence were then converted to mpeg movies.

To calibrate the images, a ruler with $1mm$ increments was included in each visualisation experiment. The top dead center of the roll was determined using a fine length of fishing line held tight from one end of the roll mount to the other. The position of this was based on the bearing locations at either end of the roll. Visualisation of the coating bead by the injection of a small pulse of dye within the roll groove downstream of the coating bead allowed streamlines to be observed. The roll surface was constructed from clear acrylic and therefore aided in the illumination. However, the clarity of the acrylic was insufficient after being turned/machined to permit the visualisation of flow lines within grooves. The only flow lines that could be observed were those in the web-to-roll gaps upstream and downstream of the roll to web contact.

2.8 Typical Operating Procedure

The mode of operation of the coating apparatus is simple. At the start of each test run a new reel of film was fitted onto the unwind spindle, fed through the apparatus and attached to the empty rewind roll. The coating roll was positioned in its cradle and a dial gauge placed at either end of the roll to ensure concentricity by adjusting three grub screws at either end of the roll. The coating bath was filled and the coating roll set in motion. The doctor blade was then positioned against the roll with the appropriate weights used to hold it in place. A check was made at a low rotational speed with the dial gauge to confirm that concentricity had been maintained, this was repeated at regular intervals to confirm the correct alignment of the roll. The roll speed was then set using the roll speed indicated on the control panel. As some of the rolls were of a diameter slightly less than $100mm$, due to surface skimming of the rolls during their manufacturing process, the speed indicated on the control panel (based on a roll diamter of $100mm$) was corrected to ensure that the required peripheral roll speed was set.

The web was tensioned by manually winding the rewind roll. The wrap angle of the roll was then fixed using a combination set and by adjusting the eccetrically mounted wrap angle roll. The web was then accelerated up to the experimental condition to be examined and its speed and tension allowed to stabilise. The sensitivity of the controls meant that it was important to change the web speed and tension slowly to prevent the web feedback controls becoming unstable. The scraper was then positioned so as to be held firmly against the web and confirmation made that there was no trace of residual fluid remaining on the web after scraping. The system was allowed to stabilise for around 30 seconds to ensure that the fluid collection apparatus had reached a steady state.

Fluid was collected for a measured duration which varied according to the running conditions. A volume of around $90ml$ of fluid was collected for each data point and took between 20 seconds and 5 minutes to collect. The web and/or roll speed was then changed and, after allowing the apparatus to stabilise, the process was repeated.

Two regular checks were made during a sequence of experiments to confirm that: (i) there was no trace of residual fluid on the web after scraping, by holding tissue against the scraped web; (ii) roll ecentricity was maintained by testing with a dial gauge.

Chapter 3

Film Forming Models

3.1 Introduction

The modelling of the process of depositing a thin liquid film onto a moving substrate is one of the key components of the predictive model for tri-helical gravure roll coating developed in subsequent chapters. There are a number of analyses of this process such as the Landau-Levich equation [2], Bretherton law [3] and the Coyne & Elrod cavitation model [6], which find a large number of applications in the analysis of multiphase flows, including coating flows, thin film lubricating flows, injection moulding and oil extraction.

Perhaps the simplest of the film forming models is the Landau-Levich equation (derived explicitly by Bretherton), which relates film thickness (H), meniscus radius (R) and capillary number ($Ca = \frac{\mu U_{\text{substrate}}}{\sigma}$) via the following simple equation:

$$\frac{H}{R} = 1.337 Ca^{\frac{2}{3}}. \tag{3.1}$$

The main limitation of the Bretherton law is the small range of capillary numbers for which it is considered valid ($Ca < 0.01$), as a result of the assumed constant meniscus radius - a simplifying assumption required to make the equation tractable. Accordingly, the more complex Coyne &

Elrod model was chosen for the analysis of the tri-helical gravure coating process for Newtonian fluids; for this model the upper limit of applicable capillary numbers is $Ca = 0.1$.

In order to include the case of simple shear thinning fluids a new model had to be formulated, based on lubrication flow of the developing liquid film and a balance of pressure terms, derived from the meniscus pressure discontinuity and the viscous forces within the fluid; a problem made tractable by solving the resulting set of ordinary differential equations as a BVP. A simple power law model was chosen to represent the fluid. The following section outlines the Coyne & Elrod model, as limited literature exists on solving the system of Ordinary differential equation (ODE)s derived by these authors despite the application of the model to a number of problems [102, 63, 13]. A shear thinning film forming model is then derived, the solution of which is compared with the experimental data of Kamisli & Ryan [7] for the case of a semi-infinite bubble driven along a tube by measuring the residual fluid remaining on the tube wall, as used by a number of authors [121, 122] for Newtonian fluids.

3.2 Coyne & Elrod Model

The commonly used Coyne & Elrod cavitation model [5, 6] provides an accurate means of determining the shape of a liquid film being swept out of a flooded stationary gap for a Newtonian liquid with constant density and surface tension. The model is considered applicable for capillary numbers less than 0.1 allowing a greater range of capillary numbers to be examined than would be the case with the Landau-Levich model [3] as derived in Appendix A. The Coyne & Elrod model has been used successfully in conjunction with lubrication analysis by a number of authors [123, 124, 102, 63, 125, 13]. However the instabilities arising in the solution of the equations makes its application difficult. Indeed, some authors [13] have resorted to using the numerical results obtained by Coyne & Elrod, fitting an interpolation function to the film thickness data.

The two important dependent variables obtained from the model are the gap to film thickness ratio and local radius of curvature of the meniscus at the point of film splitting, which allows the pressure discontinuity across the meniscus to be obtained. Unlike the Landau-Levich equation the

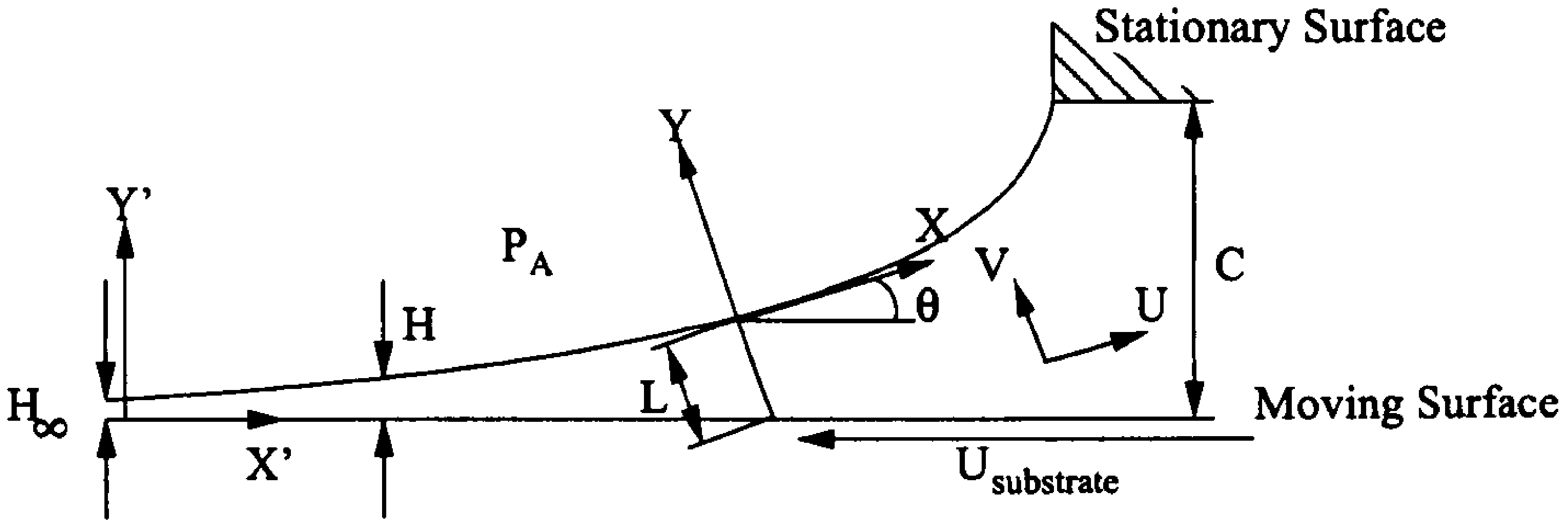

Figure 3.1: A schematic of the problem studied by Coyne & Elrod, namely that of a liquid film being drawn from a flooded gap by a moving surface

local pressure discontinuity across the meniscus is determined from the local radius of curvature rather than from a constant radius of curvature (as is reasonably assumed by Landau-Levich for low capillary number flows), allowing higher capillary number separating flows to be modelled. To accurately apply the Coyne & Elrod model to the coating problem of interest more data points than those given by Coyne & Elrod were calculated. The solution of the equations past the point where the gap is three times the final film thickness is extremely unstable and the method of solution is not elucidated in their paper, with only scant information provided:

> "Because of numerical stability considerations, extreme precautions were required to obtain the interface shapes between the surface stagnation points and the detachment points" [6].

Although more detail is contained in Coyne's thesis [5] a clear method of solving the equations is still not provided.

3.2.1 Theory

The basis of the theory developed by Coyne & Elrod is the Navier–Stokes equation solved along the gas-liquid interface, as shown in figure 3.1. The problem is made tractable by assuming a velocity profile (perpendicular to the film surface) in the liquid phase and by neglecting viscous forces arising from the gas phase. As a result the shear stresses vanish at the interface. The equation describing the normal stresses at the interface is a balance of surface tension and cavity pressures:

$$\sigma\frac{d\theta}{dS} = P_a - P - 2\mu \left.\frac{\partial U}{\partial X}\right|_{Y=L}. \tag{3.2}$$

At the free surface boundary the tangential stresses vanish based on the assumption that the gas within the cavity has negligible viscosity and/or density, this leads to:

$$\mu\left(\frac{\partial U}{\partial Y}+\frac{\partial V}{\partial X}\right)_{Y=L} = 0. \tag{3.3}$$

Satisfying the x-component of the Navier–Stokes equation for Newtonian fluids at this boundary leads to:

$$\left.\frac{\partial P}{\partial X}\right|_{Y=L} = \mu\left(\frac{\partial^2 U}{\partial X^2}+\frac{\partial^2 U}{\partial Y^2}\right)_{Y=L} - \rho\left(U\frac{\partial U}{\partial X}+V\frac{\partial U}{\partial X}\right)_{Y=L} - \rho g\sin\theta. \tag{3.4}$$

Using the property that the shear stresses vanish at the interface an expression describing the change in θ with distance along the interface (S) can be derived:

$$\frac{d\theta}{dS} = \frac{1}{U_L}\frac{\partial U}{\partial Y}. \tag{3.5}$$

Equation (3.4) can be rearranged (as $X = S$ at $Y = L$) to give:

$$\frac{dP}{dS} = \mu\frac{d^2U_L}{dS^2} + \mu\left.\frac{\partial^2 U}{\partial Y^2}\right|_{Y=L} - \rho\frac{d}{dS}\left(\frac{U_L^2}{2}\right) - \rho g\sin\theta. \tag{3.6}$$

Using the geometric relationship:

$$\frac{dh}{ds} = \sin\theta, \tag{3.7}$$

equation (3.6) can be integrated from $S = -\infty$ giving:

$$P - P_a = \mu\frac{dU_L}{dS} + \int_{-\infty}^{S} \mu\left.\frac{\partial^2 U}{\partial Y^2}\right|_{Y=L} \partial S - \frac{\rho\left(U_L^2 - U_{\text{substrate}}^2\right)}{2} - \rho g\left(H - H_\infty\right). \tag{3.8}$$

The pressure terms can be eliminated from equation (3.8) using equation (3.2):

$$3\mu\frac{dU_L}{dS} = -\sigma\frac{d\theta}{dS} - \int_{-\infty}^{S} \mu\left.\frac{\partial^2 U}{\partial Y^2}\right|_{Y=L} dS + \frac{\rho\left(U_L^2 - U_{\text{substrate}}^2\right)}{2} + \rho g\left(H - H_\infty\right). \tag{3.9}$$

A quadratic velocity profile perpendicular to the film surface is then assumed based on the velocity at the plate and at the liquid-gas interface and conservation of mass, written respectively as:

$$\left.\frac{U}{U_{\text{substrate}}}\right|_{Y=0} = \cos\theta \tag{3.10}$$

$$\left.\frac{U}{U_{\text{substrate}}}\right|_{Y=L} = u \tag{3.11}$$

$$\int_0^L U dY = U_{\text{substrate}} H_\infty \tag{3.12}$$

The quadratic velocities and the first and second derivative with respect to Y are derived in Appendix B. Substituting these velocity functions into equations (3.5) and (3.9) and non-dimensionalising all lengths using the final film thickness (H_∞) and all velocities in terms of the plate velocity ($U_{\text{substrate}}$) leads to the following equation set:

$$\frac{d\theta}{ds} = \frac{6\cos\theta}{hu}\left[\cos\theta\left(\frac{1}{h}-\frac{1}{3}\right)-\frac{2u}{3}\right], \tag{3.13}$$

$$\frac{d\psi}{ds} = \frac{2\cos^2\theta}{h^2}\left[\cos\theta + u - \frac{2\cos\theta}{h}\right], \tag{3.14}$$

$$\frac{du}{ds} = \frac{1}{Ca}\frac{d\theta}{ds} - \psi - \frac{Re}{6}\left(u^2-1\right) - \frac{St}{3}\left(h-1\right), \tag{3.15}$$

where

$$h = \frac{H}{H_\infty} \qquad Ca = \frac{3\mu U_{\text{substrate}}}{\sigma} \qquad Re = \frac{\rho U_{\text{substrate}} H_\infty}{\mu} \qquad St = \frac{\rho g H_\infty^2}{3\mu U_{\text{substrate}}}, \tag{3.16}$$

and

$$\psi = \frac{H_\infty^2}{3U_{\text{substrate}}}\int_{-\infty}^{S}\frac{\partial^2 U}{\partial Y^2}ds, \tag{3.17}$$

where s is the distance along the surface from the origin far downstream of the fluid filled gap. The following geometric relation also applies:

$$\frac{dx'}{ds} = \cos\theta, \tag{3.18}$$

3.2.2 Numerical Implementation

The above equations were linearised and solved in the region far downstream of the gap, their resultant solutions being:

$$h = 1 + Ae^{\lambda s}, \tag{3.19}$$

$$\theta = A\lambda e^{\lambda s}, \tag{3.20}$$

$$\psi = \left(\frac{2 - \lambda^2}{2\lambda}\right) Ae^{\lambda s}, \tag{3.21}$$

$$u = 1 - \left(\frac{\lambda^2 + 6}{4}\right) Ae^{\lambda s}, \tag{3.22}$$

where λ is given as the only real positive root of:

$$\frac{3}{4}\lambda^4 + \left[\frac{3}{Ca} + \frac{Re}{4}\right]\lambda^3 + 6\lambda^2 + \left[\frac{3Re}{2} - St\right]\lambda - 3 = 0. \tag{3.23}$$

Using the solutions to these equations, where $s = 0$ far downstream of the gap, equations (3.13), (3.14), (3.15), (3.7) and (3.18) can then be integrated toward the gap. It is possible to dispense with the linearised equations by starting with the asymptotic values of h, θ, ψ and u and perturbing h by $\Delta h = 0.0001$. A predictor-corrector method can then be used to obtain the perturbations of the other variables to be solved for. Using a typical integration method (e.g. Euler, 4th order Runge-Kutta or predictor-corrector methods) allows integration up to the first stagnation point. The second stagnation point is located at the point of separation where the meniscus contacts the stationary surface at an angle of 90° (which occurs at a height of three times the final film thickness, from inspection of equation (3.13)).

When the gap is less than three times the final film thickness there is no stagnation point on the film surface other than at the attachment point and the numerical integration of equations (3.13) to (3.15) is relatively simple. However when the fixed gap is more than three times the film thickness (and a stagnation point occurs on the free surface), the equations become extremely unstable between the two stagnation points. Numerous numerical methods were employed to solve the equations, these included using the stiff ODE solvers within Matlab (ode15s, ode23s, ode23t and ode23tb), the Rosenbrock method [126] and 4th order Runge-Kutta method; however

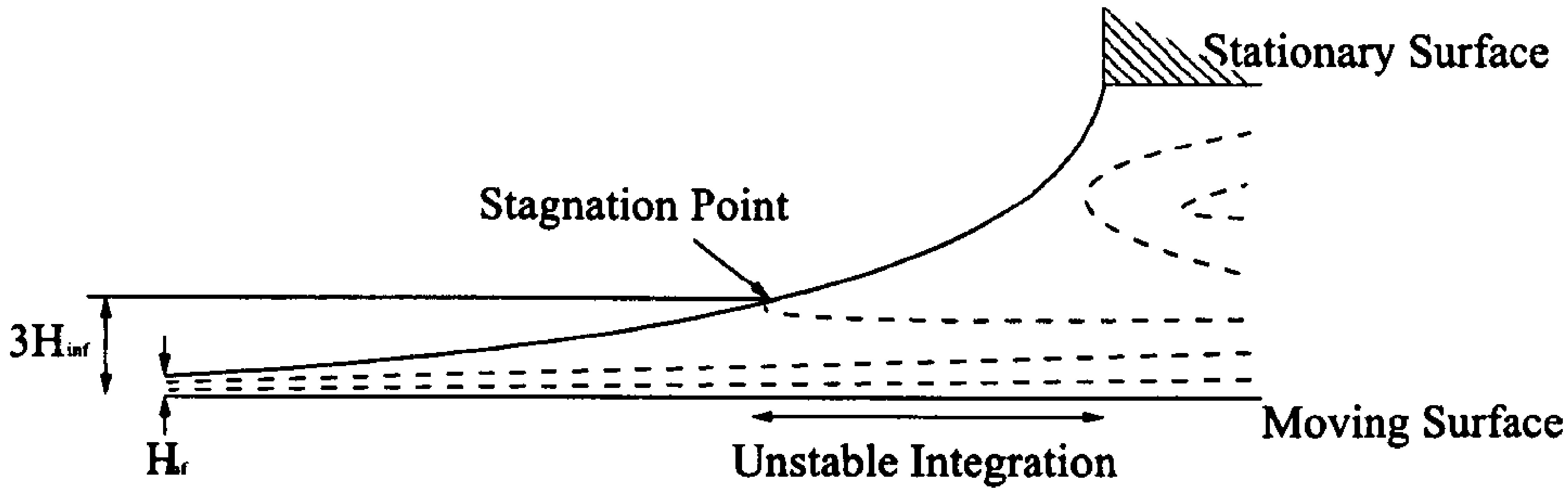

Figure 3.2: Unstable integration region

they all proved unsuccessful. At the first stagnation point a singularity in $\frac{d\theta}{ds}$ occurs when V goes to zero and if H is not equal to 3. Correspondingly huge variations in $\frac{d\theta}{ds}$ occur due to small numerical inaccuracies in the integration schemes. Stepping over the stagnation point was also unsuccessful (as also noted in Coyne's thesis [5]), even past the stagnation point the equations were still unstable.

A solution was found to this problem by using the equation for $\frac{d\theta}{ds}$ (equation (3.13)) to determine the velocity, rather than incrementing it using the equation for $\frac{du}{ds}$. Using a predictor-corrector method, convergence of the required values was obtained. Steps of a fixed $d\theta$ were used and from $\frac{d\theta}{ds}$ the value of ds was determined. The final method applied to solve the problem is outlined below.

1. From equation (3.23) the only real positive value of λ was obtained.
2. For an initial perturbation ($\Delta h = A$) of the asymptotic final film thickness (h_∞) the linearised equations (3.19), (3.20), (3.21) and (3.22) were used to determine the initial variables h, θ, ψ and u (x' is determined by equation (3.18)).
3. The predictor corrector method was used to solve iteratively for the five unknowns (h, θ, ψ, u and x') using the following equations:

$$u_{n+1} = u_n + \left.\frac{du}{ds}\right|_{n+1} \Delta s \tag{3.24}$$

$$x'_{n+1} = x'_n + \left.\frac{dx'}{ds}\right|_{n+1} \Delta s \tag{3.25}$$

$$\theta_{n+1} = \theta_n + \left.\frac{d\theta}{ds}\right|_{n+1} \Delta s \tag{3.26}$$

$$\psi_{n+1} = \psi_n + \left.\frac{d\psi}{ds}\right|_{n+1} \Delta s \tag{3.27}$$

$$\text{and,} \quad h_{n+1} = h_n + \left.\frac{dh}{ds}\right|_{n+1} \Delta s, \tag{3.28}$$

where $\Delta s = 0.001$ and their derivatives, with respect to s, are given by equations (3.13), (3.14), (3.15), (3.7) and (3.18).

4. Step 3 is repeated until $h = 3$, the location of the stagnation point. Continuing the numerical integration using the predictor-corrector method given in step 3 was not possible due to numerical instabilities, without varying the incremental step.

5. The incremental step, Δs, was then varied, based on a constant $\Delta\theta$ this helped to maintain numerical stability:

$$\Delta s_{n+1} = \frac{\Delta\theta}{\left.\frac{d\theta}{ds}\right|_{n+1}}. \tag{3.29}$$

Typically a step size of $\Delta\theta = 0.01$ was used, and found to give the most stable results. Equations (3.13), (3.14), (3.15), (3.7) and (3.18) were then rearranged to give:

$$\theta_{n+1} = \theta_n + \Delta\theta, \tag{3.30}$$

$$h_{n+1} = h_n + \Delta s \sin\theta_{n+1}, \tag{3.31}$$

$$u_{n+1} = \frac{\left.\frac{d\theta}{ds}\right|_{n+1}}{\cos\theta_{n+1}\left(\frac{1}{u_{n+1}} + \frac{1}{3}\right) - \frac{2u_{n+1}}{3}} \tag{3.32}$$

$$\psi_{n+1} = \psi_n + \Delta s_{n+1}\left(\frac{2\cos^2\theta_{n+1}}{h^2_{n+1}}\left[\cos\theta_{n+1} + u_{n+1} - \frac{2\cos\theta_{n+1}}{h_{n+1}}\right]\right), \tag{3.33}$$

$$\text{and,} \left.\frac{d\theta}{ds}\right|_{n+1} = Ca\left(\frac{u_{n+1} - u_n}{\Delta s_{n+1}} + \psi_{n+1} + \frac{Re}{6}(u_{n+1} - 1) + \frac{St}{3}(h_{n+1} - 1)\right),. \tag{3.34}$$

Equations (3.29), (3.30), (3.31), (3.32), (3.33) and (3.34) were then solved iteratively to obtain u_{n+1}, h_{n+1}, θ_{n+1}, ϕ_{n+1} and $\left.\frac{d\theta}{ds}\right|_{n+1}$. x'_{n+1} was then found via equation (3.25).

6. Step 5 was repeated up to an angle of $\theta = \frac{\pi}{2}$, or the desired contact angle.

3.2.3 Source Code

Both a C++ header and source code were written. To call the function the following line was used:

```
EFM_ROB::CoyneAndElrodCavitationModel
      (Ca,R,G,theta,psi,u,h,x,dthetadS);
```

where `Ca`, `Re`, and `St` are declared double precision variables containing the capillary number, the Reynolds number and the Stokes number, respectively. `theta`, `psi`, `u`, `h`, `x` and `dthetadS` return the values of θ, ψ, u, h, x' and $\frac{d\theta}{ds}$ at the attachment point; θ was also returned to confirm the limit of the numerical integration was correct.

3.2.4 Results

Comparison between the model results obtained here and those due to Bretherton [3] as well as those obtained empirically by Ruschak [4] and the published results of Coyne & Elrod is provided in figures 3.3 and 3.4.

Figure 3.3 shows the calculated film thickness as a function of capillary number. There is very good agreement between the results of Coyne & Elrod [127] and those from the numerical solver described here, at all but the lowest capillary number. This could be due to the different numerical approach adopted by Coyne & Elrod, or a different step sizes being used. The gap to film thickness ratio is in closest agreement with that of Landau-Levich at low capillary numbers, where the assumption that the curvature is constant within the Landau-Levich model is most accurate. At intermediate capillary numbers the gap to film thickness ratio from Ruschak's empirical equation matches well with the results of the Coyne & Elrod model, but there is significant deviation at higher capillary numbers.

Figure 3.4 shows the match for radius of curvature obtained with Ruschak's equation (1.18) and the Landau-Levich equation (3.1). The agreement is poor at higher capillary numbers, since the

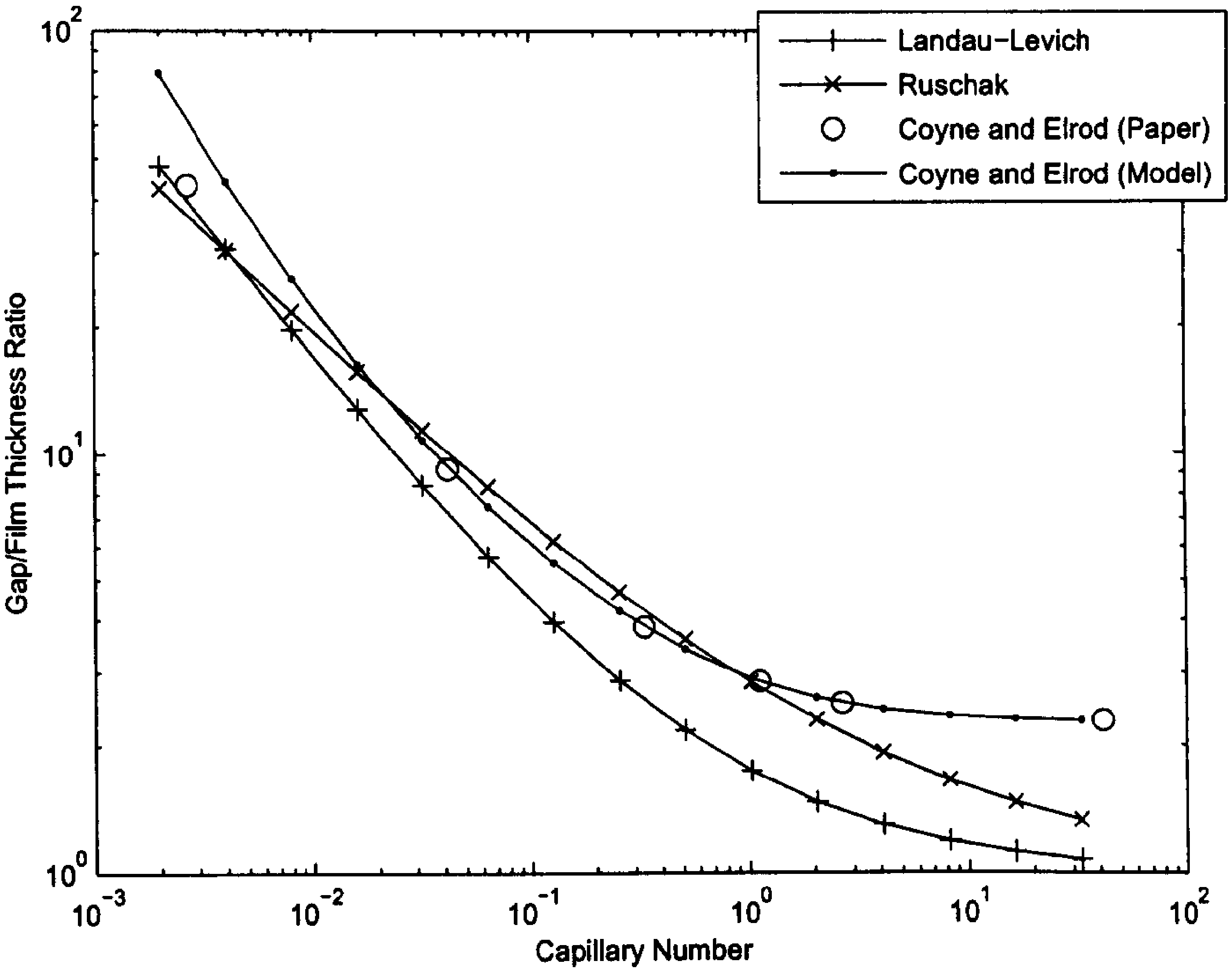

Figure 3.3: Calculated film thicknesses compared with values calculated using the Landau-Levich equation [2, 3] (equation (3.1)) and the empirical relationship obtained by Ruschak [4] (equation (1.18)).

Ruschak model cannot capture the variation in the radius of curvature along the meniscus. The use of both the local radius of curvature and the gap to film thickness ratio is clearly therefore necessary in examining pressure dependent coating operations for capillary numbers outside the applicable range of the Landau-Levich equation.

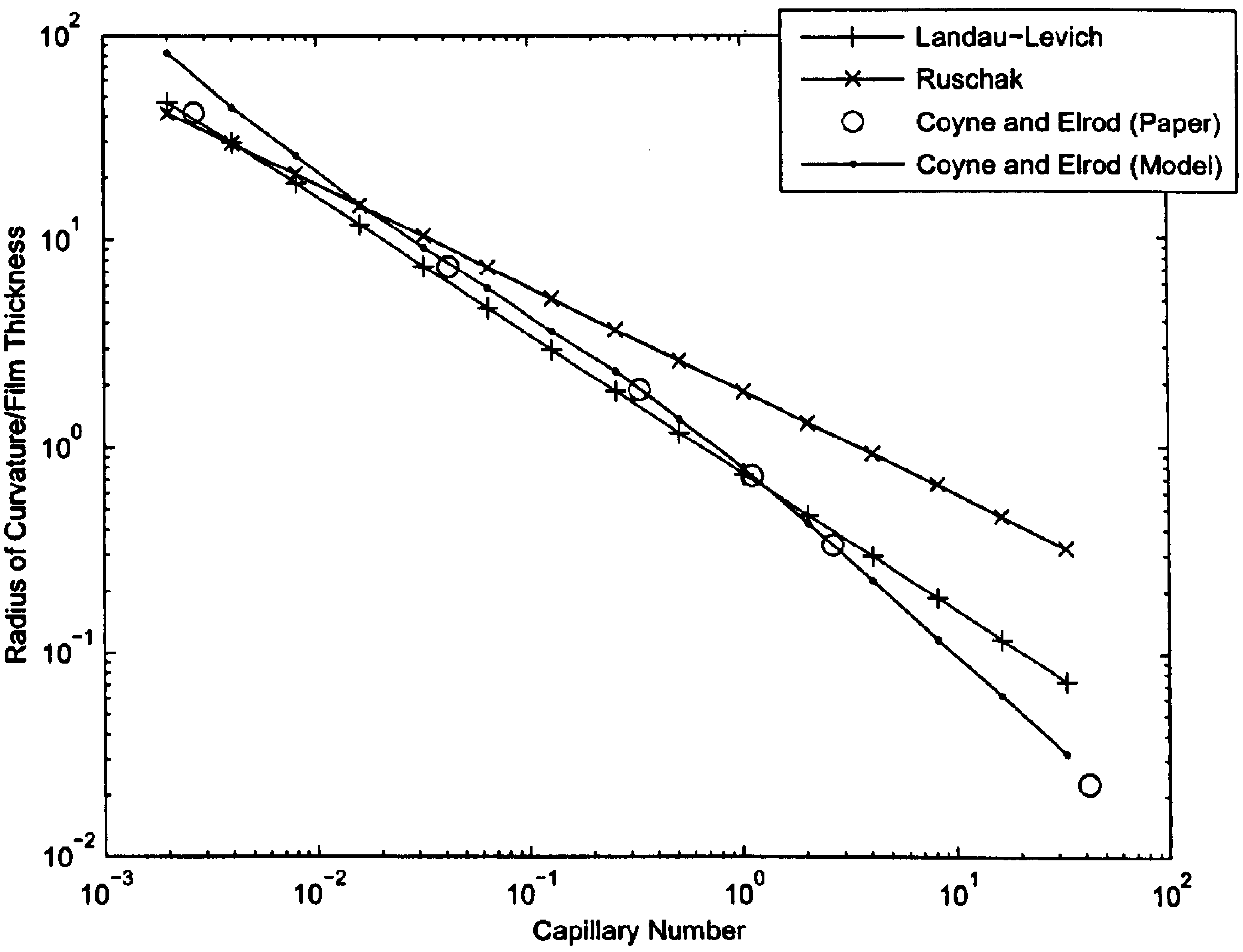

Figure 3.4: Calculated radii of curvature compared with values calculated using the Landau-Levich equation [2, 3] (equation (3.1)) and the empirical relationship obtained by Ruschak [4] (equation (1.18)).

3.3 Non - Newtonian Boundary Value Problems Film Splitting Model

This section details the development of a model capable of predicting the forming of a thin liquid film of fluid obeying a power law model onto a moving substrate. The model consists of a set of four ordinary differential equations that are then solved as a boundary value problem (BVP).

3.3.1 Theory

Figure 3.5 specifies the coordinate system; a local system aligned with the free surface is defined. The flow profile is assumed to be perpendicular to the free surface rather than the rigid surface sweeping the fluid from the gap, as is more common [3, 18]. This coordinate system brings the benefit of allowing regularly spaced nodes to be located along the interface. This is important for two reasons: firstly it allows a greater degree of resolution of the free surface; secondly it avoids difficulty in determining the curvature of the free surface close to the point of separation. Under this coordinate system, the curvature is simply given as $\kappa = \frac{d\theta}{dx}$. As will be seen later, the viscous forces are most dominant where θ approaches zero (region A in figure 3.5), it is here that the lubrication assumptions are most applicable due to the one dimensional nature of the flow in this region. Indeed, it is for this reason that the Landau-Levich equation has been so successful in predicting film formation for Newtonian fluids.

The basis of the current analysis is that by neglecting inertial terms and assuming that the flow is unidirectional, a balance between pressure gradient terms and viscous terms is arrived at from the Navier–Stokes equations:

$$\frac{\partial P}{\partial X} = \frac{\partial \tau}{\partial Y}, \tag{3.35}$$

where τ is the shear stress and P the local pressure. As is consistent with the usual lubrication assumptions $\frac{\partial P}{\partial Y} = 0$, and by assuming that the viscosity and/or density of the gas phase is much less than the liquid phase the following equation, describing the shear stress of a generalised Newtonian fluid, based on the boundary conditions that $\tau = 0$ at $Y = 0$, is obtained:

$$\tau = \frac{dP}{dX} Y. \tag{3.36}$$

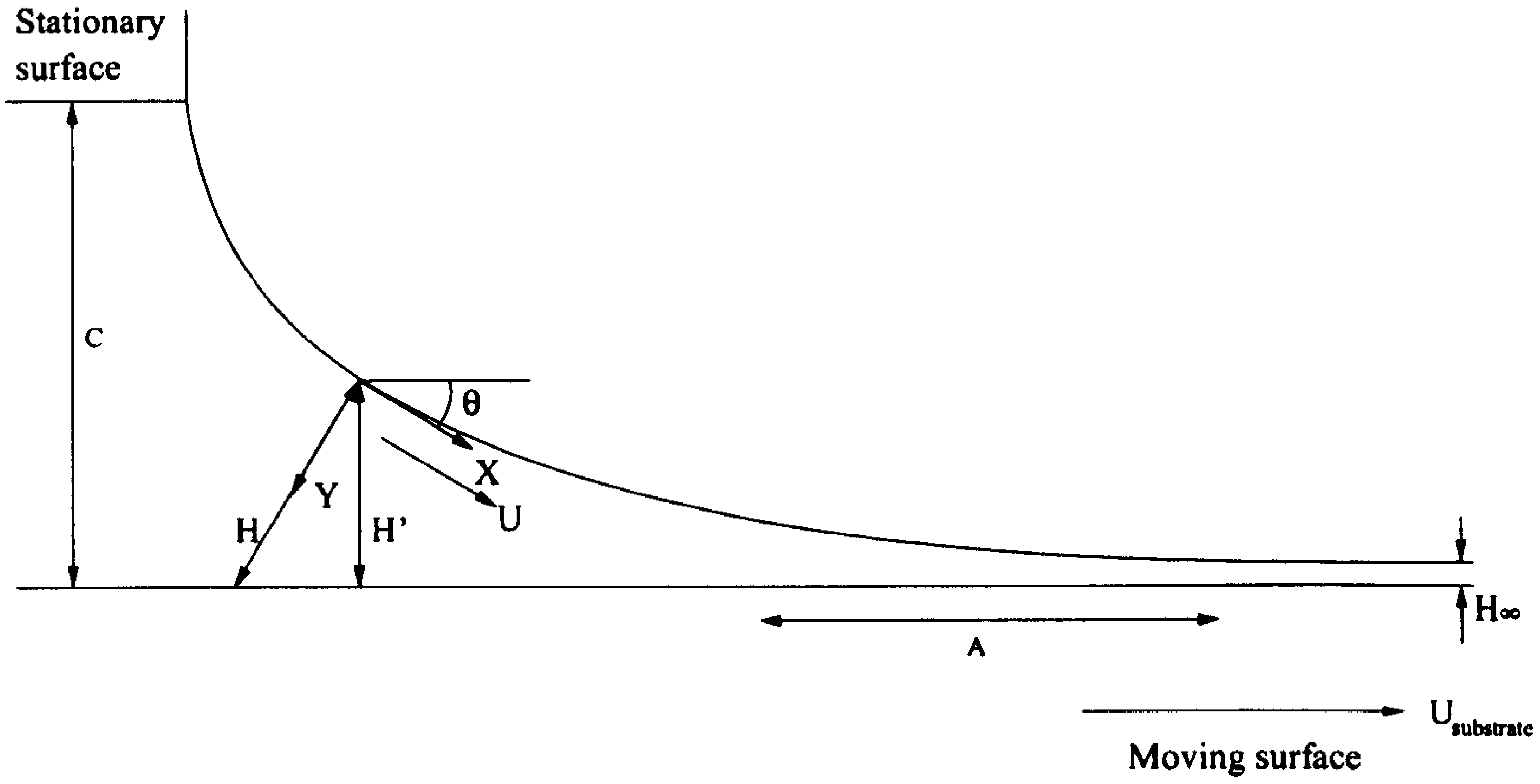

Figure 3.5: Schematic of the film forming geometry analysed as a BVP for non-Newtonian fluids obeying a power law.

For a shear thinning fluid which obeys the power law the shear stress is defined as:

$$\tau = \lambda \left| \frac{dU}{dY} \right|^{n-1} \frac{dU}{dY}, \tag{3.37}$$

where n is the power law index and λ is the consistency factor for a given fluid with n and λ determined experimentally using a rheometer. Equating the right hand sides of equations (3.36) and (3.37) gives:

$$\lambda \left| \frac{dU}{dY} \right|^{n-1} \frac{dU}{dY} = \frac{dP}{dX} Y, \tag{3.38}$$

which in non-dimensional form is written:

$$\left| \frac{du}{dy} \right|^{n-1} \frac{du}{dy} = \frac{dp}{dx} y. \tag{3.39}$$

The following non-dimensional scalings are used throughout the analysis:

$$u = \frac{U}{U_{\text{substrate}}}, \quad (x, y, h, h') = \frac{(X, Y, H, H')}{H_\infty} \quad \text{and} \quad p = \frac{P H_\infty^n}{\lambda U_{\text{substrate}}^n}.$$

To obtain a simple solution to equation (3.39) the sign of the pressure gradient needs to be considered. Consider the fluid being drawn into an increasingly narrow gap. Far downstream, the fully developed film on the moving substrate has a flux of one and in the absence of any pressure gradient the velocity in the x' direction would be $\cos\theta$ (based on the zero shear boundary condition at the free surface and x' velocity at the moving substrate). The gap perpendicular to the surface would be $h = \frac{h'}{\cos\theta}$ resulting in the flux at any location being $\frac{h\cos\theta}{\cos\theta} \equiv h$, which from continuity of mass considerations is not possible if $h > 1$. Consequently, a retarding force must be present to reduce the flux for the case when $h > 1$, this takes the form of a positive pressure gradient, i.e. when $h \geq 1$, $\frac{dp}{dx} \geq 0$. As $y \leq h$ the equation describing the velocity gradient is:

$$\frac{du}{dy} = \left(\frac{dp}{dx}y\right)^{\frac{1}{n}}, \tag{3.40}$$

which can be integrated with respect to y to obtain the velocity profile perpendicular to the free surface. The velocity boundary condition of the substrate $u_{y=h} = \cos\theta$ leads to:

$$u = \cos\theta + \frac{\left(\frac{dp}{dx}y\right)^{\frac{1}{n}} ny - \left(\frac{dp}{dx}h\right)^{\frac{1}{n}} nh}{n+1}. \tag{3.41}$$

Further integration from $y = 0$ to y_1 leads to the flux (q) from the film surface to y_1 as given by equation (3.42):

$$q = \frac{-(2n+1)\,hny_1\left(\frac{dp}{dx}\right)^{\frac{1}{n}} + y_1^{\frac{2n+1}{n}} n^2 \frac{dp}{dx}^{\frac{1}{n}} + (n+1)\,(2n+1)\cos\theta y_1}{3n+1+2n^2}. \tag{3.42}$$

By equating y_1 to h and q to 1, and after some manipulation the pressure gradient is obtained:[1].

$$\frac{dp}{dx} = \left(\frac{(2n+1)\,(h\cos\theta - 1)}{nh^{\frac{2n+1}{n}}}\right)^{n}. \tag{3.43}$$

Balancing the pressure discontinuity across the interface with the surface tension forces leads to:

$$p = -\frac{1}{Ca_{ST}}\frac{d\theta}{dx}, \tag{3.44}$$

where Ca_{ST} is the capillary number, defined as:

$$Ca_{ST} = \frac{\lambda U^{n}_{\text{substrate}}}{\sigma H_{\infty}^{n-1}}. \tag{3.45}$$

---

[1] The general pressure gradient equation for both positive and negative pressure gradients takes the form:

$$\frac{dp}{dx} = \left(\frac{(2n+1)\,(h\cos\theta - 1)}{nh^{\frac{2n+1}{n}}}\right)\left|\frac{(2n+1)\,(h\cos\theta - 1)}{nh^{\frac{2n+1}{n}}}\right|^{n-1}, \quad \text{for} \quad h > 0.$$

The following geometric relations also apply,

$$\frac{dh'}{dx} = \sin\theta, \tag{3.46}$$

and

$$\frac{dx'}{dx} = \cos\theta. \tag{3.47}$$

Equations (3.43), (3.44), (3.46) and (3.47) are the set of four first order ordinary differential equations describing the film forming process. Equation (3.47) is not coupled to the other three so need not be solved for if x' is not required.

An interesting result obtained from equations (3.42) and (3.43) is that of the location of the stagnation point on the film surface. By equating the flux (q) to zero in equation (3.42), the separating streamline can be determined, where the fluid above the streamline continues to circulate in the cavity and that below the streamline emerges from the gap in the form of the liquid film. The location at which the separating streamline is attached to the free surface can easily be obtained from equation (3.41) which describes the velocity perpendicular to the free surface. Substituting the pressure gradient from equation (3.43) into equation (3.41) and setting $y = 0$ (i.e. on the free surface) the location of the stagnation point is:

$$h_{stag} = \frac{2n+1}{n\cos\theta}, \tag{3.48}$$

which leads to the film height h'_{stag} at which the stagnation point is located:

$$h'_{stag} = \frac{2n+1}{n}. \tag{3.49}$$

This is in clear agreement with the location of the stagnation point predicted by Coyne & Elrod [5, 6] for Newtonian fluids ($n = 1$), where the stagnation point is located at $h'_{stag} = 3$. The prediction of the position of the free surface stagnation point is shown in figure 3.6 - note that this is dependent only on the power law index.

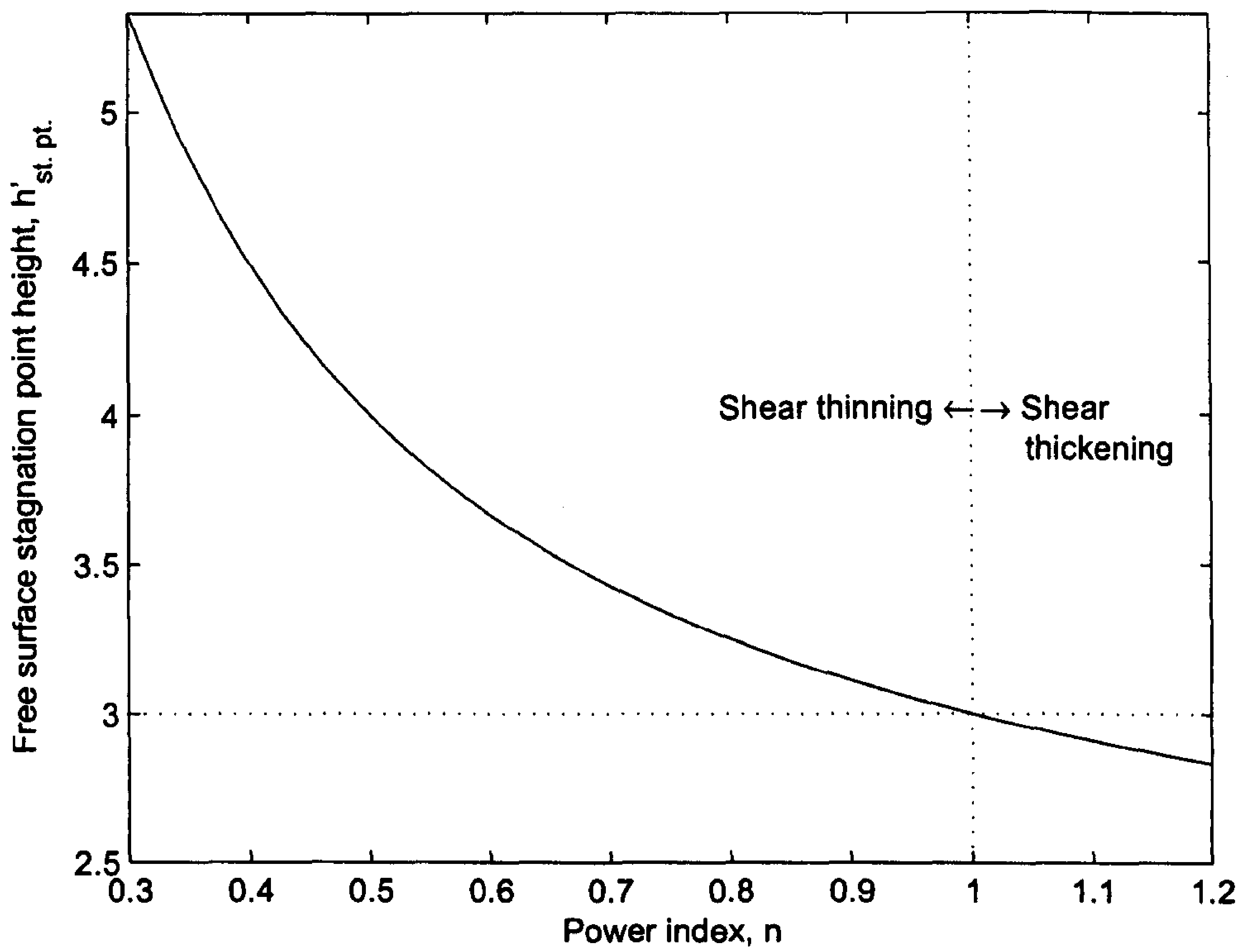

Figure 3.6: Predicted variation of the position of the free surface stagnation point with power law index given by equation (3.49)

Boundary Conditions

The set of four first order differential equations (3.43), (3.44), (3.46) and (3.47) require four boundary conditions in order to be numerically tractable. The boundary conditions that were applied are:

1. $p_{x\rightarrow\infty} = 0$
2. $h_{x\rightarrow\infty} = 1$
3. $x'_{x=0} = 0$
4. $\theta_{x=0} = -\frac{\pi}{2}$

The first two correspond to a fully developed film; condition 3 is a consequence of the geometry and determines the x' distance from the gap and is not required if equation (3.47) is not solved for; condition 4 relates the angle the free surface makes at $x = 0$. For the case studied here the angle, $\theta_{x=0}$, is specified and the height $h_{x=0}$ is determined as part of the solution. Alternatively, condition 4 can be replaced with $h_{x=0} = c$, where c is gap height - this boundary condition would be relevant in situations where the meniscus is pinned to a corner, as is common in knife coating.

3.3.2 Numerical Implementation

Equations (3.43) (using the geometric relation $h = \frac{h'}{\cos\theta}$), (3.44), (3.46) and (3.47) were solved using the BVP solver in the Matlab package (BVP4C). Continuation was used with a progressively reduced relative tolerance to ensure that the BVP solver converged successfully [128].

The method of continuation leads to a stable solution method, capable of producing results for a wide range of capillary numbers and power indices without the need to change the minimum mesh resolution or domain length. Indeed it was possible to find a solution anywhere in the range

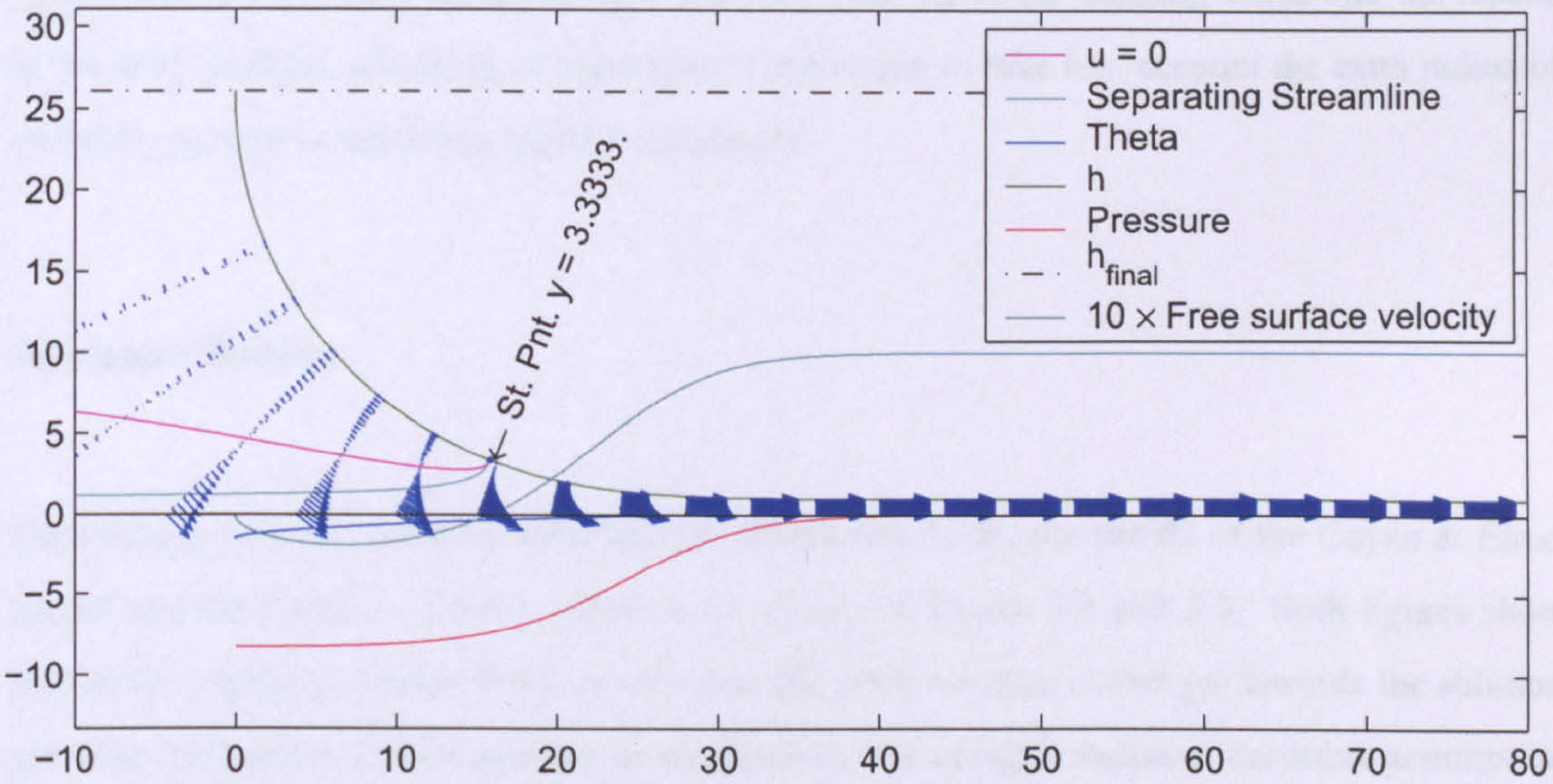

Figure 3.7: A typical solution of the BVP for the formation of a thin film with a shear thinning fluid, $Ca = 0.005, n = 0.75$.

$0.001 \leq Ca \leq 100$ with the power index $0.5 < n \leq 1$ without any difficulty. However, it was not possible to obtain results for power indices $n < 0.5$ due to numerical instability of the solution method. In each case the number of nodes was 2000 and the downstream was taken to be at a distance 200 film thicknesses away from the initial film split. The MATLAB implementation for the problem is given in Appendix C; the simplicity of the code is testament to the ease with which problems can be solved with MATLAB.

Following solution of the BVP, the film surface profile, pressure profile, surface angle and distance, x', can be plotted, as shown in figure 3.7. Also shown is the position of the separating streamline above which the fluid recirculates in the gap and below which fluid is drawn out of the gap onto the plate, and the line along which $u = 0$; these converge at the stagnation point.

3.3.3 Results

This section is subdivided into two parts, the first deals with results for Newtonian fluids where the BVP method, the Coyne & Elrod cavitation model and the Landau-Levich equation are compared.

The second shows a comparison between Kamisli & Ryan's [7] experimental data for the case of a semi-infinite bubble driven along a capillary tube for shear thinning fluids and the results of the BVP method, involving an approximate correction to take into account the extra radius of curvature present in the driven bubble experiment.

Newtonian Results

Comparison between the BVP solutions for Newtonian fluids, the results of the Coyne & Elrod model and the Landau - Levich equation are shown in figures 3.8 and 3.9. Both figures show that as the capillary number tends to zero then the BVP solution converges towards the solution given by the Landau-Levich equation as it reproduces the constant radius of curvature assumption at low capillary number. Comparison with the Coyne & Elrod data shows good agreement for the gap to film thickness ratio at higher capillary numbers, however agreement apropos the radius of curvature is not as good. The inherent instability associated with solving the Coyne & Elrod model can be observed in the spurious data curves at capillary numbers of around $Ca = 0.1$.

Shear Thinning Results

The results of the BVP for the formation of a thin fluid film are compared with the experimental data of Kamisli & Ryan [7] who undertook experiments where a semi-infinite bubble was driven along a tube. The capillary number defined by Kamisli & Ryan uses the tube radius as the non-dimensionalising length scale and is given by:

$$\begin{aligned} Ca_{K\&R} =& \lambda\frac{U^{n}_{\text{bubble}}}{\sigma R^{n-1}}, && (3.50)\\ =& Ca_{ST}\frac{H_{\infty}}{R}^{n-1}, && (3.51)\\ =& Ca_{ST}h^{n-1}_{x=0} \equiv Ca_{ST}c^{1-n}, && (3.52) \end{aligned}$$

where U_{bubble} is the bubble velocity (analogous to the substrate velocity in the BVP analysis) and R is the tube internal diameter. While the capillary number is based on the final film thickness in the BVP analysis, the capillary number used by Kamisli & Ryan ($Ca_{K\&R}$) is independent of the final

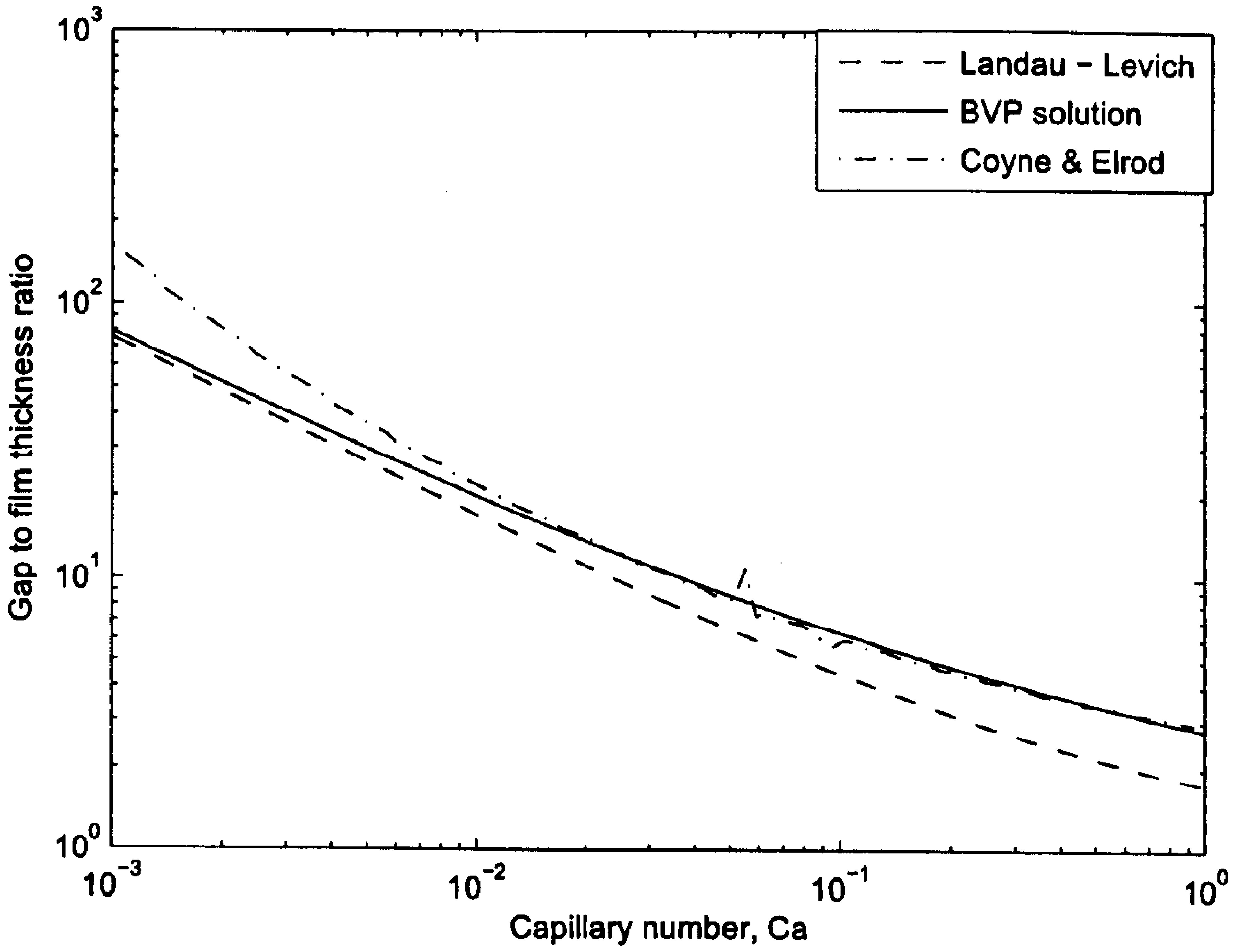

Figure 3.8: Comparison of gap to film thickness ratio for the BVP, Landau-Levich equation (equation (3.1)) and Coyne & Elrod model [5, 6] for Newtonian fluids.

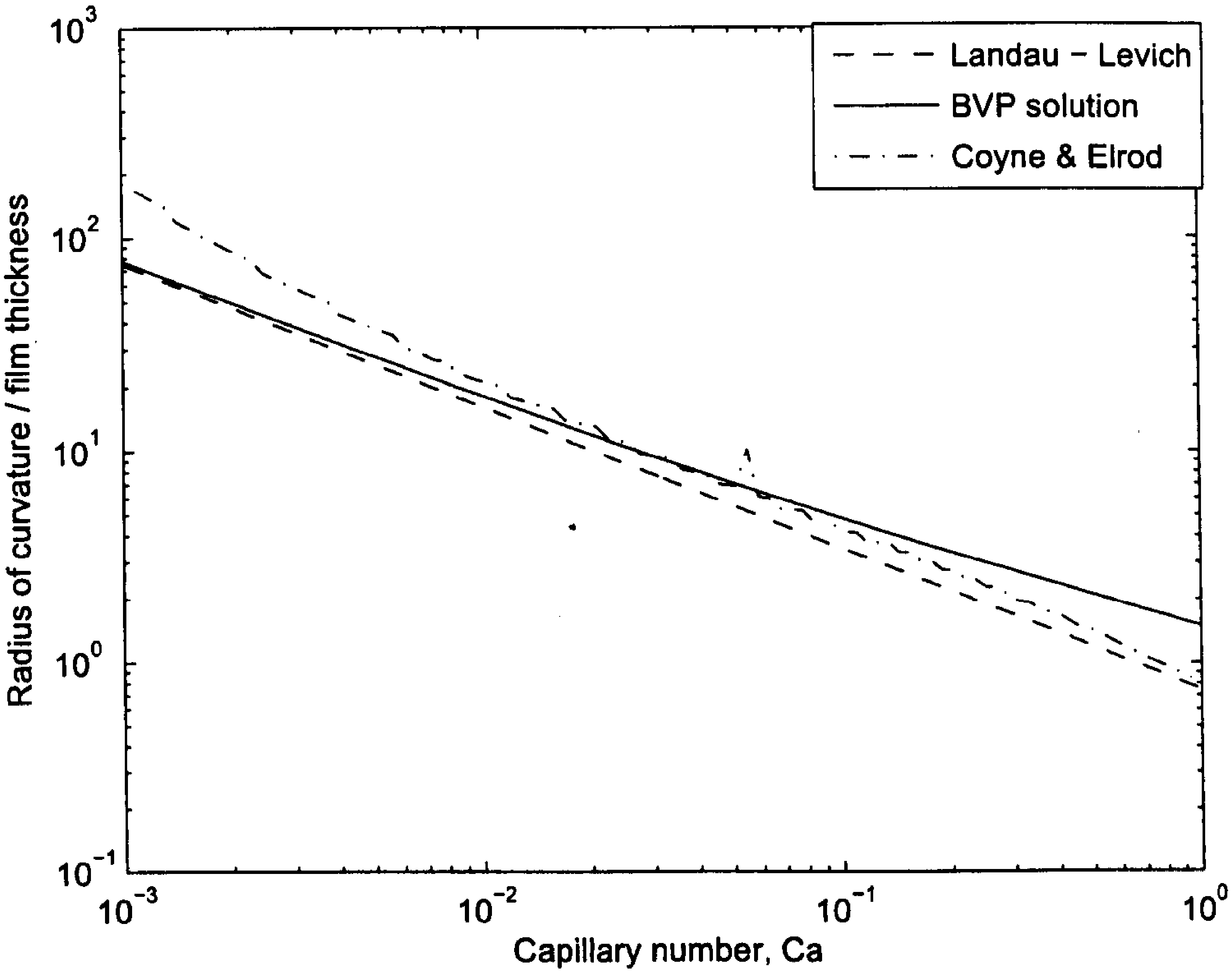

Figure 3.9: Comparison of menicsus radius at the point of film splitting to film thickness ratio for the BVP, Landau-Levich equation (equation (3.1)) and Coyne & Elrod model [5, 6] for Newtonian fluids.

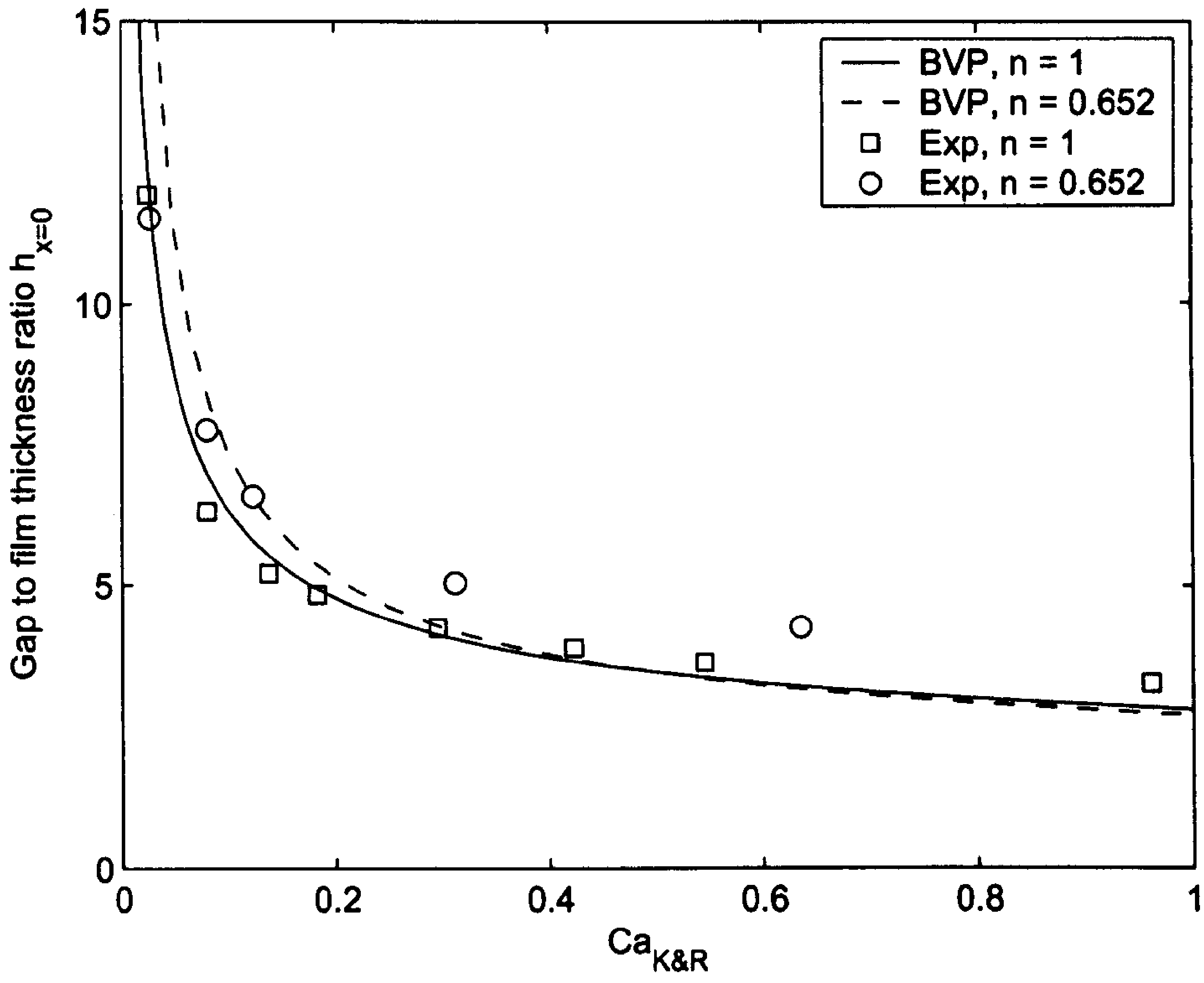

Figure 3.10: A comparison of the BVP predictions and Kamisli & Ryan's [7] tube radius to film thickness ratio with Newtonian and shear thinning data ($n = 0.652$)

film thickness making comparison with their experimental data simpler. It allows a comparison of film thickness forming on the inside of the tube rather than a comparison of the tube diameter for a given film thickness. Figures 3.10 and 3.11 show the agreement between the experimental data and the BVP solution to be very good, with the effect of decreasing power index leading to a reduction in the final film thickness (or fluid deposited) for capillary numbers less than 0.55. The level of agreement is best at lower capillary numbers ($Ca_{K\&R} < 0.2$). The region of least agreement is most likely due to the increase in viscous forces, which became significant at greater θ values, where the validity of the lubrication approximation breaks down.

3.3.4 Conclusion

Agreement between the results of the formulated BVP and the experiments of Kamisli & Ryan is excellent. The effect of an increase in the shear thinning properties of the test fluid results in

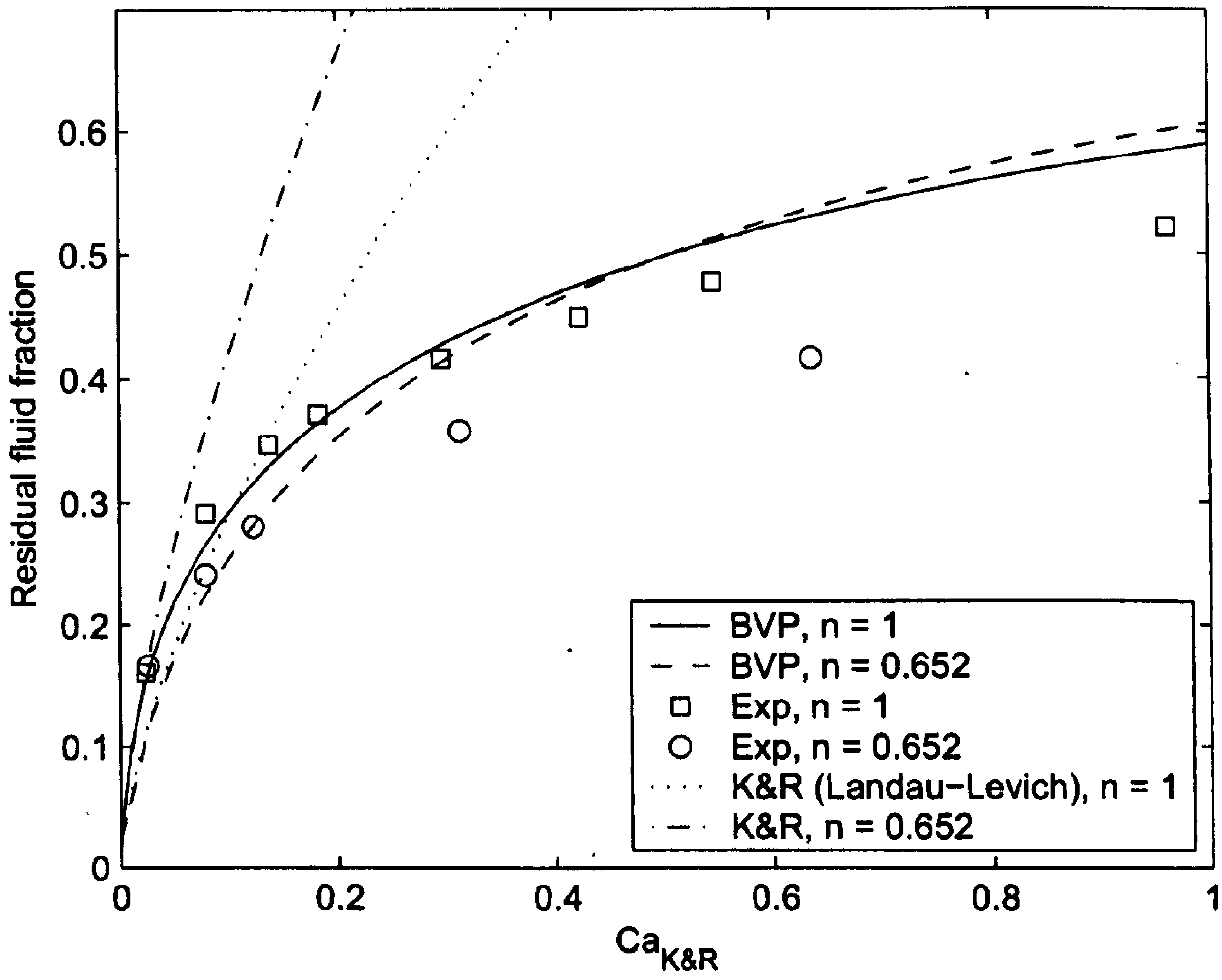

Figure 3.11: A comparison of the BVP predictions and Kamisli & Ryan's [7] residual fluid fraction with Newtonian and shear thinning data ($n = 0.652$)

a decrease in the residual fluid deposited on the inside of the tube. Since the level of agreement is seen to deteriorate as the capillary number increases, a conservative limit for which the BVP can be deemed applicable is perhaps $Ca_{K\&R} < 0.1$. The reason for the drop off in agreement beyond this point is possibly due to the increase in viscous forces in regions of the flow where the lubrication approximation is not strictly valid.

Chapter 4

Zero Groove Angle Model

4.1 Introduction

Both direct and offset discrete cell gravure roll coating have, to date, proved resistant to predictive theoretical analysis - see Chapter 1. This is not surprising given the associated transient behaviour and accompanying web deformation that occurs. Accordingly, attention is focused on the simpler, but by no means trivial case of tri-helical gravure roll coating where an analytical solution becomes tractable. The continuous domain present in this coating process removes the transient nature of the problem and, as seen in section 4.3.1 and subsequent chapters, the process can be modelled successfully when no web deformation is assumed.

The analysis of the process can be divided into two parts: the first is made up of the hydrodynamic pressure equations describing the flow between the two menisci; the second models the locations of and pressure at the menisci. The method of solution employed involves a search for a (constant) flux throughout the coating bead that results in consistent pressures as obtained from the film splitting and hydrodynamic equations.

The problem is similar in nature to that of smooth rigid roll coating, in that the geometry varies slowly in the x-direction, the derivation of which is given in the following section for the sake of completeness. This forms one component of the model - that of flow between the web and the lands, but also can be extended (as shown in section 4.2.2), to describe the flow with grooves present in the roll surface.

4.2 Governing Flow Equations

In order to make the problem tractable, the flow between the web and roll needs to be described mathematically. Accordingly, we firstly examine the derivation of the hydrodynamic pressure equations for the simpler case of smooth rigid roll coating.

4.2.1 Lubrication Flow Between Parallel Plates

Lubrication theory has long been used to model flow in the nip region of roll coating systems [1, 21, 23, 25, 41, 45] due to the unidirectional nature of the flow there. This theory is based on the assumption that the geometry is varying slowly in the principal flow direction. Consider the case of two plates, of infinite length, moving in directions parallel to the plate geometry as shown in figure 4.1. If the flow is fully developed there is no variation in velocity in the X-direction and the solution is independent of X. A pressure gradient can exist in the domain, since an infinite pressure is possible and the flow is assumed to be incompressible. Although it is clear that this purely theoretical problem does not arise physically, it forms a reasonable starting point for similar geometries where the flow is essentially uni-dimensional.

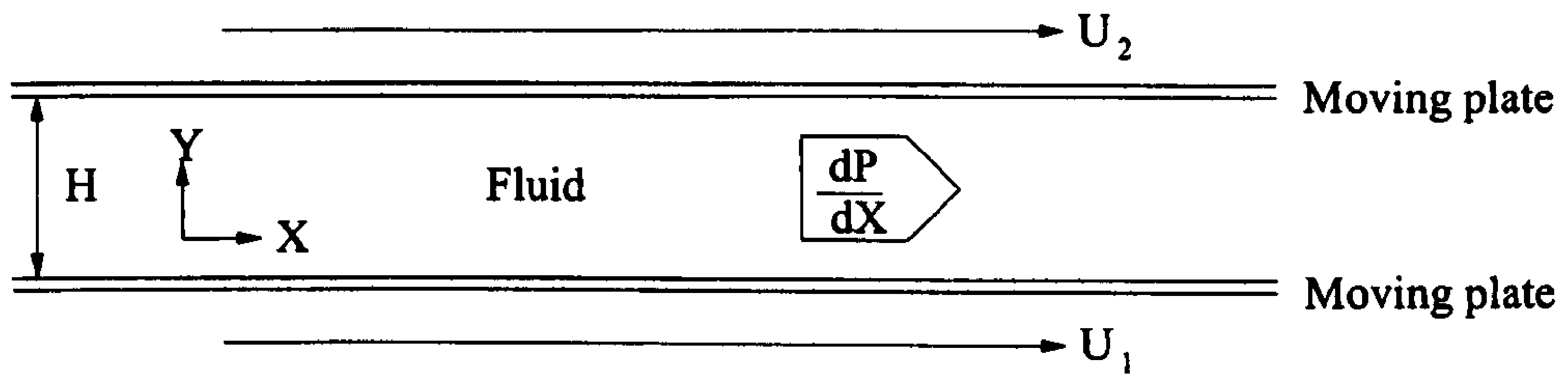

Figure 4.1: Flow between infinite parallel plates

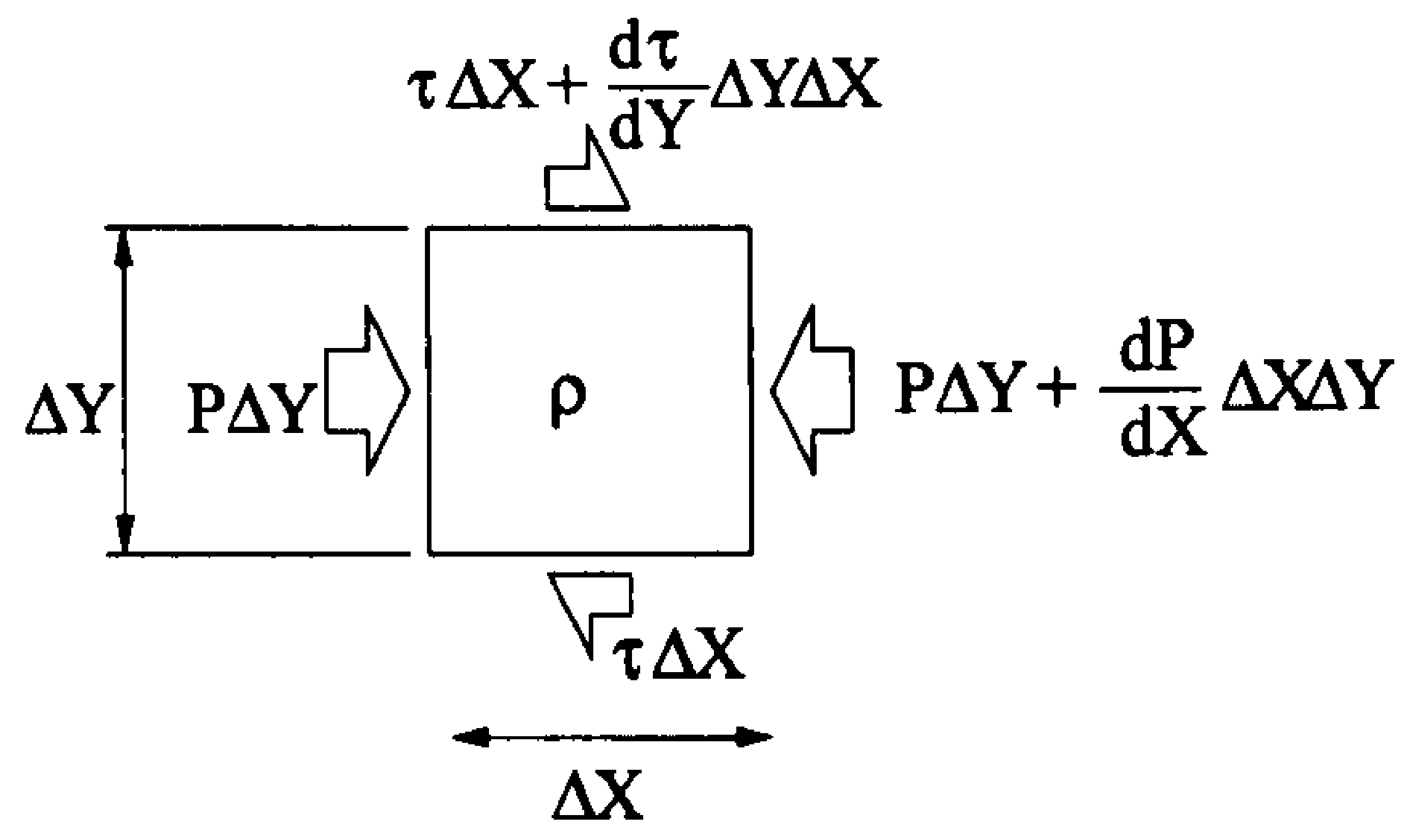

Figure 4.2: Forces encountered by a fluid element in lubrication flow

By considering a fluid element, as shown in figure 4.2, we can examine the forces present. As the velocity is independent of X the inertial effects must be zero. This requires that the resultant force on the fluid element is zero since there is no acceleration of the fluid element in the X-direction. This can be expressed mathematically:

$$P\Delta Y + \frac{dP}{dX}\Delta X\Delta Y - P\Delta Y = \tau\Delta X + \frac{d\tau}{dY}\Delta Y\Delta X - \tau\Delta X, \tag{4.1}$$

where τ is the shear stress, P is the local pressure and X and Y are the co-ordinates in the direction parallel and perpendicular to the plates respectively. Equation (4.1) simplifies to give:

$$\frac{\partial P}{\partial X} = \frac{\partial \tau}{\partial Y}. \tag{4.2}$$

The shear stress of a fluid is proportional to its rate of strain, γ, such that:

$$\tau = \mu\gamma, \tag{4.3}$$

where μ, the constant of proportionality, is the viscosity. For a simple shearing flow between two parallel plates the fluid strain rate is simply the velocity gradient ($\gamma = \frac{du}{dy}$). Substituting this into equation (4.3) results in the following relationship:

$$\frac{\partial P}{\partial X} = \frac{\partial}{\partial Y}\left(\mu\frac{\partial U}{\partial Y}\right) \quad \left[\equiv \mu\frac{\partial^2 U}{\partial Y^2} \quad \text{for a Newtonian fluid}\right]. \tag{4.4}$$

By definition Newtonian fluids have a constant viscosity, in which case the viscosity can be taken outside of the differential, as shown in the bracketed term. This equation can also be derived directly from the Navier–Stokes X-momentum equation by setting $\frac{\partial U}{\partial X} = 0$ and by invoking the conservation of mass equation.

Equation (4.4), when integrated twice with respect to Y (noting that $\frac{dP}{dX}$ is independent of Y), gives an equation for the velocity in the gap:

$$\frac{dU}{dY} = \frac{1}{\mu}\frac{dP}{dX}Y + C_1, \tag{4.5}$$

$$U = \frac{1}{2\mu}\frac{dP}{dX}Y^2 + C_1 Y + C_2. \tag{4.6}$$

The constants of integration (C_1 and C_2) can be found by applying the velocity boundary conditions at $Y = 0$ and $Y = H$ where $U = U_1$ and $U = U_2$, respectively. The resulting velocity distribution is:

$$U = \underbrace{\frac{1}{2\mu}\frac{\partial P}{\partial X}Y(Y-H)}_{\text{Poiseuille term}} + \underbrace{\frac{Y}{H}(U_2 - U_1) + U_1}_{\text{Couette term}}. \tag{4.7}$$

Equation (4.7) has two components, one based on the pressure gradient (Poiseuille term) and the other based on the velocity of the plates (Couette term); the flow described by the two terms is called Poiseuille-Couette flow. The application of equation (4.7) to flows where the two surfaces are not infinite is valid provided they are a lot longer than the separation between them and that the velocity of the plates is predominantly in a direction parallel to their surfaces. It is therefore reasonable to conclude that as the geometry becomes less like the idealised situation on which equation (4.7) is based, it becomes less applicable. That said, the lubrication equations have been applied successfully applied to flows where abrupt changes in geometry exist and the assumptions used in the derivation are not strictly valid [18]. Further integration of the velocity profile between the two plates leads to the equation describing the volume flow, Q, between them:

$$Q = \frac{H(U_1 + U_2)}{2} + \frac{H^3}{12\mu}\frac{dP}{dX}. \tag{4.8}$$

In the case of tri-helical gravure roll coating, the height of the grooves is of the same order as their width. For this reason a second equation is required to describe the flow in this two dimensional geometry. As will be shown, the equations describing the flow along the roll's groove include an additional term that accounts for the viscous forces exerted from the groove walls. The tri-helical gravure roll coating flow under consideration is shown schematically in figure 4.3.

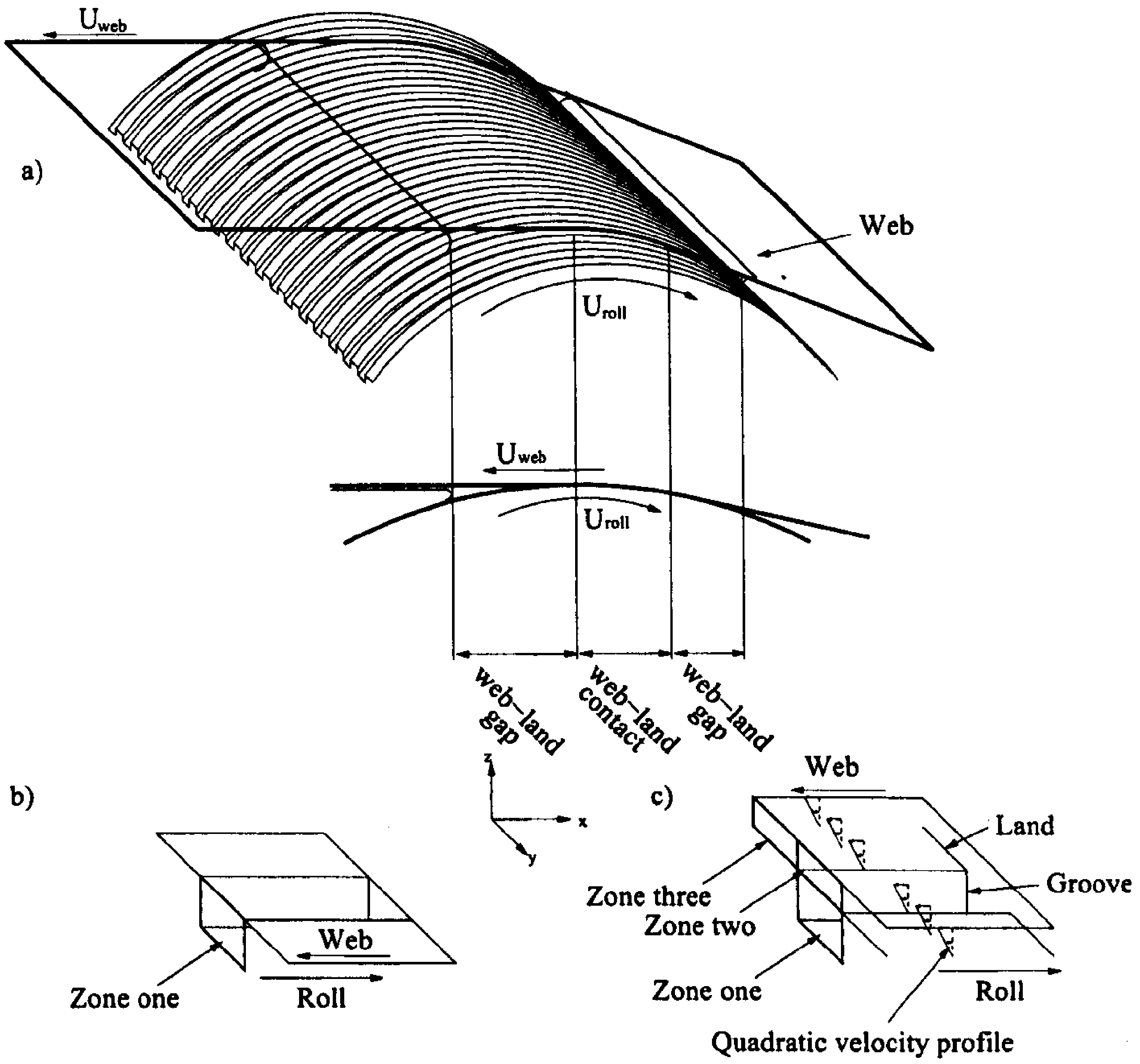

Figure 4.3: A schematic diagram of: (a) the coating bead in cross section; (b) roll-web contact geometry ('basic' solution); (c) roll-web gap geometry ('extended' solution).

4.2.2 Flow Along Grooved Channels

With the Navier–Stokes X-momentum equation as the starting point a simplified equation describing the flow in the coating bead can be derived. The three dimensional Navier–Stokes X-momentum equation for a Newtonian fluid is:

$$\frac{\partial U}{\partial T} + U\frac{\partial U}{\partial X} + V\frac{\partial U}{\partial Y} + W\frac{\partial U}{\partial Z} = -\frac{1}{\rho}\frac{\partial P}{\partial X} + \frac{\mu}{\rho}\left(\frac{\partial^2 U}{\partial X^2} + \frac{\partial^2 U}{\partial Y^2} + \frac{\partial^2 U}{\partial Z^2}\right), \tag{4.9}$$

where U, V and W are the velocities in the X, Y and Z directions, P is the pressure, μ is viscosity and ρ is the fluid density.

Assuming a slowly varying geometry in the X-direction, the change in U gives: $\frac{\partial U}{\partial X} = 0$. The slowly changing geometry results in negligible viscous and pressure forces in the the Y and Z directions, as a consequence of which the V and W velocities are negligible. Applying these assumptions reduces equation (4.9) to:

$$\frac{1}{\mu}\frac{\partial P}{\partial X} = \frac{\partial^2 U}{\partial Y^2} + \frac{\partial^2 U}{\partial Z^2}, \tag{4.10}$$

an equation representing a simple balance between viscous forces and the pressure gradient force applied to a fluid element and applicable for the case of grooves with zero pitch.

Equation (4.10) can be written in the non-dimensional form:

$$\frac{\partial p}{\partial x} = \frac{\partial^2 u}{\partial y^2} + \frac{\partial^2 u}{\partial z^2}, \tag{4.11}$$

using the following non-dimensional scalings throughout:

$$z = \frac{Z}{A}, \quad y = \frac{Y}{A}, \quad S = \frac{U_{web}}{U_{roll}}, \quad p = \frac{PA}{\mu U_{roll}},$$

where A is the groove width and U_{roll} and U_{web} are the roll and web velocities, respectively.

The solution of equation (4.11) is required to determine the relationship between the pressure gradient and the flux (calculated by integrating the velocity across the domain). This relationship can then be used to obtain the pressure distribution between menisci for a given flux, and can therefore be used to search for a flux that has a pressure distribution consistent with the meniscus models employed.

4.3 The Geometry of the Fluid Domain

Before the relationship between the pressure distribution and flux can be determined, the domain over which equation (4.11) is solved has to be specified. The following section describes the basis of the underpinning geometry. As with any problem a series of assumptions are required - a key one here (justified in the next section) is that the web profile does not change, whether fluid is or is not present - equivalent to the case of an infinitely tensioned web.

4.3.1 Justification of Model Geometry

In the reverse mode direct tri-helical gravure roll coating models developed here, the assumption that the web profile is unaffected by the hydrodynamic pressures within the coating bead can be justified as follows:

- Flow visualisations of the roll to web region, see Chapter 7, indicate no appreciable change in the web path due to hydrodynamic forces over a wide range of capillary numbers and speed ratios.
- The pressures within the coating bead are predicted to be negative [51] as a consequence of the negative pressures at the upstream and downstream meniscii. Consequently these pressures, if sufficiently large, would result in the web being *"sucked"* downward to the roll surface. The lands of the roll will support the web, which effectively acts as a "lid" on the grooves.
- The study of discrete cell gravure roll coating has shown that the web appears to be in contact with the roll at least intermittently, as scratched have been observed on a plastic web with a thin layer of aluminium, caused by roll to web contact [66]. It may be that the

two gravure coating processes, tri-helical and discrete cell are fundamentally different, with elasto-hydrodynamic lubrication an important factor in the latter but not the former, so the relevance of this evidence is disputable as explored later.

4.3.2 Analytical Solution of the Hydrodynamic Equation

An analytical solution of equation (4.10) can be obtained if the grooves are taken to be rectangular. If, as is the case in industry, the grooves are either triangular or semi-circular in cross section a more complex numerical solution (see chapter 5) has to be sought.

Perhaps the simplest domain to model is when there is web-to-roll contact and the domain is rectangular (as shown in figure 4.3b)). A solution of Poisson's equation in this situation, with relevant boundary conditions, is relatively simple, although not trivial, and can be found in some general engineering mathematics text books [129].

The complexity of the problem greatly increases when the web is not in contact with the roll (as shown in figure 4.3c)). In this case there is fluid above the lands as well as within the groove resulting in an (upside down) L-shaped domain. The problem is solved by dividing it into three rectangular sub-domains.

4.3.3 Method of Solution

The solution to equation (4.11) is obtained by the application of Fourier sine transforms (FSTs), in this case in the y - direction.

Finite Fourier Sine Transform (FFST)

Taking the finite Fourier sine transform (FFST) of equation (4.11) in the y-direction leads to the following transformed equation (dimensions are given in figure 4.3):

$$\mathcal{F}_y\left(\frac{\partial p}{\partial x}\right) = \mathcal{F}_y\left(\frac{\partial^2 u}{\partial y^2}\right) + \mathcal{F}_y\left(\frac{\partial^2 u}{\partial z^2}\right). \tag{4.12}$$

The second derivative of the velocity, u with respect to y can be manipulated using FFSTs. Consider the FFST of a second derivative as shown below.

$$\mathcal{F}_y\left(\frac{\partial^2 u}{\partial y}\right) = \int_0^{\pi} \frac{\partial^2 u}{\partial y^2} \sin(n\pi y)\, dy \quad n = 1, 2, 3, \ldots \tag{4.13}$$

This equation can be solved thus:

$$\begin{aligned}
\mathcal{F}_y\left(\frac{\partial^2 u(y,z)}{\partial y}\right) &= \int_0^{\pi} \frac{\partial^2 u(y,z)}{\partial y^2} \sin(n\pi y)\, dy, && (4.14)\\
&= \left[\sin(n\pi y) \frac{\partial u(y,z)}{\partial y}\right]_0^{\pi} - \int_0^{\pi} \frac{\partial u(y,z)}{\partial y} n\pi \cos(n\pi y)\, dy, && (4.15)\\
&= -\, n\pi \int_0^{\pi} \frac{\partial u(y,z)}{\partial y} \cos(n\pi y)\, dy, && (4.16)\\
&= -\, n\pi \left(\left[\cos(n\pi y)\, u(y,z)\right]_0^{\pi} - \int_0^{\pi} u(y,z)\left[-n\pi \sin(n\pi y)\right] dy \right), && (4.17)\\
&= -\, n\pi \left[\cos(n\pi)\, u(1,z) - u(0,z) + n\pi \mathcal{F}_y u(y,z)\right], && (4.18)\\
&= -\, n^2\pi^2 \mathcal{F}_y u(y,z) + n\pi \left(u(0,z) - (-1)^n u(1,z)\right). && (4.19)
\end{aligned}$$

This result can be substituted into equation (4.12) which, with some manipulation, leads to:

$$\frac{\partial p}{\partial x}\left(\frac{1-(-1)^n}{n\pi}\right) = -n^2\pi^2 \mathcal{F}_y u(y,z) + n\pi\left(u(0,z) - (-1)^n u(1,z)\right) + \frac{\partial^2 u^{\star}(n,z)}{\partial z^2}, \tag{4.20}$$

that can be solved by imposing appropriate boundary conditions. These boundary conditions depend on whether there is web-to-roll contact or whether the web is not in contact with the roll. These two situations are depicted in figure 4.3.

4.3.4 Basic Flow Solution

When the web is in contact with the roll (web-to-land contact shown in figure 4.3b), the domain has a rectangular cross section. Changing the frame of reference to that of a stationary roll surface improves the convergence of the solution and the number of terms required in the infinite expansion is decreased. Note that for the reverse mode of operation studied here $S < 0$. Transforming equation (4.11) and applying the boundary conditions $u = 0$ at $y = 0$ and $y = 1$ gives:

$$\frac{\partial p}{\partial x}\left(\frac{1-(-1)^n}{n\pi}\right) = -\left(n\pi\right)^2 u^\star\left(n,z\right) + \frac{\partial^2 u^\star\left(n,z\right)}{\partial z^2}, \tag{4.21}$$

which can now be solved as the length variables y and z have been separated:

$$u^\star\left(n,z\right) = a\left(n\right)e^{\pi n z} + b\left(n\right)e^{-\pi n z} - \frac{\partial p}{\partial x}\left(\frac{1-(-1)^n}{\left(n\pi\right)^3}\right). \tag{4.22}$$

The variables $a\left(n\right)$ and $b\left(n\right)$ are functions of n, where $n = 1, 2, 3, \ldots$ and the boundary condition $u = 0$ at $z = 0$ results in:

$$0 = a\left(n\right) + b\left(n\right) - \frac{\partial p}{\partial x}\left(\frac{1-(-1)^n}{\left(n\pi\right)^3}\right), \tag{4.23}$$

while the boundary condition $u = S - 1$ at $z = r$ leads to:

$$\left(S-1\right)\frac{\left(1-(-1)^n\right)}{\left(n\pi\right)} = a\left(n\right)e^{\pi n r} + b\left(n\right)e^{-\pi n r} - \frac{\partial p}{\partial x}\left(\frac{1-(-1)^n}{\left(n\pi\right)^3}\right). \tag{4.24}$$

$a\left(n\right)$ and $b\left(n\right)$ can be solved for using equations (4.23) and (4.24) , giving:

$$a\left(n\right) = -\frac{\left(-\frac{\partial p}{\partial x}e^{-n\pi r} + n^2\left(S-1\right)\pi^2 + \frac{\partial p}{\partial x}\right)\left(-1+(-1)^n\right)}{n^3\pi^3\left(e^{n\pi r} - e^{-n\pi r}\right)}, \tag{4.25}$$

$$b\left(n\right) = -\frac{\left(e^{n\pi r}\frac{\partial p}{\partial x} - n^2\left(S-1\right)\pi^2 - \frac{\partial p}{\partial x}\right)\left(-1+(-1)^n\right)}{n^3\pi^3\left(e^{n\pi r} - e^{-n\pi r}\right)}. \tag{4.26}$$

The transformed velocity $u^\star\left(n,z\right)$ can now be transformed back to $\left(y,z\right)$ space. This gives the velocity as an infinite Fourier sine series:

$$u\left(y,z\right) = 2\sum_{n=1}^{\infty} u^\star\left(n,z\right)\sin n\pi y, \tag{4.27}$$

which, along with equations (4.22), (4.25) and (4.26), give the velocity solution within a groove as $n \to \infty$.

Integration of equation (4.27) across the domain provides the relationship between flux and pressure gradient:

$$q = \int_0^r \int_0^1 2 \sum_{n=1}^{\infty} u^\star (n, z) \sin n\pi y dz dy, \tag{4.28}$$

$$= 2 \sum_{n=1}^{\infty} \int_0^r \int_0^1 u^\star (n, z) \sin n\pi y dz dy, \tag{4.29}$$

which can be rearranged to give pressure gradient in terms of flux, see Appendix D.

4.3.5 Extended Flow Solution

The solution of equation (4.11) when the web is not in contact (web-to-land gap shown in figure 4.3c) with the roll is more complex due to the non-rectangular nature of the domain. A solution is obtained by subdividing it into three rectangular zones as shown in figure 4.3(c). Within zones one and two equation (4.11) is solved using FFSTs in the y-direction with the boundary conditions given in table 4.1. In the third zone the flow is solved using a one dimensional Poiseuille-Couette flow, making the problem tractable. This assumption neglects shear stresses derived from velocity gradients in the y-direction, the validity of which was confirmed by comparing the flux results with those obtained using a finite element solution of the problem as outlined in chapter 5.

The transformed velocity along the boundary of zones one and two was obtained by matching both the velocities and the velocity gradients in the z-direction: i.e. $u_{\text{Zone One}} = u_{\text{Zone Two}}$ and $\frac{du}{dz}\big|_{\text{Zone One}} = \frac{du}{dz}\big|_{\text{Zone Two}}$.

The solution in zone one is similar to that for the case when the web is in contact with the land, the difference being the boundary condition located at $z = r$. At the interface between zones one and two, the interface velocity is $u^\star = u^\star_{interface}$. Applying the $z = 0$ and $z = r$ boundary conditions

Zone	Dimensionless Boundary Condition	
	Location (y, z)	u
Zone One	$(0, 0 \rightarrow r)$	0
	$(1, 0 \rightarrow r)$	0
	$(0 \rightarrow 1, 0)$	0
	$(0 \rightarrow 1, r)$	$u_{interface}(y)$
Zone Two	$(0 \rightarrow 1, r)$	$u_{interface}(y)$
	$(0, r \rightarrow (r+d))$	$\frac{1}{2}\frac{\partial p}{\partial x}(z-r)((z-r)-d) + \frac{(S-1)(z-r)}{d}$
	$(1, r \rightarrow (r+d))$	$\frac{1}{2}\frac{\partial p}{\partial x}(z-r)((z-r)-d) + \frac{(S-1)(z-r)}{d}$
	$(0 \rightarrow 1, (r+d))$	$(S-1)$

Table 4.1: Boundary Conditions

to equation (4.22) results in equations (4.23) and (4.30), respectively. Accordingly:

$$u^{\star}_{interface} = a_1(n)\, e^{n\pi r} + b_1(n)\, e^{-n\pi r} - \frac{\frac{\partial p}{\partial x}\left(1-(-1)^n\right)}{n^3\pi^3}. \tag{4.30}$$

The application of these boundary conditions can now be used to obtain $a_1(n)$ and $b_1(n)$:

$$a_1(n) = \frac{\frac{\partial p}{\partial x}\left(-1+(-1)^n\right)e^{-n\pi r} + u^{\star}_{interface} n^3\pi^3 + \frac{\partial p}{\partial x} - \frac{\partial p}{\partial x}(-1)^n}{n^3\pi^3\left(-e^{-n\pi r}+e^{n\pi r}\right)}, \tag{4.31}$$

$$b_1(n) = \frac{\left(\frac{\partial p}{\partial x} - \frac{\partial p}{\partial x}(-1)^n\right)e^{n\pi r} - u^{\star}_{interface} n^3\pi^3 - \frac{\partial p}{\partial x} + \frac{\partial p}{\partial x}(-1)^n}{n^3\pi^3\left(-e^{-n\pi r}+e^{n\pi r}\right)}. \tag{4.32}$$

The solution of the flow in domain one is now a function of the transformed interface velocity $u^{\star}_{\text{interface}}(n, z)$. The flow in zone two is obtained using the boundary conditions given in table 4.1 with a Poiseuille-Couette flow velocity distribution forming the boundary conditions at $y = 0$ and $y = 1$. Similarly, the transformed interface velocity forms the boundary condition at $z_2 = 0$ (where a change of coordinate frame is made in accordance with $z_2 = z - r$ as this simplifies the solution).

Applying the boundary conditions at $y = 0$ and $y = 1$ to equation (4.20) and solving for the transformed velocity $u^{\star}(n, z)$ results in the following transformed velocity equation:

$$u^{\star}(n, z_2) = a_2(n)\, e^{n z_2 \pi} + b_2(n)\, e^{-n z_2 \pi} + \frac{\left(1-(-1)^n\right)\left(\frac{1}{2}\frac{\partial p}{\partial x}\left(z_2^2 - z_2 d\right) + \frac{(S-1)z_2}{d}\right)}{n\pi}. \tag{4.33}$$

Applying the boundary conditions $u^{\star} = u^{\star}_{interface}$ at $z_2 = 0$ and $u = S - 1$ at $z_2 = d$ to equation (4.33) gives:

$$u^{\star}_{interface}(y) = a_2(n) + b_2(n), \tag{4.34}$$

and

$$0 = a_2(n)\, e^{n\pi d} + b_2(n)\, e^{-n\pi d}, \tag{4.35}$$

respectively. It is interesting to note that these equations, resulting from the quadratic velocity profiles, are simpler than those encountered in the basic flow and zone one solutions.

The unknowns $a_2(n)$ and $b_2(n)$ can now be solved for:

$$a_2(n) = \frac{-u^{\star}_{interface}(n)\, e^{-n\pi d}}{e^{n\pi d} - e^{-n\pi d}}, \tag{4.36}$$

$$b_2(n) = \frac{u^{\star}_{interface}(n)\, e^{n\pi d}}{e^{n\pi d} - e^{-n\pi d}}. \tag{4.37}$$

The remaining unknown is the velocity at the interface between the two zones. This transformed velocity along this interface is found by equating the velocity gradients of the interface for the two zones:

$$\frac{\partial u_{interface}}{\partial z} = \left.\frac{\partial \left(2\sum_{i=1}^{\infty} u^{\star}_{ZoneOne}(n,z) \sin n\pi y\right)}{\partial z}\right|_{z=r} = \left.\frac{\partial \left(2\sum_{i=1}^{\infty} u^{\star}_{ZoneTwo}(n,z_2) \sin n\pi y\right)}{\partial z}\right|_{z_2=0} \tag{4.38}$$

Equation (4.38) is respected if:

$$\left.\frac{\partial u^{\star}_{ZoneOne}(n,z)}{\partial z}\right|_{z=r} = \left.\frac{\partial u^{\star}_{ZoneTwo}(n,z_2)}{\partial z}\right|_{z_2=0}. \tag{4.39}$$

This leads to the solution for the transformed interface velocity:

$$\begin{aligned} u^{\star}_{interface} &= \frac{1}{4}\left[\left(e^{nr\pi} - e^{-nr\pi}\right)\left(n\left(\frac{\partial p}{\partial x}\, d^2 + 2 - 2\, S\right)\pi + 2\, d\frac{\partial p}{\partial x}\right) - 4\, d\frac{\partial p}{\partial x}\right] \\ &\times \frac{\left(e^{n\pi\, d} - e^{-n\pi\, d}\right)\left(-1 + (-1)^n\right)}{n^3\pi^3 d\left(e^{n\pi\, d}e^{nr\pi} - e^{-n\pi\, d}e^{-nr\pi}\right)}, \end{aligned} \tag{4.40}$$

where d is the web-to-roll surface gap and r is the groove depth.

As outlined previously, a Couette-Poiseuille flow is imposed in zone three. This is based on the assumption that the velocity gradients in the y-direction are less than those in the z-direction, since there is close proximity of the lands and web in this zone. The Couette-Poiseuille flow also determines the boundary conditions for zone two at:

$$(y, z) = (0, r \rightarrow (r + d)), (1, r \rightarrow (r + d)). \tag{4.41}$$

The transformed velocities in zone one and two can now be written in terms of y and z by summing up the individual terms of the Fourier sine series from $n = 1 \rightarrow \infty$. It is at this stage that the roller velocity is superimposed onto the velocities so that the frame of reference is moved back to a laboratory one.

As with the basic groove flow model, the velocity in each zone can be integrated to obtain the corresponding flux. Similarly the flux equations for each zone can be separated into drag and pressure parts, analogous to the Couette and Poiseuille components in the one-dimensional case. It is interesting to note that as with Poiseuille-Couette flow, the flux and pressure gradient have a linear relationship - this was found to be extremely useful in finding solutions to the problem, as detailed in chapter 5. The total flux is therefore given as:

$$\begin{aligned} Flux =& \underbrace{r + 2\sum_{n=1}^{\infty} f_{ZoneOne}\left(n, r, \frac{\partial p}{\partial x}, S, d\right)}_{ZoneOne} \\ &\underbrace{+ d + 2\sum_{i=1}^{\infty} f_{ZoneTwo}\left(n, r, \frac{\partial p}{\partial x}, S, d\right)}_{ZoneTwo} \\ &\underbrace{+ gl + f_{ZoneThree}\left(n, \frac{\partial p}{\partial x}, S, d, l\right)}_{ZoneThree}. \end{aligned} \tag{4.42}$$

After the pressure and drag components are separated the pressure gradient term can be moved outside the summation:

$$
\begin{aligned}
Flux = \; & \underbrace{r + \sum_{n=1}^{\infty} f_{drag}(n,r,S,d) + \frac{\partial p}{\partial x}\sum_{n=1}^{\infty} f_{pressure}(n,r,d)}_{ZoneOne} \\
+ \; & \underbrace{d + \sum_{i=1}^{\infty} f_{drag}(n,r,S,d) + \frac{\partial p}{\partial x}\sum_{i=1}^{\infty} f_{pressure}(n,r,d)}_{ZoneTwo} \qquad (4.43) \\
+ \; & \underbrace{dl + f_{Couette}(S,d,l) + \frac{\partial p}{\partial x} f_{Poiseuille}(S,d,l)}_{ZoneThree}.
\end{aligned}
$$

The pressure gradient can now be determined in terms of the flux, roll geometry, speed ratio and web-to-roll gap. The link between pressure gradient and flux together with conservation of mass, is used to determine the pressure distribution in the coating bead subject to pressure boundary conditions.

4.4 Meniscus Models

In order to close the problem and make it tractable numerically, appropriate boundary conditions at the ends of the domain, for the pressure gradient equations, are required. These boundary conditions take the form of meniscus models that link pressure and location of the menisci to the flux.

At a free surface the pressure is equal to the capillary pressure due to surface tension, the forms of which are:

$$P = \frac{\kappa}{\sigma} \qquad p = \frac{\kappa}{Ca}, \qquad (4.44)$$

where κ and κ are the dimensional and non-dimensional meniscus curvatures, σ is the surface tension and Ca is the capillary number:

$$Ca = \frac{\mu U_{\text{roll}}}{\sigma}. \qquad (4.45)$$

4.4.1 Downstream Meniscus

The downstream meniscus (where the web leaves the coating bead) is modelled using the Coyne & Elrod cavitation model [5, 6]. As described fully in Chapter 3, this model provides a greater range of capillary numbers over which it is valid when compared to the more commonly used [51, 130, 131, 45] Landau-Levich equation [2, 3].

The pressure at the point of film splitting is based on the local radius of curvature of the meniscus. Film thickness is determined from the coating flux as:

$$h_w = \frac{q}{(1+l)\,|S|}. \tag{4.46}$$

From the film thickness and therefore the web-to-roll gap, as obtained from the Coyne & Elrod model, the location of the meniscus can be determined, using a parabolic approximation for the roll surface (see equation (4.65) later), and is given by:

$$x_{dsm} = -\sqrt{2r_{roll}h_w\,(2c-1)}. \tag{4.47}$$

The pressure at this location is also obtained as part of the solution as the radius of curvature is calculated from the Coyne & Elrod model.

4.4.2 Upstream Meniscus

At the upstream meniscus, a simplification of the complex three dimensional meniscus shape is required. Only the dominant radii of curvature are considered for the meniscus between the roll surface (comprising the land and the groove) and the web; with an extra radius contribution due to the curvature of the meniscus entirely within the groove. These contributions are represented pictorially in figure 4.4. Figure 4.5 shows the film thickness coated onto the land, groove walls and groove bottom, from which the film thickness can be derived:

$$h_1 = \frac{r+d}{c_\theta}, \qquad h_2 = \frac{1}{2c_{90}}, \qquad h_3 = \frac{d}{c_\theta}, \tag{4.48}$$

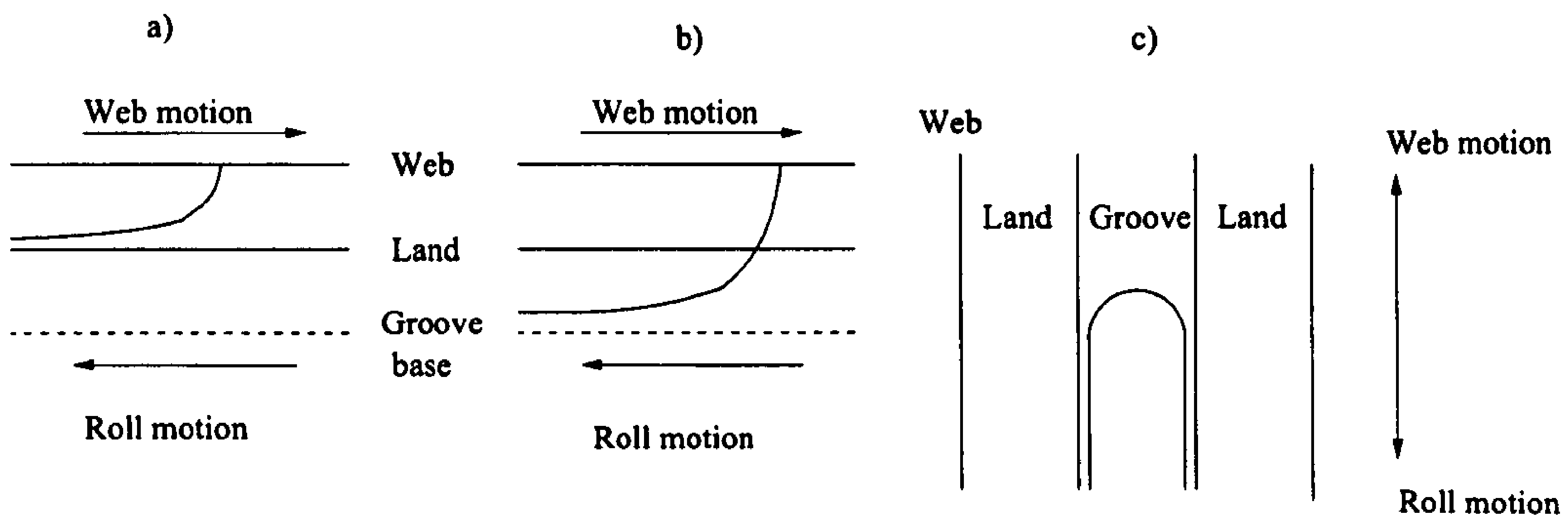

Figure 4.4: Dominant radii of curvature considered in the upstream meniscus model: a) Side view showing dominant radius of curvature between the web and land; b) side view showing dominant radius of curvature between web and groove; c) top view looking through web showing dominant radius of curvature within a groove.

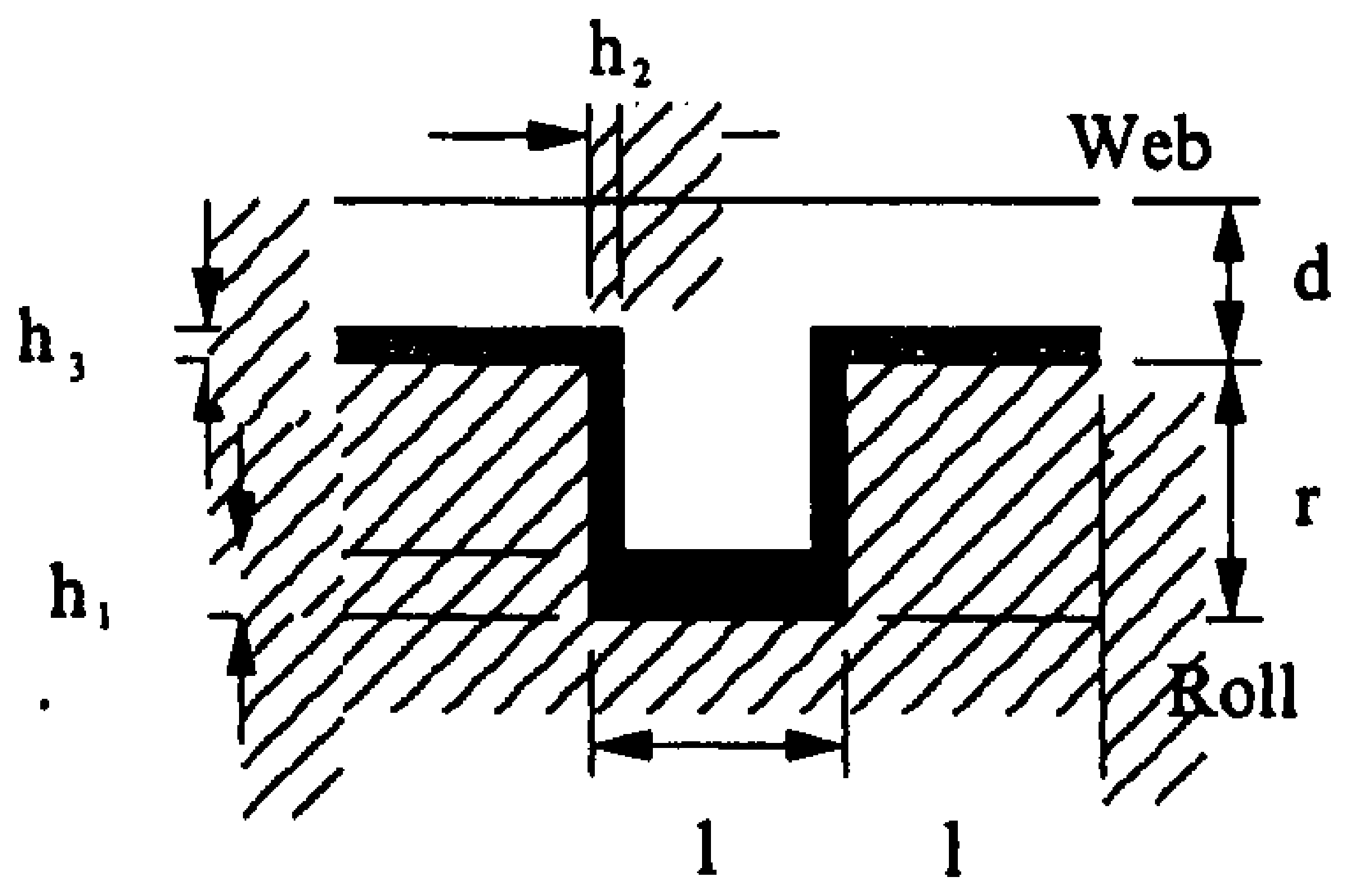

Figure 4.5: Simplified filling of grooves at upstream meniscus

where c_θ and c_{90} are the gap to film thickness for contact angles of θ_D (the dynamic contact angle) and 90° respectively. The flux on the roll can now be written as:

$$q_{roll} = h_1 + h_2\left(r - h_1 + h_3\right) + h_3 l, \tag{4.49}$$

which can be solved for in terms of web-to-roll gap (*d*), roll geometry (l and r) and gap to film thickness ratios (c_θ and c_{90}) using equation (4.48), giving:

$$q_{roll} = \frac{\left(2r + \left(2 + 2l\right)d\right)c_{90} + r\left(c_\theta - 1\right)}{2c_{90}c_\theta}. \tag{4.50}$$

Making d the subject of equation (4.50) gives:

$$d = \frac{\left(2c_\theta q_{roll} - 2r\right)c_{90} - rc_\theta + r}{2c_{90}\left(1 + l\right)}, \tag{4.51}$$

which can then be used to determine the meniscus location, via equation (4.65) for $x > \beta r_{roll}$:

$$x = \beta r_{roll} + \sqrt{2dr_{roll}}. \tag{4.52}$$

In addition to the location of the upstream meniscus the pressure there is also required as a boundary condition for the model. When curved in two dimensions the meniscus pressure is calculated thus:

$$p_{usm} = \frac{\kappa_y + \kappa_z}{Ca}, \tag{4.53}$$

where κ_y and κ_z are the meniscus curvatures perpendicular to one another. κ_y is based on the two different radii of curvature, that between the land and web (κ_{y2}) and the other between the groove base and web (κ_{y1}):

$$\kappa_y = \frac{\left(\kappa_{y1} + l\kappa_{y2}\right)}{1 + l}. \tag{4.54}$$

κ_z is simply based on the width of the groove. This leads to the following expression for the upstream meniscus pressure:

$$p_{usm} = \frac{1}{Ca}\left(\kappa_z + \frac{\kappa_{y1} + l\kappa_{y2}}{1 + l}\right). \tag{4.55}$$

4.4.3 Dynamic Contact Angle Model

A challenge for any model such as the one above is the way in which the dynamic contact angle is represented (θ_D). Others have simply specified a value [51], used Tanner's law [112] or employed the asymptotics of Shikhmurzaev [45]. The empirical dynamic contact angle model used in the present analysis is that of Jiang, Oh and Slattery [116], relating dynamic contact angle (θ_D) to the static contact angle (θ_A) and capillary number (Ca). This model ensures the dynamic contact angle is bounded between 0 and 180° and when implemented into the tri-helical gravure roll coating model ensures it remains robust:

$$\frac{\cos\theta_A - \cos\theta_D}{\cos\theta_A + 1} = \tanh\left(4.96Ca^{0.702}\right). \tag{4.56}$$

Based on the specific operating conditions equation (4.56) is used to determine the final meniscus angle specified in the Coyne & Elrod model. Due to the unstable nature of the latter and the different step sizes required to obtain a solution for film thickness and curvature, a matrix of data was obtained for a range of capillary numbers and contact angles. Linear interpolation between these points was then used within the coating model to obtain solutions.

The dynamic contact angle model represents the only empirical part of the coating model developed here and as such tests were carried out to determine the sensitivity of the solution to using a fixed contact angle ($\theta_D = 90°$). Minimal variation in results with contact angle was confirmed.

4.4.4 Roll Surface Approximation

The web-to-roll gap is obtained from a parabolic representation of the roll surface. Close to the top dead center of the roll the gap (d) is much smaller than the roll radius (r_{roll}) as shown in figure 4.6. Clearly:

$$r_{\text{roll}} = y + d, \tag{4.57}$$

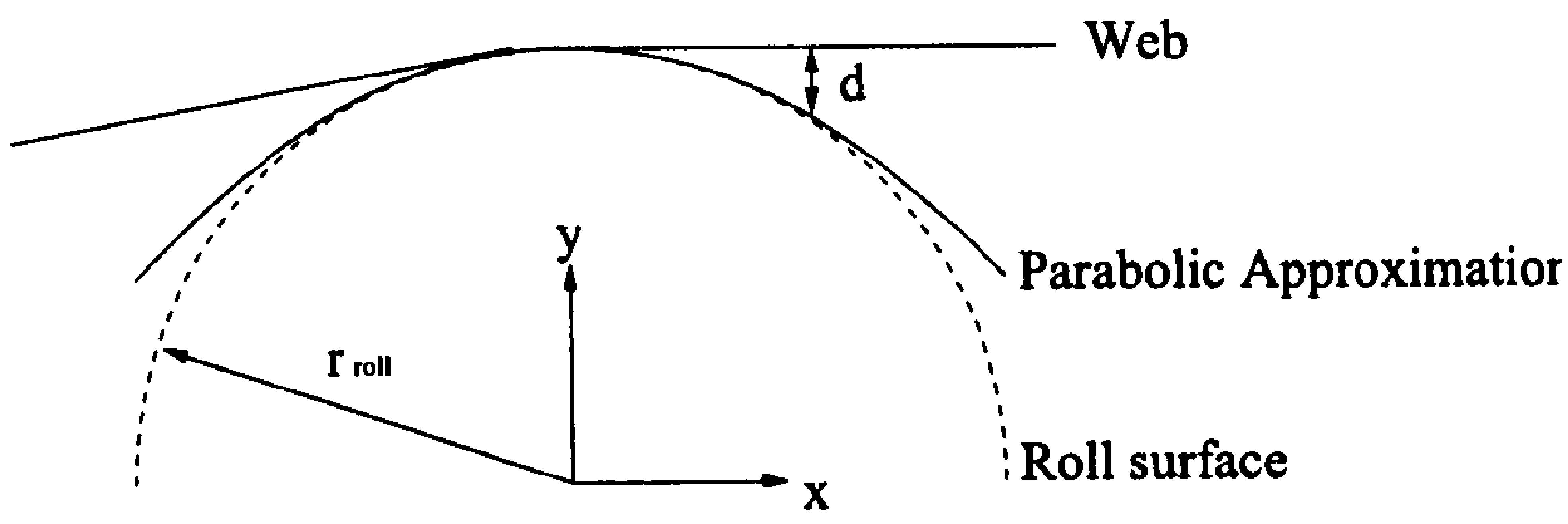

Figure 4.6: Derivation of a Parabolic Representaion of Roll Surface

which in turn leads to:

$$r_{\text{roll}}^2 = (y+d)^2, \tag{4.58}$$

$$= y^2 + 2dy + d^2, \tag{4.59}$$

$$r_{\text{roll}}^2 \approx y^2 + 2dy \quad \text{as} \quad d << y. \tag{4.60}$$

From the equation of a circle $r_{\text{roll}}^2 = x^2 + y^2$:

$$r_{\text{roll}}^2 - x^2 = y^2, \tag{4.61}$$

$$r_{\text{roll}}^2 - x^2 = r_{\text{roll}}^2 - 2dy, \tag{4.62}$$

$$x^2 = 2dy. \tag{4.63}$$

As $y \approx r_{\text{roll}}$ the gap (d) can be given explicitly as:

$$d = \frac{x^2}{2r_{\text{roll}}}, \tag{4.64}$$

$$d = \frac{x^2}{2r_{roll}} \quad (x < 0) \quad \text{and} \quad d = \frac{(x - \beta r_{roll})^2}{2r_{roll}} \quad (x > \beta r_{roll}). \tag{4.65}$$

4.5 Implementation of the Equations in C++

The equations were programmed in C++ with the assistance of *Maple*[1] due to the algebraic complexity of the equations. A set of eight functions were obtained from the different solutions of

---

[1] A comprehensive suite of mathematical procedures capable of manipulating complex mathematical equations. Maple was written by Maplesoft, a division of Waterloo Maple Inc.

Poisson's equation, as shown in table 4.2.

Equations	Zone	Drag Term	Pressure Term
Basic	N/A	$\sum_{n=1}^{\infty} f(n, r, S, d)$	$\sum_{n=1}^{\infty} f(n, r, d)$
Extended	Zone One	$\sum_{n=1}^{\infty} f(n, r, S, d)$	$\sum_{n=1}^{\infty} f(n, r, d)$
	Zone Two	$\sum_{n=1}^{\infty} f(n, r, S, d)$	$\sum_{n=1}^{\infty} f(n, r, d)$
	Zone Three	$f(S, d, l)$	$f(S, d, l)$

Table 4.2: Fundamental flow equations programmed in C++

Rearranging each of these allowed four functions to be produced from these eight. They provide the pressure gradient in terms of flux (and vice versa) for the basic and extended groove flow problem. The equations giving the pressure gradients can be integrated numerically with respect to x to obtain the pressure distribution within the coating bead, see Appendix D.

4.6 Analytical Model: Method of Solution

The basic philosophy is to determine the flux through the nip which give rise to pressures consistent with those at the meniscus (the latter calculated for the local geometry). This ensures that both conservation of mass and momentum (from the application of the simplified x-momentum equation in the form of Poisson's equation) are observed.

Ideally an analytical solution for the pressure throughout the coating bead might be derived, however the complexity of the equations makes this unachievable at the present time. The pressure distribution within the bead is therefore obtained via numerical integration of the pressure gradient equations using the following steps:

1. From an initial guess of the flux though the coating bead, the meniscus models were applied to locate both the upstream and downstream menisci as well as to determine the pressures at these locations.

2. The hydrodynamic pressure gradient equations were then integrated numerically from the downstream meniscus to the upstream one, with the starting pressure equal to that obtained from the meniscus model.

3. For a flux though the coating bead to be consistent then pressure at the upstream meniscus, based on the numerical integration of the hydrodynamic pressure gradient equations, must be equal to that calculated in step 1.

4. Until a pressure match is achieved, a search method is employed to determine the flux that satisfies the required pressure condition. This takes the form of a quadratic search to determine the flux for which the magnitude of the error is less than 10^{-7}. Typically 20 to 30 iterations are required, and the search method proved to be extremely robust.

For the fully flooded case, there are no menisci and the condition of $p = 0$ was applied at $x = \pm 50$. Tests showed that this was far enough away from the minimum roll separation to represent $p = 0$ at $x = \pm\infty$. A flow chart of the calculation process is shown in figure 4.7. Similar calculation procedures were used to solve for both flooded and non-flooded cases.

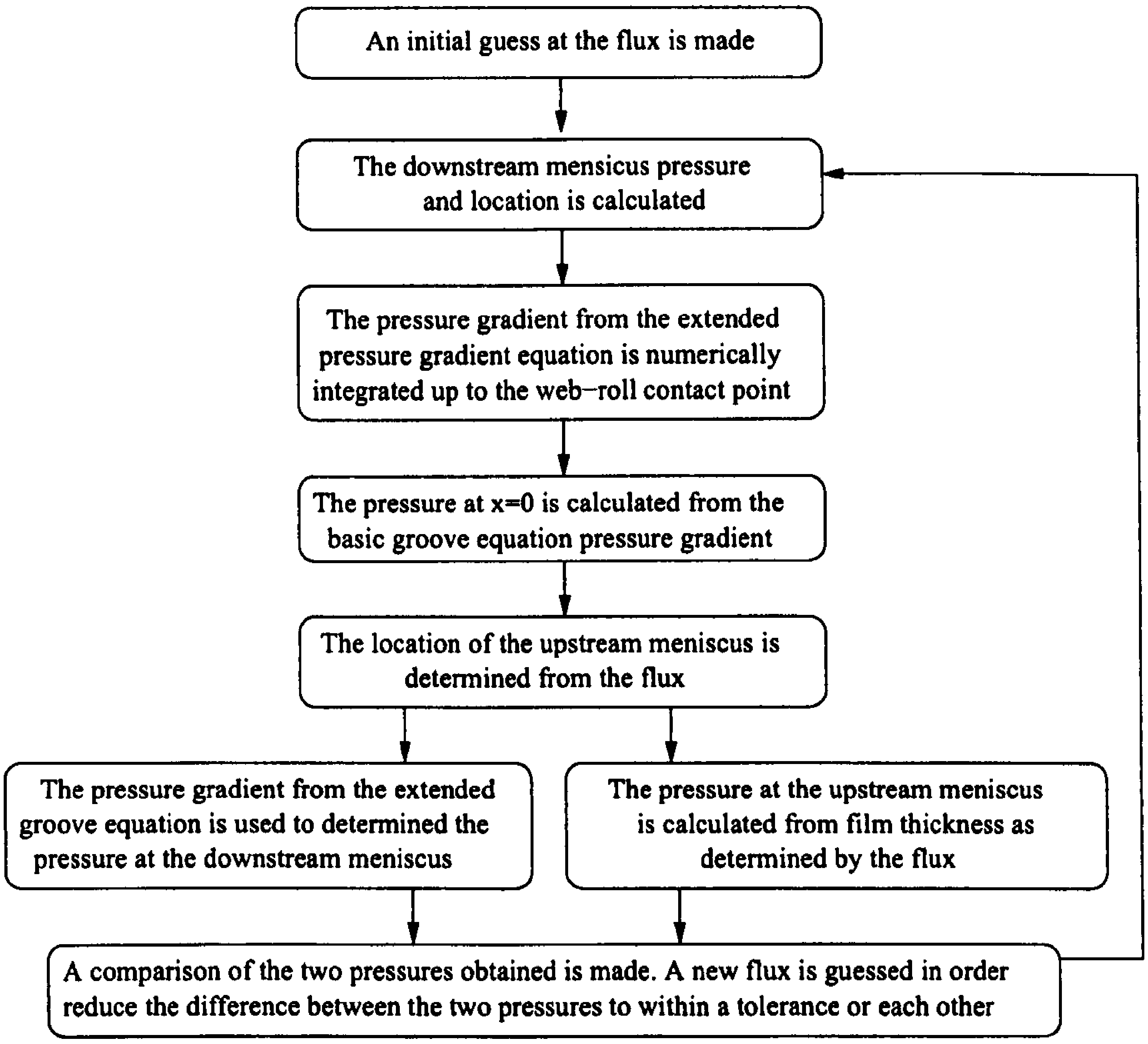

Figure 4.7: Calculation Procedure

4.7 Numercial Verification of the Flooded Case

One of the reasons for developing a flooded version of the analytical model was to allow comparison with a corresponding full finite element solution of the problem. The reason for undertaking the comparison was twofold:

- To compare the solution of Poisson's equation with that obtained from the solution of the incompressible Navier–Stokes equations for inertialess fluids (for inertialess flow the problem becomes one of Stokes flow). This would confirm the validity of the assumption that the flow is essentially one dimensional in the direction of web motion and that the complex x-momentum Navier–Stokes equation can be simplified to Poisson's equation.
- To extend the comparison to encompass fluids with inertia comparable to that present in the experimental work undertaken as well as in typical industrial processes. The aim being to confirm that inertial forces are not large enough to influence the fluid flow, for the Reynolds numbers typically encountered in the industrial scenario.

The complexity of developing a three dimensional computation fluid dynamics model of the multiphase problem was beyond the scope of the current research, so the flooded analytical model proved to be a valuable method of validating the reduction of the x-momentum Navier–Stokes equation to Poisson's equation.

In chapter 5 the pressure gradient-flux relationship based on Poisson's equation is obtained from a finite element solution of the equation, thereby allowing modelling of non-rectangular groove geometries. However as the computational time required to solve the problem increases rapidly with increasing web-to-roll gap, the coating model based on the finite element solution of Poisson's equation is not extended to the flooded coating case. In addition to the solution being of interest from a mathematical viewpoint the speed of solution of Poisson's equation (the solution of a single data point takes of the order of $1 \rightarrow 10$ seconds) makes parametric investigations into the effects of different speed ratios, groove aspect ratios and capillary numbers a lot faster than the finite element based solution.

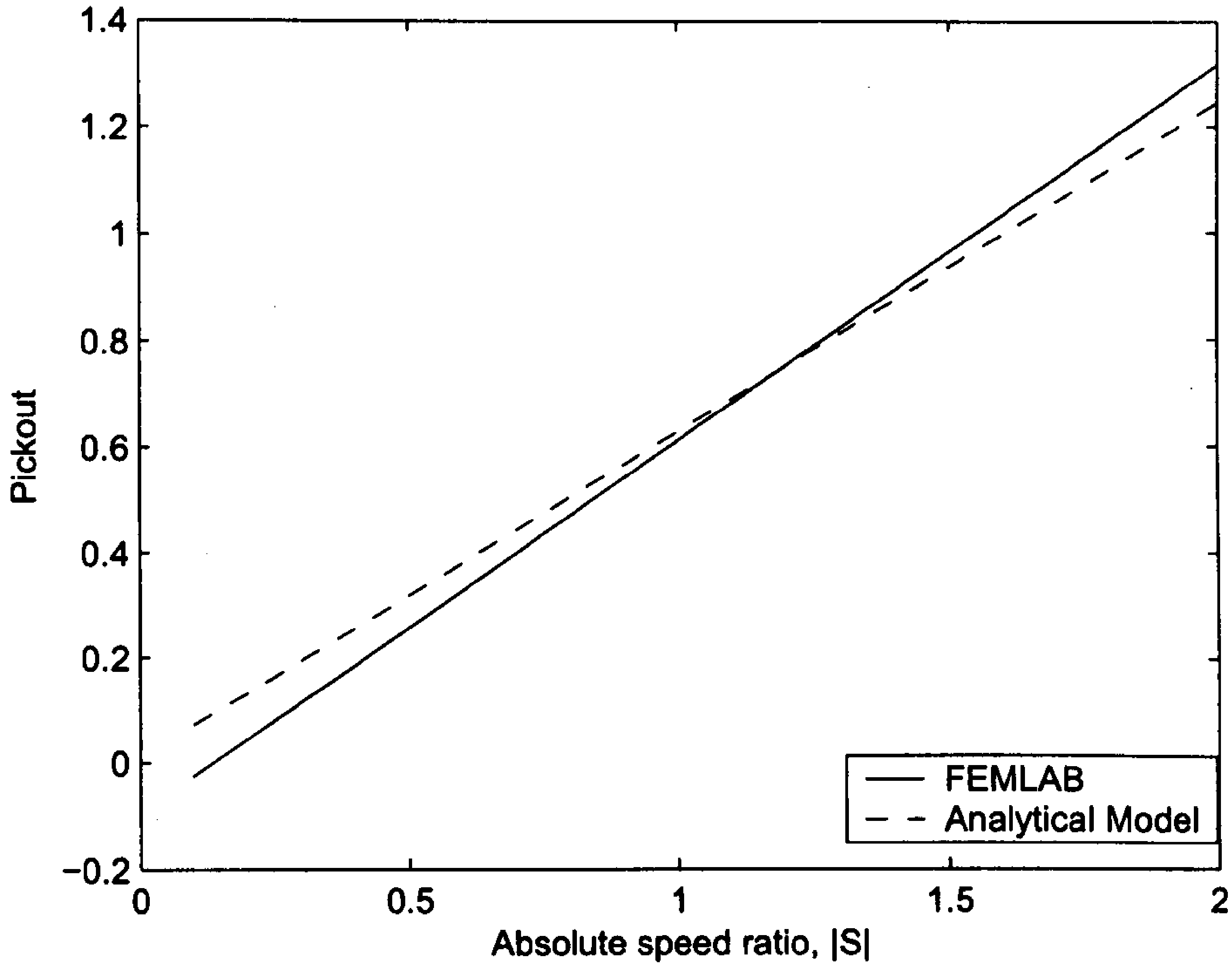

Figure 4.8: Analytical and FEM comparisons of pickout for a fully submerged roll, $r = 1$, $r_{\text{roll}} = 100$, $\beta = 0°$. The FEM results for $Re = 0, 1, 10, 100, 1000, 10000$ all lie on the same curve.

The full solution of the flooded coating problem was undertaken using femlab (now Comsol Multiphysics[2]), a powerful and relatively new commercial finite element program capable of solving a wide range of differential equations, including user defined equations and multi-physics problems, such as electro-statically driven fluid flows, deformable electrically heated beams and reacting flows. Femlab is closely integrated with matlab and allows data to be exported to the matlab environment for analysis using femlab commands, as well as allowing problems to be programmed within the matlab environment using matlab "*.m*" files.

A range of Reynolds numbers was examined in the finite element simulation and as can be seen from figure 4.8 there do not appear to be any inertial effects on pickout; as Reynolds number increases the finite element pickout curves are seen to lie on top of each other.

The pickout comparison clearly shows that as the Reynolds number increases, the pickout does not vary. This lends confidence to the use of the two dimensional Poisson's equation to describe

---

[2] Comsol Inc. 1 New England Executive Park, Suite 350, Burlington, MA 01803.

the fluid flow within the coating bead. The comparison does show some difference between the two sets of data; the probable reason for this small disagreement is the assumption that the flow above the roll lands can be described by Couette-Poiseuille flow rather than the full solution of Poisson's equation which takes into account the viscous forces in the y-direction. Generally the agreement is good with the worst agreement at low and high speed ratios, outside the typical operating conditions of the tri-helical gravure roll coating process. It should be noted that at high speed ratios the pickout is greater than unity, although this is not possible in the non-flooded case it occurs for the flooded case when fluid is drawn from the upstream location by the web and the net flow though the nip is from the upstream to dosntream side of roll-to-web contact.

Chapter 5

Finite Element Model of Zero Groove Angle Coating Process

5.1 Introduction

In Chapter 4 an analytical model was derived and then solved for the idealised case of tri-helical gravure roll coating with rectangular grooves at zero angle of pitch. Here a corresponding numerical formulation for such problems is presented which enables both verification of the assumptions underpinning the analytical model and a number of important and practical extensions to be made. The latter include:

- The consideration of groove shapes more typical of those found in industry - for example ones with triangular cross-section.
- The effect of non-Newtonian fluid behaviour, in which case the general two dimensional equation describing the steady-state motion of a shear dependent (Generalised Newtonian) fluid, in the absence of body forces, is given by:

$$\frac{\partial P}{\partial X} = \frac{\partial \tau_{XY}}{\partial Y} + \frac{\partial \tau_{XZ}}{\partial Z}. \tag{5.1}$$

where τ is the shear stress, such that:

$$\tau_{ij} = \eta \frac{\partial U_i}{\partial x_j}, \tag{5.2}$$

and η is the local viscosity which can itself be a function of shear rate.

Various numerical methods exist for the purpose of discretising one or more non-linear partial differential equations typical of those which govern the motion of fluids and the deformation of solids. These include the finite volume [132], finite difference [133], finite element [134], spectral element [135] and spectral methods [136]. Of the five the FEM has emerged as the most popular for solving coating flow problems. The reasons for this are that it offers a high degree of flexibility in terms of: (i) solving for flows in irregular shaped domains, such as the groove geometries considered here; (ii) handling free surfaces and their associated boundary conditions [137].

5.1.1 Finite Element Method

The name 'finite element' derives from dividing the solution domain of interest into a series of contiguous regions (elements) over which the dependent variables to be solved for, such as velocity, pressure, etc., are approximated by interpolating functions - typically polynomials expressed in terms of the elements nodal values. The finite element formulation adopted to solve equation (5.1) employs the weighted residuals method which is a very convenient means of deriving finite element equations for both linear and non-linear boundary value problems. The behaviour of the dependent variables over an element satisfy only approximately the solution there.

Accordingly, when the variables in a governing partial differential equation are replaced by their corresponding interpolation function and the results weighted and integrated over an element a residual is formed which when minimised, that is set to zero, yields a set of element equations which when solved over the entire domain lead to the required global solution.

The above process is illustrated by considering the following one-dimensional differential equation for the dependent variable ϕ:

$$L(\phi) - f(x) = 0, \tag{5.3}$$

where L is the differential operator and $f(x)$ is the known function of the independent variable, x. The exact solution ϕ is approximated as $\overline{\phi}$:

$$\phi \approx \overline{\phi} = \sum_{i=1}^{m} N_i C_i, \tag{5.4}$$

where the N_is are the approximating interpolating functions and the C_is are the unknowns at each node. Substitution of equation (5.4) into equation (5.3) leads to:

$$L(\overline{\phi}) - f(x) = R, \tag{5.5}$$

where R is the associated residual which is required to be minimised by determining the unknown C_is for which the residual over the entire domain is small - ideally zero. The method of weighted residuals, of which there are a number of variants - collocation, least squares, Galerkin [138], accomplish this by weighting the error and specifying that it vanishes over an element and hence over the entire domain.

Taking W_i as the weighing function and specifying that the residual vanishes when averaged over the element (Ω) gives:

$$\int_{\Omega} \left(L(\overline{\phi}) - f(x)\right) W_i d\Omega = 0, \quad i = 1, 2, 3, \ldots, r, \tag{5.6}$$

where r is the number of nodes in the element.

The choice of W_i clearly affects the error distribution and therefore the FEM solution. The Galerkin method [138], used here, sets the weighting functions to be the same as the interpolation functions used to approximate the dependent variables over an element. Accordingly, equation (5.6) becomes:

$$\int_{\Omega} \left(L(\overline{\phi}) - f(x)\right) N_i d\Omega = 0, \quad i = 1, 2, 3, \ldots, r, \tag{5.7}$$

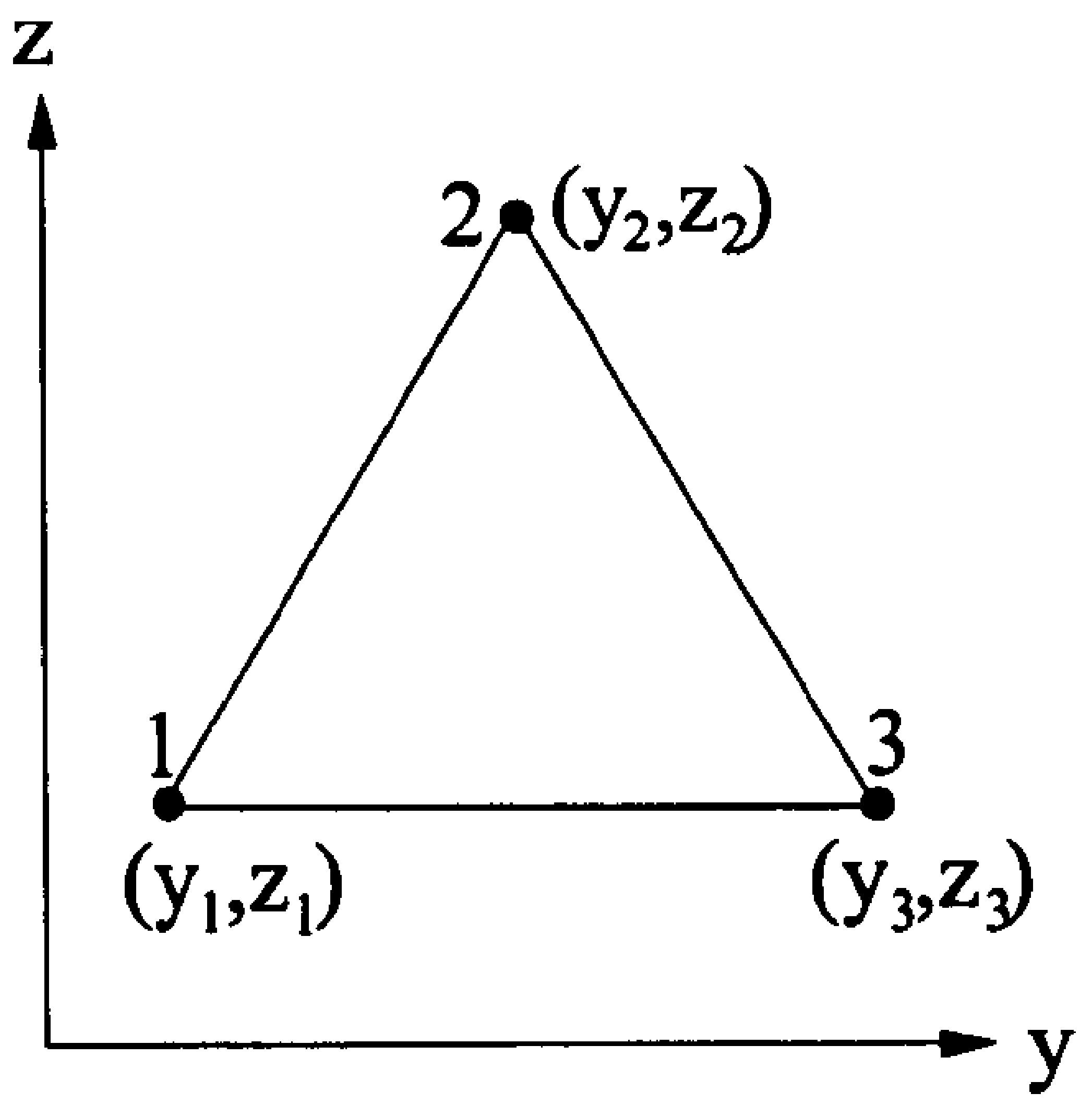

Figure 5.1: Node Generation

which when arranged into known and unknown components can be written:

$$\int_\Omega L\left(\overline{\phi}\right) N_i d\Omega = \int_\Omega f\left(x\right) N_i d\Omega, \quad i = 1, 2, 3, \ldots, r. \tag{5.8}$$

This process results in a set of i equations for each element. These elemental equations are each assembled to form a global solution matrix which is singular until the boundary conditions are entered enabling a unique solution for the problem of interest to be found.

5.1.2 Interpolation Functions

The choice of interpolation function will depend on the element type - in the case of the two-dimensional problems considered here they might be triangular or quadrilateral, or a combination of the two - which will dictate the number of nodes employed. The greater the number of nodes in an element the higher the order of the resulting interpolation function. The obvious choice is to use interpolating functions whose order is the same as that of the highest derivative a dependent variable is subjected to. From equations (5.1) and (5.2) this would suggest the need for quadratic interpolation functions in velocity, since $\frac{\partial p}{\partial x}$ is constant. However, as we shall see later, integration by parts can be used to avoid second derivatives and linear interpolation can be used for velocity.

Simple linear, three noded, triangular elements are employed - see figure 5.1 - such that the unknown dimensionless velocity, u, expressed in terms of (y, z) co-ordinates (see Chapter 4 for non-dimensional scalings) over an element is:

$$u^e = a_0 + a_1 y + a_2 z. \tag{5.9}$$

The unknowns a_0, a_1 and a_2 can be solved for at each node which when substituted into equation (5.9) gives:

$$u^e = N_1 u_1 + N_2 u_2 + N_3 u_3, \tag{5.10}$$

where u_1, u_2 and u_3 are the velocities at nodes 1, 2 and 3 respectively and the corresponding interpolation functions N_1, N_2 and N_3 are given by:

$$N_1 = \frac{1}{2\triangle}\left[(y_2 z_3 - y_3 z_2) + (z_2 - z_3)\, y + (y_3 - y_2)\, z\right], \tag{5.11}$$

$$N_2 = \frac{1}{2\triangle}\left[(y_3 z_1 - y_1 z_3) + (z_3 - z_1)\, y + (y_1 - y_3)\, z\right], \tag{5.12}$$

$$N_3 = \frac{1}{2\triangle}\left[(y_1 z_2 - y_2 z_1) + (z_1 - z_2)\, y + (y_2 - y_1)\, z\right], \tag{5.13}$$

(5.14)

and where,

$$2\triangle = \begin{vmatrix} 1 & y_1 & z_1 \\ 1 & y_2 & z_2 \\ 1 & y_3 & z_3 \end{vmatrix} \quad \text{(twice the element area.)} \tag{5.15}$$

5.2 Boundary Conditions

Two types of boundary conditions were used to solve for the flow along a groove (see figure 5.2). Both Dirichlet and Neumann boundary conditions are present and correspond to the specification of (a) an explicit value (see equation (5.16)), (b) the normal derivative (see equation (5.17)), respectively. The advantage of using symmetric boundary conditions is that only half the groove needs to be considered, reducing the computational time required to obtain a solution.

$$u = u_B \quad \text{Dirichlet} \tag{5.16}$$

$$n \cdot \nabla u = g \quad \text{Neumann} \tag{5.17}$$

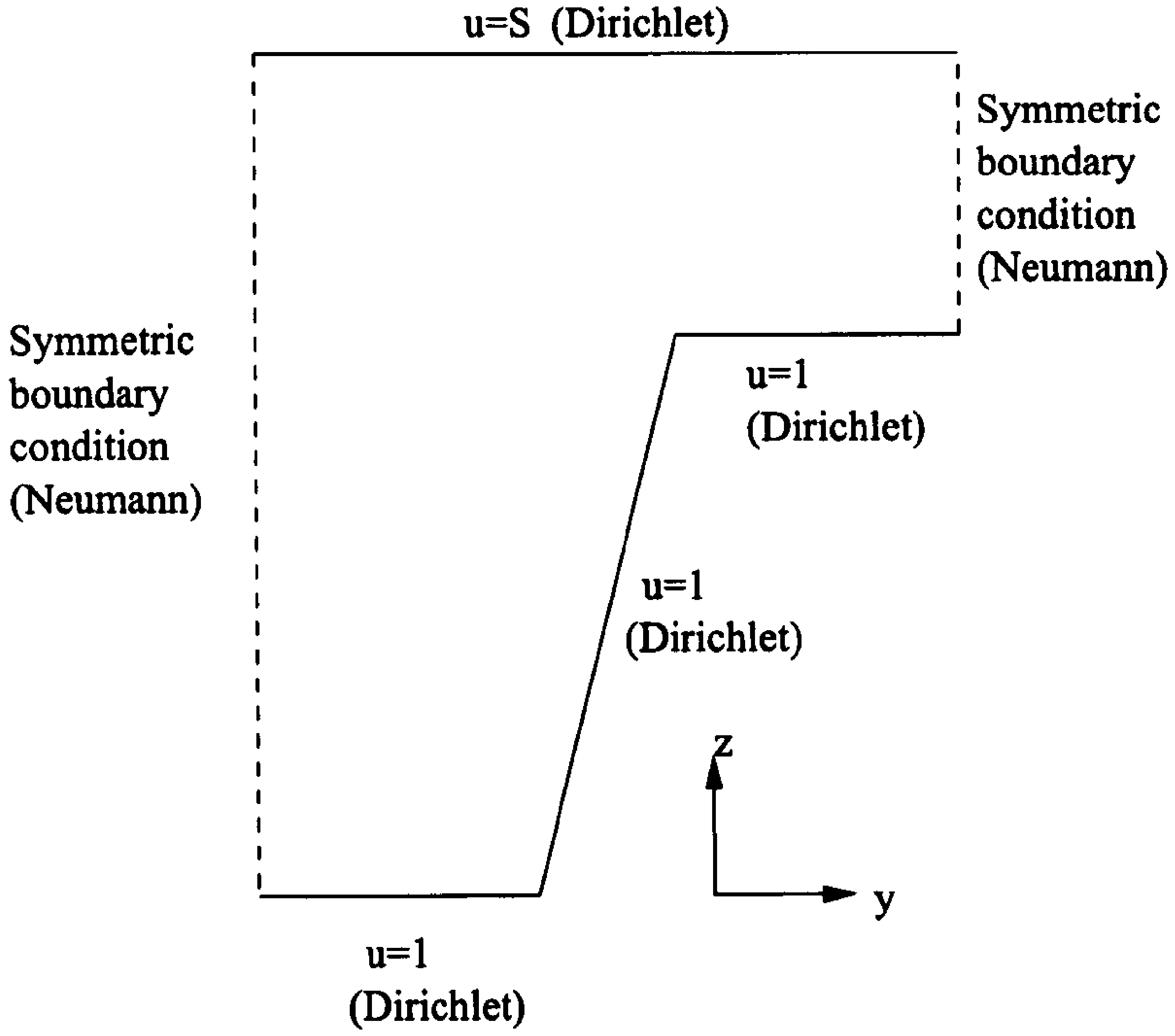

Figure 5.2: Solution domain for groove flow showing symmetry and boundary conditions.

5.3 Mesh Generation

Meshing the problem was undertaken by dividing the solution domain into triangular elements with the nodes evenly spaced across the groove. In order to accommodate varying geometries and grid refinement the number of nodes across the top of the groove was specified and the number of nodes across the other dimensions (groove depth and land-web distance) apportioned accordingly.

Figure 5.3 shows a typical node distribution for a quadrilateral groove. As the width of the groove changes (moving downwards), the number of nodes across it remains the same, whilst the node spacing in the y-direction changes (note the cross section is taken in the $y-z$ plane). This meshing strategy, whilst simple, does have a number of advantages:

1. Since the nodes are all aligned in the y direction the integration of the forcing functions (see later) is simpler than would be the case for less regular alignment.

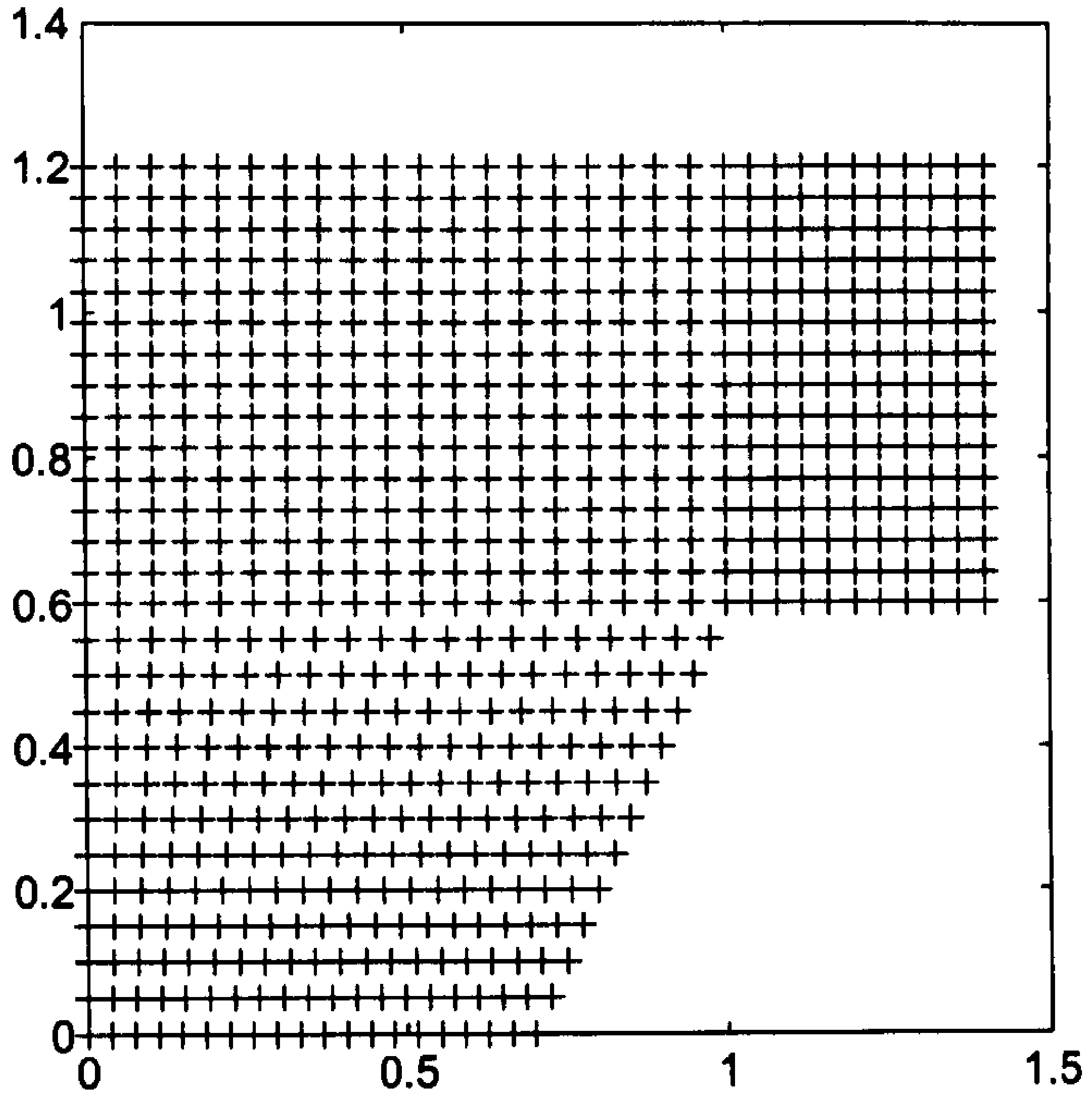

Figure 5.3: Node Generation

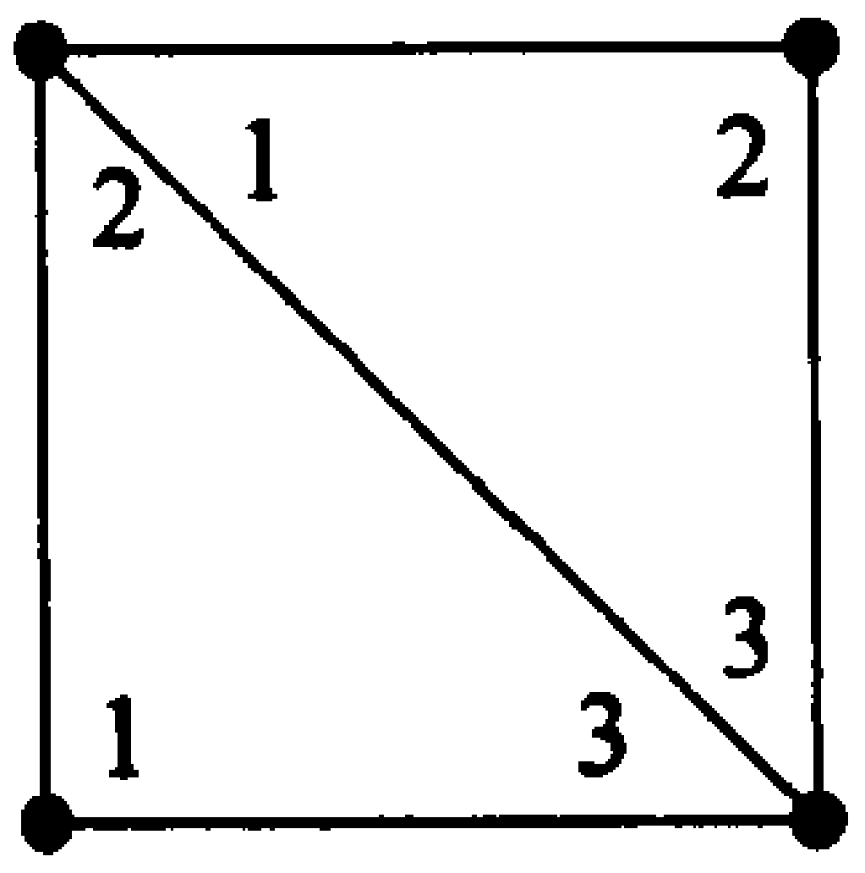

Figure 5.4: Element Numbering

2. Calculation of the Jacobian was not necessary; the solution could be based on the actual mesh rather than a transformed one.

Nodes were numbered locally as shown in figure 5.4, while globally the numbering of the nodes was arranged with node 1 at the bottom left hand corner and increasing as shown in figure 5.5. The numbering scheme gave an algebraic relationship between the node row and column, and by careful indexing of the problem the node location and index were algebraically linked.

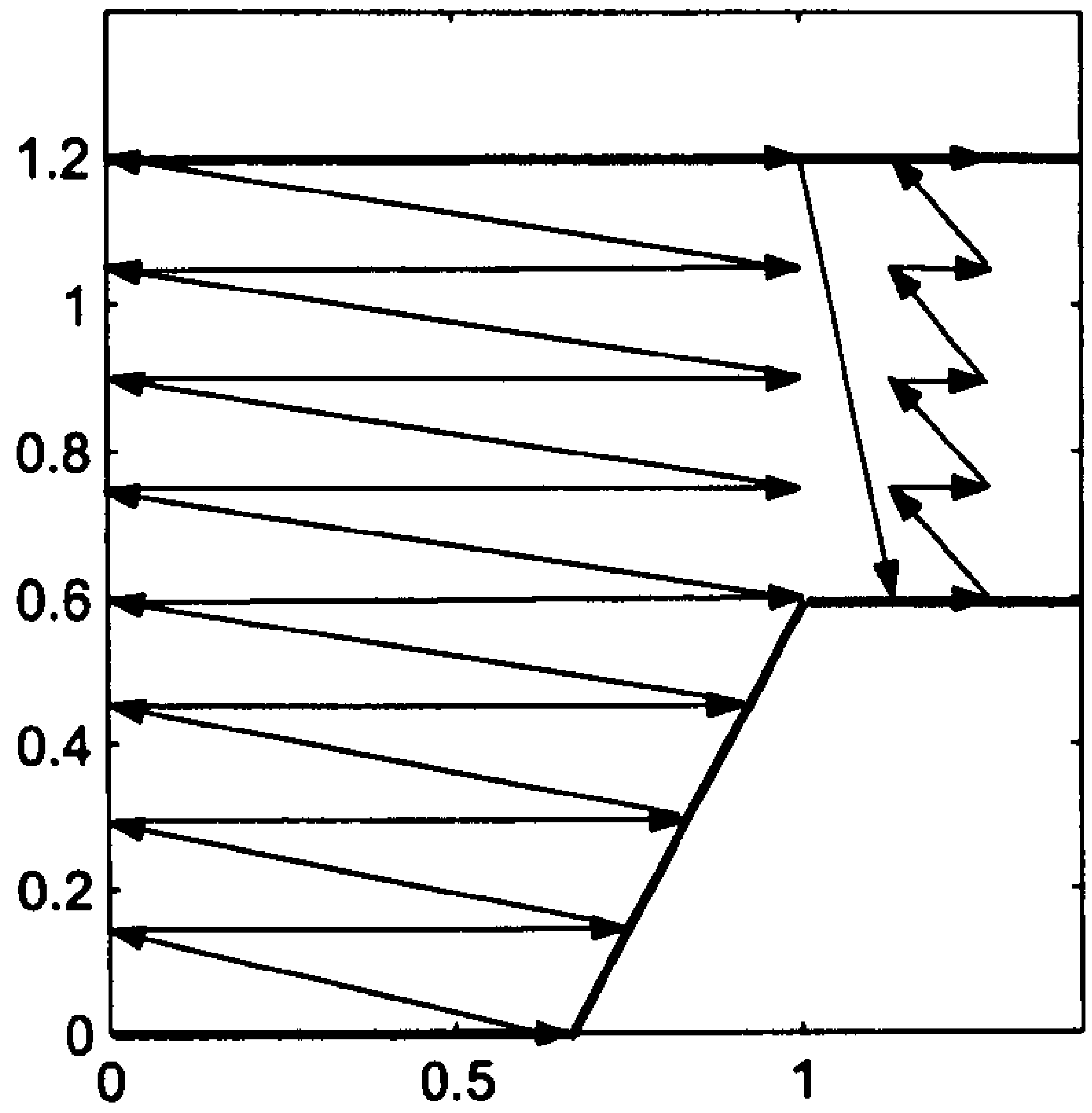

Figure 5.5: Pattern of global numbering of nodes within the groove.

5.4 Finite Element Formulation of Poisson's Equation (Newtonian Case)

By formulating Poisson's equation (equation (4.11)) using the Bubnov-Galerkin finite element method the stiffness matrix and forcing function is obtained:

$$\mathbf{K}^{(\mathbf{e})}u^{(e)} = \mathbf{F}^{(\mathbf{e})}, \tag{5.18}$$

where $\mathbf{K}^{(\mathbf{e})}$ is the element stiffness matrix, $u^{(e)}$ is the matrix of unknown velocity variables at each node and $\mathbf{F}^{(\mathbf{e})}$ is the element forcing function. The element stiffness matrix is obtained thus:

$$\mathbf{K} = \iint_e N_i \left[\frac{\partial^2 N_j}{\partial y^2} + \frac{\partial^2 N_j}{\partial z^2} \right] dydz. \tag{5.19}$$

Since linear interpolation functions are being employed integration by parts is used to rewrite equation (5.19) as:

$$\mathbf{K}^{(\mathbf{e})} = \iint_e \left[\frac{\partial N_i}{\partial y}\frac{\partial N_j}{\partial y} + \frac{\partial N_i}{\partial z}\frac{\partial N_i}{\partial z} \right] dydz. \tag{5.20}$$

The forcing function is obtained from the left hand side of equation (4.11), as this is the known part of the equation, based on the pressure gradient across the entire domain:

$$\mathbf{F} = \int_e \frac{dp}{dx} N_i dydz. \tag{5.21}$$

The element matrix is then entered into the global matrix spanning the entire domain.

The boundary conditions are then implemented. The symmetric boundary conditions (Neumann) do not require any rearrangement of the global stiffness matrix or forcing function. The Dirichlet boundary conditions were applied by multiplying the stiffness matrix by the vector of known velocities and adding this vector to the forcing functions (unknown velocities are set to zero). The rows and columns of the forcing function corresponding to the known velocities are then removed from the stiffness matrix, forcing function and velocity vector. This results in the global stiffness matrix and velocity vector only being used to solve for the unknown velocities, and with the known velocity components contributing to the forcing function terms. The stiffness matrix is then inverted and multiplied by the forcing function matrix, giving:

$$u = \mathbf{K}^{-1}\mathbf{F}. \tag{5.22}$$

The results are then combined with the velocity boundary conditions to produce a global matrix containing the domain velocities.

The flux was calculated by numerically integrating the velocity over the element area, which for a linear element is the same as multiplying the average velocity within an element by the element area. The FEM was implemented in Matlab[1], in which functions can be written that utilise powerful array and matrix handling capabilities. This simplified the process of implementing the model when compared to creating ones own program in a lower level language such as C++. The ease which Matlab handles matrices makes the process simpler and reduces the volume of code required for simple housekeeping tasks [139].

---

[1] Published by Mathworks, Natick, Massachusettes, USA.

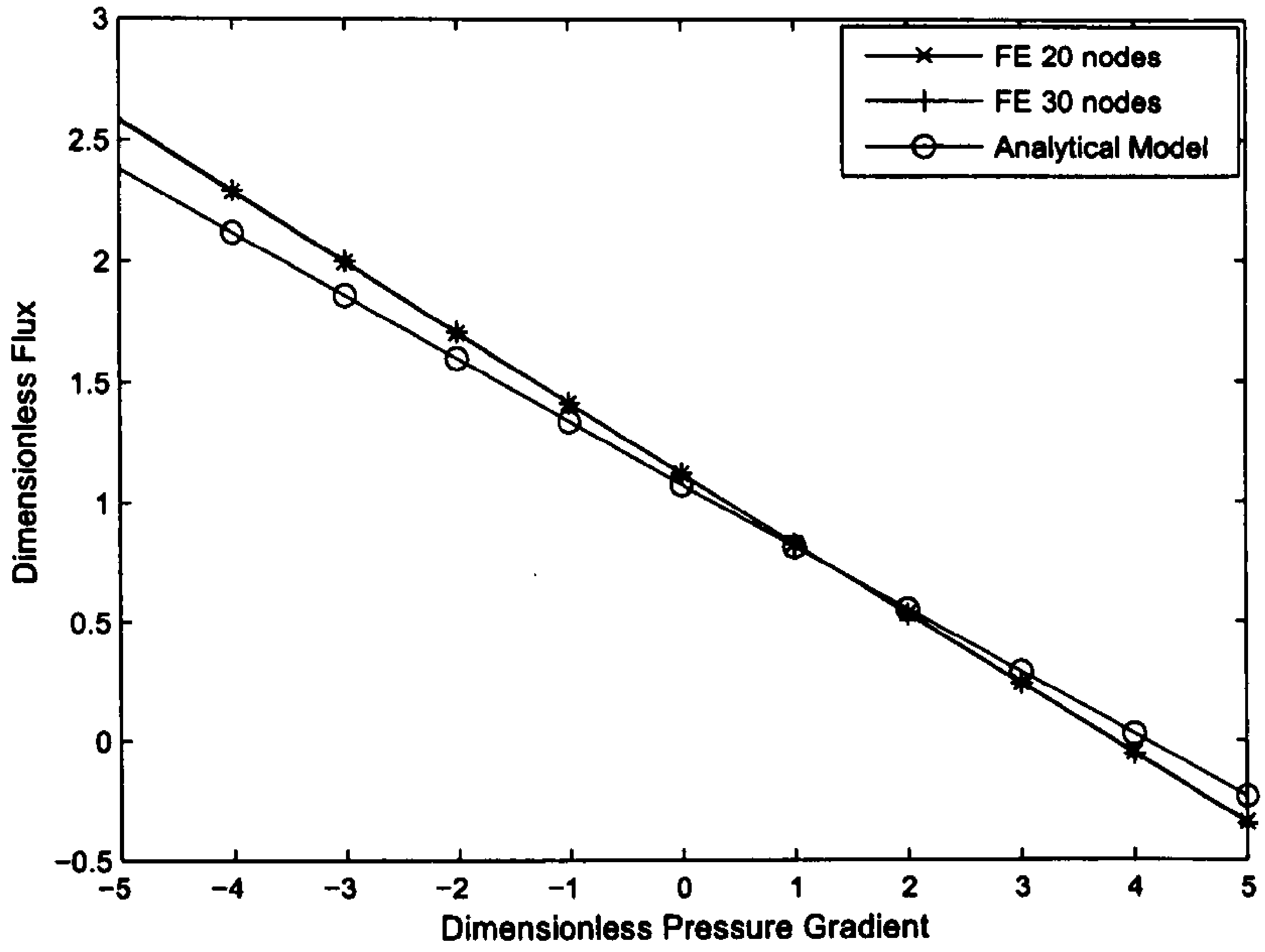

Figure 5.6: Flux in a single rectangular groove and corresponding web-to-land gap as a function of pressure gradient: $S = 1, r = 1, d = 1$ and $l = 1$.

5.5 Comparison of FE and Analytical Solutions

Comparison is made between analytical and FEM solutions for flow along a single cross sectional groove geometry. In particular this allows the assumption made in chapter 4, that above the lands the velocity profile is close to that of one dimensional Poiseuille-Couette flow, to be tested. Grid independence was confirmed by running the FEM code with both 20 and 30 nodes across the groove width. Figures 5.6, 5.7 and 5.8 show that the overall agreement between the solutions is good, with the best agreement occurring for slightly positive pressure gradients - at this point the net effect of the viscous terms in the y (along the surface) direction is zero.

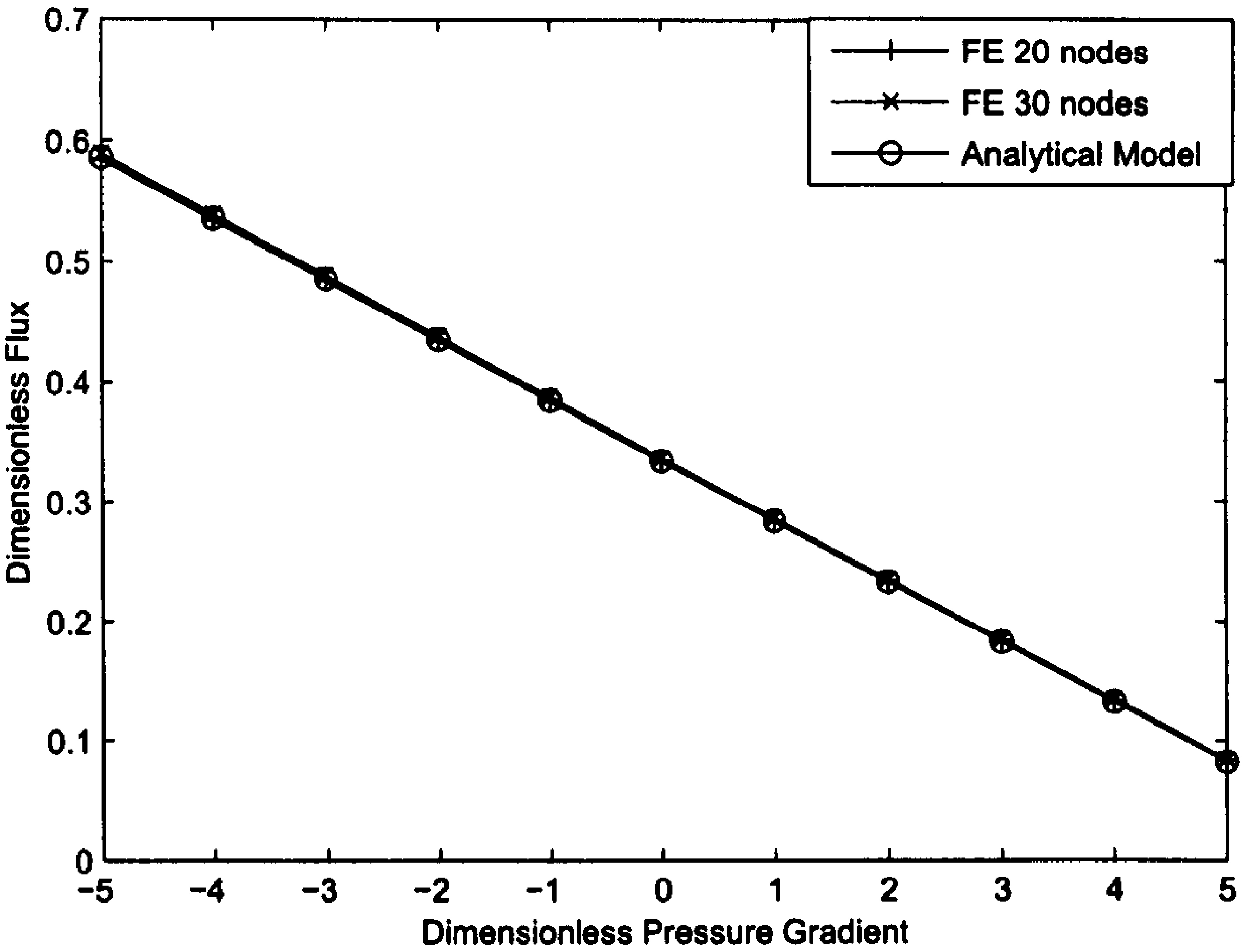

Figure 5.7: Flux in a single rectangular groove and corresponding web-to-land gap as a function of pressure gradient: $S = 1$, $r = 1$, $d = 0.2$ and $l = 0.5$.

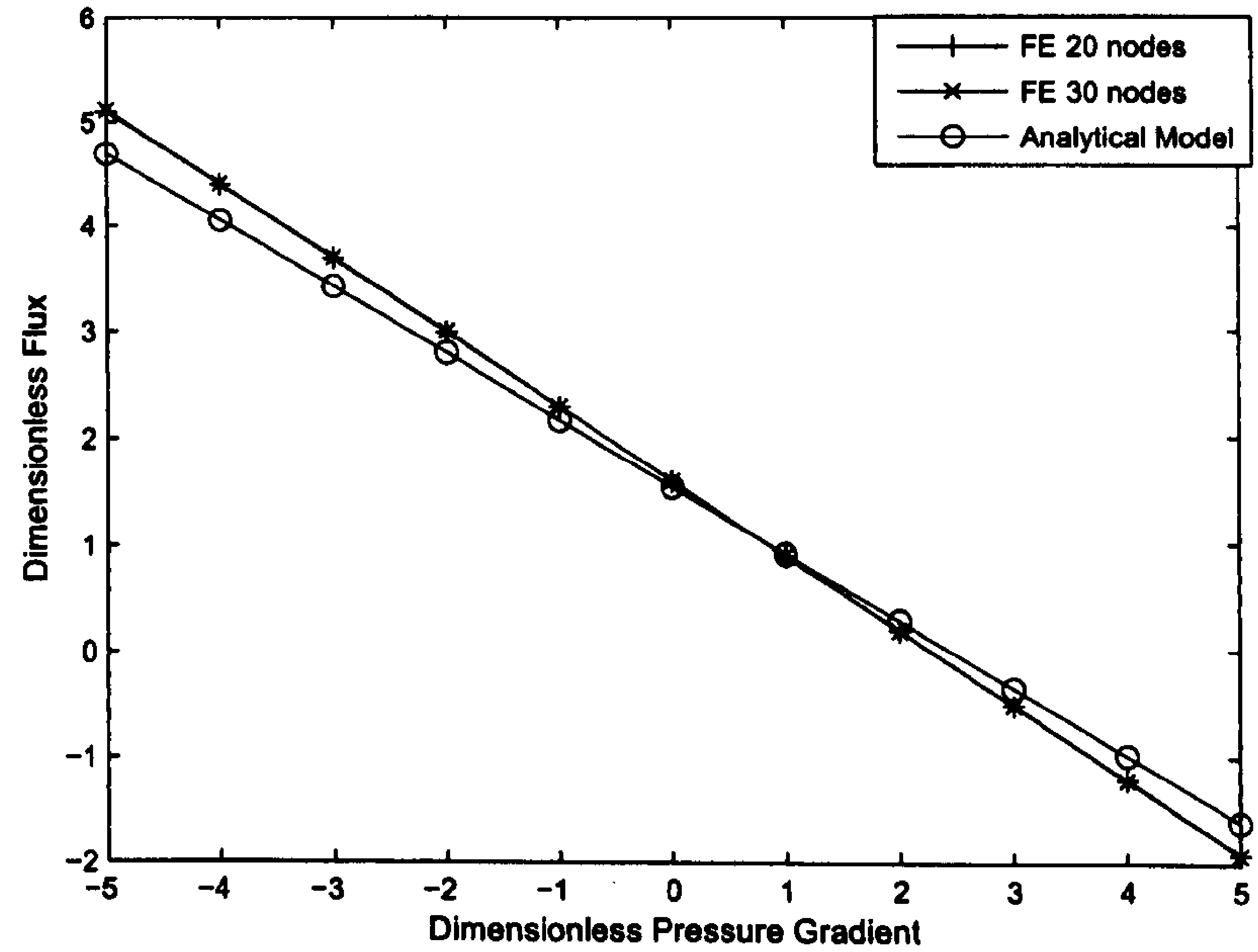

Figure 5.8: Flux in a single rectangular groove and corresponding web-to-land gap as a function of pressure gradient: $S = 1$, $r = 0.5$, $d = 0.1.5$ and $l = 1$.

5.6 Finite Element Formulation for Power Law Fluids

5.6.1 Introduction

We now remove the constraint that the fluid in the process is Newtonian. From equations (5.1) and (5.2) the momentum equation for flow along an infinitely long domain becomes:

$$\frac{\partial}{\partial Y}\left[\eta\frac{\partial U}{\partial Y}\right]+\frac{\partial}{\partial Z}\left[\eta\frac{\partial U}{\partial Z}\right]-\frac{\partial P}{\partial X}=0 \qquad (5.23)$$

A range of models exist to describe the local viscosity, perhaps the most common one being the power law model [83]. This is considered to capture reasonably well the viscosity at high shear rates for polymer solutions [8] under conditions of unidirectional flow, and describes the local fluid viscosity as a function of the shear rate:

$$\eta=\lambda\left[\left(\frac{\partial U}{\partial Y}\right)^2+\left(\frac{\partial U}{\partial Z}\right)^2\right]^{\frac{n-1}{2}} \qquad (5.24)$$

where λ is the consistency factor and n is the power law index. The reader is referred to the previous studies that have been undertaken where the FEM has been applied to solve equation (5.23) in tandem with the power law model [140, 141, 142, 143].

Finite Element Formulation

As in the previous section, for the case of Newtonian fluids, only linear triangular elements, as shown in figure 5.1, are required, and hence the same linear interpolation functions apply. Equation (5.23) is made dimensionless using the following scalings:

$$y,z=\frac{Y,Z}{A} \quad u=\frac{U}{U_{\text{roll}}} \quad \text{and} \quad p=\frac{PA^n}{\lambda U_{\text{roll}}^n}, \qquad (5.25)$$

giving:

$$\int\!\!\int_{\Omega} N_i \left[\frac{\partial}{\partial y} \left(\left[\left(\frac{\partial N_j}{\partial y} \right)^2 + \left(\frac{\partial N_j}{\partial z} \right)^2 \right]^{\frac{n-1}{2}} \frac{\partial N_j}{\partial y} \right) + \frac{\partial}{\partial z} \left(\left[\left(\frac{\partial N_j}{\partial y} \right)^2 + \left(\frac{\partial N_j}{\partial z} \right)^2 \right]^{\frac{n-1}{2}} \frac{\partial N_j}{\partial z} \right) \right] \partial\Omega - \int\!\!\int_{\Omega} N_j \frac{\partial p}{\partial x} \partial\Omega = 0 \qquad (5.26)$$

Integrating equation (5.26) by parts and applying Green's theorem leads to the following expression for each element:

$$\int\!\!\int_{\Omega} \left(\frac{\partial N_i}{\partial y} \frac{\partial N_j}{\partial y} + \frac{\partial N_i}{\partial z} \frac{\partial N_j}{\partial z} \right) \left[\left(\frac{\partial N_j}{\partial y} \right)^2 + \left(\frac{\partial N_j}{\partial z} \right)^2 \right]^{\frac{n-1}{2}} \partial\Omega = \int\!\!\int_{\Omega} N_j \frac{\partial p}{\partial x} \partial\Omega \qquad (5.27)$$

5.7 Implementation of FEM for grooves of non-rectangular cross section

As with the analytical solution of the tri-helical coating process, the flux - pressure gradient relationship forms the basis of the predictive approach. Whilst the pressure gradient cannot be obtained directly from the flux, there is a linear relationship between the flux and pressure gradient for Newtonian fluids. This can clearly be seen from figures 5.6, 5.7 and 5.8 and is supported by the analytical solution of Poisson's equation for rectangular grooves given by equation (4.44). However, for shear thinning fluids the relationship between pressure gradient and flux is no longer linear.

5.7.1 Non-rectangular groove meniscus model

A means of describing the locations and pressure discontinuities across the upstream and downstream menisci was required in order to close the problem. The two dimensional downstream meniscus model remains unchanged from that derived in section 4.4.1 where the grooves entering

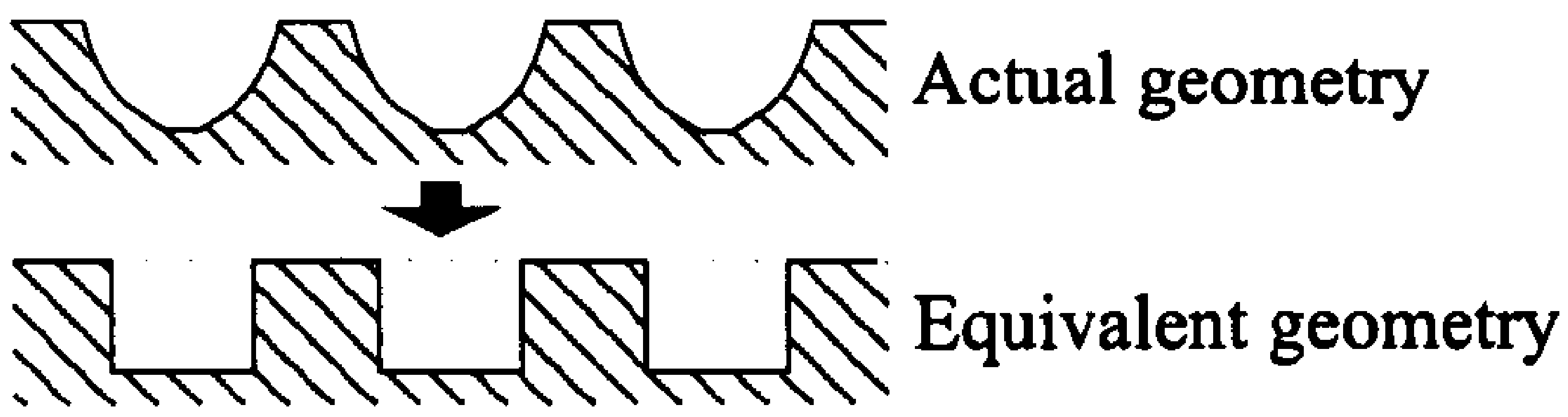

Figure 5.9: Simplified upstream meniscus geometry

the bead are full.

The complexity of the upstream meniscus makes the description of the meniscus location and pressure extremely complex and it is for this reason that a simplified groove geometry within which the meniscus lies was considered. The transformation from the generalised groove cross section to a representative rectangular one, as shown in figure 5.9, is based on the following rules:

- maximum groove depth (r) remains the same for the transformed groove;
- cross sectional area is maintained, resulting in groove cross section area $= ar$, where a is the width of the groove;
- groove line count is maintained, giving a line width $= l + a$.

From these three rules a representative rectangular groove geometry was constructed, with the groove width and land to groove ratio given by:

$$a = \frac{\text{groove area}}{r} \quad \text{and} \quad l = \text{line width} - \frac{\text{groove area}}{r}. \tag{5.28}$$

The pressure discontinuity across the upstream meniscus and its location were determined using the same model as that used for the rectangular groove geometry (section 4.4), the only difference being that the groove width is not necessarily equal to one as in the rectangular groove case due to the scalings involved. These minor changes in geometry definitions led to the following relations for the fluid film thicknesses:

$$h_1 = \frac{r+d}{c_\theta} \quad , \quad h_2 = \frac{a}{2c_{90}} \quad \text{and} \quad h_3 = \frac{d}{c_\theta}, \tag{5.29}$$

based on the dimensions given in figure 5.10 and where c_θ and c_{90} are the gap to film thickness

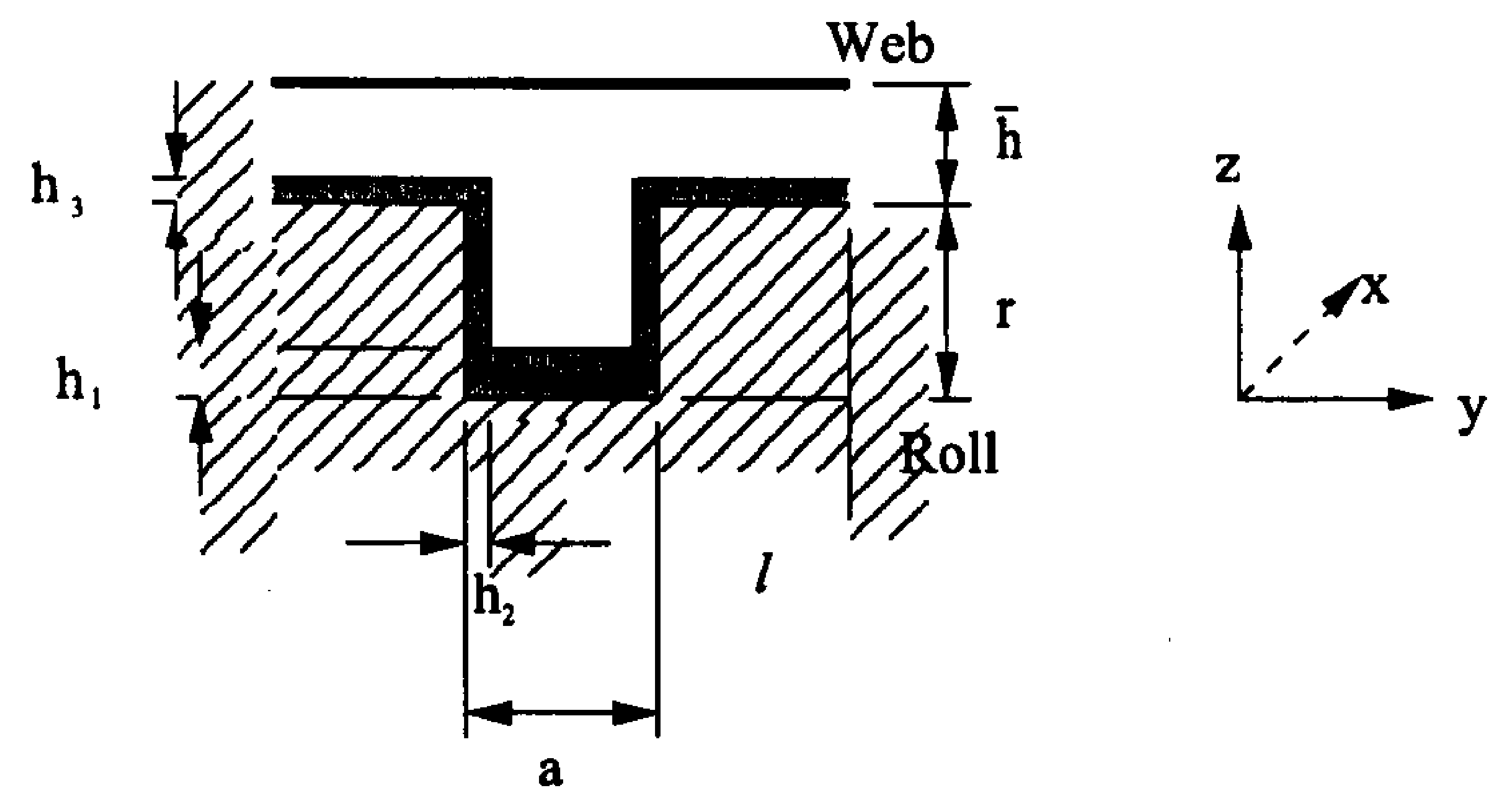

Figure 5.10: Simplified upstream meniscus geometry

ratios for contact angles of θ_D (the dynamic contact angle) and 90° respectively.

Newtonian Fluid Meniscus Models By making the same assumptions as those made for the rectangular groove geometry (i.e. neglecting the curved corners of the film) the flux remaining on the roll is given by equation (5.30):

$$q_{roll} = \frac{(2r + (2 + 2l)\, d)\, c_{90} + ar\,(c_\theta - 1)}{2c_{90}c_\theta}, \tag{5.30}$$

which was rearranged to give the gap between the roll surface and the point of separation, d:

$$d = \frac{(2\, q_{roll}c_\theta - 2\, r)\, c_{90} - ar\,(c_\theta - 1)}{2c_{90}\,(1 + l)}. \tag{5.31}$$

Equation (5.31) was used to determine the meniscus location by parabolic representation of the roll surface as described in section 4.4.4.

$$x = \beta r_{roll} + \sqrt{2\bar{h}r_{roll}}, \tag{5.32}$$

where β is the wrap angle. The pressure at the upstream meniscus is determined using the same equations as for the rectangular groove geometry:

$$p_{usm} = \frac{1}{Ca}\left(\kappa_y + \kappa_z\right), \tag{5.33}$$

where $\kappa_y$and κ_z are the meniscus curvatures perpendicular to one another. κ_y is based on the two different radii of curvature, that between the land and web and the other between the groove base and web. Correspondingly it includes an averaging of the pressure due to these radii as given by:

$$\kappa_y = \frac{a\kappa_{y1} + \kappa_{y2}}{a + l}. \tag{5.34}$$

κ_z is simply based on the width of the groove and when combined with equation (5.33) leads to an equation for the upstream meniscus pressure:

$$p_{usm} = \frac{1}{Ca}\left(\frac{a\kappa_{y1} + \kappa_{y2}}{a + l} + \kappa_z\right). \tag{5.35}$$

The dynamic contact angle was modelled using the empirical model of Jiang, Oh and Slattery [116] as detailed in section 4.4.3.

Power Law Fluid Meniscus Models Implementation of the non-Newtonian cavitation model derived in section 3.3 follows the same method as for Newtonian fluids using the Coyne & Elrod model, although here the dynamic contact angle was fixed at 90° since there was no reliable contact angle model for a power law fluid. As stated previously for the Newtonian case, the predicted film thicknesses were found to be insensitive to the contact angle model employed, strengthening the case for fixing the contact angle for the shear thinning model. A second difference was that the capillary number for each film thickness on the roll surface was different as the capillary number of the formed film was a function of film thickness. This led to the equation for the flux on the roll surface being described by:

$$q_{roll} = \frac{a\left(\left(d + r\right)c_2 + rc_1 - d - r\right)c_3 + 2d\left(lc_2 + a\right)c_1}{2c_1c_2c_3}, \tag{5.36}$$

which can be rearranged to give the web to roll gap (*d*):

$$d = -\frac{c_3\left(ar\left(c_2 + c_1 - 1\right) - 2q_{roll}c_1c_2\right)}{\left(c_3c_2 - c_3 + 2c_1\right)a + 2c_1lc_2}. \tag{5.37}$$

5.8 Use of Distributed Computing For Large Data Array Processing

The model described in this chapter was implemented in Matlab which solved typical problems in 5 minutes on a 1.8GHz desktop PC (for speed ratios of around $S = -1$) although lower speed ratios increased the computational time greatly due to the increased bead size and correspondingly larger computational domain for which the flow equation was solved.

The time required to solve large arrays of data points was reduced by implementing a distributed computing form of the Matlab code. Solving numerous data points simultaneously on different processors was achieved using MatlabMPI [144, 145], a set of Matlab script files that allow Matlab to be run in a parallel computing environment. The data was communicated between processors by means of a set of shared data files residing on disk, the communication between processors was therefore not very fast when compared to the more usual method of sharing data in memory. This meant that the parallel environment could only realistically be used for problems which could be divided into large computational chunks where communication speed is less important than the time spent in numerical processing and a small part of the overall solution time. As the solution for low speed ratio problems requires the longest computing time due to the larger fluid bead the array of problems was ordered with the low speed ratio data points being solved first. This made best use of the available processors since it ensured that jobs were scheduled efficiently, as illustrated in figure 5.11.

The benefits of careful job allocation is clear in that it reduces the overall computation time and minimises the time processors are idle. Calculations were undertaken on "Leeds Node One" of the White Rose Grid and ABAX. "Leeds Node One" is a computational resource comprising of 60 processors and makes up a computational grid with resources from the Universities of Leeds, Sheffield and York. ABAX is a Beowolf cluster comprised of 48 processors operated by the EFM research group at the University of Leeds. Up to 15 processors on the Leeds Node One White Rose Grid were used at a time to compute arrays of data points quickly, the setup of ABAX meant that up to 4 processors could be used.

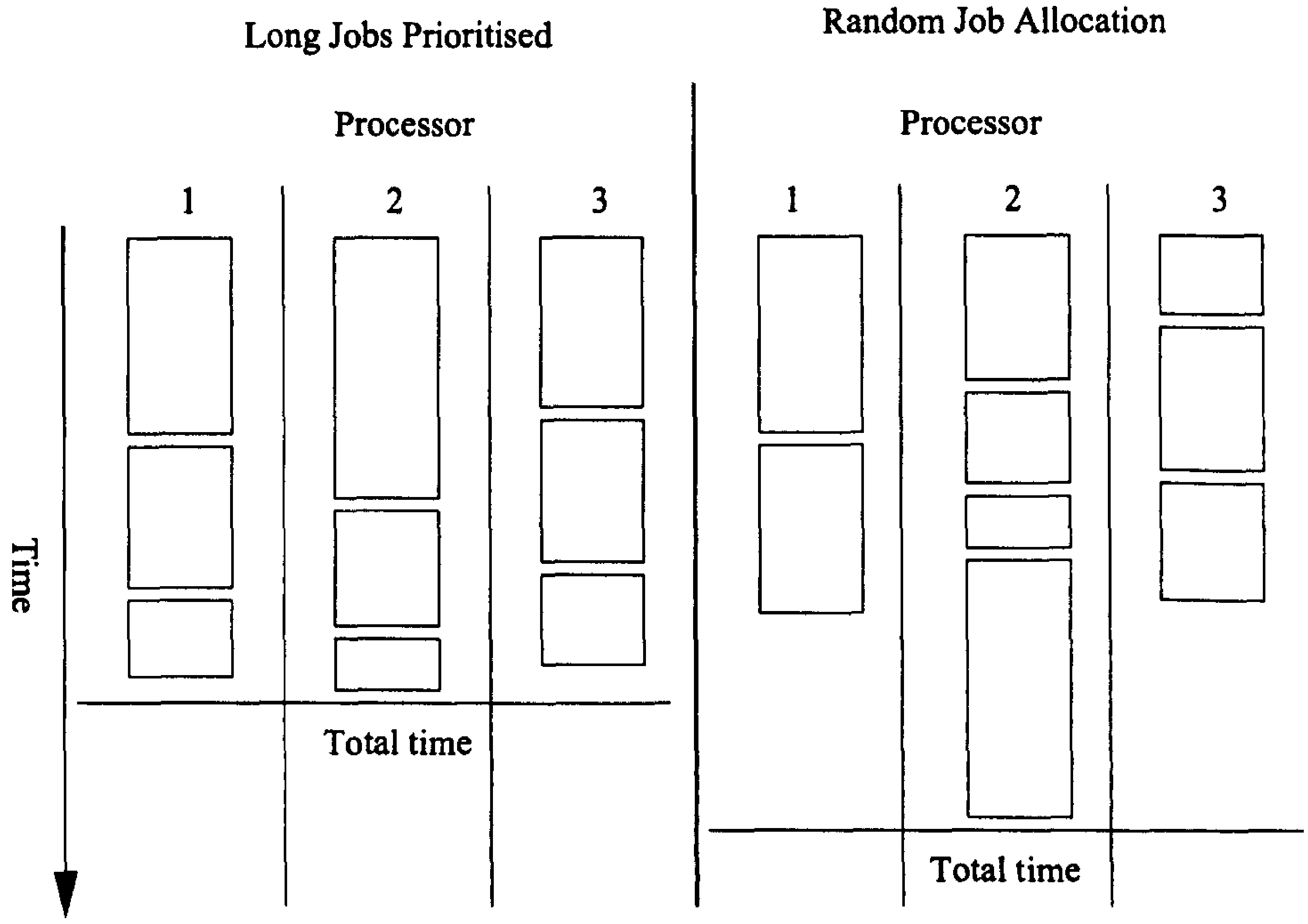

Figure 5.11: Benefits of job allocation based on processor time required

Chapter 6

Non-Zero Pitched Groove Model of Tri-Helical Gravure Roll Coating Process

6.1 Introduction

Any analysis of tri-helical gravure roll coating would not be complete without considering non-zero pitched grooves, since its industrial use typically involves rolls with grooves pitched between 30° and 60° to the roll axis. In formulating an approximate model it is worth reminding ourselves of the assumptions underpinning the zero pitched groove solutions determined previously, namely:

- that the flow is essentially unidirectional in the direction of the motion of the roll and the web.
- inertial forces are negligible within the coating bead due to the slowly varying geometry in the direction of the flow.

For non-zero pitched grooves the first assumption is clearly no longer valid. However, we can still assume inertia forces to be negligible but in this case on the basis that viscous forces dominate relative to inertial forces due to the close proximity of the web and roll resulting in high shear rates within the grooves.

The methodology used to solve the flow for pitched grooves is to resolve the flow into two directions - along and perpendicular to the groove. Unfortunately, since the shear rate is dependent on the flow both parallel and perpendicular to the groove it is not possible to further extend the analysis to encompass non-Newtonian flows. Nevertheless, important insight can be gained from the Newtonian case alone.

6.2 Elementary Resolution of Flow Directions

In the following section the method of resolving the flow in two directions perpendicular to one another is described. The resolved fluxes are then used to obtain the total flow and pressure gradient in the direction of web motion. A simple illustration is used to outline the method involved in resolving the flow. Consider the system shown in figure 6.1. The total flux passing across the dotted line is clearly Ua. The velocity U can be resolved into two components, $U\cos\Phi$ and $U\sin\Phi$ by rotating the geometry through an arbitrary angle Φ. Similarly resolving the length a gives the lengths, $a\cos\Phi$ and $a\sin\Phi$; the two velocity components pass across and the corresponding flux components $U\cos\Phi a\cos\Phi$ and $U\sin\Phi a\sin\Phi$ respectively. Adding these two fluxes clearly shows that the flux is independent of the angle the velocities are resolved through, namely:

$$\begin{aligned} Flux =& U\cos\Phi a\cos\Phi + U\sin\Phi a\sin\Phi, \\ =& Ua\cos^2\Phi + Ua\sin^2\Phi, \\ =& Ua. \end{aligned} \tag{6.1}$$

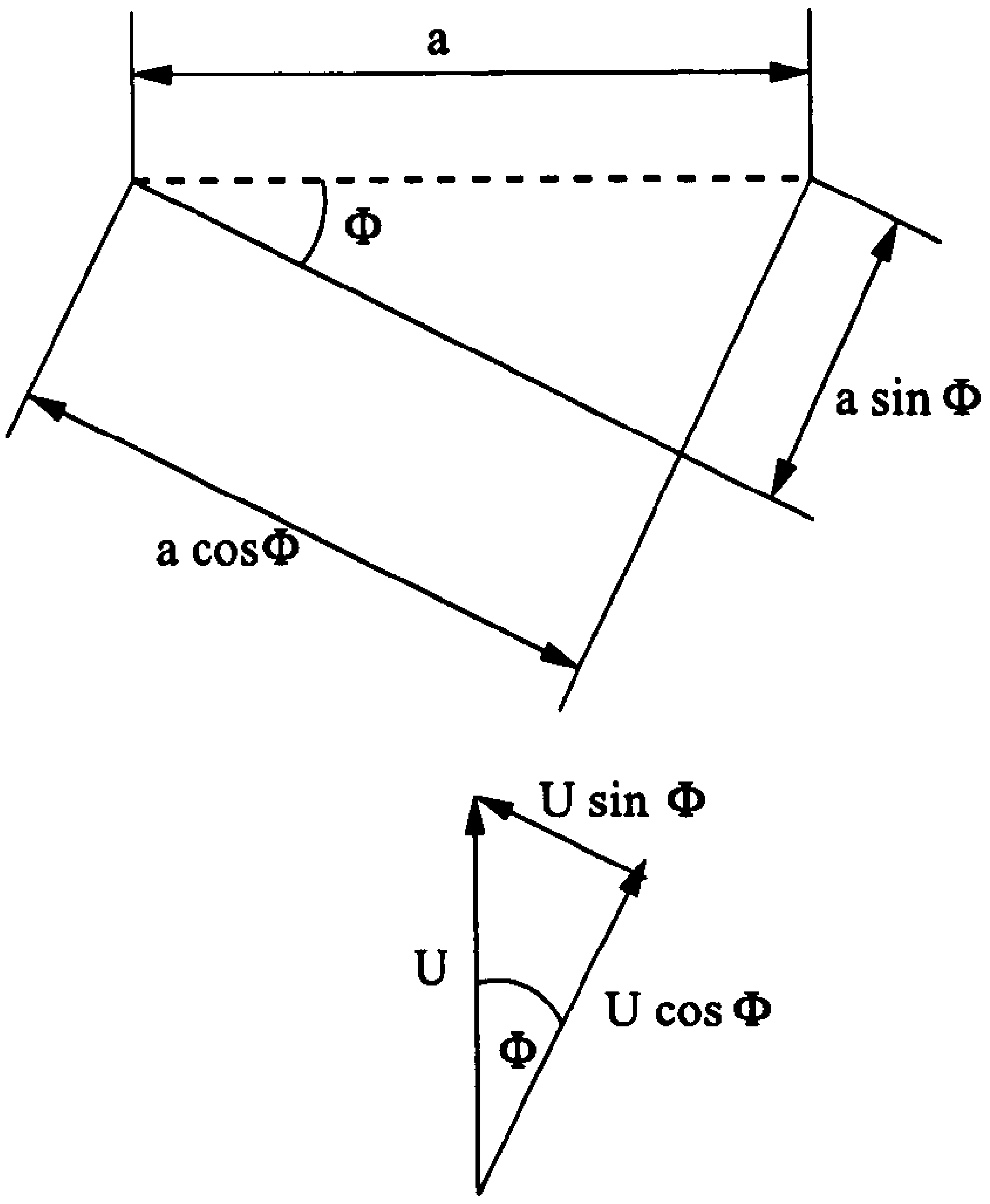

Figure 6.1: Elementary flux example

6.3 Resolution of Flow Along Pitched Grooves

As for the simple problem outlined above we consider the flow in both the groove direction (x') and cross-groove direction (y') separately. The resolved velocities in the x' and y' directions are shown in figure 6.2. By sub-dividing the groove geometry parameters through which the flux passes into x' and y' components, the problem can be broken down into the two components.

x' direction flux

The flux in the x' direction is obtained, as outlined in chapter 5, using the boundary conditions that the web is moving with velocity $S \cos \Phi$ and the groove walls with velocity $\cos \Phi$. By neglecting inertial terms the x' momentum equation simplifies, resulting in a two dimensional Poisson's equation:

$$\frac{\partial p}{\partial x'} = \frac{\partial^2 u'}{\partial y'^2} + \frac{\partial^2 u'}{\partial z^2}, \tag{6.2}$$

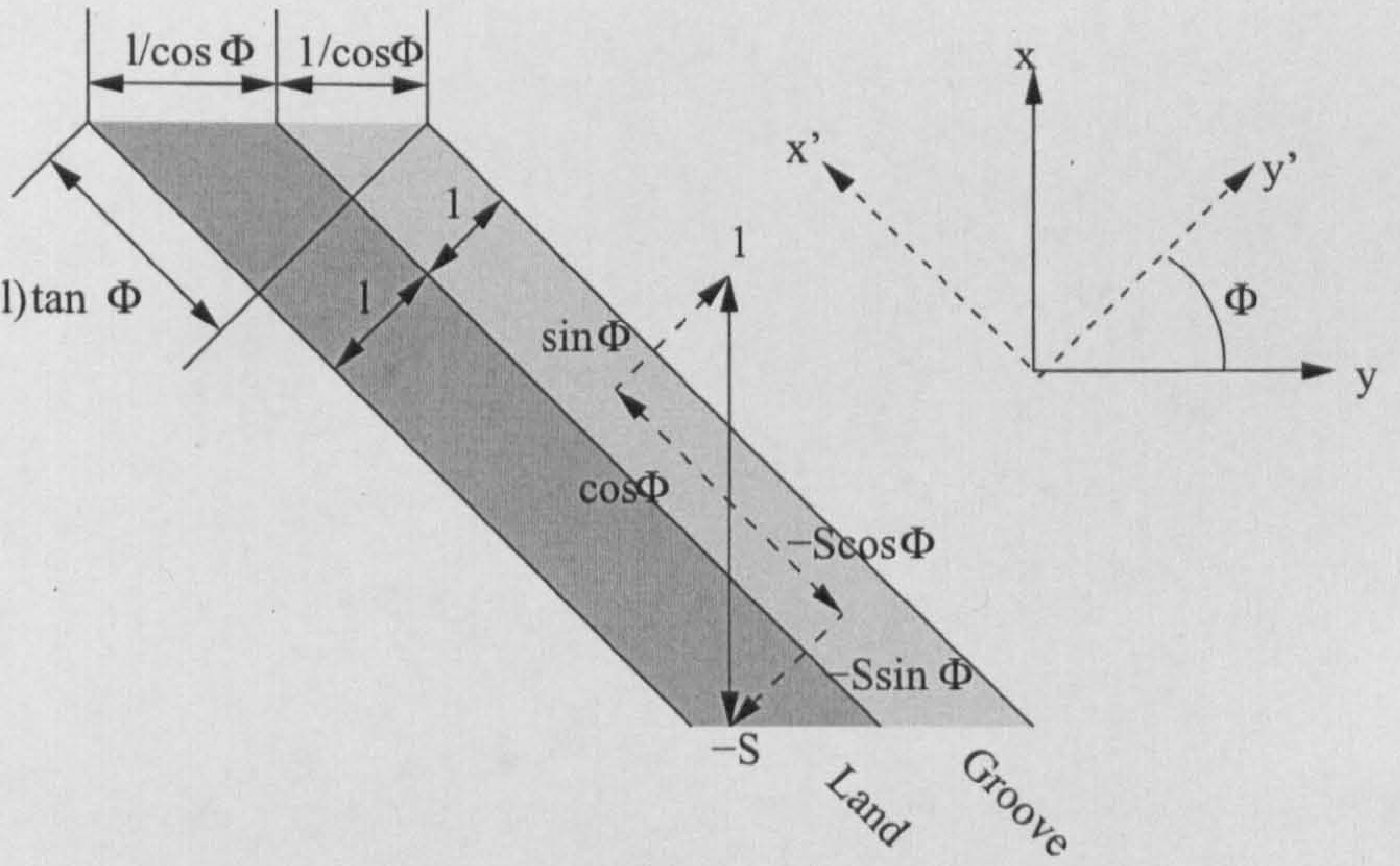

Figure 6.2: Resolution Of Velocities In Coating Model

where the notation and non-dimensionalising parameters are the same as those used in chapter 5, and dashed variables are with respect to the pitched coordinate frame. Equation (6.2) is solved using the finite element method described in chapter 5. Because of the inherent symmetry at the centre of the groove and land only half the groove domain needs to be solved for. The final number of nodes in a typical solution was of the order of 100, being sufficient to ensure mesh independence.

y' direction flux

Determining the flux in the y' direction necessitated a series of further simplifications:

1. That the flux contained within the grooves is transported by the roll with velocity $\sin\Phi$, and is the product of (i) the velocity of the roll in the y' direction, (ii) the equivalent film thickness (the average depth of fluid on the roll) and (iii) the length the flux passes though per groove ($(l+a)\tan\Phi$). The flux is therefore given by:

$$Flux = \underbrace{k}_{\text{average groove depth}} \times \underbrace{(1+l)\tan\Phi}_{\text{groove dimension projected in the } y' \text{ direction}} \times \underbrace{\sin\Phi}_{\text{roll velocity in the } y' \text{ direction}} \tag{6.3}$$

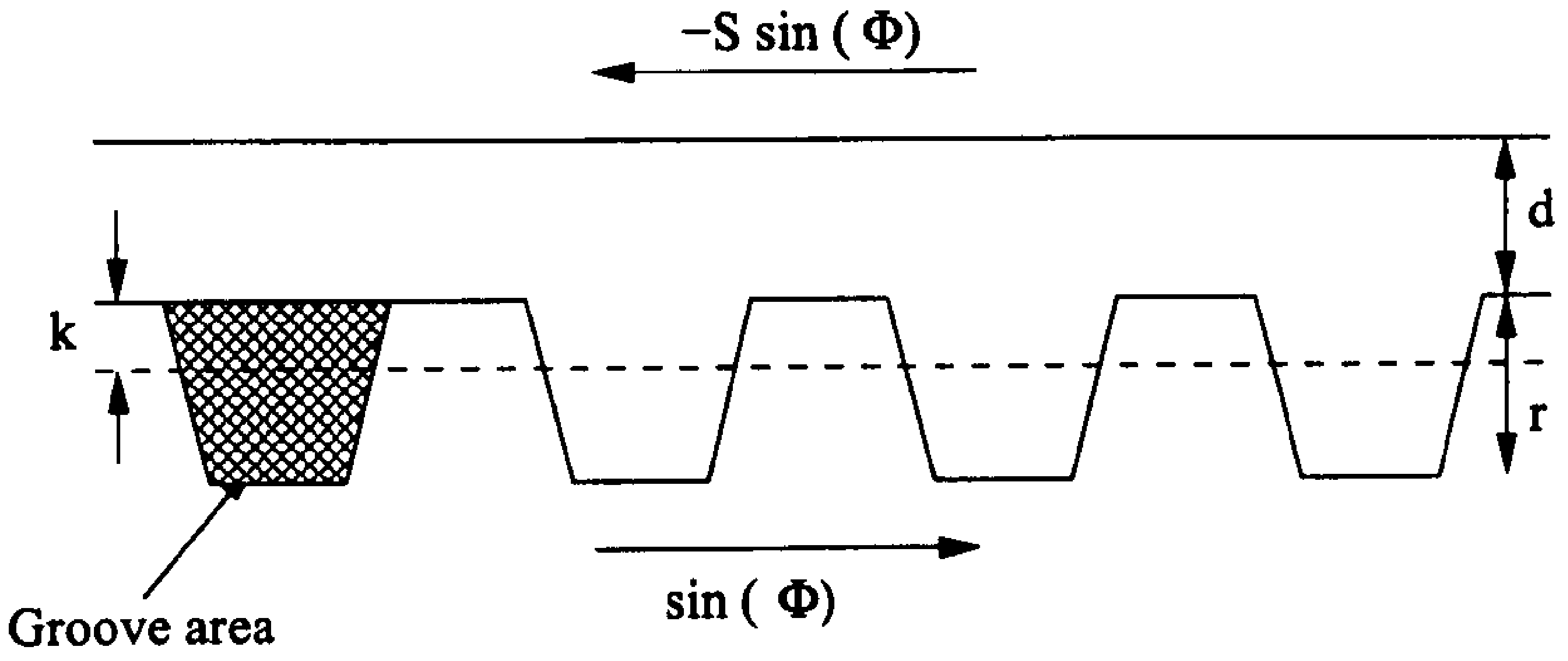

Figure 6.3: Cross Flow Geometry

2. That in the web-to-roll gap the flux is determined by Poiseuille-Couette flow. The analysis requires an assumption to be made about the boundary conditions. The flow is based on the following equation,

$$\frac{\partial^2 v'}{\partial z^2} = \frac{\partial p}{\partial y'} \equiv \frac{\partial p}{\partial x} \sin \Phi \tag{6.4}$$

Integrating equation (6.4) twice with respect to z, gives:

$$v' = \frac{z^2}{2} \frac{dp}{dx} \sin \Phi + z c_1 + c_2 \tag{6.5}$$

where c_1 and c_2 are arbitrary constants to be determined. Due to the varying geometry in the y' direction, the average groove depth is used, and at this location the velocity is assumed to be that of the roll. The other boundary condition used to obtain c_1 and c_2 is based on the web motion. The two boundary conditions are therefore:

$$v' = \sin \Phi \quad \text{at} \quad z = 0 \quad \text{and} \quad v' = S \sin \Phi \quad \text{at} \quad z = d + k, \tag{6.6}$$

giving,

$$c_1 = \frac{2S - 2 - \sin \Phi \, (d+k)^2 \frac{dp}{dx}}{2d + 2k} \quad \text{and} \quad c_2 = \sin \Phi, \tag{6.7}$$

and hence

$$v' = \frac{\left(z^2 \frac{dp}{dx} (d+k) + \left(-(d+k)^2 \frac{dp}{dx} + 2S - 2\right) z + 2d + 2\,k\right) \sin (\Phi)}{2d + 2k}. \tag{6.8}$$

The flux per unit width, is obtained by integrating equation (6.8), the limits of integration being taken between the land surface to the web. In effect this gives the flow between the web and land a certain degree of slip at the roll surface. The final flux through the groove in the y'-direction, $q_{y'}$, is therefore:

$$
\begin{aligned}
q_{y'} =& \frac{\sin(\Phi)\, d\,(d+2\,k)\,(1+l)\tan(\Phi)}{2\,d+2\,k} S \\
&- \frac{\sin(\Phi)\, d^2\,(d+3\,k)\,(d+k)\,(1+l)\tan(\Phi)}{12\,d+12\,k} \frac{\partial p}{\partial x} \\
&+ \frac{\sin(\Phi)\,(1+l)\tan(\Phi)\left(d^2+2\,dk+2\,k^2\right)}{2\,d+2\,k}.
\end{aligned}
\tag{6.9}
$$

Pressure Gradient Solution

The overall flux per groove, obtained by adding the flux per groove in the x'- and y'-directions, is used to obtain the pressure distribution though the coating bead. From conservation of mass considerations, the pressure gradient is the unknown variable, to be determined from roll geometry, operating conditions and flux via a search method as described previously, and is easily accomplished due to the linear relationship between flux and pressure gradient.

6.3.1 Meniscus models

The location and pressure at the upstream and downstream menisci are boundary conditions necessary to make the pressure equation tractable. Accordingly, a meniscus model is required that relates the operating conditions to the film thickness and local radius of curvature, which along with surface tension determines the pressure discontinuity across the meniscus. As in the model described in chapters 4 and 5 the cavitation model due to Coyne and Elrod [6, 5] for the withdrawal of a plate from a flooded gap is employed.

At the downstream meniscus, the grooves arrive at the coating bead full resulting in a simple two dimensional meniscus, as confirmed experimentally. At the upstream meniscus the partially full grooves result in the meniscus dipping into the grooves and forming a complex three dimensional shape as detailed in chapter 4. A simplified geometry for the upstream meniscus is therefore required, one based on an equivalent rectangular geometry to that being modelled and using the dimensions perpendicular to the surfaces to obtain the gaps.

Downstream meniscus

The downstream meniscus model is similar to that used for the case of zero pitch angle, with the line width corrected for the groove angle, $(1+l)\cos\Phi$. The film thickness (h_{dsm}) is related to flux (q), speed ratio ($S = \frac{U_{web}}{U_{roll}}$) and line width ($(1+l)\cos\Phi$) by:

$$h_{dsm} = \frac{q}{(1+l)\,S\cos\Phi}. \tag{6.10}$$

A parabolic approximation for the roll surface enables the downstream meniscus location to be determined. Following this, the local radius of curvature is then used to obtain the pressure at the downstream meniscus, as in section 5.7.1.

Upstream meniscus

As for the case of the non-rectangular grooves the upstream meniscus model is based on an equivalent groove geometry. The equivalent geometry is obtained by maintaining the groove depth, line width and cross sectional area, see section 5.7.1, as shown in figure 6.4. The angle of the groove effectively stretches the domain in the y-direction by $\frac{1}{\cos\Phi}$. The method used to determine the

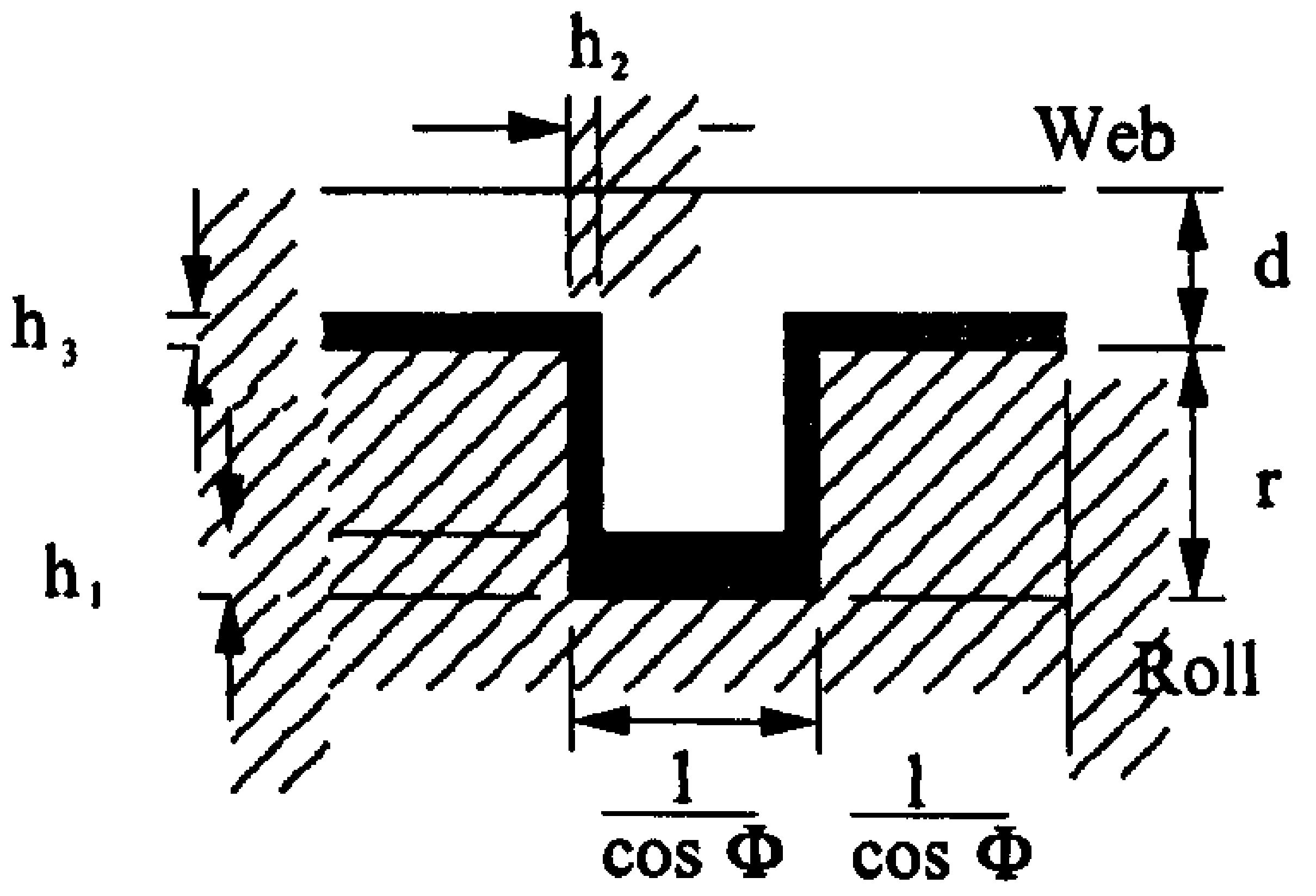

Figure 6.4: Simplified filling of grooves at the upstream meniscus

location of and pressures at the upstream meniscus follows the same method as that outlined in section 5.7.1. Once again, the contact angle that the upstream meniscus makes with the web is modelled using the empirical correlation of Jiang, Oh and Slattery [116].

6.3.2 Calculation Procedure

The method used to determine the flux is identical to that given in section 4.6 for grooves with zero pitch. A search for the flux which resulted in consistent pressures throughout the coating bead is made, the final flux being that for which the pressures match those calculated using the upstream and downstream meniscus models.

Chapter 7

Zero Pitch Results

7.1 Introduction

This chapter presents experimental and numerical results for the case of tri-helical gravure roll coating having grooves of zero pitch. The first results obtained experimentally were for three rectangular grooved rolls[1] with relatively large grooves of width $1mm$. There were difficulties interpreting the results from these rolls as detailed below, and a second set of experiments and simulations were carried out with smaller grooves, more representative of those used industrially.

The theoretical results (based on the analytical and FE solutions of Poisson's equation, chapters 4 and 5 respectively) were found to compare well with the experimental data obtained with rectangular grooves. Grooves with a non-rectangular cross section were also investigated with data compared with the results from the FE solution of Poisson's equation describing flow along the grooves.

One of the most important coating parameters for stable gravure coating operations is the volume of fluid transfered from the grooves to the web. Flow visualisation of the coating bead is also of importance as it highlights the location of eddies where bubbles and solid residues may accumu-

---

[1] Roll names are given in tables 2.1, 2.2, 2.3 and 2.4.

late. It also provides evidence as to whether the assumptions made in formulating the analytical models are valid.

The positions of the menisci were also measured. The characterisation of the coating bead by this sensitive parameter helps understand the onset of streaking (lines of uncoated web) as well as providing another means to check that coating models are correctly capturing the physics of the process.

7.2 Rectangular Groove Results

7.2.1 Visualisation of the coating bead

Figures 7.1(a) and 7.1(b) show images of the coating bead, taken from the edge of the roll. A pulse of dye was used to highlight the vortex structure within the bead. A number of observations can be made. Firstly the web lies on, or extremely close to the roll surface. Secondly, the bead is bounded by an upstream and downstream meniscus that lie either side of the web-to-roll contact zone. Finally, there is an eddy structure within the bead, as shown schematically in figure 7.1(c). Recirculations upstream and downstream of the region of web-to-roll contact are similar to those observed in the case of smooth roll coating [44]. These observations underpin the assumptions on which the theoretical model is based, namely that (i) there is roll-to-web contact in the region over which the web is wrapped, (ii) the upstream and downstream menisci lie outside of the web-to-roll contact region, the exception being when streaking is present as examined later and (iii) the flow is essentially unidirectional in the coating bead except close to the menisci.

7.2.2 Pickout and Film Thickness

Perhaps the results of greatest practical importance in stable tri-helical gravure coating are those giving the volume of fluid transferred to the web from the roll. Typically this is described in two ways: (i) as a final film thickness coated onto the web; (ii) as non-dimensional fractional pickout

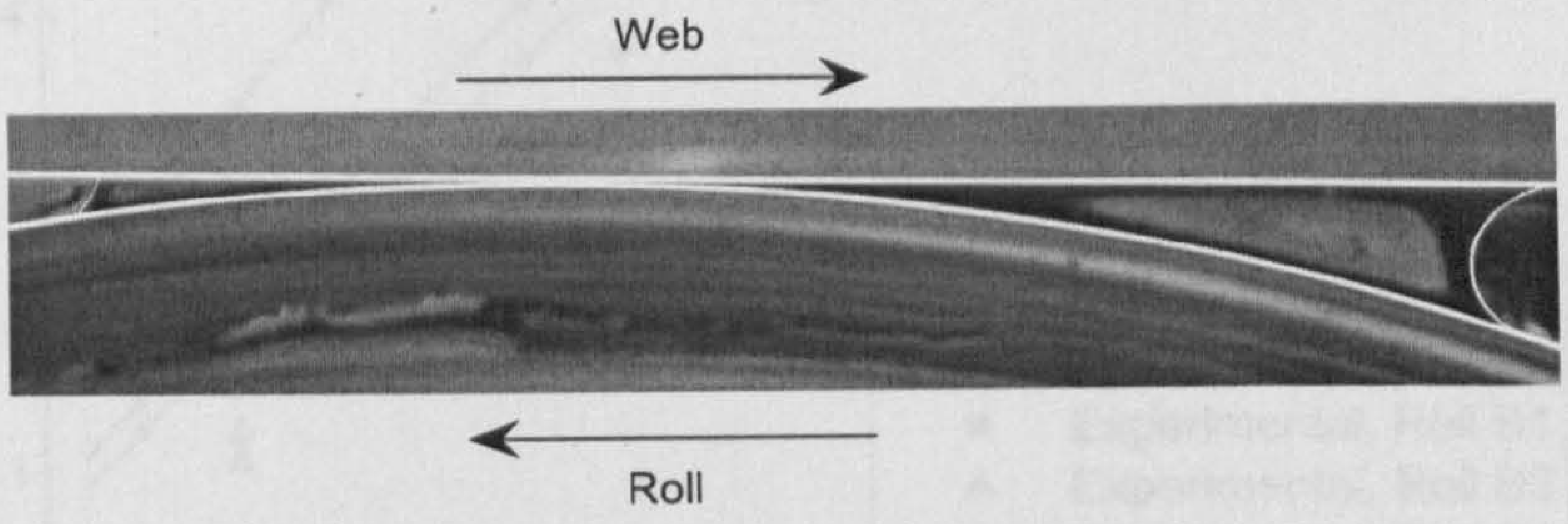

(a) $S = 0.22, Ca = 0.0074$

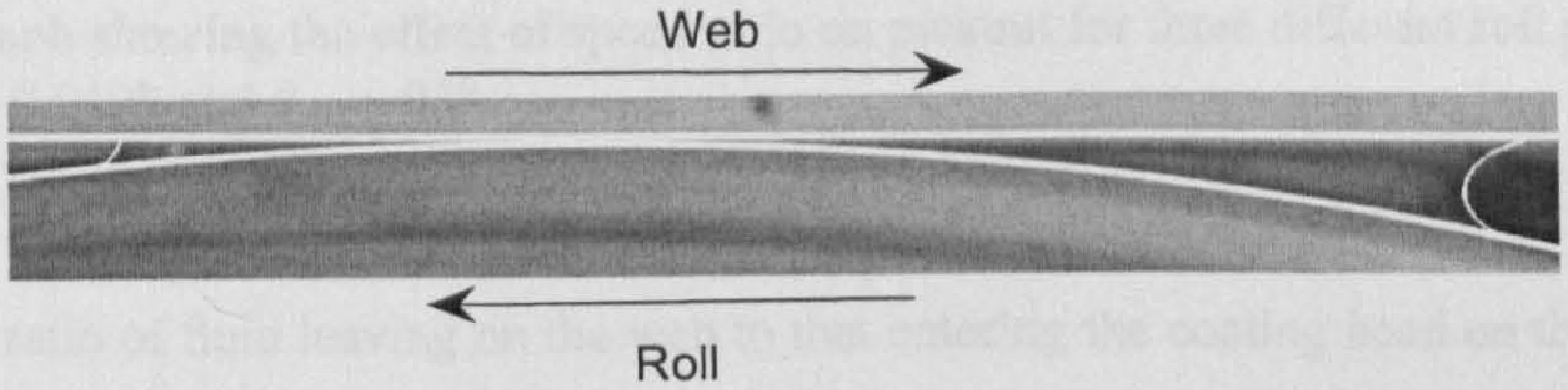

(b) $S = 1, Ca = 0.0105$

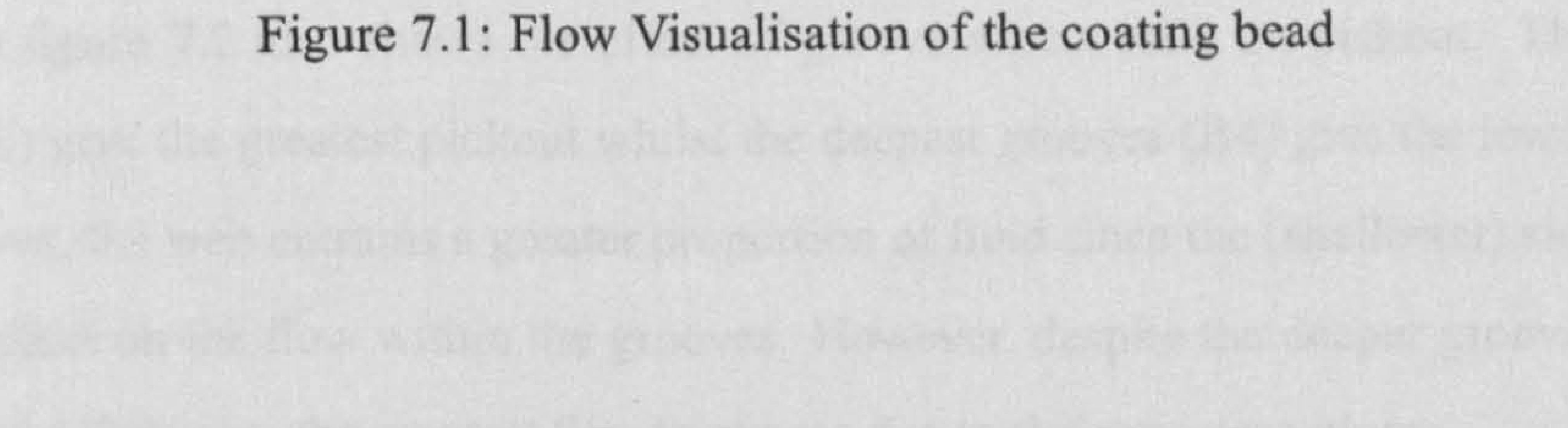

(c) Schematic of the main flow structures observed within the coating bead

Figure 7.1: Flow Visualisation of the coating bead

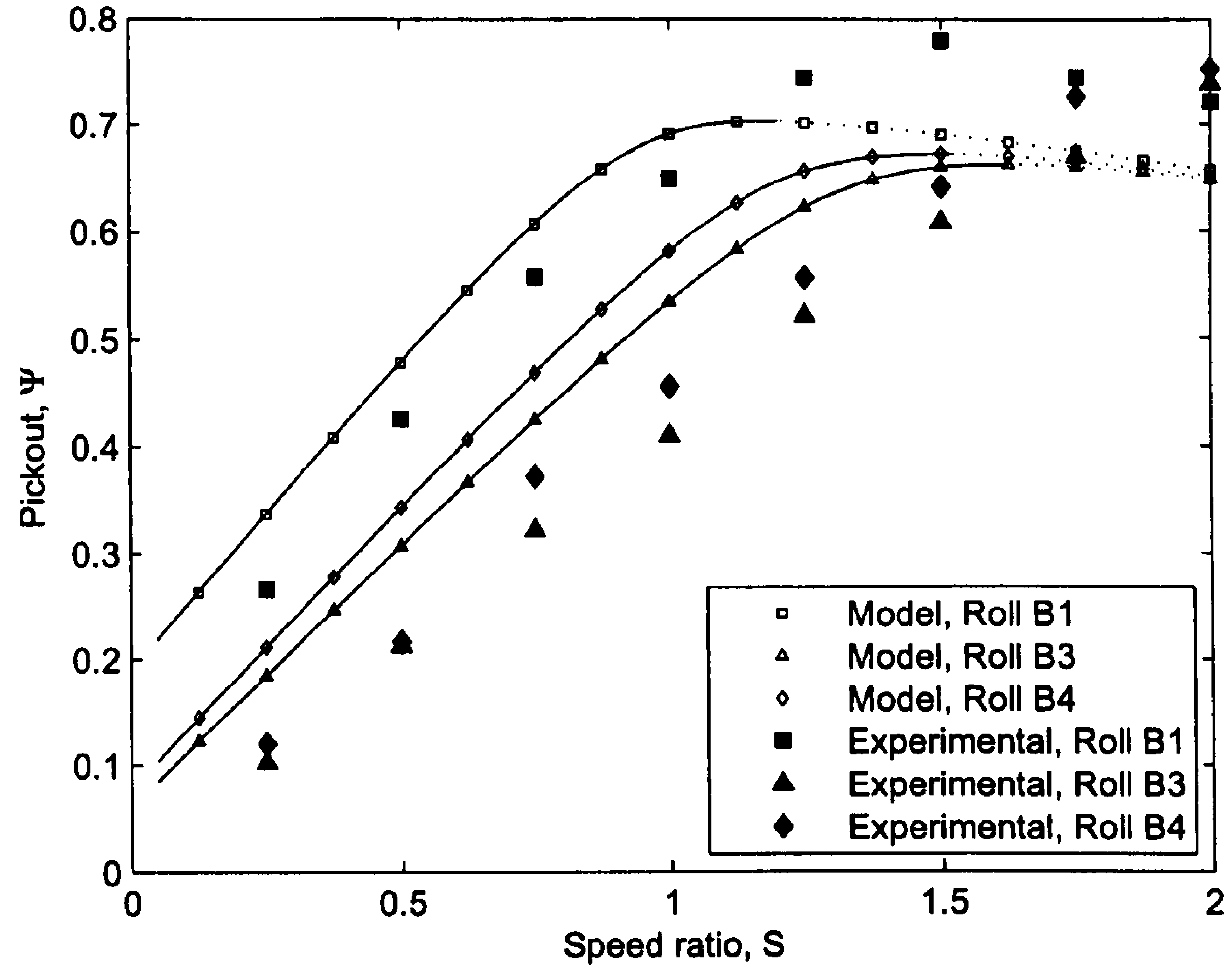

Figure 7.2: Graph showing the effect of speed ratio on pickout for three different roll geometries, $\beta = 5°$, $Ca = 0.0497$ and $\theta_A = 95°$

defined as the ratio of fluid leaving on the web to that entering the coating bead on the roll. Figures 7.2 and 7.3 show experimental and analytical results for the three different groove dimensions given in table 2.2. There is good agreement between the experimental data and prediction, both in terms of pickout and film thickness. Over the stable coating regime (up to $S \approx 1.2$) the pickout data rises approximately linearly. There is a corresponding decrease in film thickness - for these geometries at least it appears the pickout does not increase quickly enough to give an increase in film thickness, as observed for discrete-cell gravure coating, see Kapur [78].

The data in figure 7.2 also shows the effect of groove aspect ratio on pickout. The shallowest grooves (B1) give the greatest pickout whilst the deepest grooves (B4) give the lowest. For shallower grooves, the web entrains a greater proportion of fluid since the (shallower) side walls have less of an effect on the flow within the grooves. However, despite the deeper grooves having the lowest pickout they give the greatest film thickness due to their greater volume.

There are two other observations to be made from figure 7.2. Firstly, beyond the speed ratio at

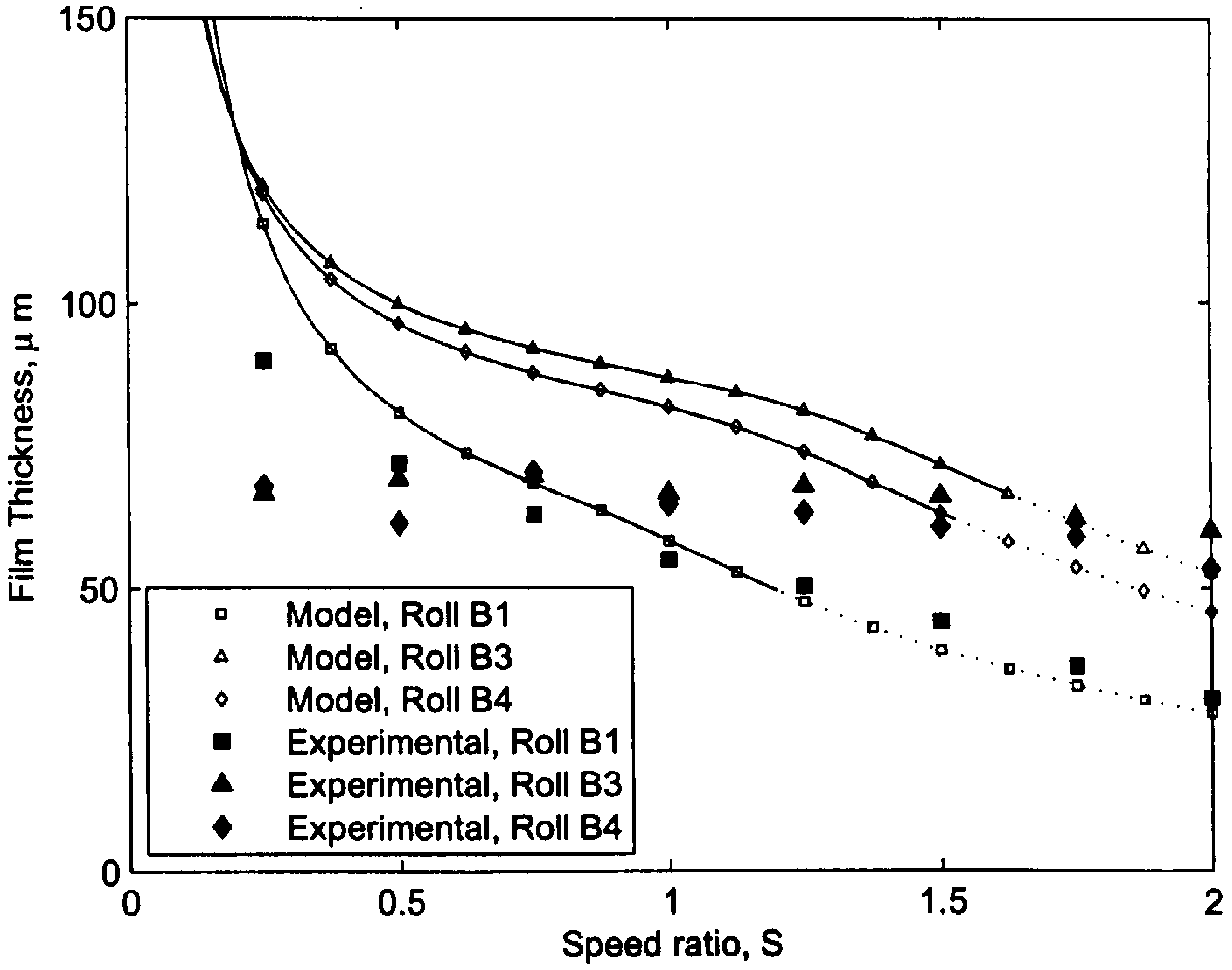

Figure 7.3: Graph showing the effect of speed ratio on film thickness for three different roll geometries, $\beta = 5°, Ca = 0.0497$ and $\theta_A = 95°$

which maximum pickout occurs, streaking is observed in the final coating - this is discussed in section 7.2.3; secondly, as the speed ratio is decreased the pickout does not tend to zero. The volume of fluid entering the bead is unable to pass through the bounded channel, where the web is wrapped over the roll. In practice this results in a collection of fluid at the downstream meniscus that either drips off the web or runs back down the roll surface into the pan, in much the same was as flooded forward roll coating [8].

Figures 7.4 and 7.5 show the effect of varying the wrap angle from 0° to 5°. For the lower wrap angle the bounded channel is smaller in length; consequently more fluid passes through the nip and leaves via the roll surface, and pickout will be lower. This effect is most pronounced at low speeds and was not observed by either Kapur [78] or Benkreira & Patel [77] due to the more limited speed ratios studied by these authors or to their work mainly focusing on discrete cell patterns. Figure 7.5 illustrates that varying the wrap angle can cause quite complex behaviour in film thickness, particularly at lower speed ratios:

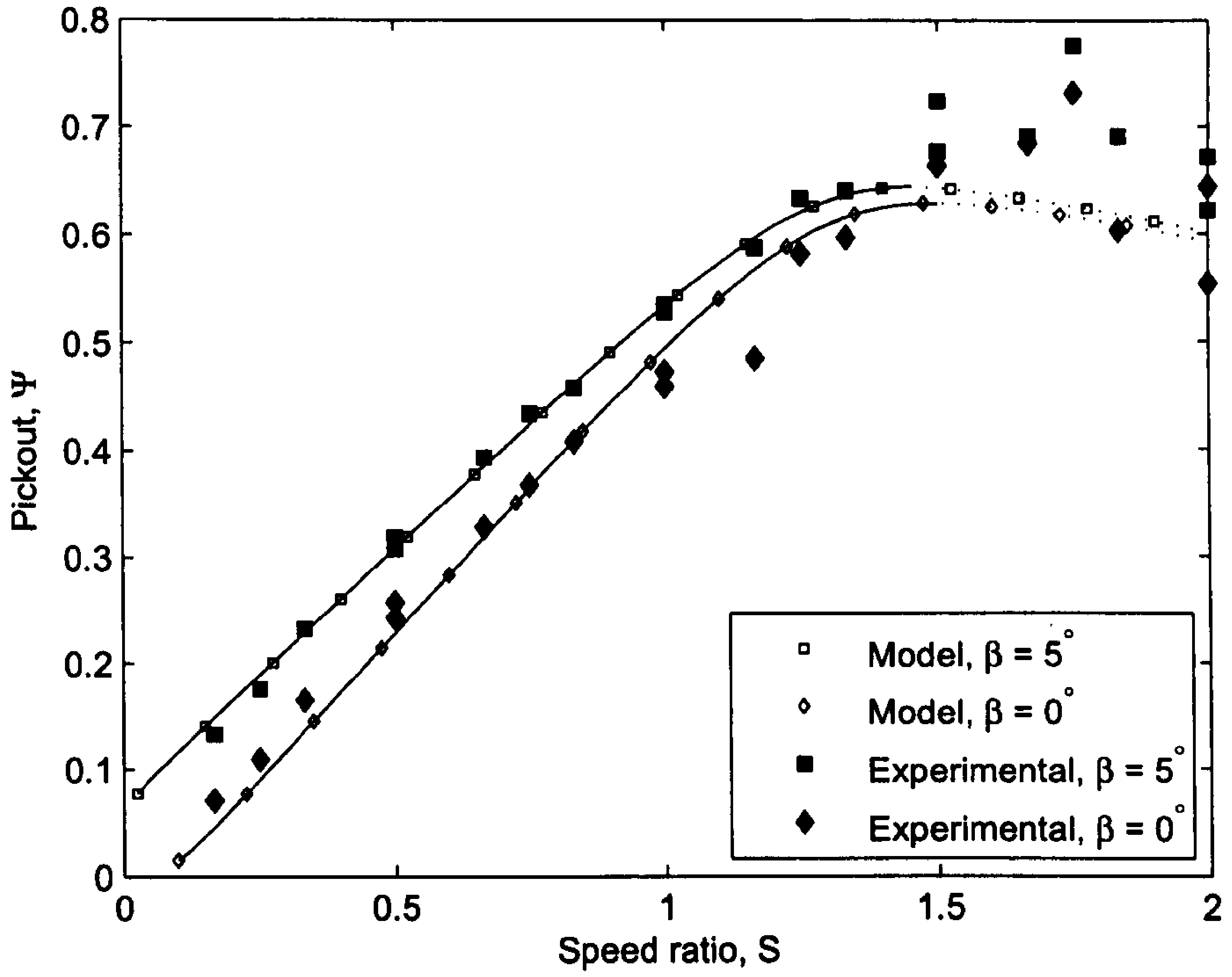

Figure 7.4: Graph showing the effect of speed ratio on pickout for two different wrap angles, model $Ca = 0.0817$, $\theta_A = 18°$, Experimental $Ca = 0.0817 \rightarrow 0.1226$, $\theta_A = 18° \rightarrow 95°$, Roll B3

- As the wrap angle is decreased the pickout falls.
- The film thickness tends to zero as the speed ratio goes to zero for a wrap angle of 0° but tends to infinity for a 5° wrap angle; this corresponds experimentally to the fluid collecting at the downstream meniscus and flowing back on the roll or along the web.

Figure 7.6 presents data showing the effect of the (roll) capillary number on pickout. The capillary number was varied by running the experiment with a more viscous fluid or with different roll speeds and corresponding web speeds, to allow a comparison over the same range of speed ratios. The experiments show that there is little dependence of pickout on capillary number so operating at a given speed ratio for any roll speed gives approximately the same film thickness (±10%). However, the capillary number does have an effect on the onset of streaking which has implications for the size of the operating window, as discussed later. The numerical predictions are, once again, in good agreement with the experimental data.

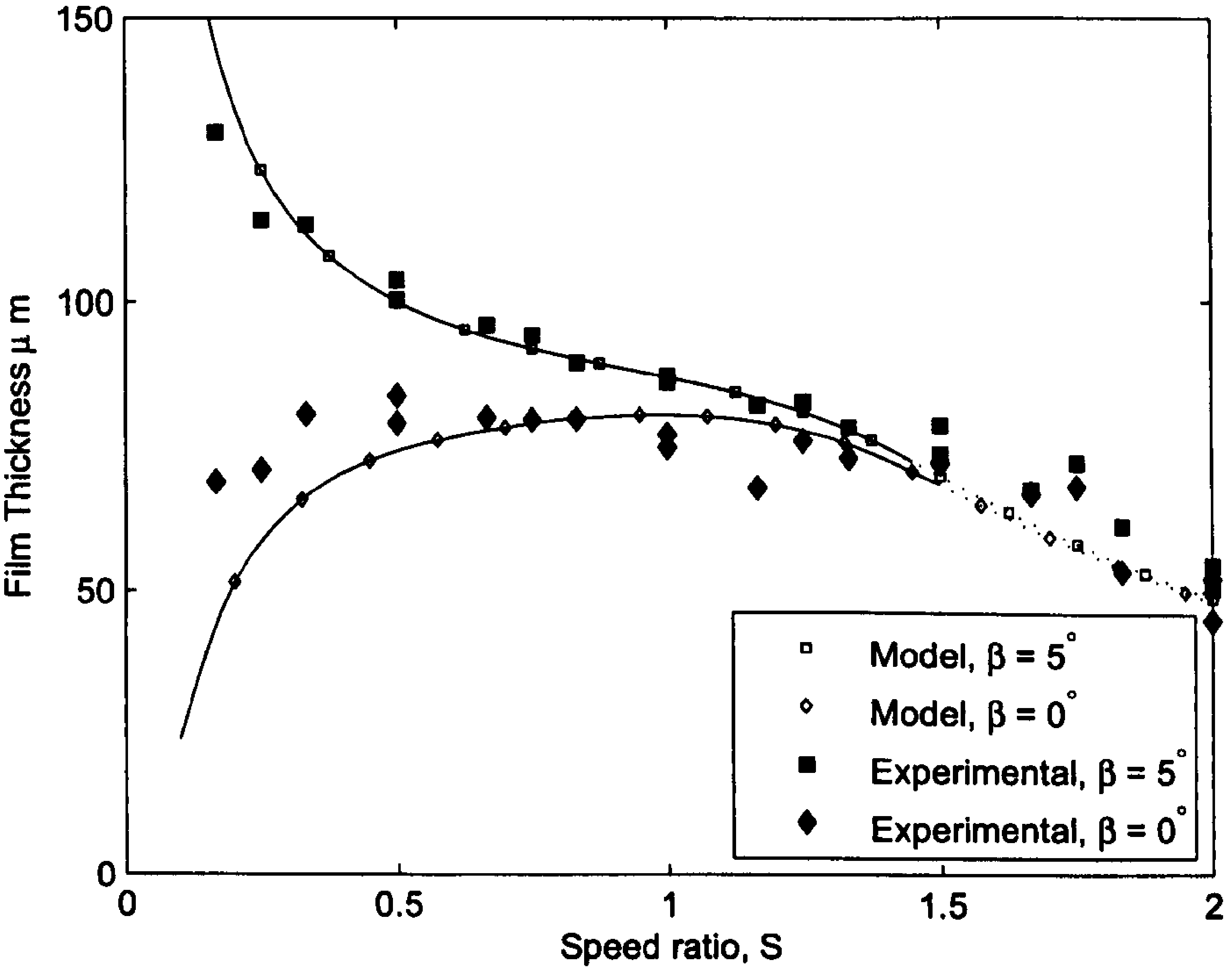

Figure 7.5: Graph showing the effect of speed ratio on film thickness for two different wrap angles, model $Ca = 0.0817$, $\theta_A = 18°$, Experimental $Ca = 0.0817 \rightarrow 0.1226$, $\theta_A = 18° \rightarrow 95°$, Roll B3

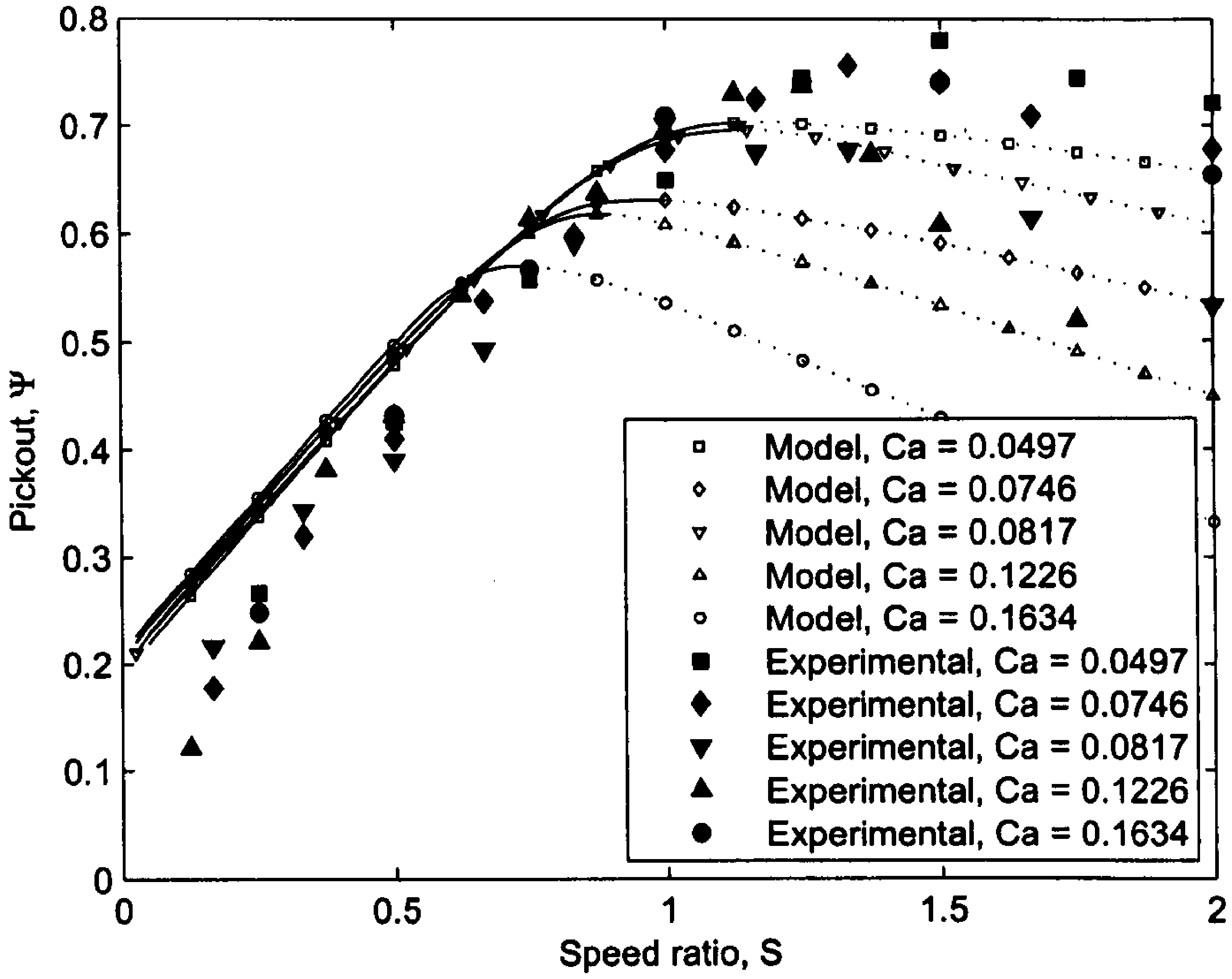

Figure 7.6: Graph showing the effect of speed ratio on pickout for five different (roll) capillary numbers, Roll B1, $\beta = 5°$

7.2.3 The onset of streaking and the operating window

As mentioned above, as the speed ratio is increased the pickout tends to rise to some maximum, beyond which streaking is observed on the web (typically greater than $S = 1.1$). Figures 7.7 and 7.8 show images of the bead taken through the transparent web. Figure 7.7 is an image of the stable bead; at the downstream meniscus the interface is straight in the y-direction and at which some very small bubbles are seen to be trapped. At the upstream meniscus the interface is stable if slightly wavy. Figure 7.8 shows the bead under conditions of streaking ($S = 1.5$). Small sections of the downstream interface are again flat, but occasionally a section of the upstream meniscus appears to be drawn thought the groove until it merges with the downstream one, resulting in a streak (a dry region) on the web. This is a temporal process. As S is increased further, streaking becomes more pronounced across the width of the web.

The conditions that cause streaking can be better understood by examining the positions of the upstream and downstream menisci. These are shown in figures 7.9 and 7.10 as a function of speed

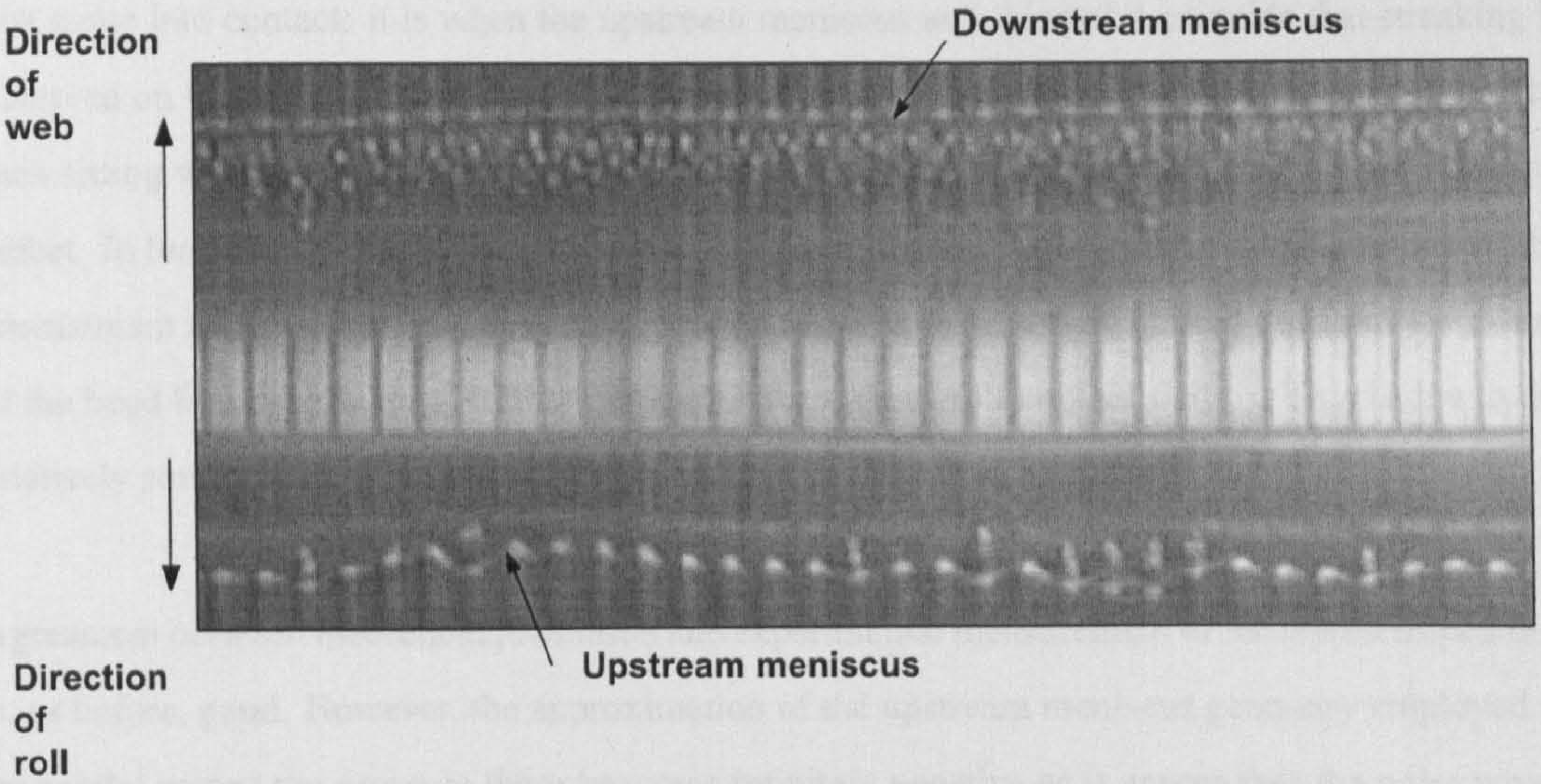

Figure 7.7: Visualisation of the coating bead from above, showing stable upstream and downstream meniscus, Stable interface, $\beta = 0°$,$Ca = 0.0746$ and $S = 0.667$

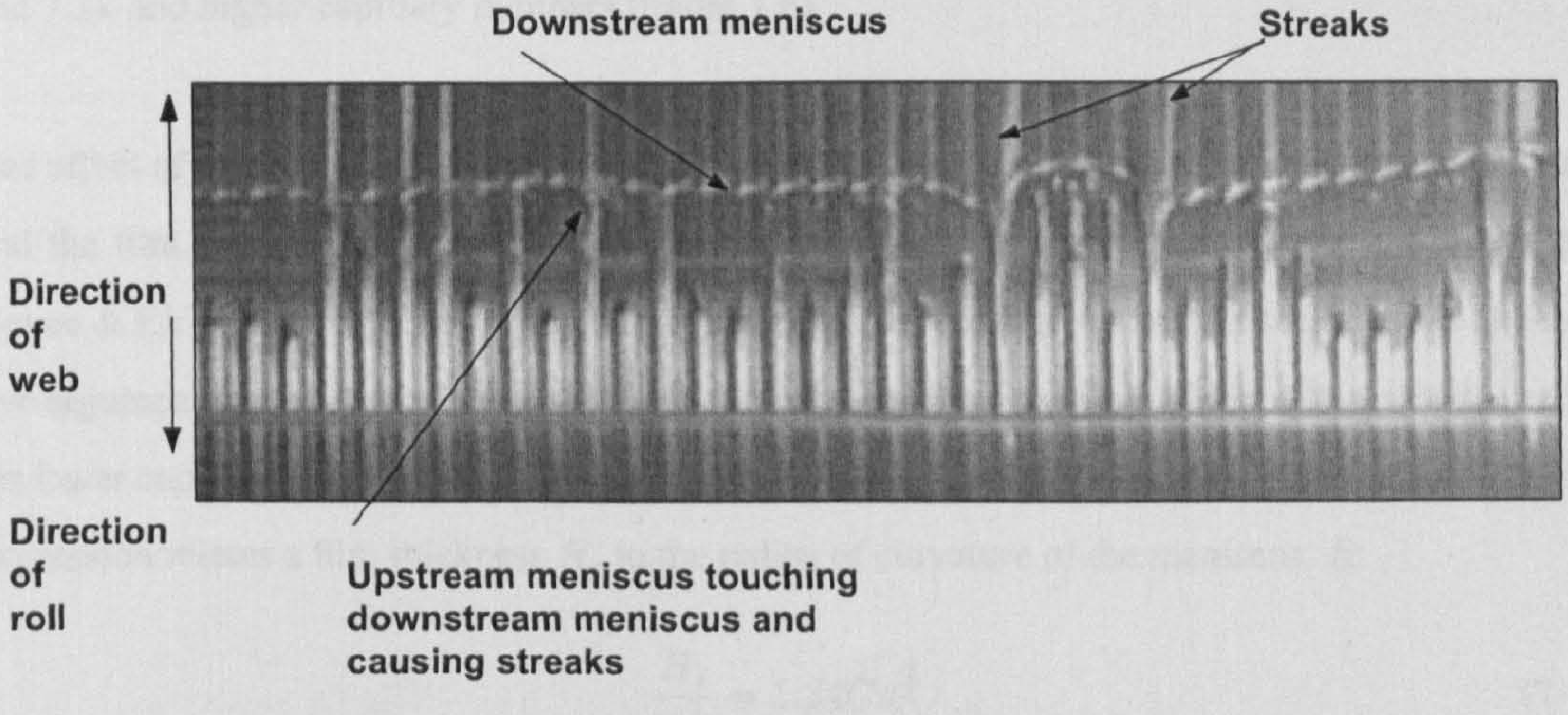

Figure 7.8: Visualisation of the coating bead from above, showing an unstable upstream meniscus causing streaks on the web, $\beta = 0°$,$Ca = 0.0746$ and $S = 1.333$

ratio and wrap angle. As the speed ratio is increased, the downstream meniscus position remains relatively constant, while the upstream meniscus moves towards the point where the web and roll first come into contact: it is when the upstream meniscus and this point coincide that streaking is observed on the web. The coating bead is now bounded upstream by a series of discrete menisci, each sitting within its own grove and periodically accelerating downstream, resulting in a coating defect. In terms of the effect of changing wrap angle there is little variation in the position of the downstream meniscus and the upstream location appears to be simply shifted out from the centre of the bead by a length equal to the increase in the web-to-roll contact βR_{roll}. This is due to the relatively small effect that wrap angle has on the film thickness on the web.

Agreement between theoretical prediction and experimental measurement of the meniscus position is, as before, good. However, the approximation of the upstream meniscus geometry employed in the model means the pressure there becomes infinitely negative as it approaches the point where the web touches the roll. Implicit within the model is that the upstream meniscus does not enter the groove, and effectively as the speed ratio is increased beyond the maximum pickout the change in film thickness with speed ratio is as a consequence of variations in contact angle.

Both the geometry of the roll and the operating conditions affect the operating window. Streaking occurs at lower speed ratios for shallower grooves (i.e. with a lower aspect ratio) (figures 7.2 and 7.3), and higher capillary numbers (figure 7.6).

The effect of capillary number can be explained by examining the relation between this parameter and the film thickness-to-gap ratio. While the analytical work presented in chapter 4 used the Coyne & Elrod model due to its greater applicability over a range of capillary numbers, a qualitative argument can be made by examining the Landau-Levich equation, which, although only valid for lower capillary numbers does clearly illustrates the mechanisms involved. The Landau-Levich expression relates a film thickness H, to the radius of curvature of the meniscus, R:

$$\frac{H_1}{R} = 1.34Ca^{\frac{2}{3}} \tag{7.1}$$

It can be seen that from equation (7.1) that as the capillary number increases, so does the ratio of film thickness to gap. Conservation of mass means that the sum of the mass leaving the coating bead on both the web and the roll has to be constant. Therefore is is reasonable to predict that

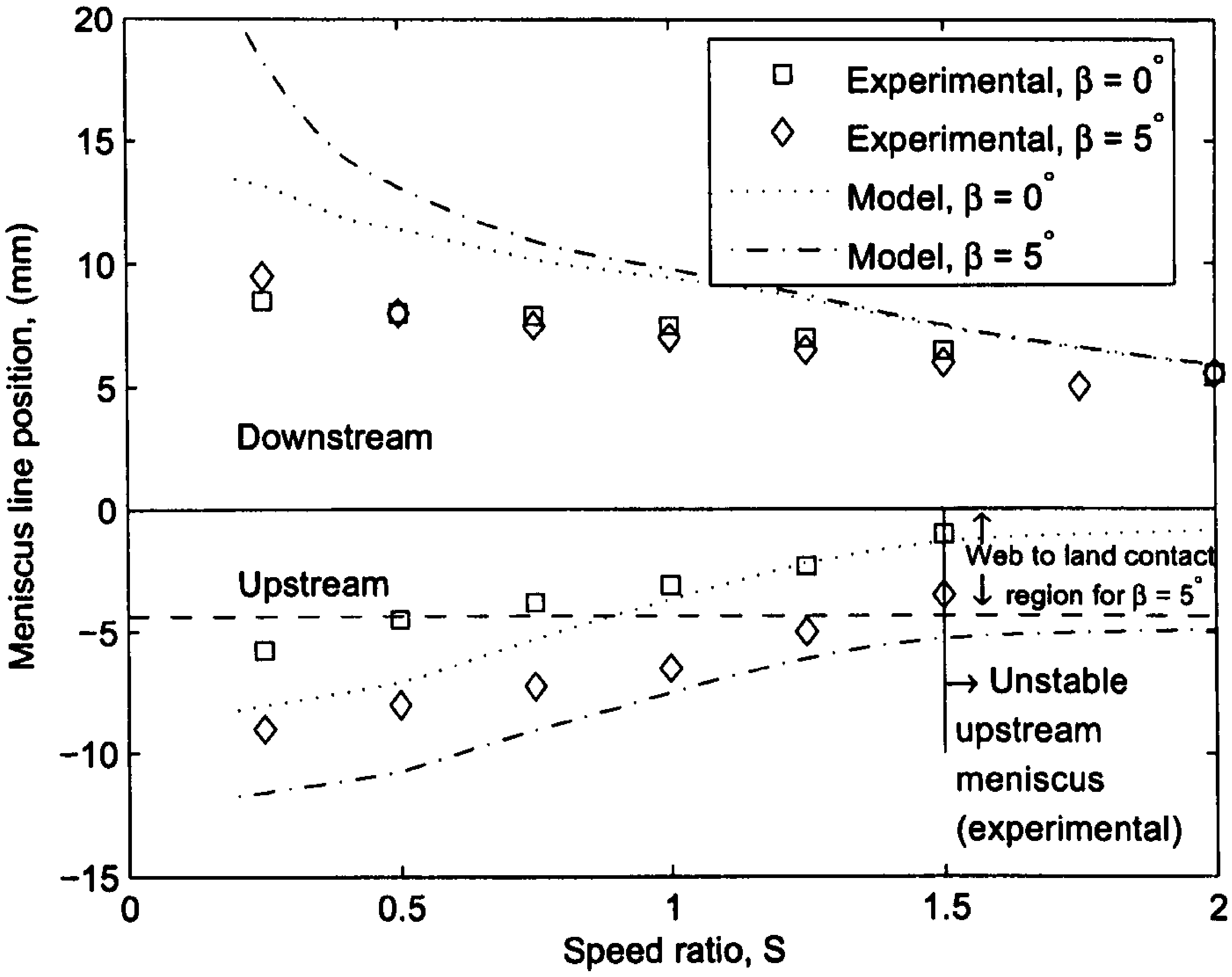

Figure 7.9: Upstream and downstream meniscus positions as a function of speed ratio for two wrap angles, Roll B4 $Ca = 0.0817$ and $\theta_A = 18°$.

the web-to-land gap has to decrease at both the upstream and downstream menisci (the pressure profile and more complex nature of the upstream meniscus determines the precise changes and may therefore have some effect on the balance of mass flow on the web and roll). This decrease in gap results in the width of the bead being reduced. This gives the potential for streaking to occur at a lower S, since the upstream meniscus will now lie closer to where the web touches the roll. Using a similar argument to analyse the effect of groove depth, the moving web has a greater effect on the fluid within the bead when the sidewalls are shallower and more fluid is picked out from the roll. Consequently less remains on the roll and (as for the capillary number number effect) the upstream meniscus responds by lying closer to the point where streaking occurs.

7.2.4 Rectangular Groove Finite Element Solution

As well as being used to validate the analytical solution of the Poisson equation (Chapter 4) based coating model, the experimental data obtained for the case of rectangular grooves was also used

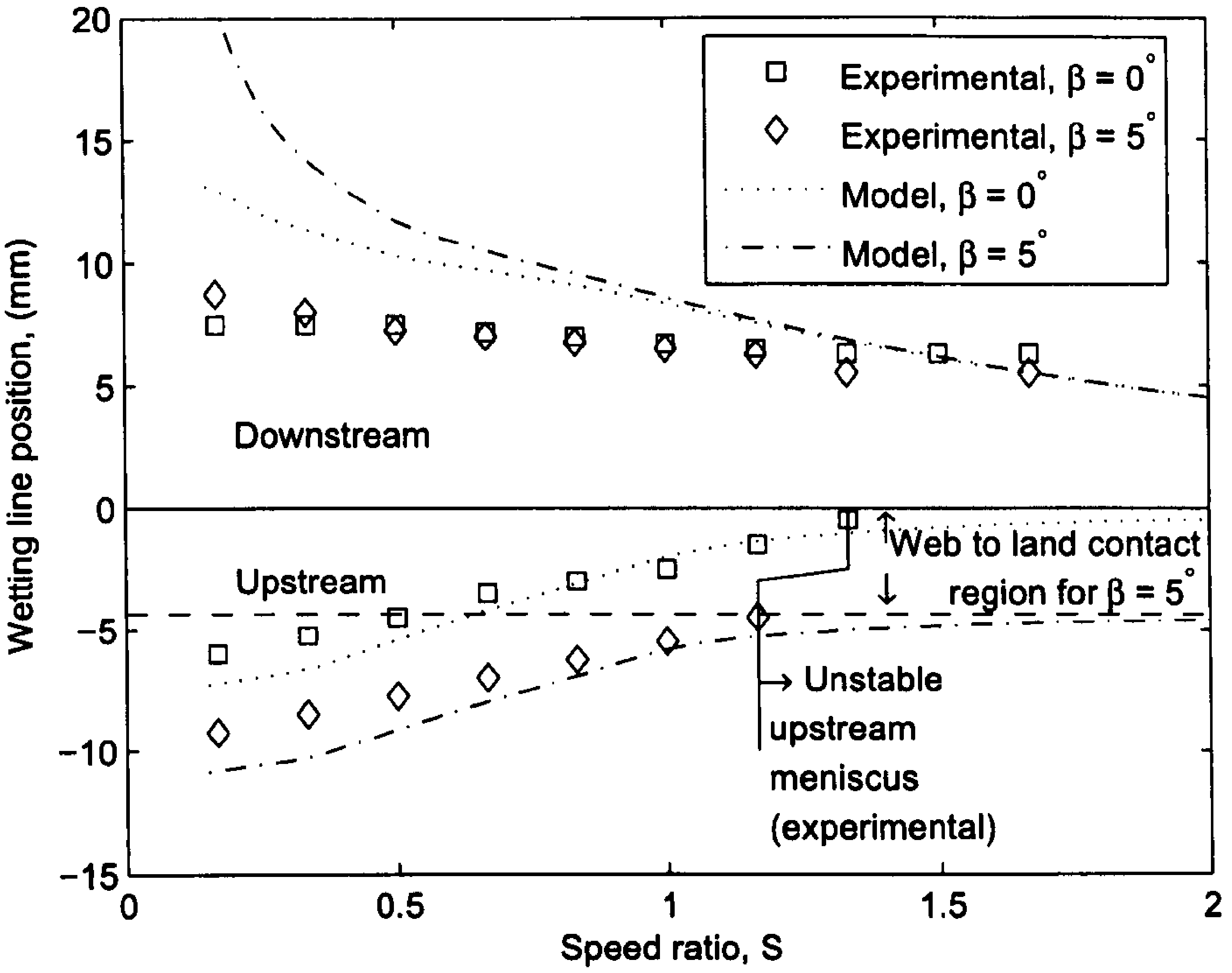

Figure 7.10: Upstream and downstream meniscus positions as a function of speed ratio for two wrap angles, Roll B4 $Ca = 0.1226$ and $\theta_A = 18°$.

to confirm the validity of the finite element based coating model. The level of agreement between experimental results and those obtained numerically is good; the results obtained numerically are similar to those obtained analytically. An example of this is shown in figure 7.11; the level of agreement between all three sets of data is good with the finite element results (solid lines) predicting a slightly lower pickout than those obtained analytically (broken lines), the former results being slightly more in line with the experimental data (points). This is found to be typically the case when comparing sets of results from the two models across all the data.

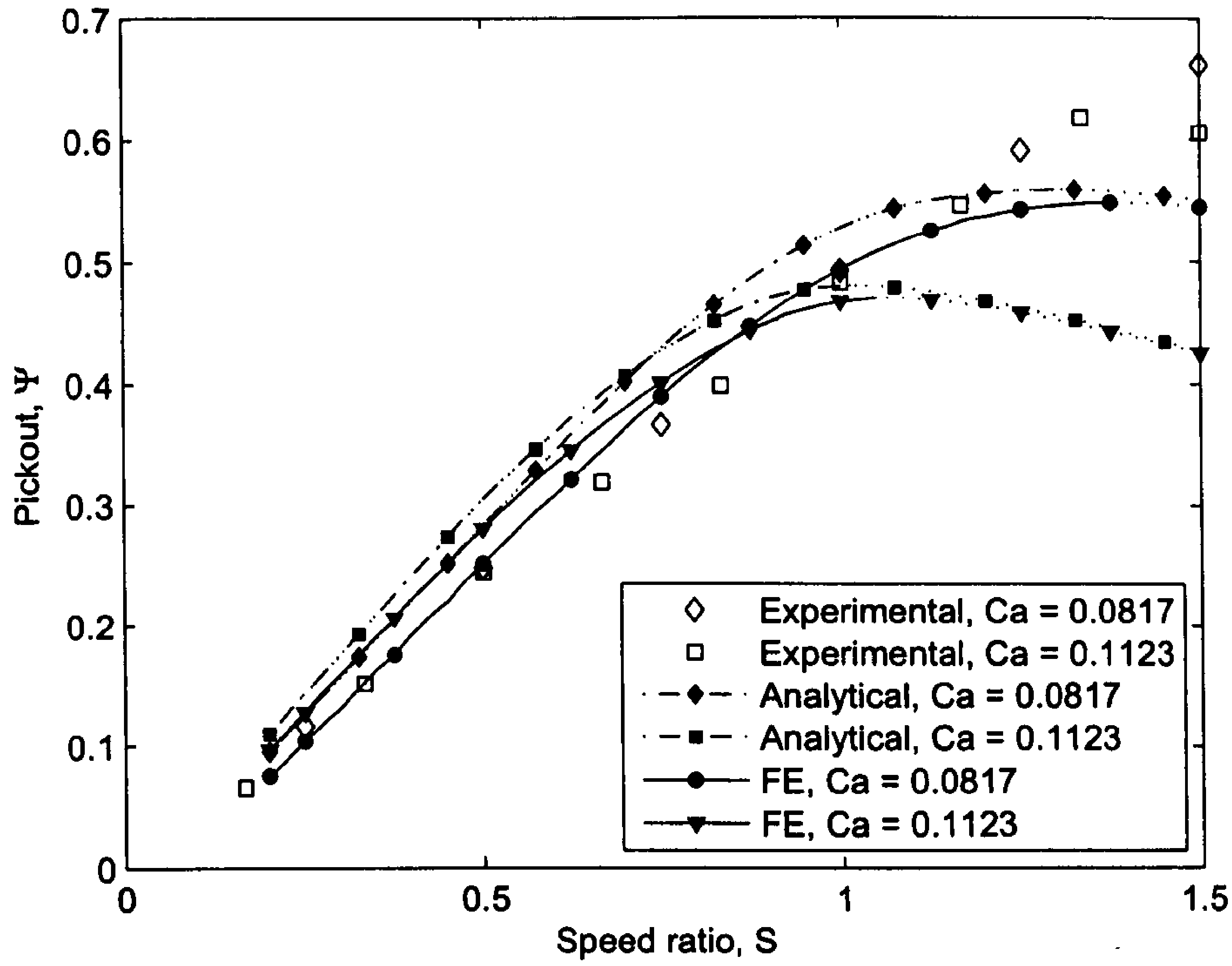

Figure 7.11: Rectangular grooved roll B4 comparison between experimental, analytical and finite element results.

7.3 Non-Rectangular Groove Results

As described in Chapter 5, a model for non-rectangular zero pitch angle grooves has been derived using the finite element method. Figures 7.12 and 7.13 show the change in pickout with speed ratio for two different triangular groove geometries (see table 2.3). It can be seen that the agreement between the experimental results and model predictions is good, and that as speed ratio increases so to does the pickout (up to some maxima). As found before, capillary number (based on roll speed) has a smaller influence on pickout.

As is the case with the rectangular grooves, the pickout increases as the speed ratio increases up to around $S \approx 1.2$. After this point streaking is observed experimentally and the model is no longer able to accurately model the coating process. The effect of wrap angle is similar to that encountered with rectangular groove geometries, with wrap angle increasing the pickout as the speed ratio tends to zero (observed experimentally and predicted from the model) with dripping from the web or fluid rolling back on the roll seen experimentally when the web was stationary.

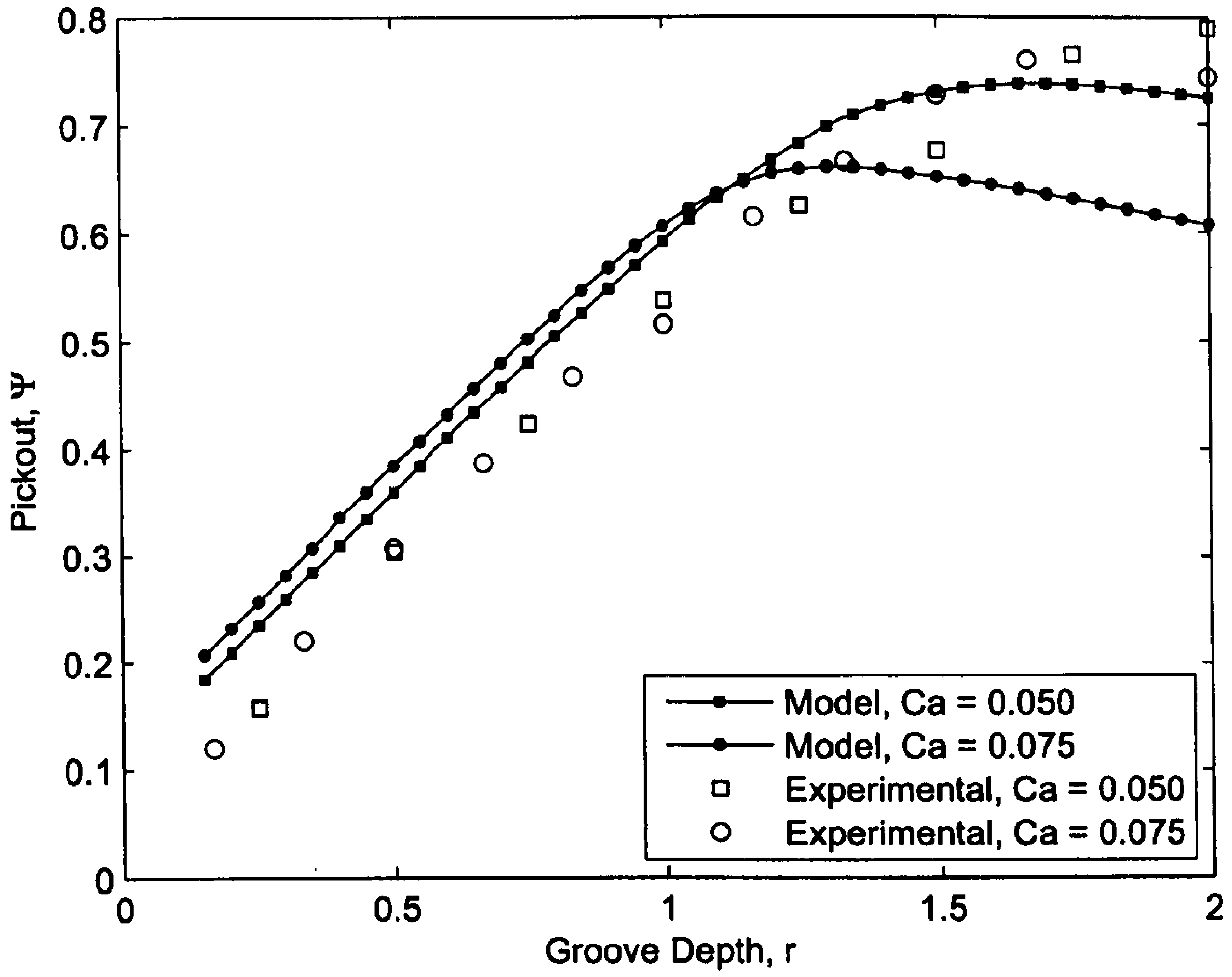

Figure 7.12: Triangular grooved roll C2, wrap angle 4.5°

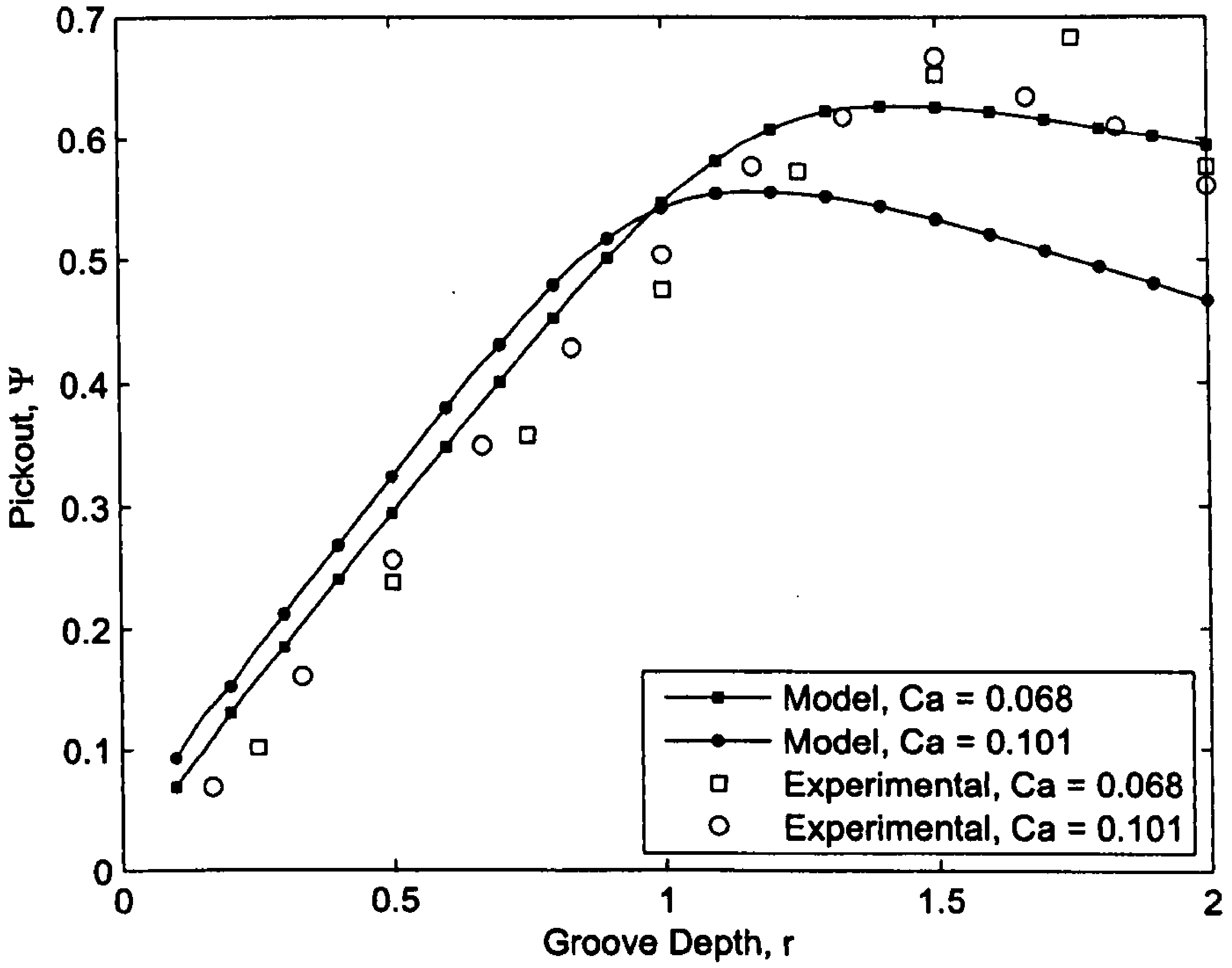

Figure 7.13: Triangular grooved roll C3 pickout predictions, wrap angle 0°

7.4 Pressure Distribution Results

The pressure distribution throughout the coating bead is an important result obtained from the coating models, providing insight into the process. Figure 7.14 shows the pressures present within a typical coating bead. The graph has been plotted in terms of dimensional pressures and distances to better gauge the magnitude of the positive pressures predicted within the bead. At low speed ratios there are positive pressures present. However, as the speed ratio increases the magnitude of the pressures decrease, due in part to the hydrodynamic effect of lower positive pressure gradients from the downstream meniscus and also due to the lower downstream meniscus pressures. With a tension of around $10kg$ per $10cm$ width of web, the predicted maximum pressure of around $200Pa$ (equivalent to a static head of around $2cm$ of water) is unlikely to cause deflection of the web. For more viscous fluids the pressures within the coating bead are greater so care was taken when using the model to confirm the maximum pressures within the coating bead and how they compared with the web tension.

A smaller wrap angle also has the effect of reducing the maximum pressure within the coating bead. The small level of disagreement in pickout between the coating models and the experimental data tends to occur for higher wrap angles, where the experimental pickout data was found to be marginally less than the model predictions. This is as would be expected if there was a small deformation of the web allowing more fluid to pass from the downstream to the upstream side due to the pressure gradient within the coating bead.

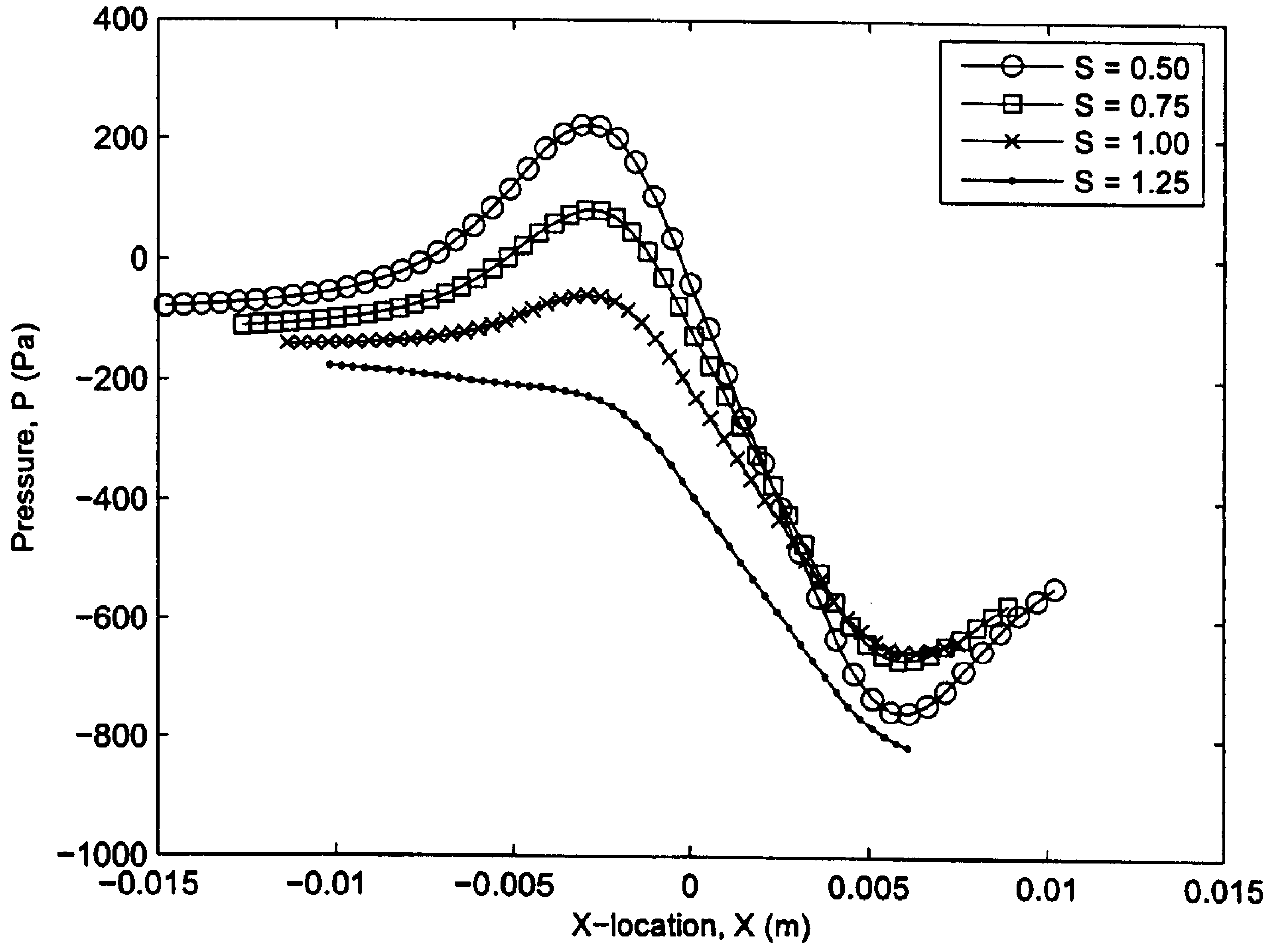

Figure 7.14: Predicted Dimensional pressure distribution within the coating pool of roll B4 with a 5° wrap angle.

Chapter 8

Pitched Grooves and Non-Newtonian Fluid Results

This chapter describes the results of two important extensions to the model:

1. The incorporation of pitched groove geometries as described in chapter 6, thereby more exactly mimicking the industrial process for Newtonian fluids.
2. The incorporation of non-Newtonian fluid behaviour for zero pitched grooves as described in chapter 5.

8.1 Pitched Groove Results

In total, a set of six rolls were manufactured for experimental purposes, three with triangular cross section and three with rectangular cross section, each set comprised of rolls with groove pitch angles of 30°, 45° and 60°. The definition of the parameters relating to the groove dimensions are shown in figure 6.2 of chapter 6. As for the earlier case of zero pitched grooves, experiments were performed to determine the film thickness and from this the pickout was calculated.

The experimental and numerical results for the case of rectangular grooves at three different pitch angles are given in figures 8.1, 8.2 and 8.3, and for the first two (30° and 45°) there is excellent agreement. In all cases (and as with grooves of zero angle pitch) an increase in speed ratio leads to a corresponding increase in pickout, up to some maximum at which point the upstream meniscus dips into the grooves leading to streaking. As before the dotted line indicates the transition to streaking. The agreement between experimental and numerical results when the grooves are pitched at 60° is not as good (figure 8.3) - while the agreement is reasonable at low speed ratios, the rapid rise in pickout observed experimentally is not captured by the model. This is discsussed in more detail later.

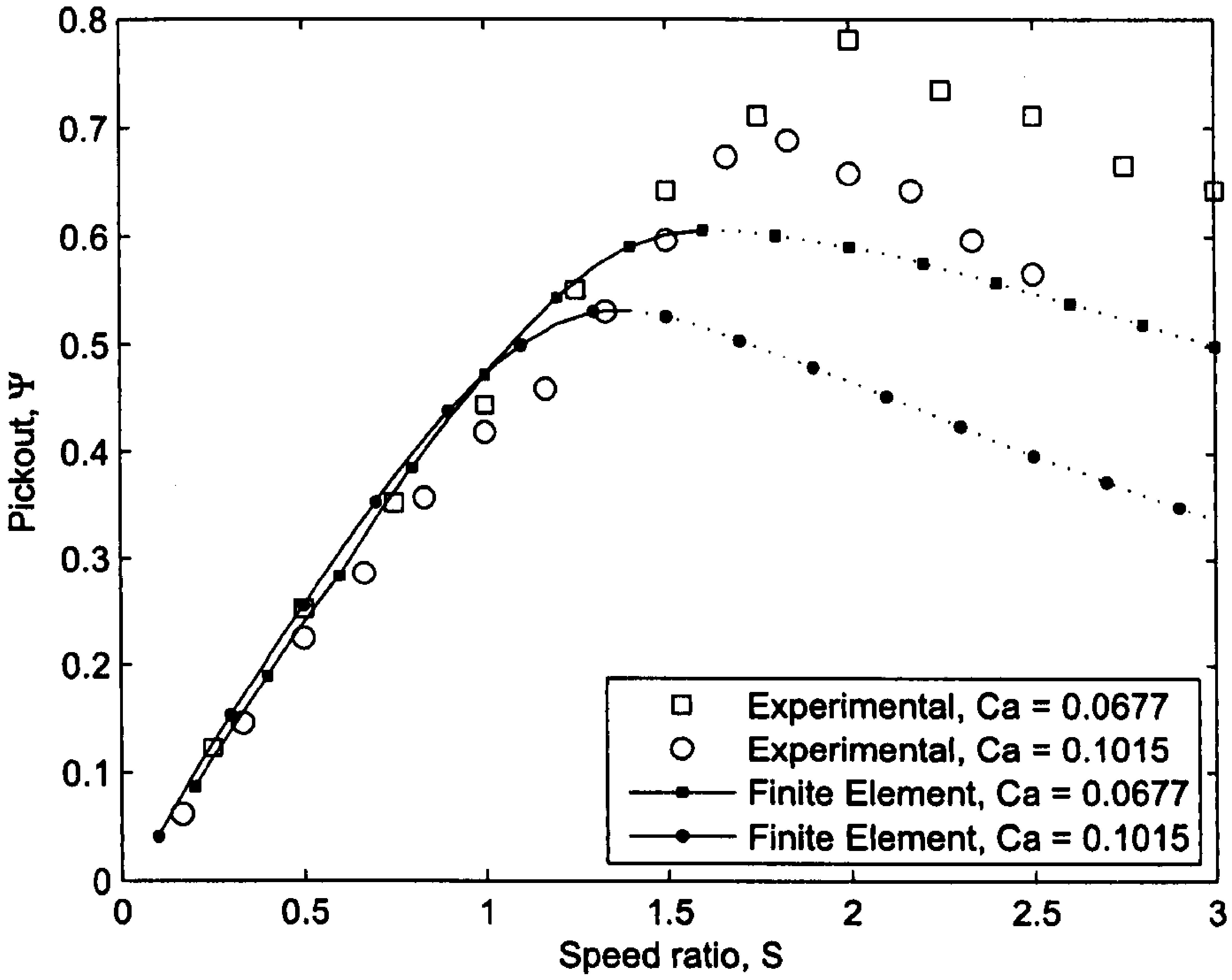

Figure 8.1: Pickout as a function of speed ratio for triangular grooves (roll E1) at a groove pitch angle of 30° and substrate wrap angle 0°. The dotted line indicates the finite element predictions shows the pickout for speed ratios greater than that for which the maximum pickout occurs.

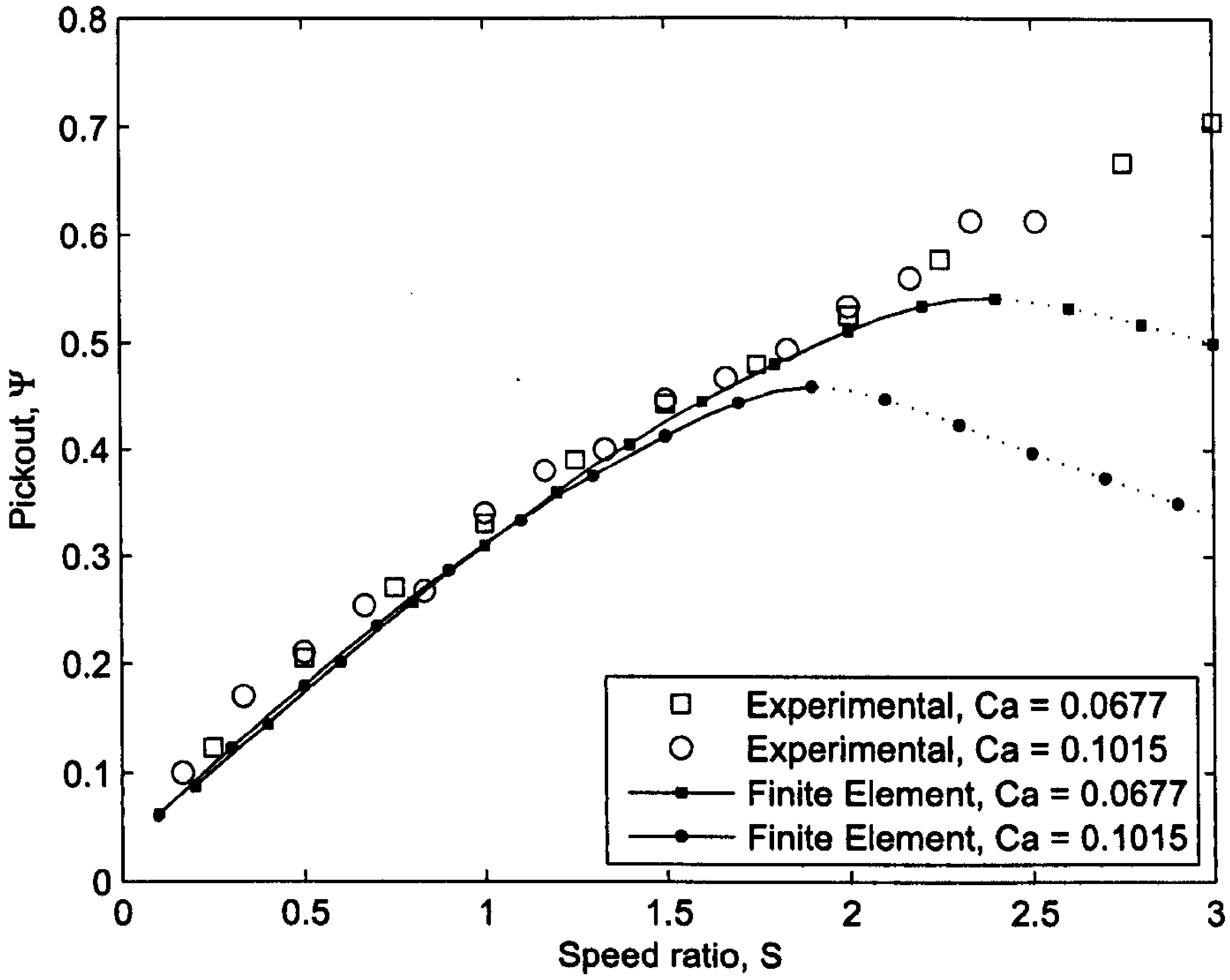

Figure 8.2: Pickout as a function of speed ratio for rectangular grooves (roll D2) at a groove pitch angle of 45° and substrate wrap angle 5°. The dotted line indicates the finite element predictions shows the pickout for speed ratios greater than that for which the maximum pickout occurs.

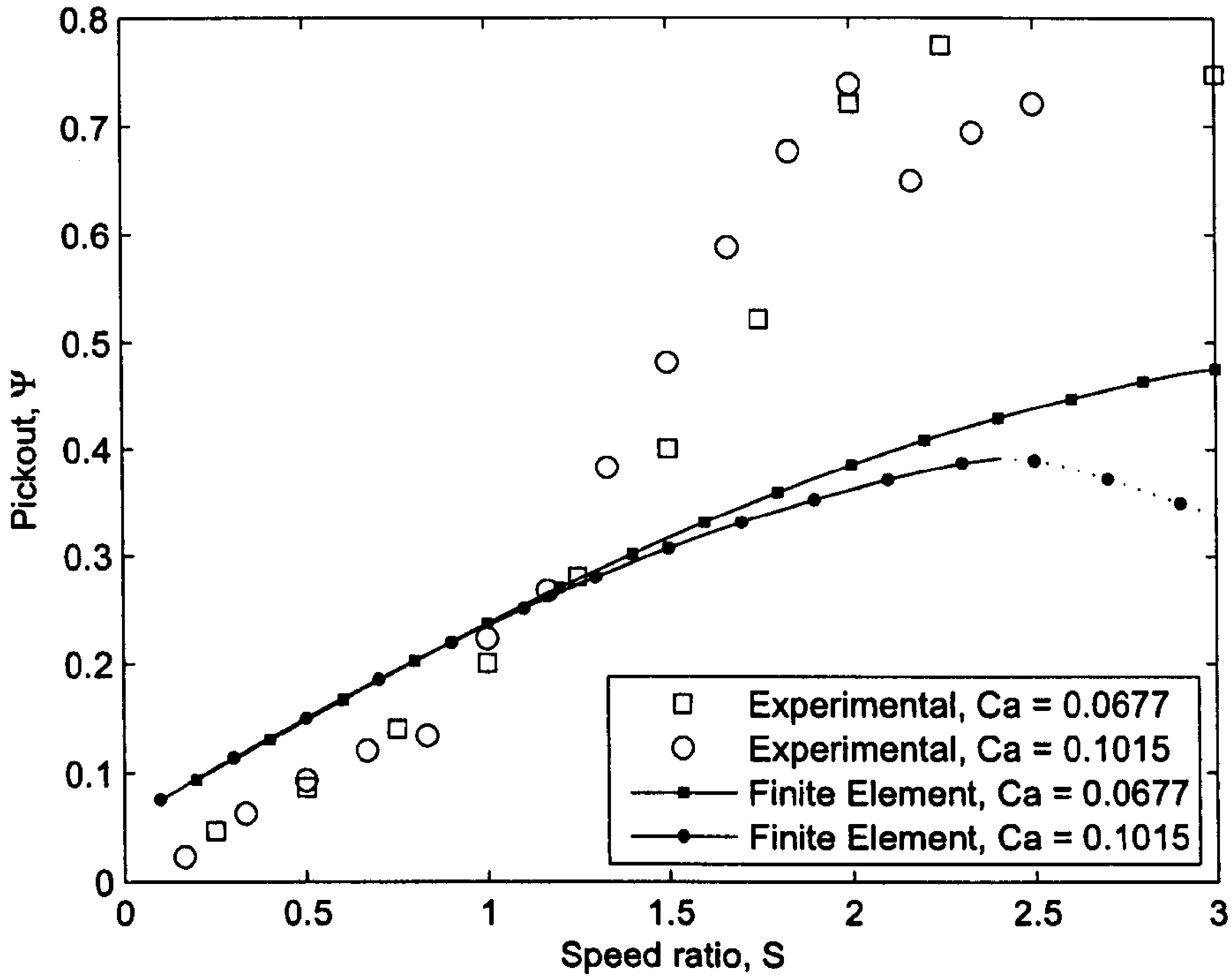

Figure 8.3: Pickout as a function of speed ratio for triangular grooves (roll E3) at a groove pitch angle of 60° and substrate wrap angle 5°. The dotted line indicates the finite element predictions shows the pickout for speed ratios greater than that for which the maximum pickout occurs.

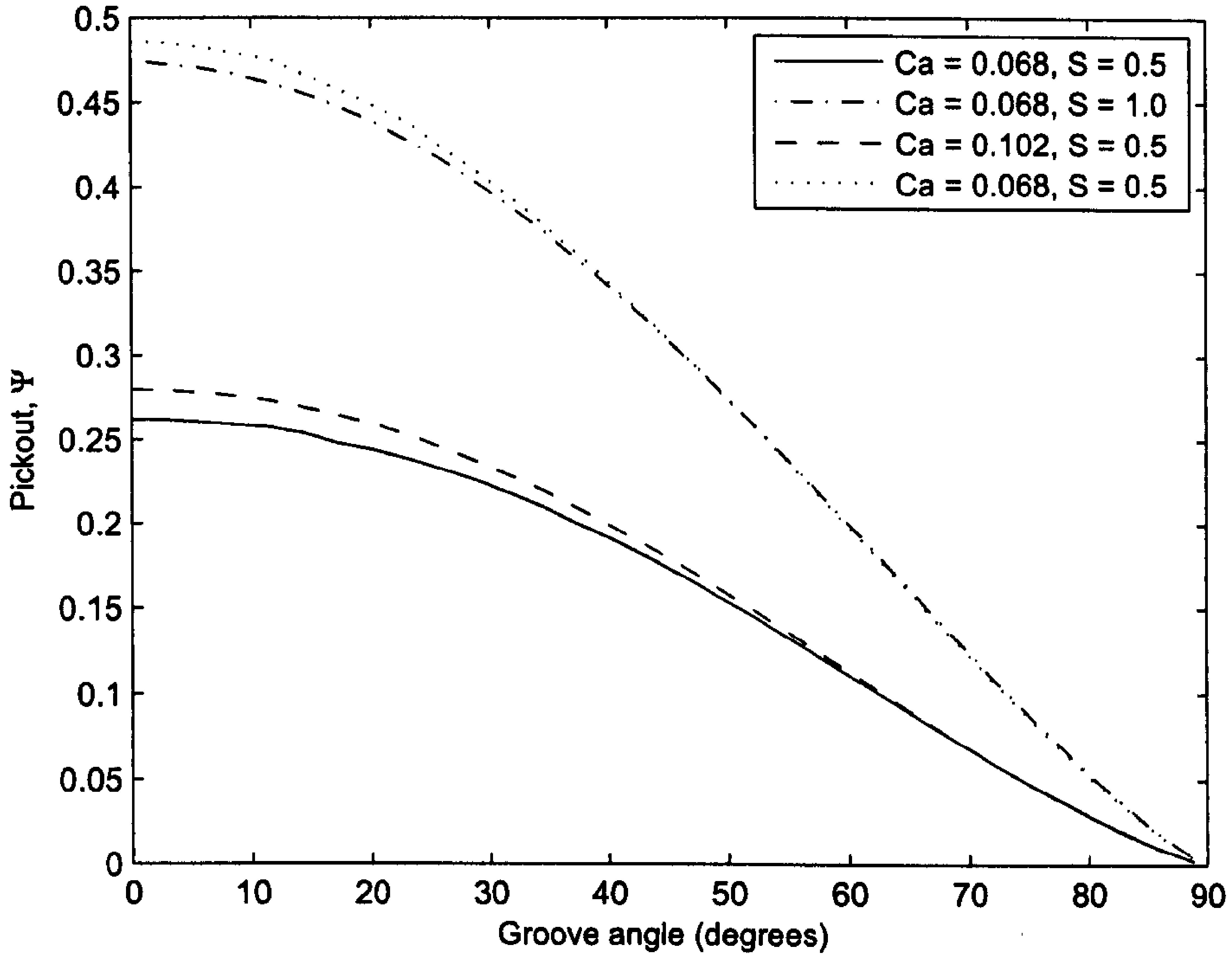

Figure 8.4: Rectangular groove angle results for grooves with a 5° substrate wrap angle

When taken together, the data from figures 8.1 to 8.3 shows that as the groove pitch increases, the pickout is reduced. The predicted pickout can be plotted as a function of groove pitch angle; this is shown in figure 8.4. The reduction in pickout with increasing pitch angle allows the coating process to operate at higher speed ratios before the onset of streaking (where the upstream meniscus passes along the grooves to the downstream side). As a final point it is observed that there is little dependence on capillary number of the pickout within the stable coating regime.

The likely explanation for the breakdown of the model as the groove pitch is increased is now analysed. The limit of the groove pitch angle going to 90° is that the grooves become discrete cells, i.e. the upstream and downstream meniscii are no longer joined by a continuous groove. In this configuration the process becomes more like a two dimensional discrete cell problem. The model is unable to predict the pickout from this configuration as inherent in the formulation is the assumption of a non-deformable web giving zero flux (which is clearly not the case).

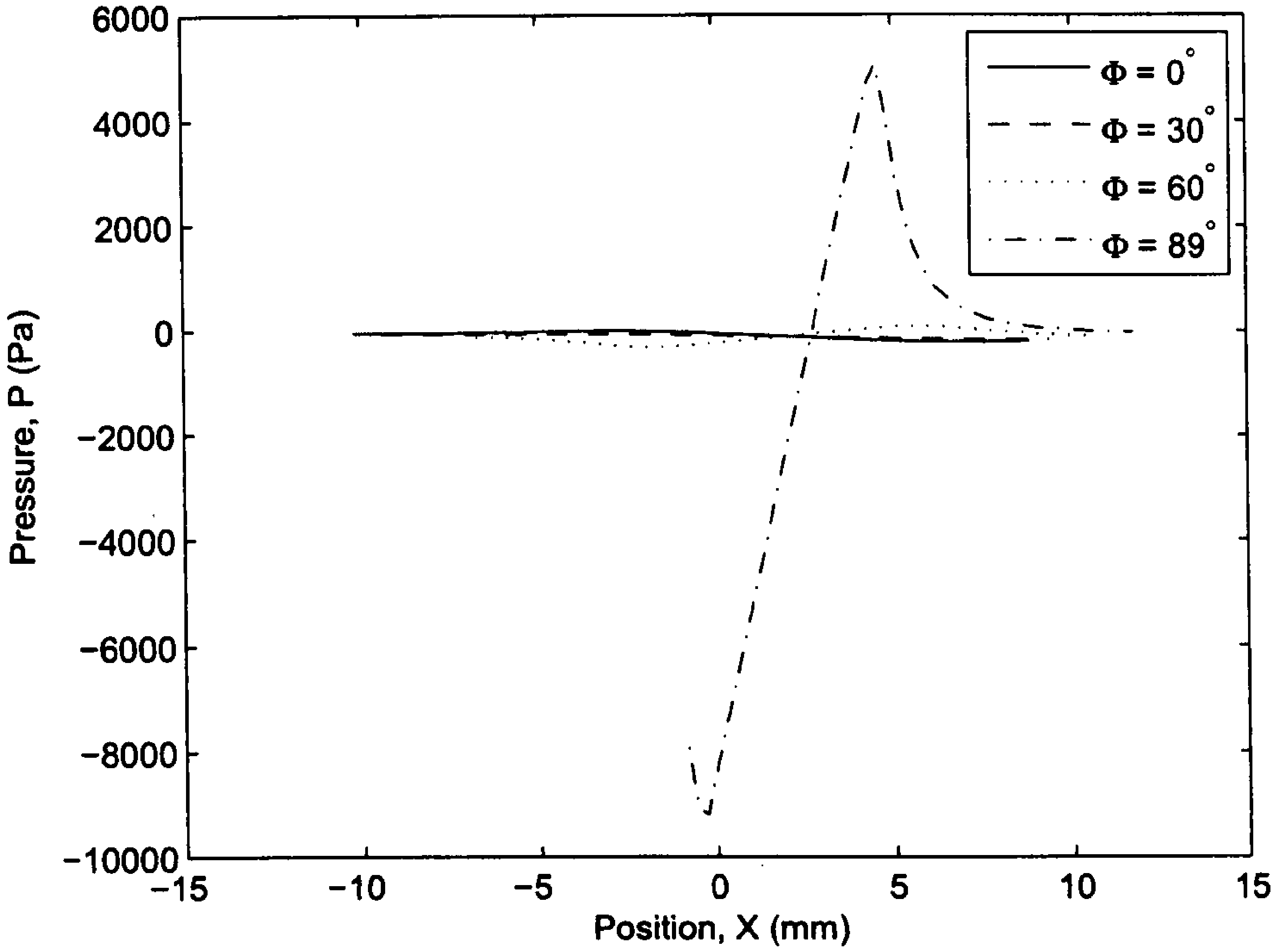

Figure 8.5: Dimensional pressure distribution throughout the coating bead as a function of pitch angle; rectangular groove width = $0.5mm$, depth = $0.5mm$ and land depth = $0.5mm$ $\mu = 0.005Pas$, $\sigma = 0.025N/m$, $\beta = 5°$

Figure 8.5 shows the predicted pressure distribution through the coating bead as the groove pitch is varied. It shows the variation for rectangular grooves with capillary number $Ca = 0.068$ and speed ratio $S = 1$. For low pitch angles the predicted pressures are entirely sub-ambient. In terms of the effect on the path of the substrate, this would effectively "suck" the web down to the roll surface with the interplay between the lands and the tension in the web effectively preventing it from being pulled into the grooves. However, for the large groove pitches there is a large positive pressure within the coating bead. This pressure will force the web away from the roll, an effect that is not captured within the model as the web is assumed to follow a predetermined path.

The pressure distributions shown in figure 8.6 show how the magnitude of the static pressure throughout the coating bead increases as the speed ratio increases, thus increasing deformation of the web. In practice, for a typical web tension of $30kg/m$ the pressure exerted by the web onto a roll of radius $0.05m$ is approximately $6,000Pa$, and for large groove pitches the pressure within the coating bead is of this order. This result not only lends weight to the hypothesis that in discrete cell gravure roll coating web deformation is an important factor in the fluid transfer mechanism, it demonstrates that web deformation is far less important in tri-helical gravure roll coating where pressures are generally sub-ambient.

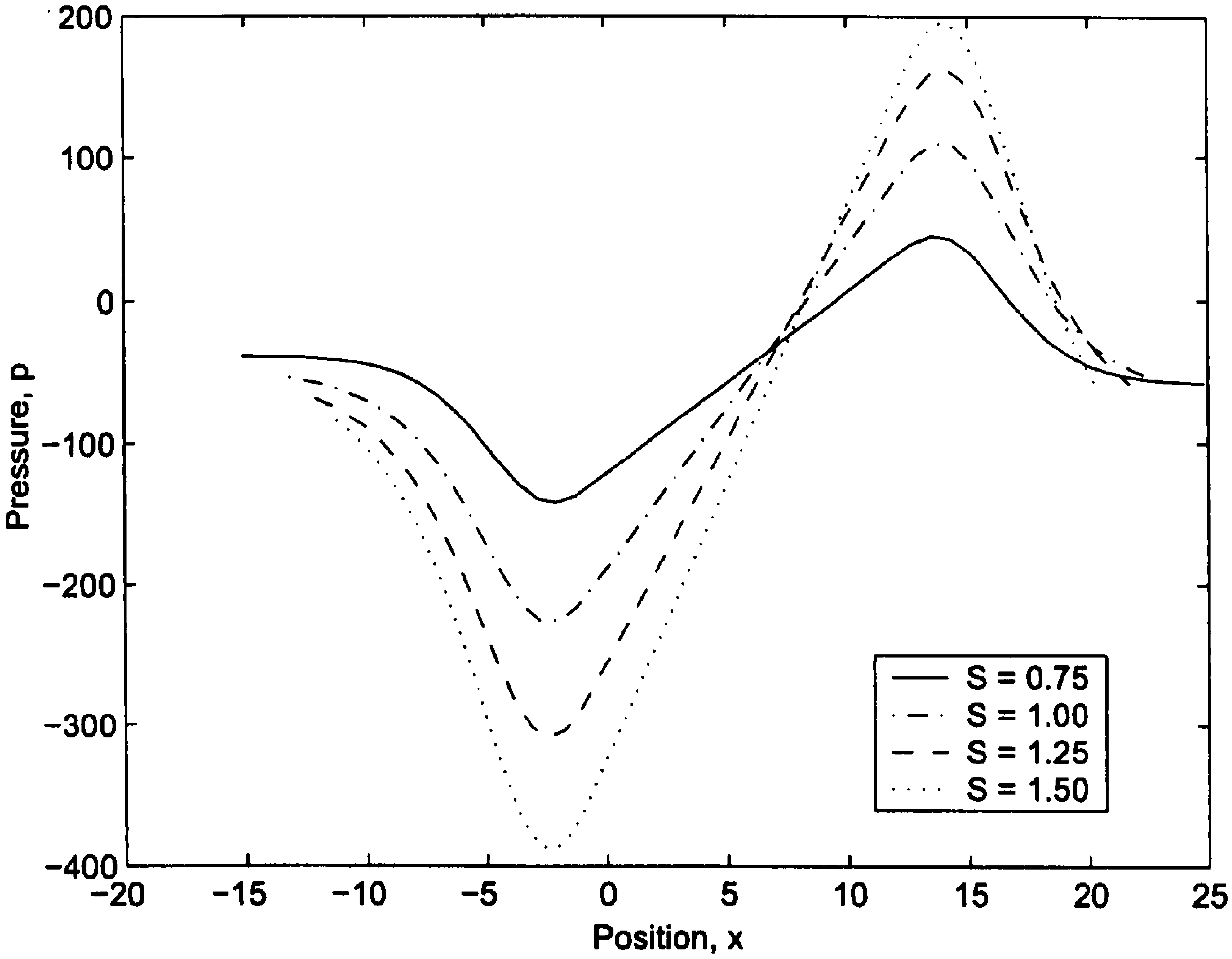

Figure 8.6: Roll E3, theoretical pressure distributions, $S = 1$, $Ca = 0.068$, wrap = 5°

8.2 Non-Newtonian Fluids Extension

In chapter 5 a model was developed for the tri-helical gravure process where the fluids had shear thinning properties that obey the power law model. This model was restricted to rolls with grooves of zero pitch since the shear rate dependent viscosity does not allow the flow to be resolved into two directions due to the complexity of the flow along the grooves. For the case of zero pitched grooves the model for shear thinning fluids managed to accurately predict the amount of fluid picked out of the grooves and transfered to the web. Predictions from this model together with experimental results are shown in figures 8.7 and 8.8.

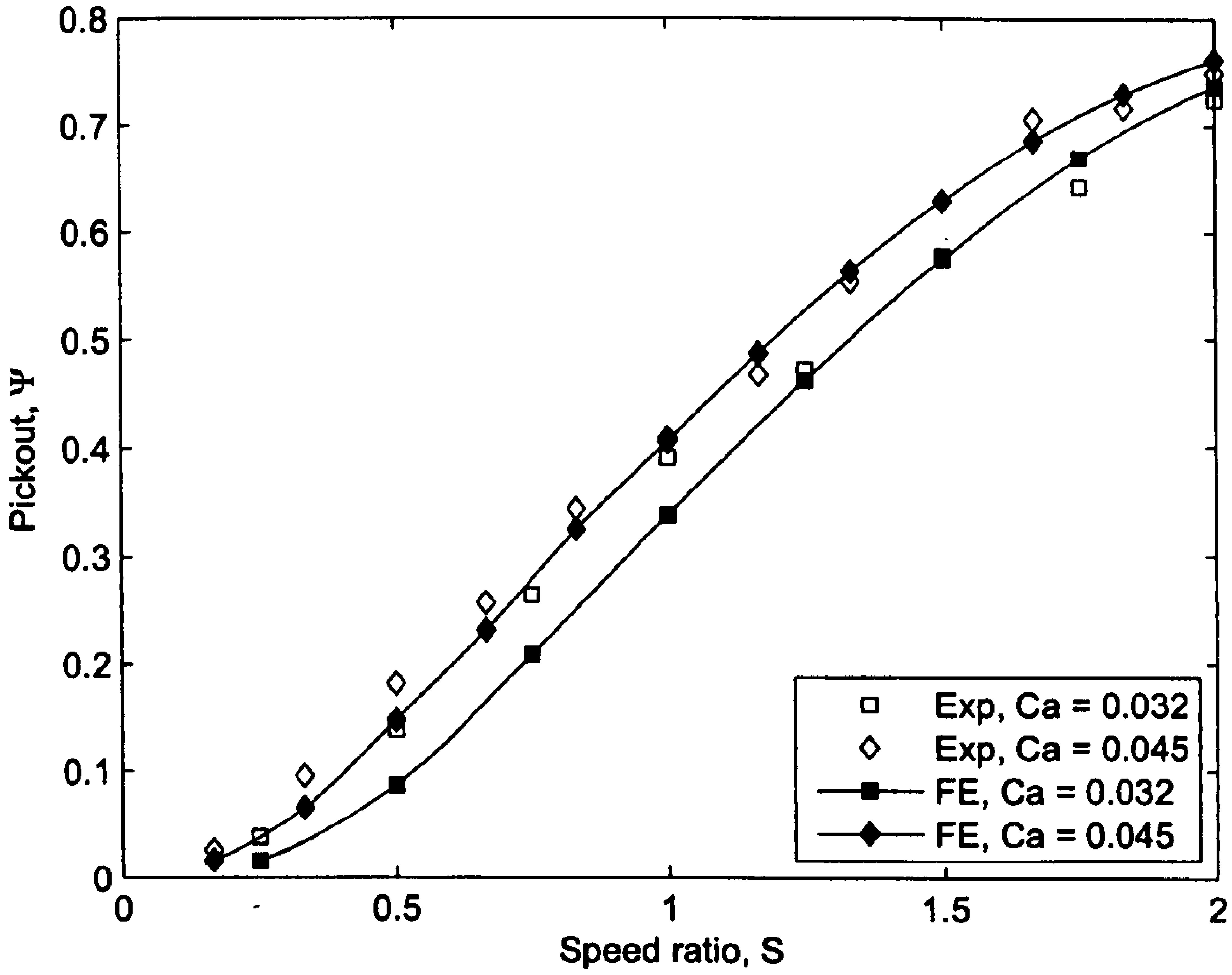

Figure 8.7: Pickout as a function of speed ratio for non-Newtonian fluids; Roll C2, wrap angle 0°, power law index $n = 0.84$

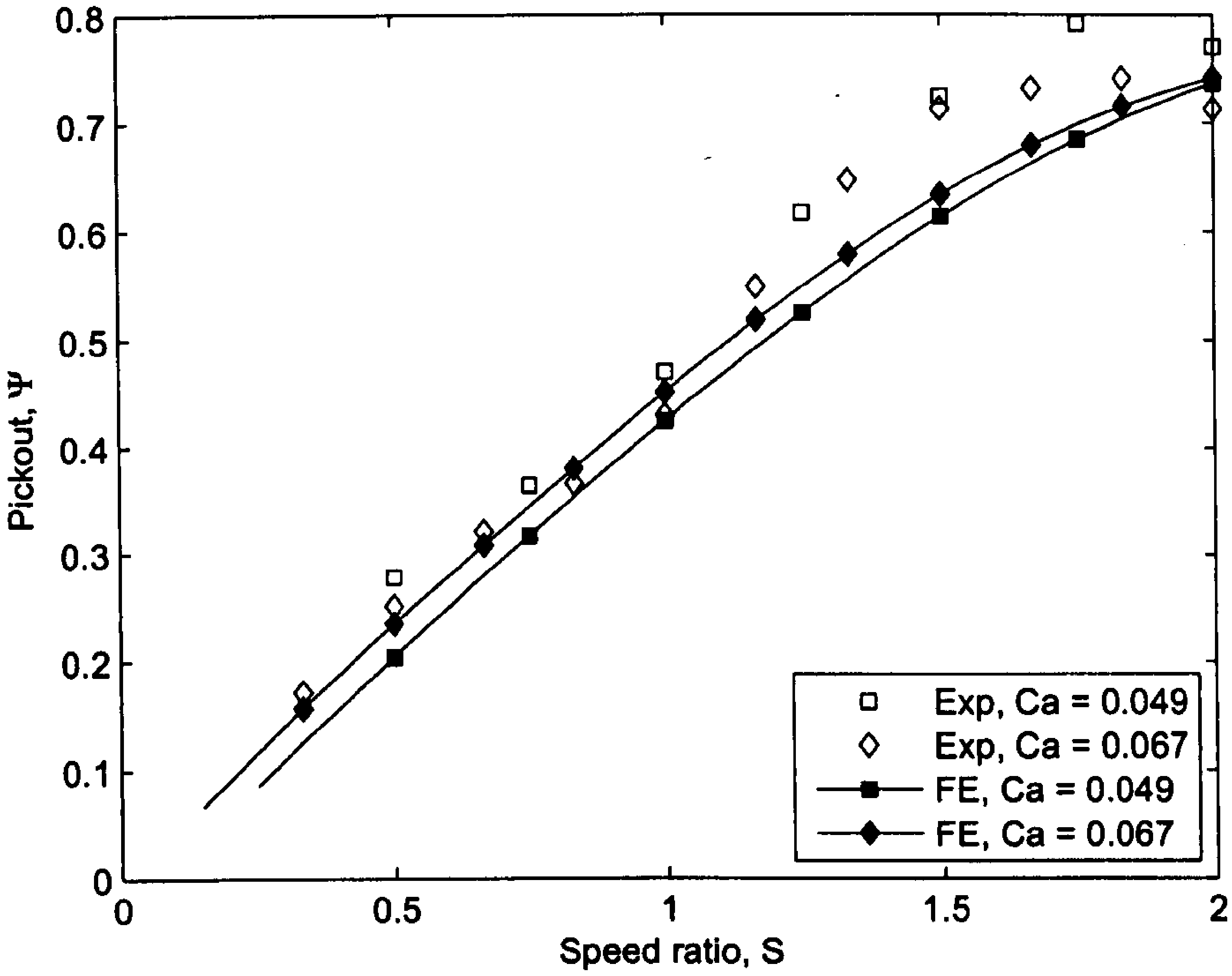

Figure 8.8: Pickout as a function of speed ratio for non-Newtonian fluids; Roll B4, wrap angle 5°, power law index $n = 0.75$

Except at low speed ratios, the figures reveal a similar pattern to that found for Newtonian fluids, showing a linear increase in pickout with the speed ratio up to a value of around $S = 1.2$ at which point streaking is observed. It should be noted that the use of a fixed dynamic contact angle of 90° no longer gives a decrease in the predicted pickout as the speed ratio increases, due to the dynamic contact angle being independent of the web capillary number ($Ca_{\text{web}} = |S|\,Ca$). As for Newtonian fluids, the dynamic contact angle was not found to alter greatly the predicted pickout within the stable coating regime.

At low speed ratios, the linear speed ratio - pickout relationship tends towards a very small negative pickout or a slight positive pickout. For some of the lower viscosity results this effect is more predominant (as seen in figure 8.7). This produces a quadratic type pickout curve as shown in figure 8.7. The reason for this may be that the high shear rates experienced in the region in or close to the web-to-roll contact lead to very low viscosities where the pressure gradients are at their greatest. This may result in the positive pressure gradients from the downstream to upstream meniscus having a greater effect on pickout.

Chapter 9

Groove Geometry of Different Cross-Section Results

9.1 Introduction

Parameters such as the speed ratio and capillary number have been examined both analytically and experimentally in previous chapters, the model for tri-helical gravure roll coating with Newtonian fluids is now used to explore the effect of changing the cross-sectional groove geometry.

9.2 Groove Aspect Ratio

A parametric study into the effect of aspect ratio on pickout and film thickness is presented. To do this the groove cross-sectional area is kept constant for a given change in the groove aspect ratio. Since dimensions are scaled with groove width, as the aspect ratio is varied the remaining parameters have to be scaled accordingly. The dimensions in table 9.1 were used to obtain the non-dimensional variables β, l, r_{roll} and r from the following equations where A was varied from

$A \times R$	$0.5mm^2$
R_{roll}	$50mm$
β	5°
$A + L$	$1mm$
θ_A	74°
Φ	0 and 45°

Table 9.1: Roll dimensions for groove aspect ratio studies

0.4 to 0.9:

$$r = \frac{0.5}{A^2}, \tag{9.1}$$

$$l = \frac{1}{A} - 1, \tag{9.2}$$

$$r_{\text{roll}} = \frac{50}{A}. \tag{9.3}$$

Figures 9.1 and 9.2 show typical results from the model where pickout is given as a function of groove aspect ratio for groove pitch angles of 0° and 45°. These figures show that as the groove aspect ratio increases (i.e. the grooves get narrower and deeper) then, as expected, the pickout falls. Since the fluid volume entering the coating bead is constant for a range of aspect ratios, the film thickness is directly proportional to pickout and is given on the secondary y-axis.

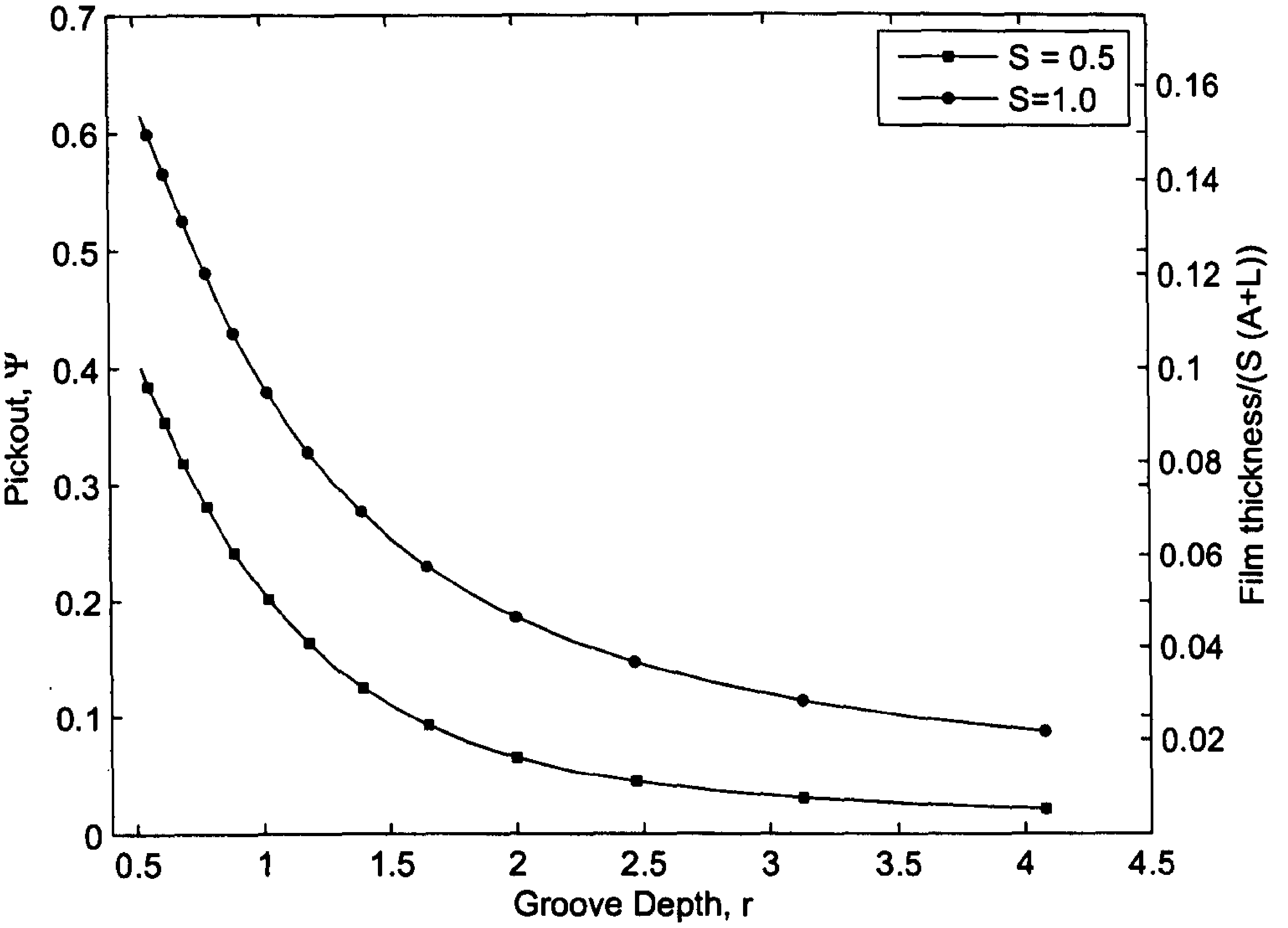

Figure 9.1: Pickout as a function of groove aspect ratio for the case of $\beta = 0°$, $\Phi = 0°$, Static Contact Anlge, $\theta_A = 45°$.

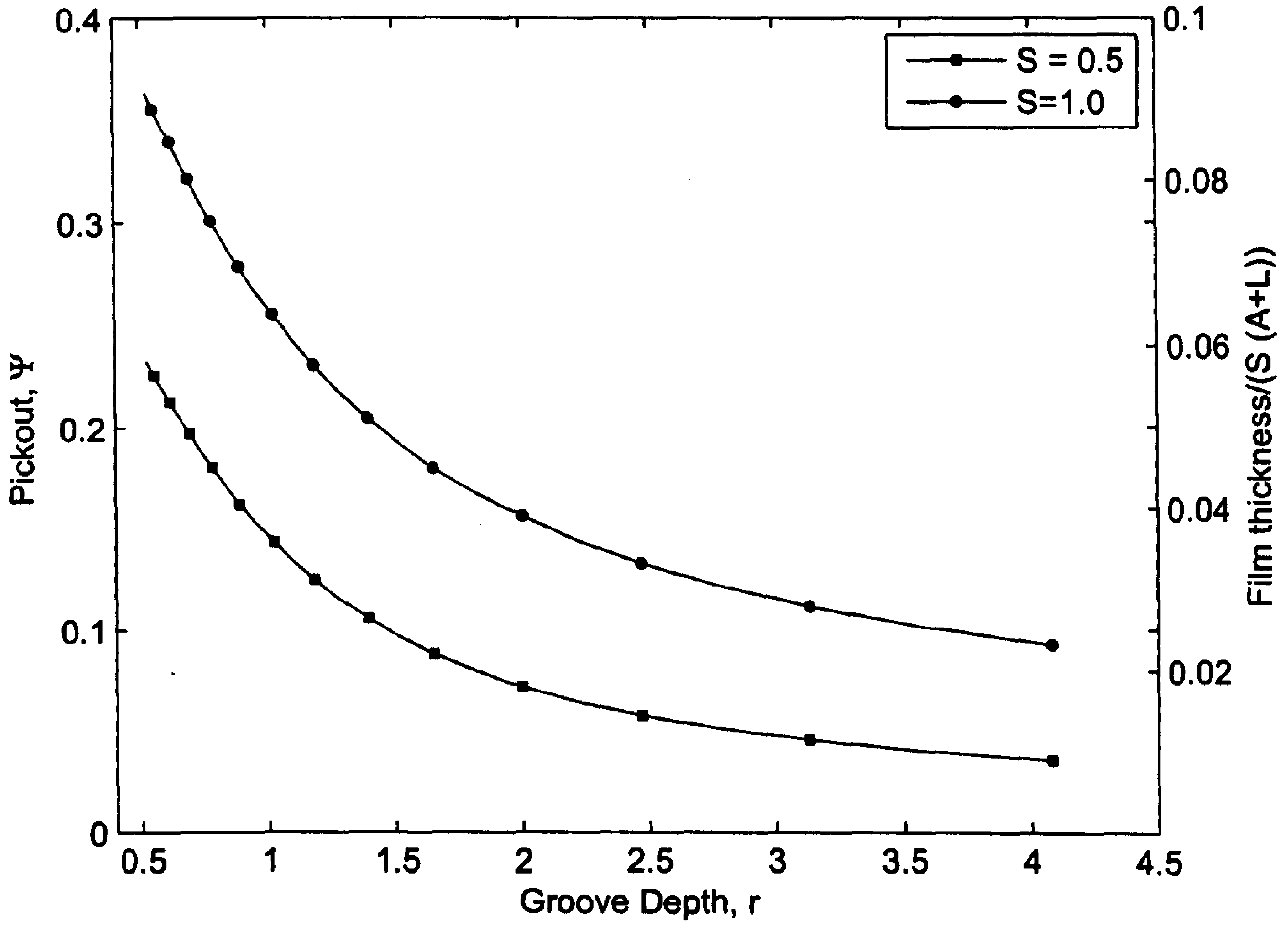

Figure 9.2: Pickout as a function of groove aspect ratio for the case of $\beta = 0°$, $\Phi = 45°$, Static Contact Anlge, $\theta_A = 45°$.

As the model is unable to predict the onset of streaking care must be taken when examining the results shown in figures 9.1 and 9.2; streaking may occur in practice for low groove depths - it is for this reason that speed ratios above $S = 1$ are not shown.

9.3 Groove Depth

The effect of increasing groove depth is also examined. Increasing the groove depth without reducing the groove width means that the volume of fluid entering the coating bead increases; figures 9.3 and 9.4 show that as the groove depth increases the pickout decreases. This is in line with the results of section 9.2, the motion of the web having a diminishing influence on the fluid at the base of a groove as the depth increases. This effect is observed for both grooves of zero pitch and the more industrially representative 45° pitched grooves.

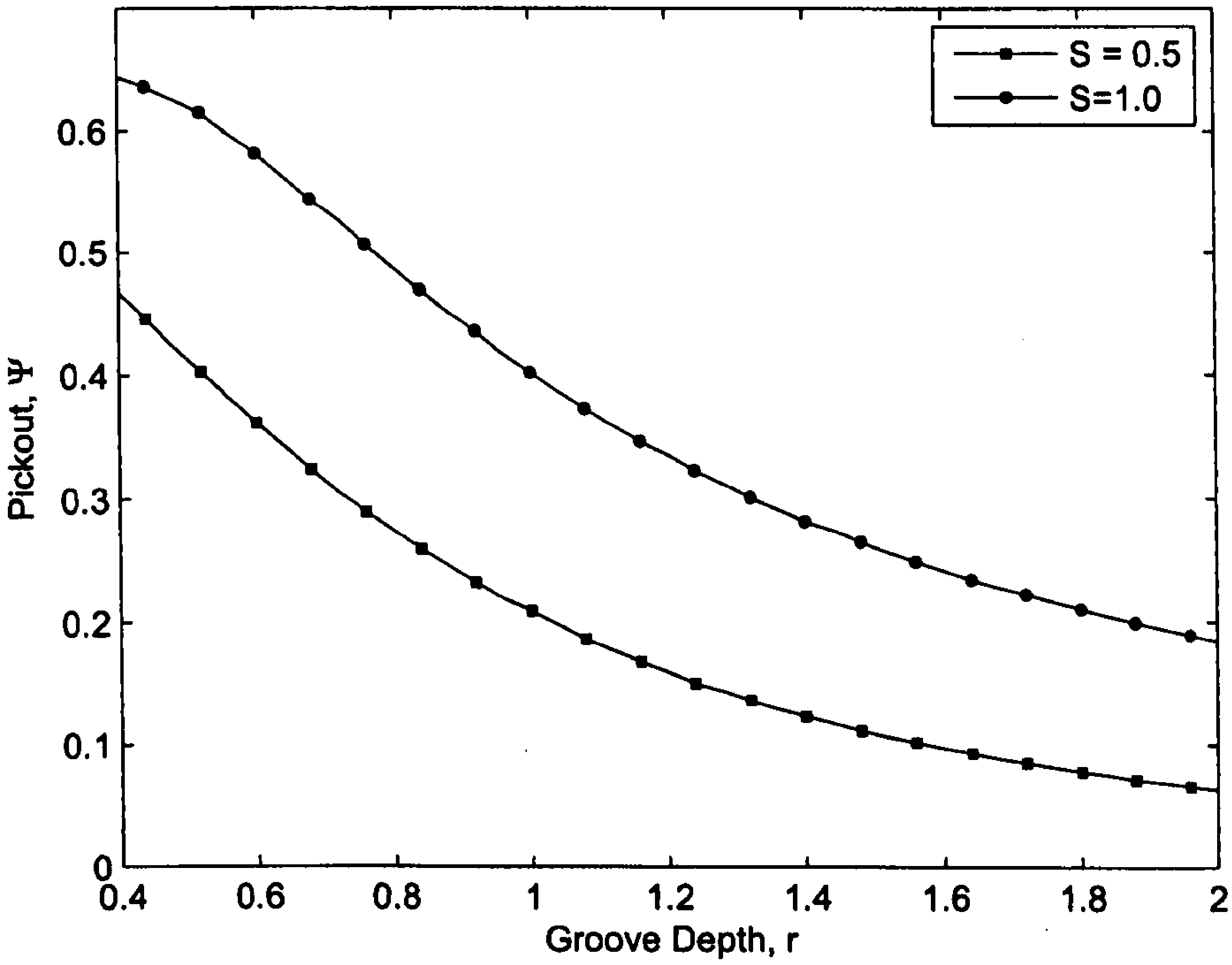

Figure 9.3: Pickout as a function of groove depth for the case of rectangular grooves, Wrap Angle, $\beta = 5°$, Static Contact Anlge, $\theta_A = 45°$, $\Phi = 0°$

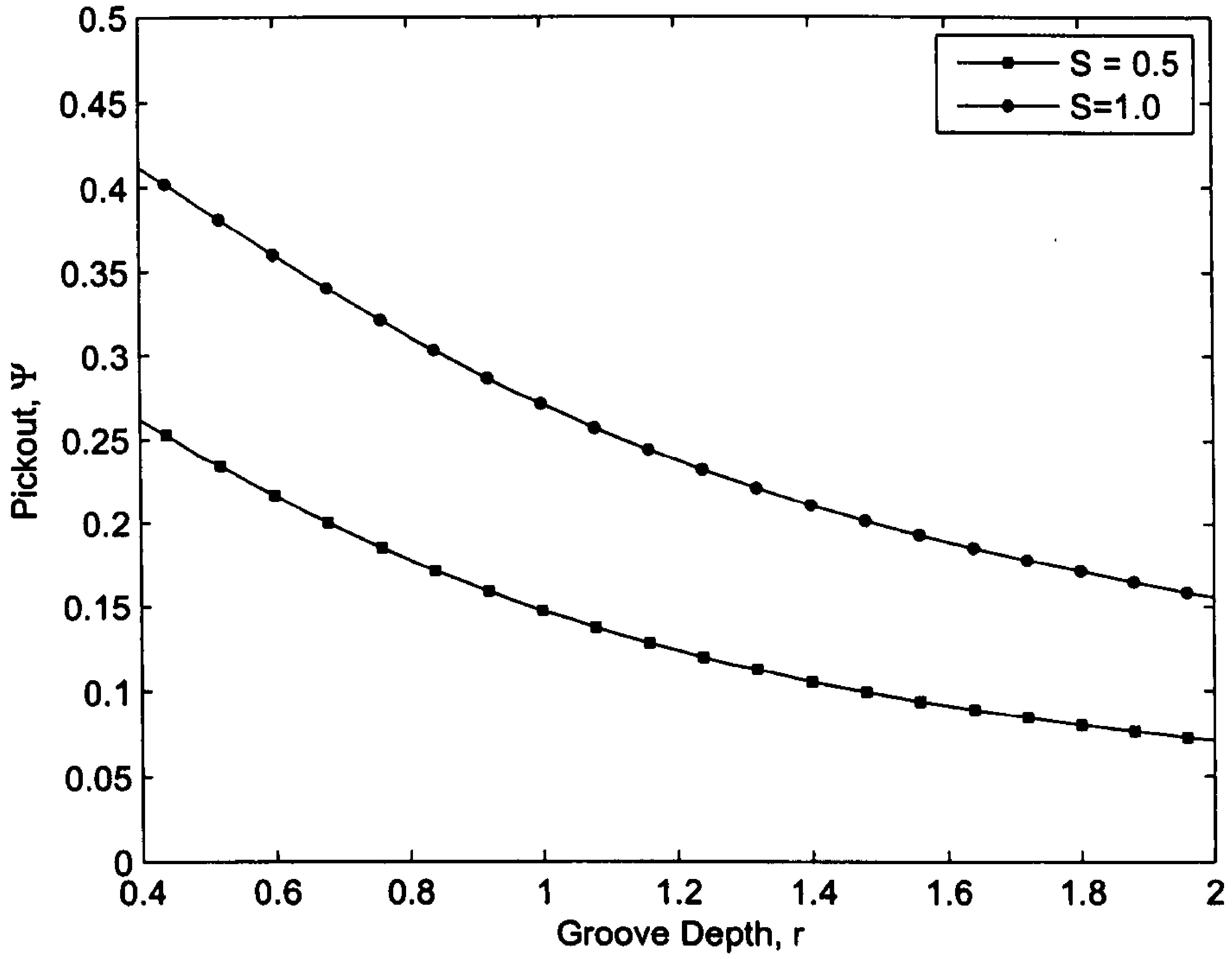

Figure 9.4: Pickout as a function of groove depth for the case of rectangular grooves, Wrap Angle, $\beta = 5°$, Static Contact Anlge, $\theta_A = 45°$, $\Phi = 45°$

The effect of groove depth on the film thickness deposited onto the web is influenced not only by the pickout from the grooves but also by the volume of fluid entering the coating bead (which clearly increases as groove depth does). Although the pickout decreases as the groove depth increases, the greater volume of fluid entering the coating bead leads to an increase in film thickness deposited (as shown in figures 9.5 and 9.6) followed by a fall in film thickness as the groove depth increases further. This decrease in film thickness can be attributed to the pressure driven flow within the coating bead. For bigger groove depths the pressure distribution between the two bounding menisci is such that there is an additional pumping of fluid from the downstream to the upstream side, resulting in a decrease in the film thickness.

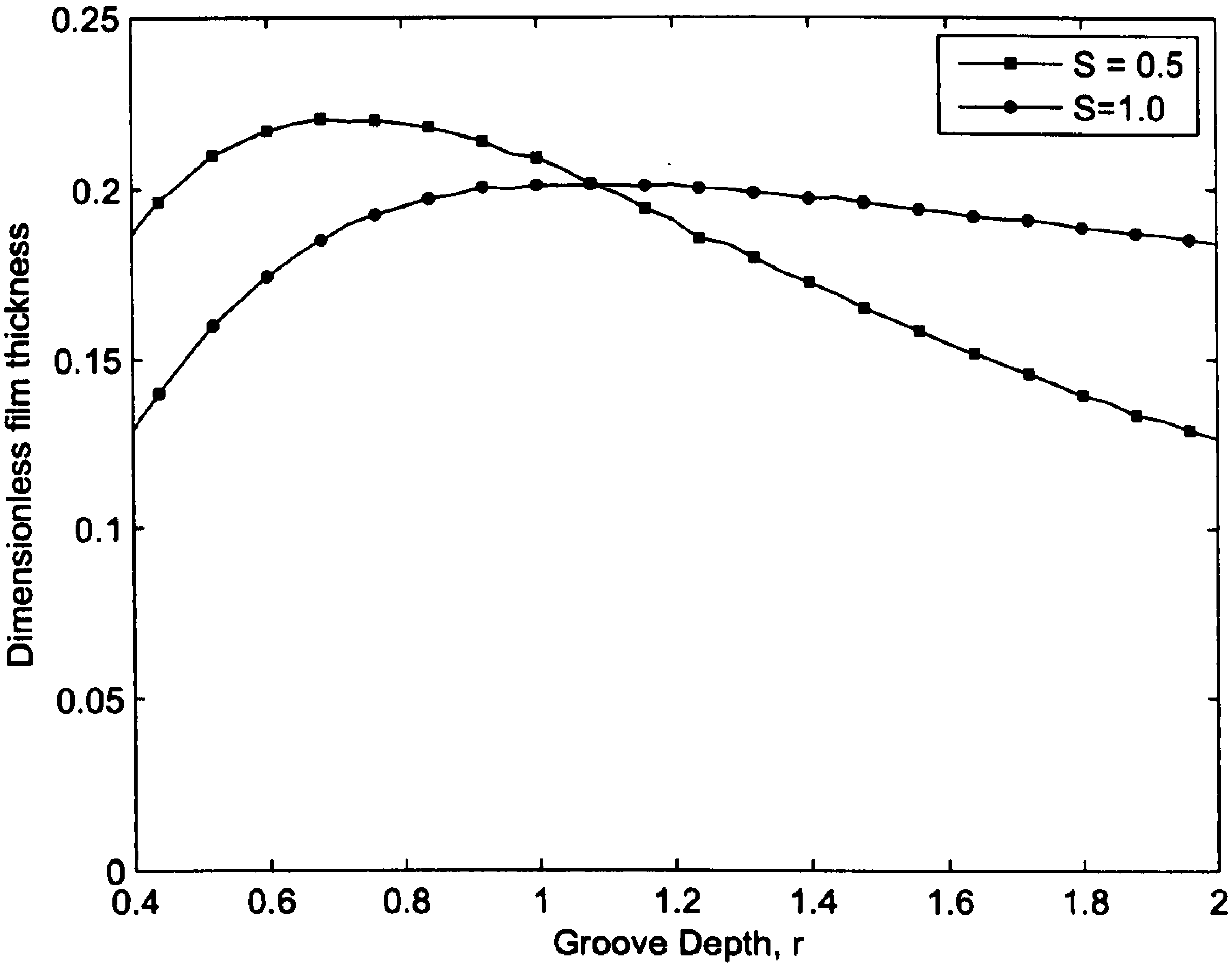

Figure 9.5: Rectangular Grooves, Roll radius, 50, Wrap Angle, $\beta = 5°$, Static Contact Angle, $\theta_A = 45°, \Phi = 0°$

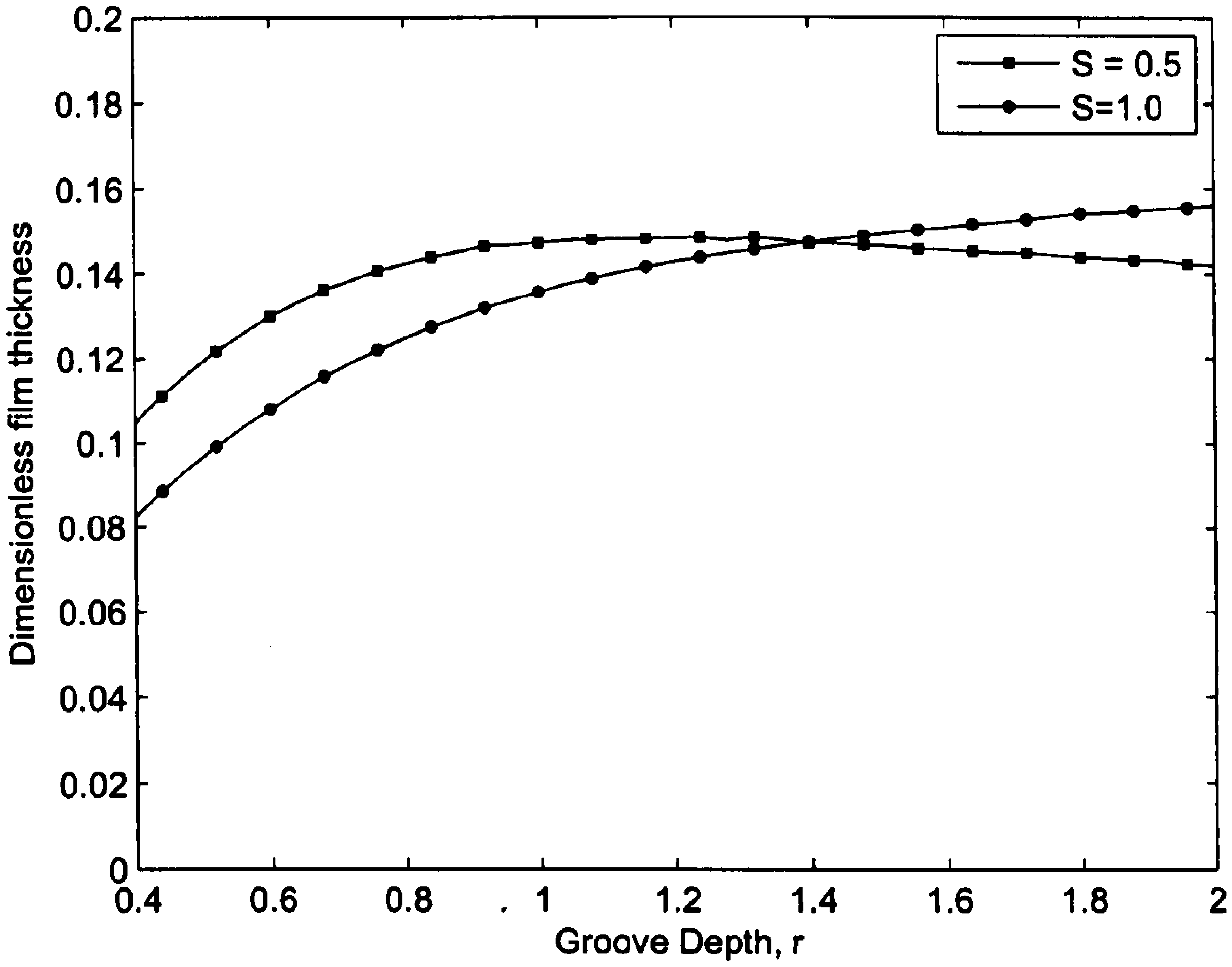

Figure 9.6: Rectangular Grooves, Roll radius, 50, Wrap Angle, $\beta = 5°$, Static Contact Angle, $\theta_A = 45°$, $\Phi = 45°$

This is illustrated in figure 9.7 which shows the typical velocity profile along the groove centreline for four different groove depths. The "bulge" in the velocity profile shows the increase in velocity, resulting in a tube of fluid moving within the groove with a velocity greater than that of the roll, thereby reducing the film thickness.

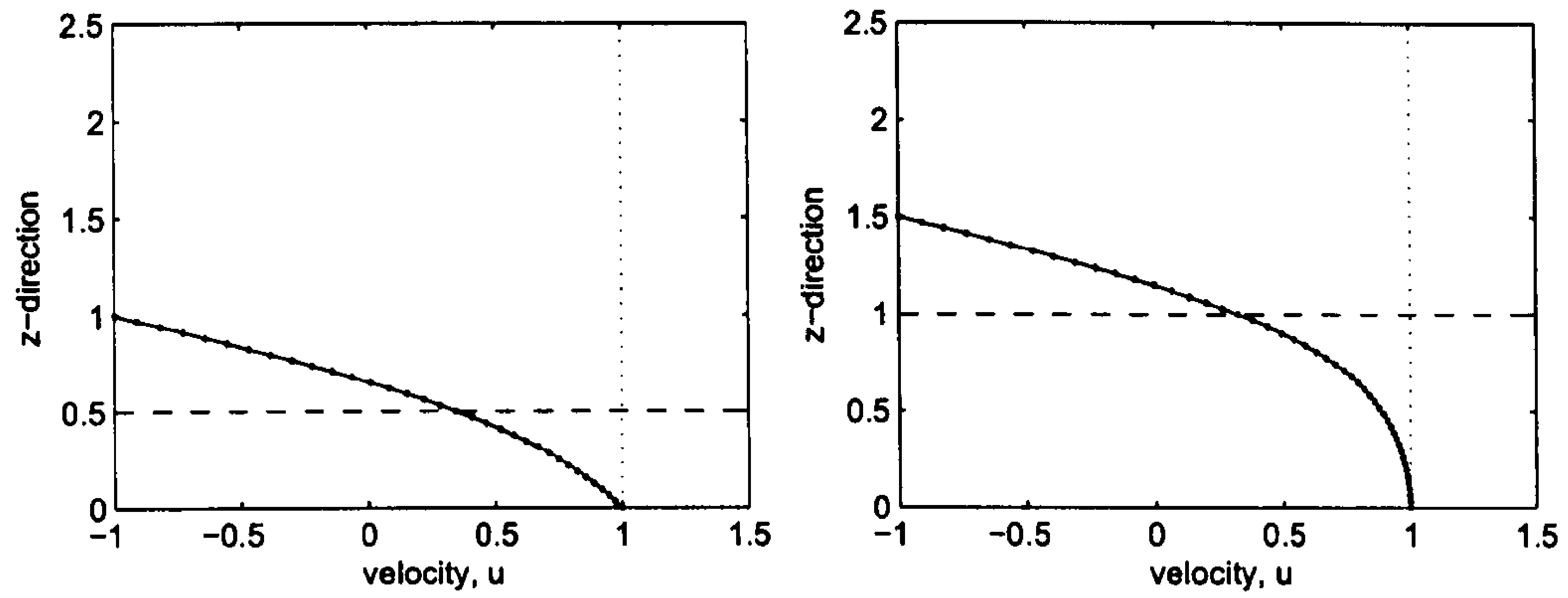

(a) $R = 0.5$

(b) $R = 1.0$

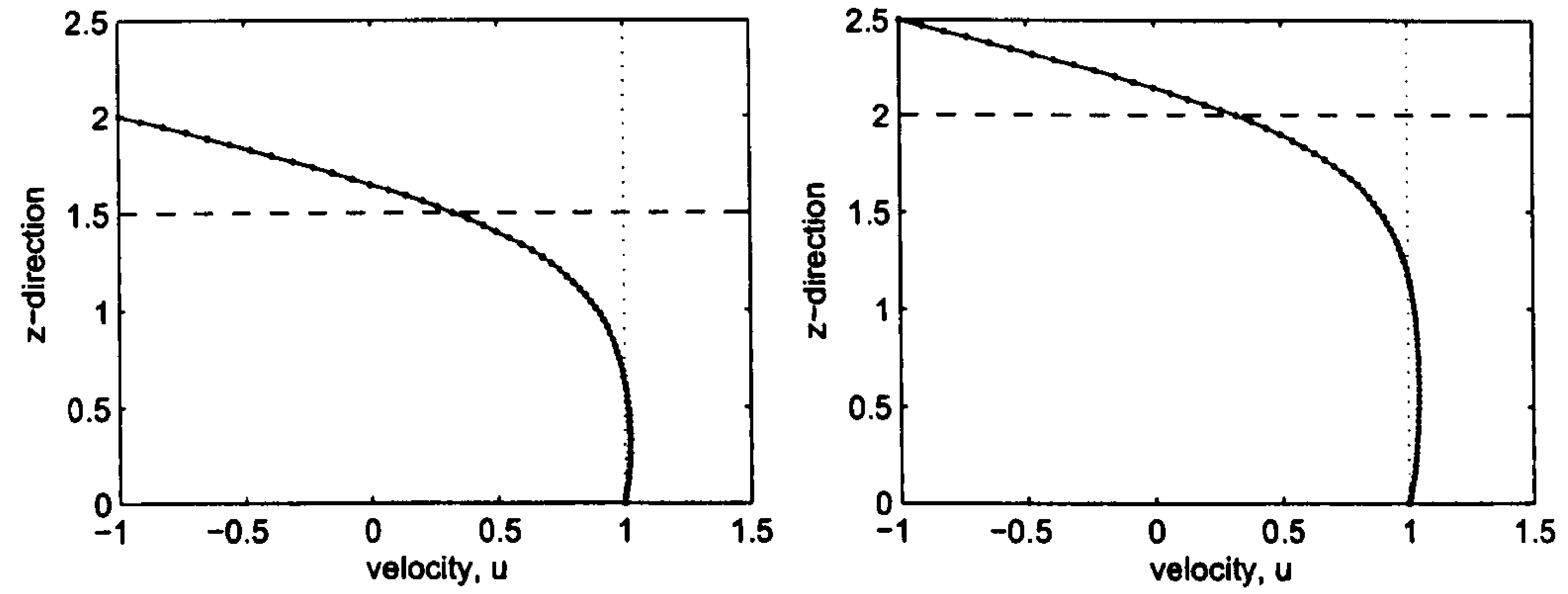

(c) $R = 1.5$

(d) $R = 2.0$

Figure 9.7: Velocity distribution taken down the centre of groove along the z-direction for different groove depths. Dotted lines $(\cdots)$ show roll velocity, dashed lines $(--)$ show the roll's land position. ($l = 1, b = 1, d = 0.5, S = -1, \frac{dp}{dx} = -0.5$)

Figures 9.7(c) and 9.7(d) clearly show the velocity within the groove increasing as the groove depth increases. The reason the decrease is delayed from $r = 0.7$ to $r = 1.2$ from a zero angle to one of 45° is due to the pressure gradients within the coating bead. As shown in section 8.1, as the pitch angle increases the relatively high pressures at the downstream meniscus decrease and the relatively low pressures at the upstream meniscus increase, reducing the pressure gradients from the downstream meniscus to the upstream side, thereby giving less pressure driven pumping.

9.4 Groove Shape

The finite element code described in chapter 5 is used to calculate the flow along a range of symmetric groove cross sections - rectangular, triangular and semi-circular.

9.4.1 Triangular to Rectangular Grooves

The effect of systematically changing the groove shape from that of rectangular, through trapezoidal to triangular is examined, as shown in figure 9.8.

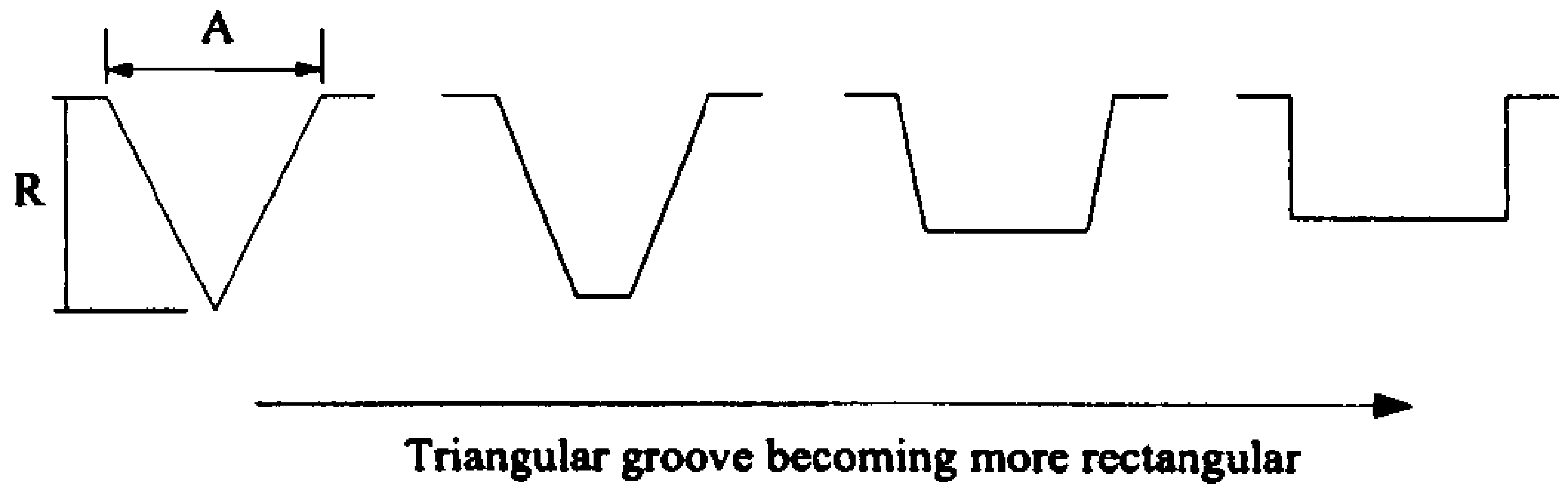

Figure 9.8: Triangle to rectangle groove geometry transformation

The width of groove opening (A) is kept constant by varying the groove depth as the width of the groove base is changed. For the geometries explored there is a clear decrease in pickout and film thickness as the grooves become more triangular in shape, as shown in figures 9.9 and 9.10, for grooves pitched at 0° and 45° respectively. The increased pickout for rectangular grooved rolls is due to the greater motion imparted to the fluid by the web due to the shallower groove geometry.

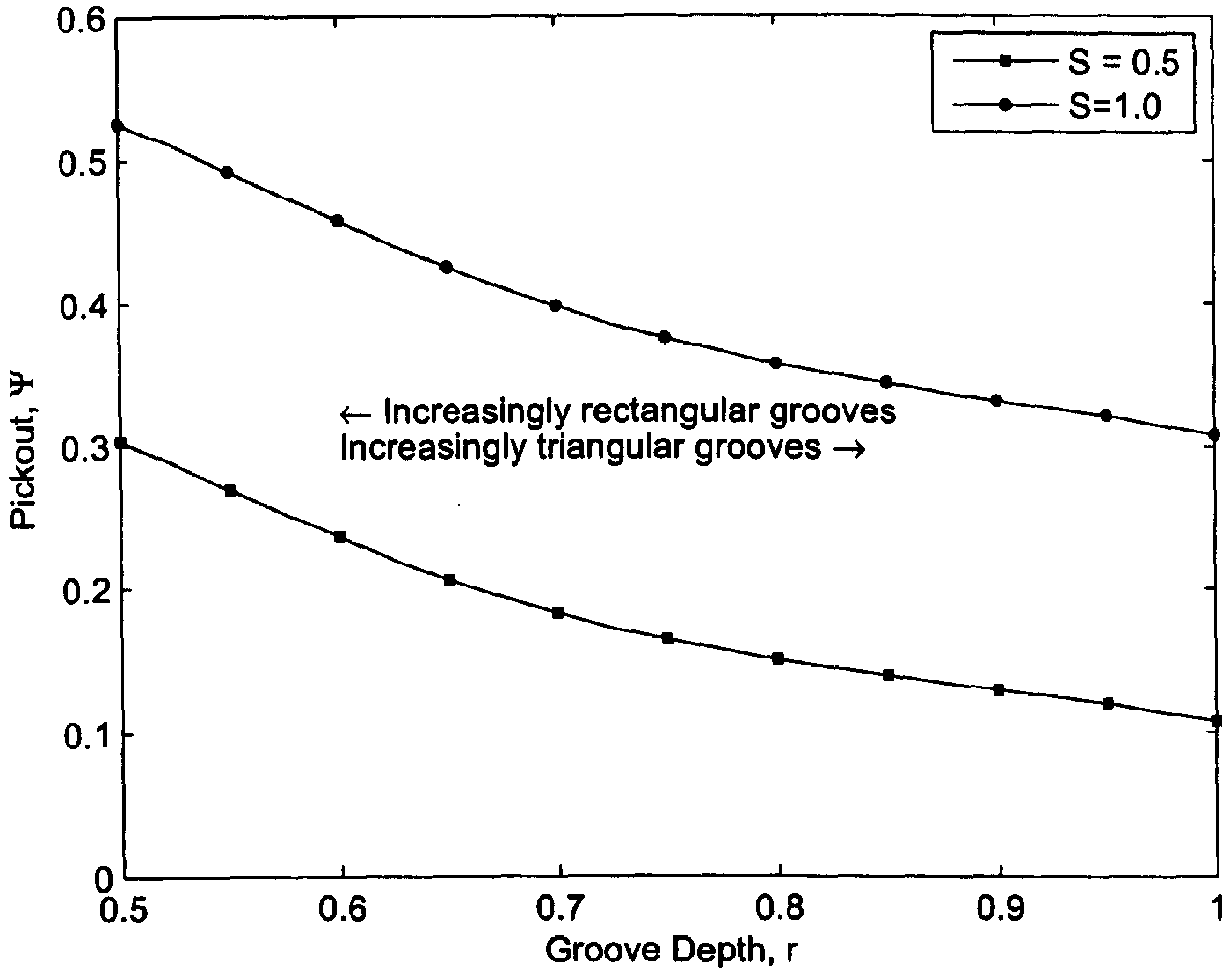

Figure 9.9: Roll Radius, $r_{\text{roll}} = 50$, Wrap Angle, $\beta = 5°$, Static Contact Angle, $\theta_A = 60°$, $\Phi = 0°$.

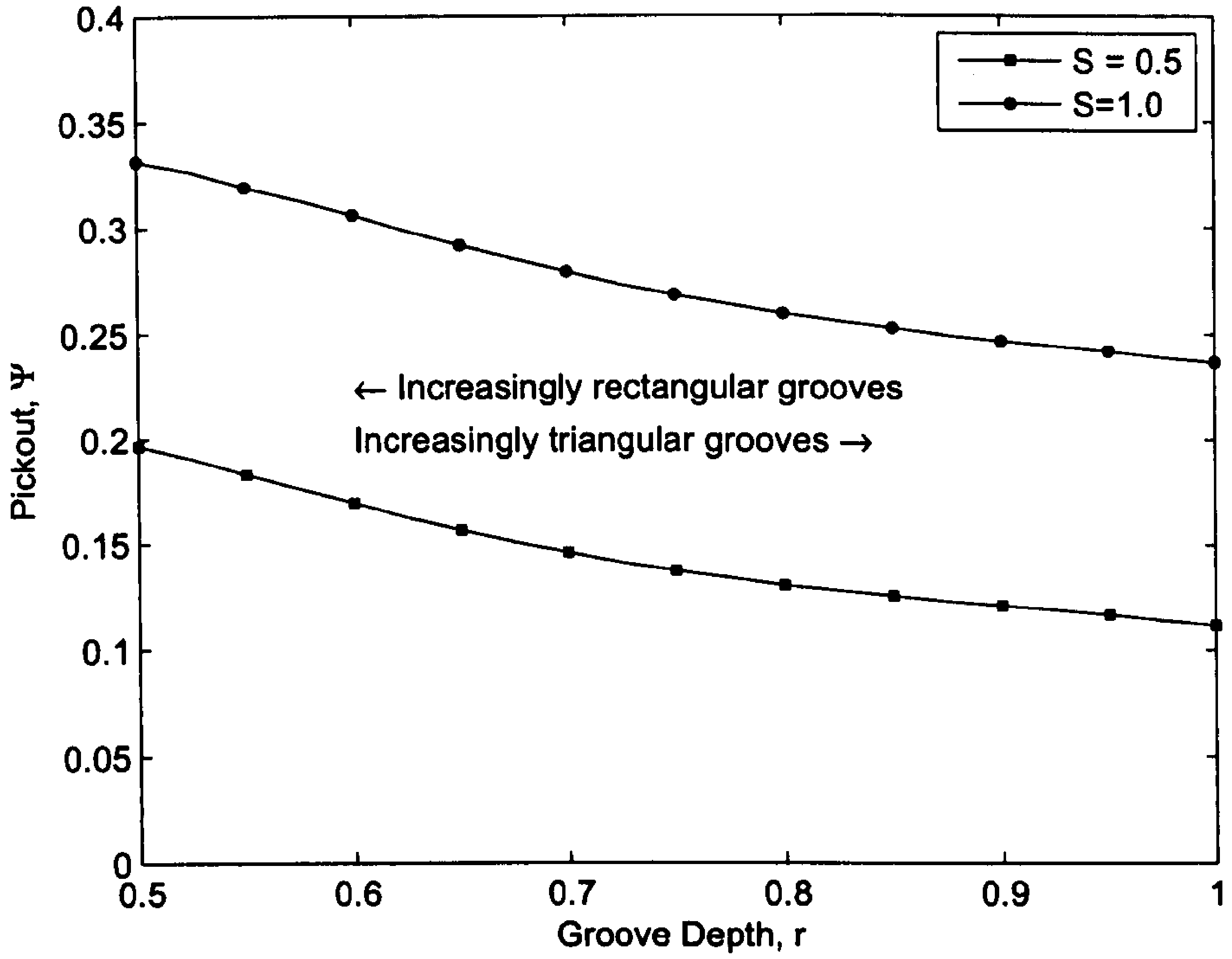

Figure 9.10: Roll Radius, $r_{\text{roll}} = 50$, Wrap Angle, $\beta = 5°$, Static Contact Angle, $\theta_A = 60°$, $\Phi = 45°$.

A further interesting result is the variation of film thickness with groove geometry as shown in figures 9.11 and 9.12. It can be clearly seen that the film thickness for $S = 0.5$ and $S = 1$ cross, highlighting the complex relationship between film thickness and speed ratio , and suggesting that it may be possible to design rolls to give constant film thicknesses for a range of speed ratios.

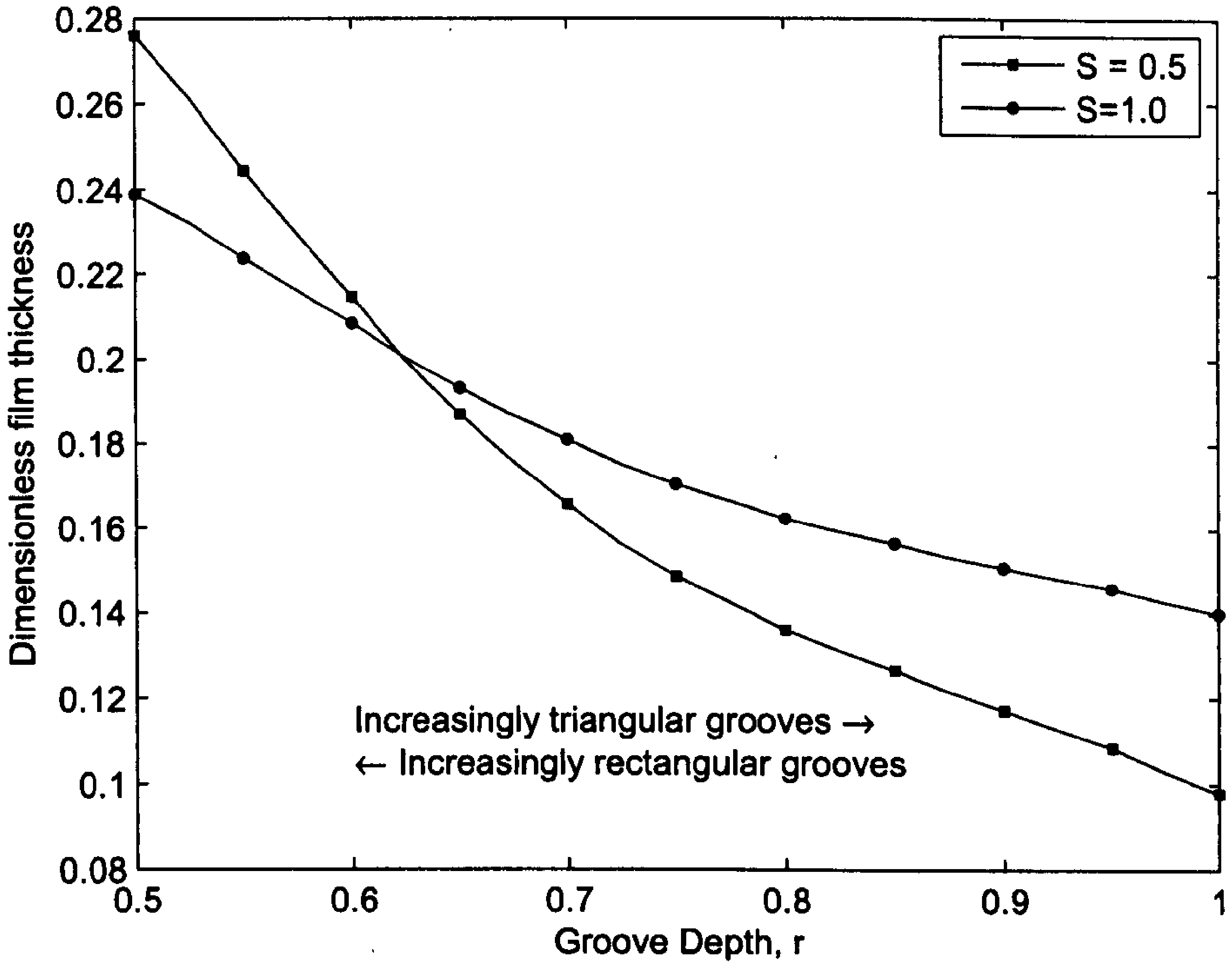

Figure 9.11: Roll Radius, $r_{\text{roll}} = 50$, Wrap Angle, $\beta = 5°$, Static Contact Angle, $\theta_A = 60°$, $\Phi = 0°$.

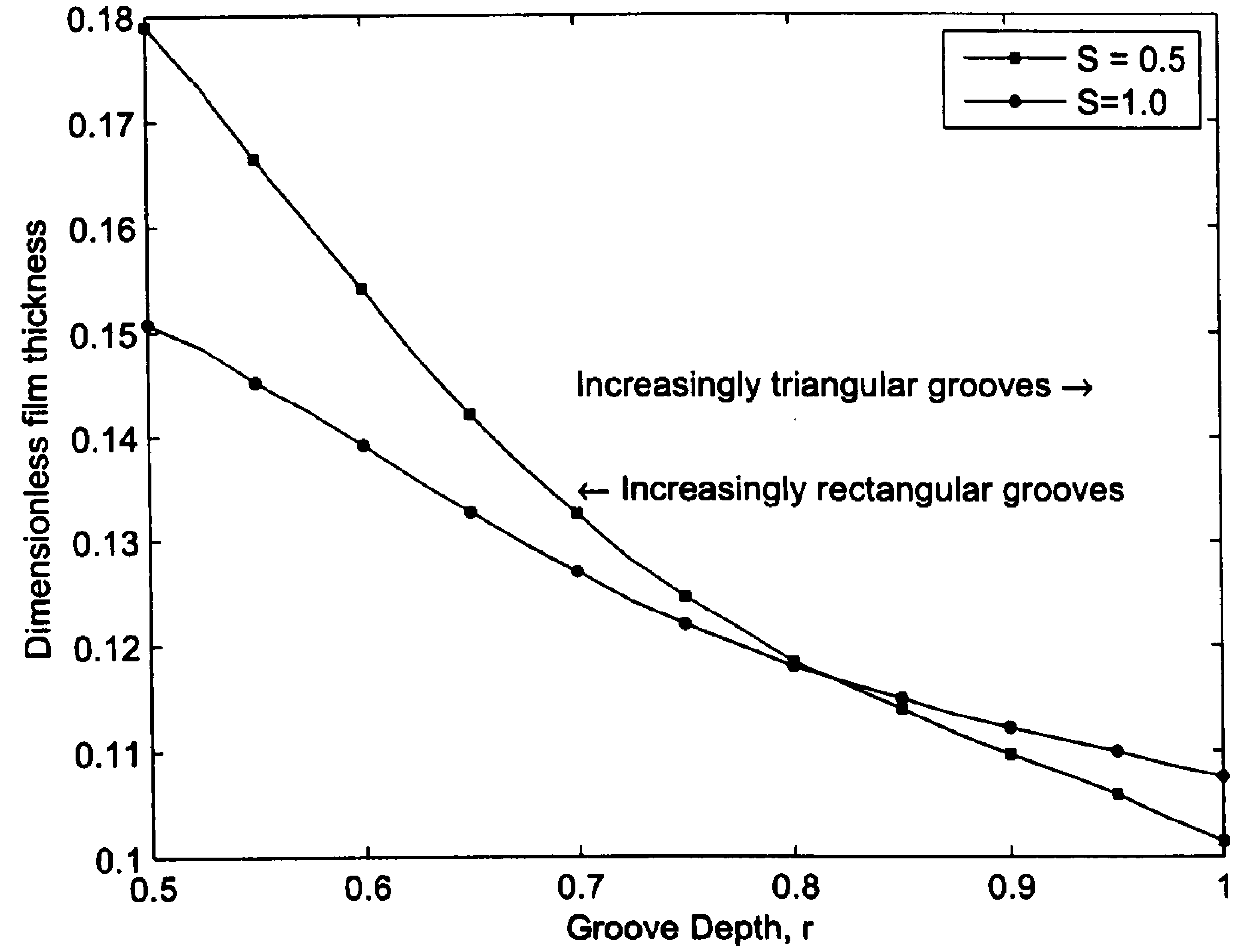

Figure 9.12: Roll Radius, $r_{\text{roll}} = 50$, Wrap Angle, $\beta = 5°$, Static Contact Angle, $\theta_A = 60°$, $\Phi = 45°$.

9.4.2 Triangular, Rectangular and Semi-Circular Grooves

The effect of three different groove geometries, as shown in figure 9.13, is examined. Each of these roll geometries have the same cross-sectional area and width of opening. The corresponding pickout results are shown in figures 9.14 and 9.15. The semi-circular and rectangular grooves give a higher pickout than the deeper triangular ones. This is consistent with the case studied in section 9.4.1 and is likely to be due to the moving web being further away from the fluid at the base of the triangular grooves, thereby imparting less motion to the fluid in the web direction.

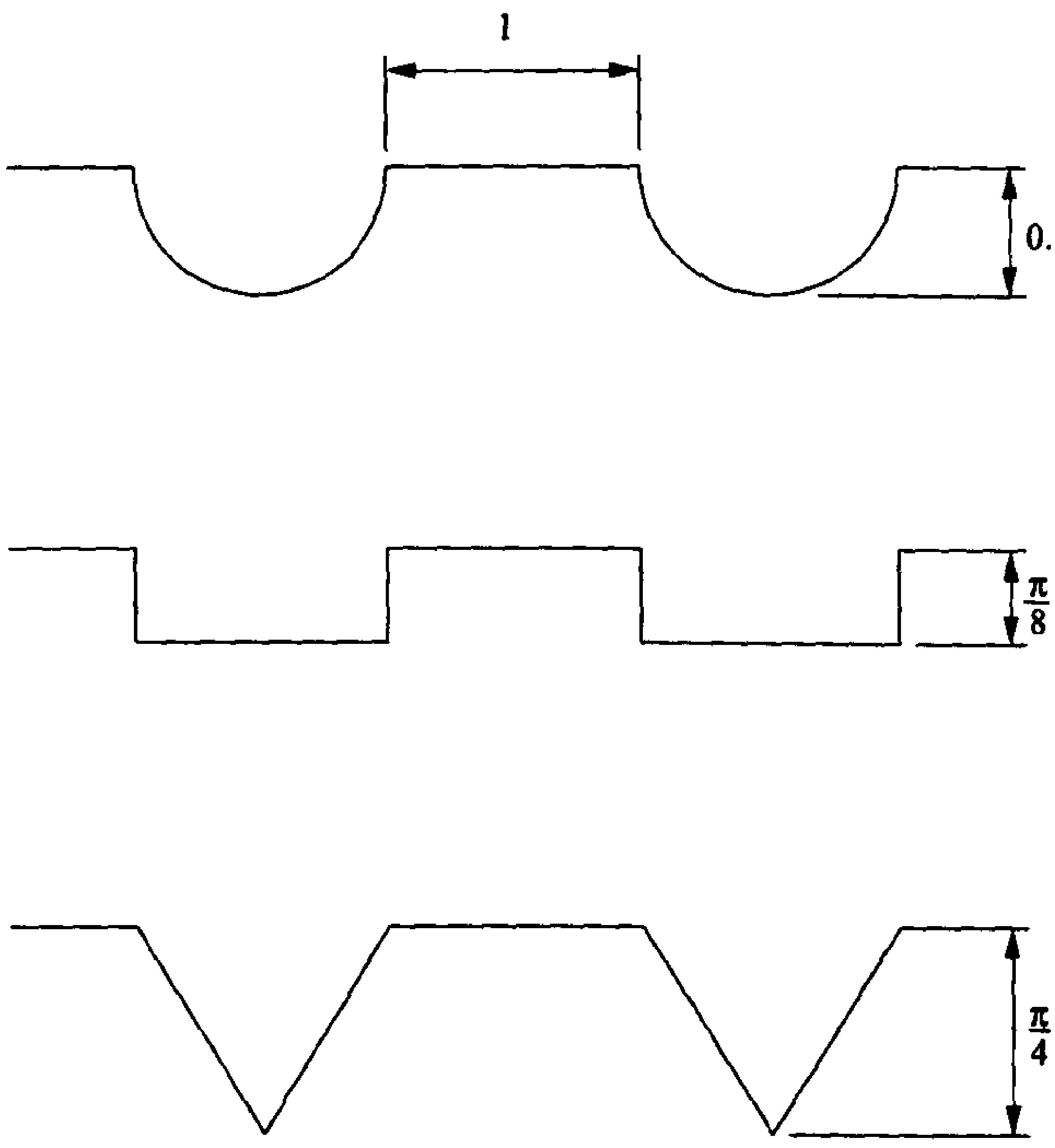

Figure 9.13: Semi circular, rectangular and triangular groove geometries studied.

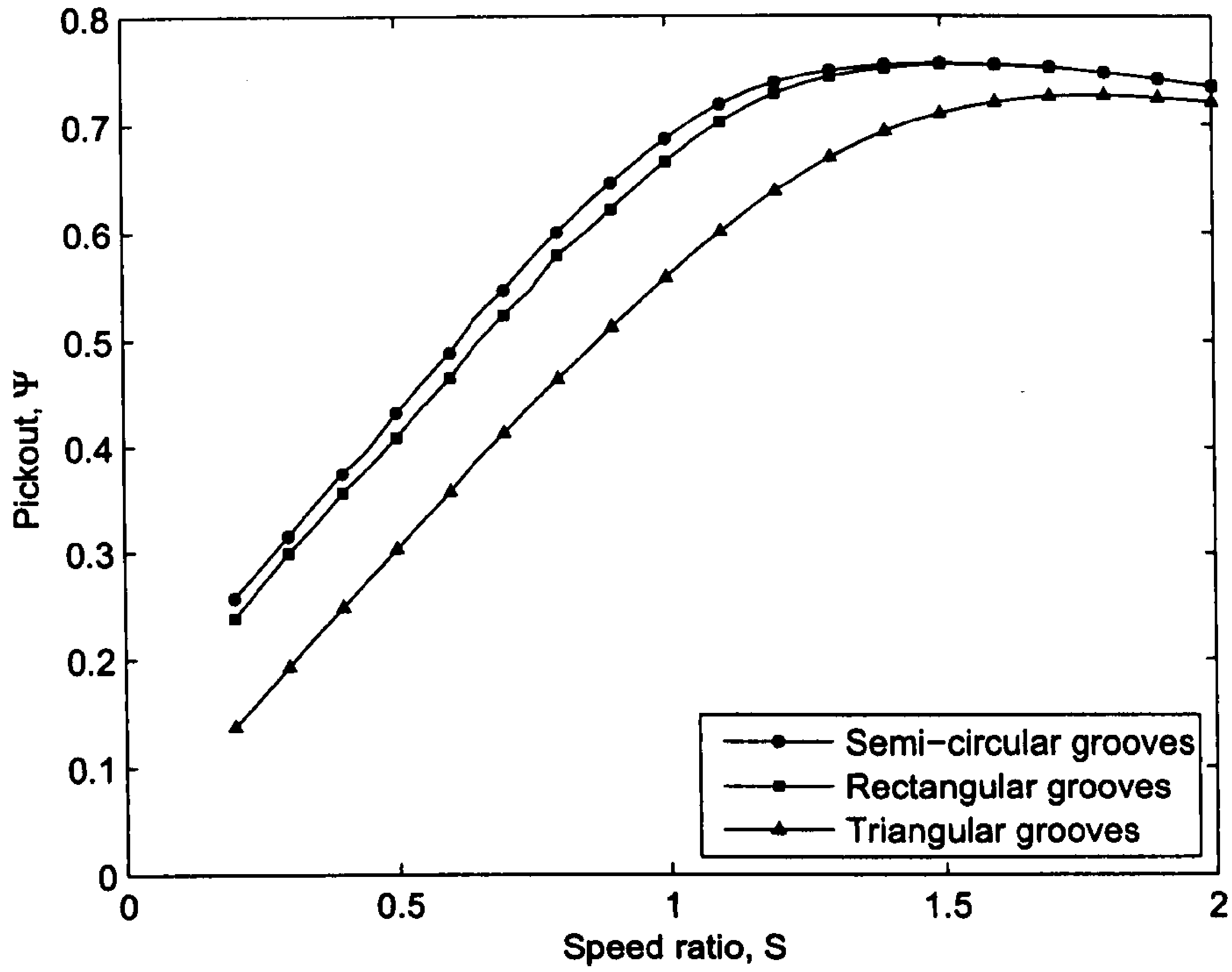

Figure 9.14: Pickout for equivalent triangular, rectangular and semi-circular groove geometries, Roll Radius , 50,Wrap Angle, $\beta = 2.5°$, Static Contact Angle, $\theta_A = 45°$, $\Phi = 0°$.

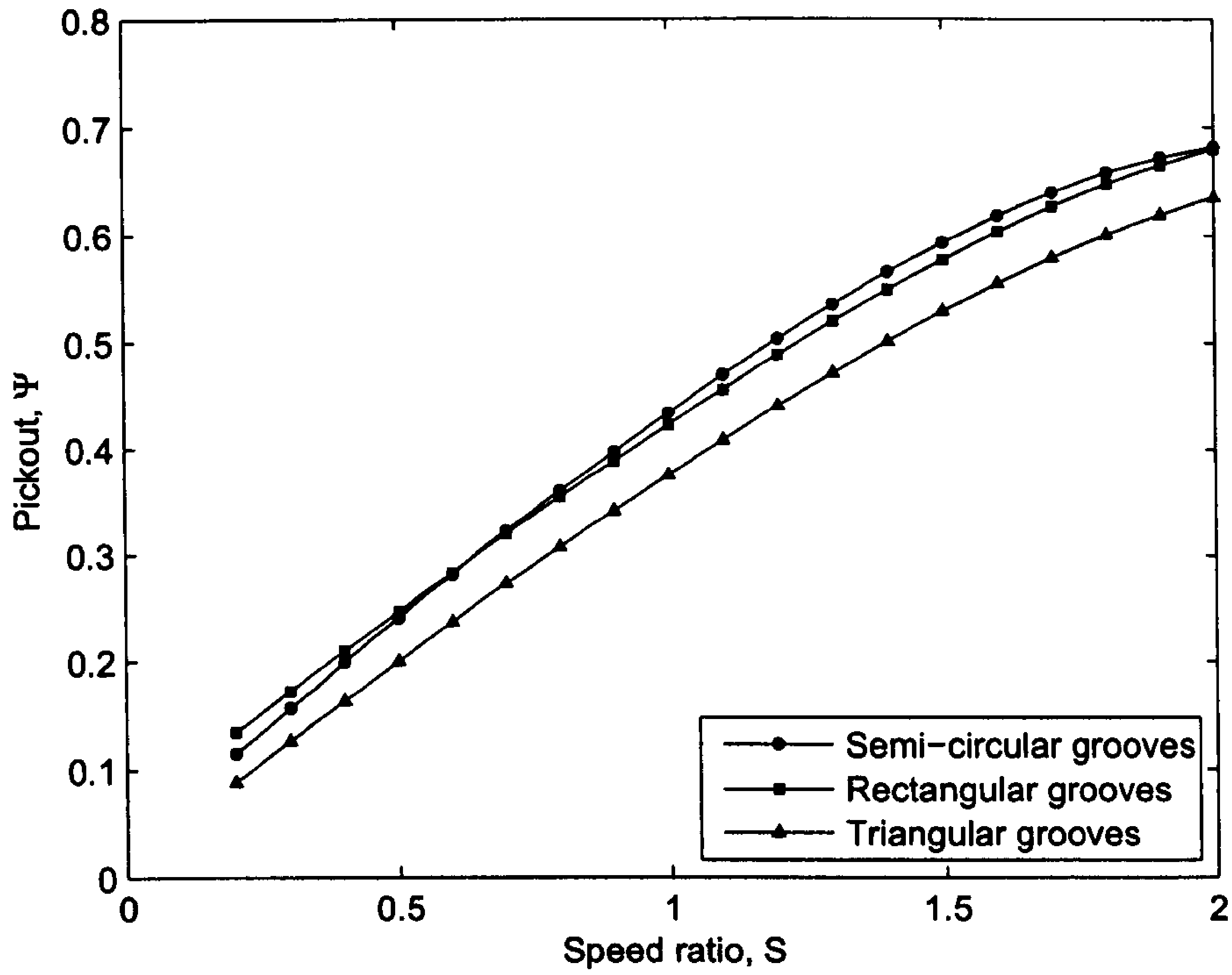

Figure 9.15: Pickout for equivalent triangular, rectangular and semi-circular groove geometries, Roll Radius , 50,Wrap Angle, $\beta = 2.5°$, Static Contact Angle, $\theta_A = 45°$, $\Phi = 45°$.

For grooves of zero pitch those of a semi-circular cross-sectional profile show a slightly greater pickout than rectangular ones; however at a pitch of 45° the pickout achieved with rectangular grooves is greater than that from semi-circular grooves. From this it is possible to deduce that the web imparts a greater motion to the fluid for the case of semi-circular grooves than it does for rectangular ones; however, the pumping of fluid due to the pressure gradient is more important for rectangular grooves. Since the pressure gradient for rolls with grooves of greater pitch is more significant, the difference between grooves of rectangular and semi-circular cross-section (and to some extent triangular grooved rolls) is reduced.

Chapter 10

Conclusion and Further Work

10.1 Conclusion

This thesis outlines the development of a theoretical model of tri-helical gravure roll coating, the first of its kind, to provide a means of predicting the operating variables of the process. Complementary experimental data has been collected in order to validate the model as well as to provide data about the flow structures within the coating bead via flow visualisation studies. Data was also gathered in relation to the instabilities present in the coating process which can lead to coating defects. The flow visualisation studies of the coating bead highlight eddies upstream and downstream of the area of web to roll contact, as observed in previous reverse meniscus roll coating studies [50].

The governing Navier–Stokes equations were simplified by neglecting inertia to give a balance between the viscous and pressure forces within the coating bead, the resulting equation taking the form of a two dimensional Poisson equation. The latter was solved using two different methods. The first, an analytical solution, was formulated for grooves of rectangular cross-section allowing solutions to be obtained quickly. These were found to compare well with the results of a full three dimensional finite element simulation of a single phase (full flooded) version of the coating problem, confirming the dominance of viscous and pressure terms in the process.

The second method for solving the Poisson type flow equation used the finite element method. Although slower to compute than the analytical approach this approach enabled non-rectangular groove geometries to be studied. The model was subsequently extended to include non-zero pitched groove roll geometries, providing a tool for modelling the industrially representative coating process, achieved by resolving the fluid flow in the groove direction and in the direction perpendicular to the grooves.

To account for the meniscii that bound the domain, for Newtonian fluids the Coyne & Elrod film forming model was employed. This has a greater range of capillary numbers over which it is applicable when compared to the simpler Landau-Levich equation. The meniscus topography at the upstream meniscus meant that approximations for the meniscus shape were required in terms of the pressures and flux remaining on the roll surface; it was found that so long as the pressure at the upstream meniscus was a function of the web-to-roll distance then agreement with experimental data was good.

A further advantage of using the FEM to solve the flow equations was that the formulation can be extended to include generalised Newtonian fluid models. Here the power law viscosity model was used to incorporate shear thinning behaviour into the model. To form suitable boundary conditions a new model was developed. This took the form of a BVP derived from the lubrication approximation of the flow, along with the local pressure field obtained from the curvature of the interface. Comparisons with the experimental results of Kamisli & Ryan [7] also confirmed the validity of the model.

Agreement between experiments and numerical simulation is found to be good in terms of film thickness and pickout from the grooves onto the coated substrate, as well as for meniscus location. The only exceptions to this were for rolls cut with large grooves, once streaking was established and for highly pitched grooves. The disagreement between prediction and experiment for rolls with large grooves was attributed to the effect of gravitational forces. The other area of disagreement between the models and the experimental results was for high speed ratios above which streaking was observed. This was due to the simple meniscus models being unable to predict the motion of the upstream meniscus into the groove. In practice, at large groove pitches the pressures within the coating bead led to deformation of the web and resulted in the actual pickout being greater than that predicted by the models. This interesting result lends weight to the argument that for discrete cell gravure roll coating elastohydrodynamic lubrication is important as without web deformation the predicted pickout goes to zero, as the grooves run along the length of the roll and the problem essentially becomes one of a two dimensional gravure roll coating process.

The high level of agreement between experiment and the theoretical models shows that the key underlying physics involved in the tri-helical coating process has been captured. Mechanisms have been put forward in the areas where the relevant model breaks down, generally found outside the industrial operating regime.

10.2 Further Work

As far as the understanding of the tri-helical form of gravure coating is concerned, analysis and experiments have helped to reveal the underpinning fundamental physics as well as providing a predictive tool to determine the performance of the process. While the mechanisms involved in the onset of streaking have been postulated a predictive tool still needs to be developed; however, this would require a more detailed model for the upstream meniscus. As well as determining the meniscus shape, based on the balance of pressure and viscous forces, it is possible that cavitation will have to be considered due to the predicted low pressures. At the very least the meniscus would almost certainly need to be modelled as a three dimensional surface. This would lead to local pressure fields with pressure being complex and no longer a function of x-location, while the transient nature of streaking may result in the only way of solving the problem being as a full three dimensional-time dependent solution (or perhaps by a three dimensional linear stability analysis) of either the Navier–Stokes equations or Stokes equations.

One of the most challenging areas for further work must be to gain an understanding of the discrete cell form of gravure coating. However, both the transient behaviour, and the elastohydrodynamic nature of the process results in a problem that is quite different from the tri-helical form. A first step to gaining an understanding of this problem would be to model it in two dimensions and assume the flow between the roll and the web could be modelled as lubrication flow (as undertaken for a single cell by Yin & Kumar [146]), despite the changes in geometry in the flow direction, casting doubt on the validity of this approach. To solve the problem as a three dimensional Navier–Stokes problem the transient deformation of the web will likely lead to numerical difficulties and would most likely have to be solved using the ALE (arbitrary Langrange-Euler) method in which the web deforms with the flow domain. The resolution of the mesh would also have to be extremely fine to capture the small indentations on the roll surface encountered in practice.

The development of the power law fluid - film forming model as part of this work could allow the non-Newtonian behaviour to be included in lubrication analysis of other coating flows, for example; smooth roll coating, meniscus roll coating or slot coating). This work could also find applications in other lubricating flows such as in bearings.

Last but not least, there is always the need for good quality experimental data, for both validation purposes and the provision of new insights. Additional experimental data of specific interest with regard to tri-helical gravure roll coating would involve the measurement of: (i) the pressure field existing within the coating bead for comparison with analytical predictions; (ii) web deformation as a consequence of the hydrodynamic forces generated within the coating bead. However, although useful, such data will be difficult to obtain due to the inherent problems associated with roll run-out and variations in web thickness associated with the process. Visualisation of the flow within the tri-helical grooves themselves would also be of value and interest. More generally new experimental data for other coating processes such as roll coating, and knife coating when operating with non-Newtonian fluids, would aid and complement the development and use of the film forming models detailed in this thesis.

Appendix A

Landau Levich Equation Derivation

A.1 Introduction

The method employed in obtaining the well known Bretherton condition is to assume a constant radius of curvature of the meniscus. This curvature is matched to the curvature where the meniscus is nearing the final film thickness based on lubrication theory and the capillary pressure.

A.2 Assumptions

The following assumptions are made for the flow in the developing fluid film:

a) The rate of change of film thickness with x is small

b) Normal lubrication assumptions that flow is typically only in the x-direction and the variation in geometry is negligible allowing inertial terms to be neglected.

A.3 Transition Region - Governing Equations

From resolving the normal stresses at the interface (i.e. balancing the pressure difference between the two phases and the capillary forces) an expression for the pressure in terms of film thickness derivatives can be obtained. This takes the form of equation (A.1) but due to assumption (a) we obtain equation (A.2).

$$p_\sigma = -\sigma \frac{\frac{d^2 y_1}{dz^2}}{\left[1 + \left(\frac{dy_1}{dz}\right)^2\right]^{\frac{3}{2}}} \tag{A.1}$$

$$p_\sigma = -\sigma \frac{d^2 y_1}{dz^2} \tag{A.2}$$

Due to assumption (b) the usual lubrication equation is obtained from the Navier-Stokes equation to produce equation (A.3).

$$\frac{\partial^2 u}{dy^2} = \frac{1}{\mu} \frac{\partial p}{\partial x} \tag{A.3}$$

A.4 Boundary Conditions

The boundary condition used are that wall the velocity is zero and that at the interface the shear stress goes to zero.

$$u = 0 \quad \text{when} \quad y = 0 \cdot \quad \text{and} \quad \frac{\partial u}{\partial x} = 0 \quad \text{when} \quad y = y_1. \tag{A.4}$$

A.5 Manipulation

The volume of fluid per width is given by equation (A.5). This is simply based on the integration of equation (A.3) with the boundary conditions from equation (A.4).

$$\begin{aligned} V &= \int_0^{y_1} u dy \\ &= -\frac{y_1^2}{3\mu}\frac{dp}{dx} \end{aligned} \tag{A.5}$$

Conservation of mass requires that the volume flux given in equation (A.4) has to be equal and opposite of the change in volume flux of the bubble which is given by equation (A.6).

$$\begin{aligned} V &= -U\left[(r-y_1)-(r-h)\right] \\ &= U\left(y_1-h\right) \end{aligned} \tag{A.6}$$

Substituting equation (A.2) (the pressure boundary condition) into equation (A.4) and equating the fluxes using equation (A.6) gives an equation describing the profile of the film in the transition region where lubrication analysis is valid, this gives equation (A.7).

$$\frac{d^3y_1}{dx^3} = \frac{3\mu U}{\sigma}\frac{y_1-h}{y_1^3} \tag{A.7}$$

At this stage it is put into universal form (dimensionless form) used by Bretherton. This is done using the identities in equation (A.8) and, based on equation (A.7) leads to equation (A.9). This equation is accredited by Bretherton to Sir Geoffrey Taylor.

$$y_1 = h\eta \quad \text{and} \quad x = h\left(\frac{3\mu U}{\sigma}\right)^{-\frac{1}{3}}\zeta \tag{A.8}$$

$$\frac{d^3\eta}{d\zeta^3} = \frac{\eta-1}{\eta^3} \tag{A.9}$$

This makes it simpler to make the following observation within the transition zone. Within the transition region where the film thickness starts to increase and is therefore slightly greater than the final film thickness it can be seen from equation (A.9) that the third derivative of η is very small as shown in equation (A.10).

$$\eta = 1 + \alpha \quad \text{when} \quad \alpha \rightarrow 0 \quad \text{then} \quad \frac{d^3\eta}{d\eta^3} \rightarrow 0 \tag{A.10}$$

We can therefore solve equation (A.9) by integrating with respect to η and using equation (A.10). This leads to the following equation,

$$\eta = \frac{1}{2}P\zeta^2 + Q\zeta + R, \tag{A.11}$$

or in dimensionless form,

$$y_1 = \frac{1}{2}P\left(\frac{3\mu U}{\sigma}\right)^{\frac{2}{3}}\frac{x^2}{h} + Q\left(\frac{3\mu U}{\sigma}\right)^{\frac{1}{3}}x + Rh \tag{A.12}$$

Equation (A.12) can be differentiated to obtain the equation describing the curvature of the interface region, equation (A.13). If this is assumed to be constant, so that the interface is described by surface tension alone then the curvature can be used to describe the entire meniscus radius, as given in equation (A.14).

$$\kappa_1 \approx \left(\frac{3\mu U}{\sigma}\right)^{\frac{2}{3}}\frac{P}{h} \tag{A.13}$$

$$\frac{h}{r} = \left(\frac{3\mu U}{\sigma}\right)^{\frac{2}{3}}P \tag{A.14}$$

By numerically integrating equation (A.9) the values of P, Q and R can be determined. When $P = 0.643$ is entered into equation (A.14) we obtain the well known Landau-Levich equation,

$$h = 1.337\left(\frac{\mu U}{\sigma}\right)^{\frac{2}{3}}r. \tag{A.15}$$

Appendix B

Coyne and Elrod Quadratic Velocity Profile Solution

B.1 Velocity Profile Justification

The main assumption used in the Coyne & Elrod cavitation model and the power law fluid version of the model is that the velocity profile is quadratic along the line perpendicular to the film surface. The justification for this is simply that there are three boundary conditions and a quadratic velocity distribution is a simple fit. This is acknowledged by Coyne & Elrod to be the principal assumption in their analysis for Newtonian fluids. For Newtonian fluids the assumed profile is valid far downstream from the point of separation where a lubricating film is essentially obtained, however there is no justification for the quadratic profile further upstream other than that there are three boundary conditions.

$$u = K + Ay + By^2 \tag{B.1}$$

B.2 Boundary Conditions

The boundary conditions used are exact and are the velocities of the moving plate (equation (B.2)) and the fluid velocity on the film surface (equation (B.3)), continuity of mass considerations form the third boundary condition, equating volume flux in the developed film to that further upstream (equation (B.4)).

$$u_{y=0} = \cos\theta \tag{B.2}$$

$$u_{y=l} = u_l \tag{B.3}$$

$$\int_0^l u dy = u_p h_\infty \tag{B.4}$$

B.3 Solution

When $y = 0$ the second and third terms vanish on the right hand side of equation (B.1), this clearly leads to $K(s) = \cos\theta$. The application of equation (B.3) results in,

$$u_l = \cos\theta + Al + Bl^2 \tag{B.5}$$

The third boundary condition can be applied

$$1 = \int_0^l \left(\cos\theta + Ay + By^2\right) dy \tag{B.6}$$

$$= l\cos\theta + \frac{Al^2}{2} + \frac{Bl^3}{3} \tag{B.7}$$

Solving equations (B.5) and (B.7) for A and equating to one another gives equation ().

$$\frac{2\left(1 - l\cos\theta - \frac{Bl^3}{3}\right)}{l^2} = \frac{u_l - \cos\theta - Bl^2}{l} \tag{B.8}$$

As $l = \frac{h}{\cos\theta}$

$$2\cos\theta - 2h\cos\theta - \frac{2Bh^3}{3\cos^2\theta} = hu_l - \cos\theta h - B\frac{h^3}{\cos^2\theta} \tag{B.9}$$

$$B = \frac{3\cos^3\theta}{h^3}\left[h + \frac{hu_l}{\cos\theta} - 2\right] \tag{B.10}$$

Substituting equation (B.10) into equation (B.5) allows $A(s)$ to be solved.

$$u_l = \cos\theta + \frac{Ah}{\cos\theta} + \frac{\cos\theta}{h}\left(-6 + 3h\frac{3hu_l}{\cos\theta}\right) \tag{B.11}$$

$$A = \frac{\cos^2\theta}{h^2}\left(6 - 4h - \frac{2hu_l}{\cos\theta}\right) \tag{B.12}$$

Appendix C

Power law fluid Matlab BVP program

Making use of Matlab's powerful mathematical functions, in particular the BVP solver `bvp4c` made the solution of the power law fluid film forming problem simple to numerically implement. The matlab code used is given below.

```
function [sol,x,y,H,rad] = PowerBVP(Ca,n)
a = 0;
b = 200;
Nsol  = 2000;
Iguess  = 0.1;
Iguessx = 1.1;
Iguessxx = 0;
Iguessxxx = 0;
x = a + b * linspace(0,1,Nsol);
solinit = bvpinit(x,[Iguess Iguessx Iguessxx Iguessxxx]);
options = bvpset('RelTol',100);
sol = bvp4c(@lode,@bc,solinit,options,n,Ca);
for i = 2:-0.1:-3
    RelTol = 10^i;
    options = bvpset('RelTol',RelTol);
```

```
    sol = bvp4c(@lode,@bc,sol,options,n,Ca);
end
y = deval(sol,x);
rad = 1/(-y(3,1) * Ca);
H = y(2,1);
% ----------------
function dydx = lode(x,y,n,Ca)
dydx = [-y(3) * Ca;
    sin(y(1));
    real((((y(2)-1)*(2*n+1)*(y(2)/cos(y(1)))^(-(1+2*n)/n))/n)^n);
    cos(y(1))];
% ----------------
function res = bc(ya,yb,n,Ca)
res = [ya(1)+pi/2 ;yb(2)-1 ;yb(3) ;yb(4)];
```

Calculations were undertaken with Matlab 6.5 in the Windows XP environement and with Matlab 7.0 on a 64 bit Linux system running both interactively and in batch mode.

Appendix D

Analytical Equations

The equations derived from the analytical solution of Poisson's equation for flow between the roll and land are fairly long and are therefore included in this appendix.

D.1 Basic Groove Flow Solution

The basic flow solution is used to describe the flow along a rectangular groove, corresponding to when the web is in contact with the roll (as outlined in section 4.3.4). The following equations are derived which give the relation between flux and pressure gradient:

$$q = 2\frac{dp}{dx}\sum_{n=1}^{\infty} f_{\text{pressure}}\left(n, r\right) + 2\sum_{n=1}^{\infty} f_{\text{drag}}\left(n, r, S\right) + r, \tag{D.1}$$

which can be rearranged to give pressure gradient as a function of flux,

$$\frac{dp}{dx} = \frac{q - r - 2\sum_{n=1}^{\infty} f_{\text{drag}}\left(n, r, S\right)}{2\sum_{n=1}^{\infty} f_{\text{pressure}}\left(n, r\right)}. \tag{D.2}$$

f_{pressure} and f_{drag} are,

$$
\begin{aligned}
f_{\text{pressure}} =& \frac{-1}{\pi^5 n^5 \left(e^{n\pi r}+1\right)} \\
&\times \Big[\Big(4\,(-1)^n + n\pi\,r - 2\,(-1)^n\, n\pi\,r + 2\,(-1)^{1+2n} + (-1)^{2n}\, n\pi\,r - 2 \Big)\, e^{n\pi\,r} \\
&+ 2 - 2\,(-1)^n + n\pi\,r + 2\,(-1)^{2n} - 2\,(-1)^n\, n\pi\,r + 2\,(-1)^{1+n} + (-1)^{2n}\, n\pi\,r \Big] \\
&\text{and} \\
f_{\text{drag}} =& \frac{\left(-1+(-1)^n\right)^2 \left(e^{n\pi r}-1\right)(S-1)}{\left(e^{n\pi r}+1\right)\pi^3 n^3}
\end{aligned}
\tag{D.3}
$$

D.2 Extended Groove Flow Solution

The extended groove flow solution refers to the more complex domain the occurs when the web is not in contact with the roll surface, this leads to the more complex relationship between pressure gradient and flux (as outlined in section 4.3.5).

$$
\begin{aligned}
Flux =\; & \underbrace{r + \sum_{n=1}^{\infty} f_{\text{drag}}\left(n, r, S, \overline{h}\right) + \frac{\partial p}{\partial x} \sum_{n=1}^{\infty} f_{\text{pressure}}\left(n, r, \overline{h}\right)}_{\text{Zone One}} \\
+\; & \underbrace{\overline{h} + \sum_{i=1}^{\infty} f_{\text{drag}}\left(n, r, S, \overline{h}\right) + \frac{\partial p}{\partial x} \sum_{i=1}^{\infty} f_{\text{pressure}}\left(n, r, \overline{h}\right)}_{\text{Zone Two}} \\
+\; & \underbrace{\overline{h}l + f_{\text{Couette}}\left(S, \overline{h}, l\right) + \frac{\partial p}{\partial x} f_{\text{Poiseuille}}\left(\overline{h}, l\right)}_{\text{Zone Three}} .
\end{aligned}
\tag{D.4}
$$

$$
f_{\text{Couette}}\left(S, \overline{h}, l\right) = \frac{(S-1)\,\overline{h}l}{2}
\tag{D.5}
$$

$$
f_{\text{Poiseuille}}\left(\overline{h}, l\right) = -\frac{\overline{h}^3 l}{12}
\tag{D.6}
$$

$$
\begin{aligned}
f_{\text{drag}}\left(n,r,S,\overline{h}\right)_{\text{Zone One}} =& \frac{(-1+(-1)^n)^2}{2\left(1-e^{2\,n\pi\left(\overline{h}+r\right)}\right)\pi^5 n^5}\\
&\times\Big[-2\,e^{n\pi\left(2\overline{h}+r\right)}n\overline{h}\pi+8\,e^{n\pi\left(2\overline{h}+r\right)}+e^{2\,n\pi\left(\overline{h}+r\right)}n\overline{h}\pi+4\,e^{2\,n\pi\left(\overline{h}+r\right)}rn\pi\\
&-6\,e^{2\,n\pi\left(\overline{h}+r\right)}+e^{2\,n\overline{h}\pi}n\overline{h}\pi-2\,e^{2\,n\overline{h}\pi}-e^{2\,nr\pi}n\overline{h}\pi-2\,e^{2\,nr\pi}\\
&+2\,e^{nr\pi}n\overline{h}\pi+8\,e^{nr\pi}-n\overline{h}\pi-4\,nr\pi-6\Big]
\end{aligned}
\tag{D.7}
$$

$$
\begin{aligned}
f_{\text{pressure}}\left(n,r,\overline{h}\right)_{\text{Zone One}} =& \frac{(-1+(-1)^n)^2}{n^4\pi^4\left(-1+e^{2\,n\pi\left(\overline{h}+r\right)}\right)\overline{h}}\\
&\times\Big[-2\,e^{n\pi\left(2\overline{h}+r\right)}S+2\,e^{n\pi\left(2\overline{h}+r\right)}+e^{2\,n\pi\left(\overline{h}+r\right)}S-e^{2\,n\pi\left(\overline{h}+r\right)}\\
&+e^{2\,n\overline{h}\pi}S-e^{2\,n\overline{h}\pi}-e^{2\,nr\pi}S+e^{2\,nr\pi}+2\,e^{nr\pi}S-2\,e^{nr\pi}-S+1\Big]
\end{aligned}
\tag{D.8}
$$

$$
\begin{aligned}
f_{\text{drag}}\left(n,r,S,\overline{h}\right)_{\text{Zone Two}} =& \frac{(-1+(-1)^n)^2}{n^4\pi^4\left(-1+e^{2\,n\pi\left(\overline{h}+r\right)}\right)\overline{h}}\\
&\times\Big[(-2\,e^{n\pi\left(\overline{h}+2\,r\right)}S+2\,e^{n\pi\left(\overline{h}+2\,r\right)}+n^2\pi^2\overline{h}^2-Sn^2\pi^2\overline{h}^2+1-S\\
&-e^{2\,n\pi\left(\overline{h}+r\right)}n^2\pi^2\overline{h}^2+e^{2\,n\pi\left(\overline{h}+r\right)}Sn^2\pi^2\overline{h}^2+e^{2\,n\pi\left(\overline{h}+r\right)}S-e^{2\,n\pi\left(\overline{h}+r\right)}\\
&+e^{2\,nr\pi}S-e^{2\,nr\pi}-e^{2\,n\overline{h}\pi}S+e^{2\,n\overline{h}\pi}+2\,e^{n\overline{h}\pi}S-2\,e^{n\overline{h}\pi}\Big]
\end{aligned}
\tag{D.9}
$$

$$
\begin{aligned}
f_{\text{pressure}}\left(n,r,\overline{h}\right)_{\text{Zone Two}} =& \frac{(-1+(-1)^n)^2}{6n^5\pi^5\left(1-e^{2\,n\pi\left(\overline{h}+r\right)}\right)}\\
&\times\Big[-6\,e^{n\pi\left(\overline{h}+2\,r\right)}n\overline{h}\pi-12\,e^{n\pi\left(\overline{h}+2\,r\right)}-3\,e^{2\,n\overline{h}\pi}n\overline{h}\pi+6\,e^{2\,n\overline{h}\pi}+e^{2\,n\pi\left(\overline{h}+r\right)}\overline{h}^3n^3\pi^3\\
&+3\,e^{2\,n\pi\left(\overline{h}+r\right)}n\overline{h}\pi+6\,e^{2\,n\pi\left(\overline{h}+r\right)}+24\,e^{n\pi\left(\overline{h}+r\right)}+6\,e^{n\overline{h}\pi}n\overline{h}\pi-12\,e^{n\overline{h}\pi}-12\,e^{nr\pi}\\
&+3\,e^{2\,nr\pi}n\overline{h}\pi+6\,e^{2\,nr\pi}-\overline{h}^3n^3\pi^3-12\,e^{n\pi\left(2\overline{h}+r\right)}-3\,n\overline{h}\pi+6\Big]
\end{aligned}
\tag{D.10}
$$

Appendix E

Three Dimensional Simulation of Flooded Case

E.1 Finite Element Implementation

Femlab's implementation of the three dimensional Navier–Stokes equations was used, as incompressible flow was assumed the Navier–Stokes equations in three dimensions consisting of four differential equations, three being a momentum balance in the x, y and z directions (momentum equations) and the fourth equation the conservation of mass, the energy equations are not required for incompressible flow as they become uncoupled from the conservation of mass and momentum equations for incompressible flow. The implementation of the steady (non-time dependent) Navier–Stokes equations employed by femlab is:

$$-\nabla \cdot \left[-PI + \eta\left(\nabla U + (\nabla U)^T\right)\right] + \rho\,(U \cdot \nabla)\,U = F, \tag{E.1}$$

$$-\nabla \cdot U = 0, \tag{E.2}$$

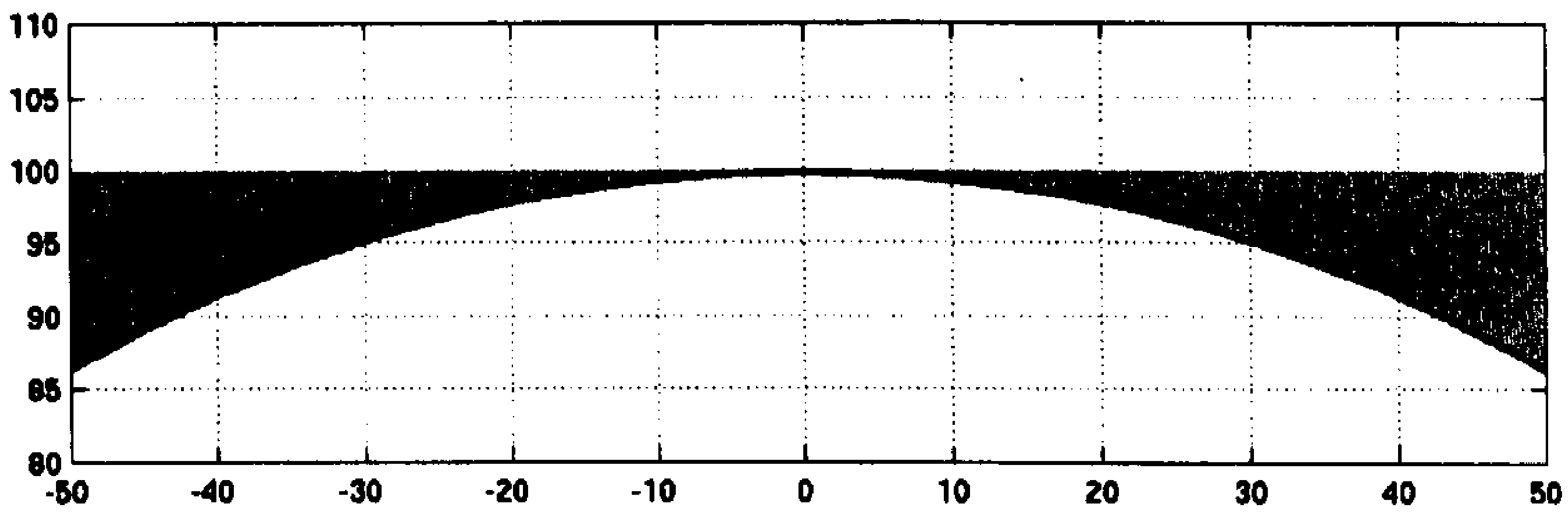

Figure E.1: Solution domain solved in femlab, the domain extends into the page in order in order to consider the groove geometry.

making femlab's implementation of the Navier–Stokes equations capable of solving the non-Newtonian fluid flows by making η a function of the flow field. The non-dimensional form of the Navier–Stokes equations to be solved becomes,

$$-\nabla\cdot\left[-pI+\frac{1}{Re}\left(\nabla u+(\nabla u)^T\right)\right]+(u\cdot\nabla)\,u=f, \tag{E.3}$$

$$\nabla\cdot u=0, \tag{E.4}$$

where the velocity vector $u=\frac{U}{U^\star}$, pressure scaler $p=\frac{P}{\rho U^{\star 2}}$, force vector $f=\frac{FL}{\rho U^{\star 2}}$, Reynolds number $Re=\frac{\rho U^\star L}{\nu}$ and ρ is the fluid density, $U^\star$ is the characteristic velocity (in this case based on the roll velocity and L is the characteristic length (based on the groove width).

The domain to be solved for is shown in figure E.1. The dimensions of the problem are shown in

Groove width	1.0
Groove depth	0.5
Land width	1.0
Roll radius	50
Wrap angle	0
Reynolds number $Re = \frac{\rho U_{roll} A}{\mu}$	0.001, 0.01, 0.1, 1, 10, 100

Table E.1: Parameters investigated in finite element analysis of flooded coating case.

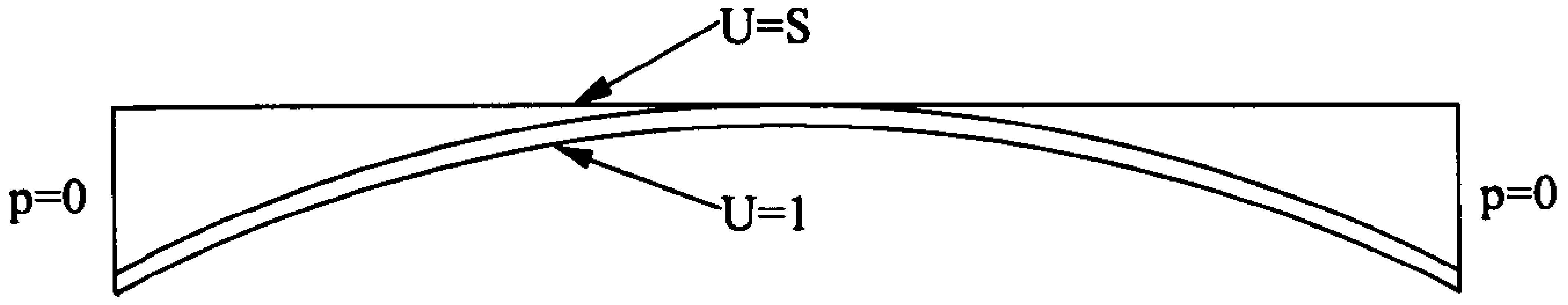

Figure E.2: Boundary conditions imposed on the finite element analysis of the flooded coating case.

table E.1. Where ρ is the fluid density, U_{roll} is the roll velocity, A is the groove width and μ is the fluid viscosity. For modelling simplicity zero wrap angle was used in this limited analysis, this also reduced the number of elements required. The reason for this was that for meshing of the problem a small web to land gap was required (2% of the groove width), the meshing in this small gap was therefore extremelly fine. The length of the domain (the distance from upstream to downstream of the point of minimum roll to web separation) was chosen to be 160. Limited data was also collected for a domain length of 80 to ensure that the solution was independent of the length of the domain when greater than 80. The boundary conditions for the problem are shown in figure E.2. In addition to the boundary conditions shown, symmetrical boundary conditions (Neumann) were implemented along the edges of the domain in the plane of the page. This ensured that only half the groove needed to be solved for, reducing the computational requirements considerably.

Triangular "U2 - P1" elements were used, these elements are second order for velocity and first order for the pressure variable. The reason for this is that the Navier–Stokes equation has higher order derivatives of velocity (second derivatives) than it does for the pressure term (first order). No artificial diffusion was used in the model as the Reynolds number was just low enough to obtain stable results. Maximum grid size was constrained by the stability considerations for the largest Reynold number setting.

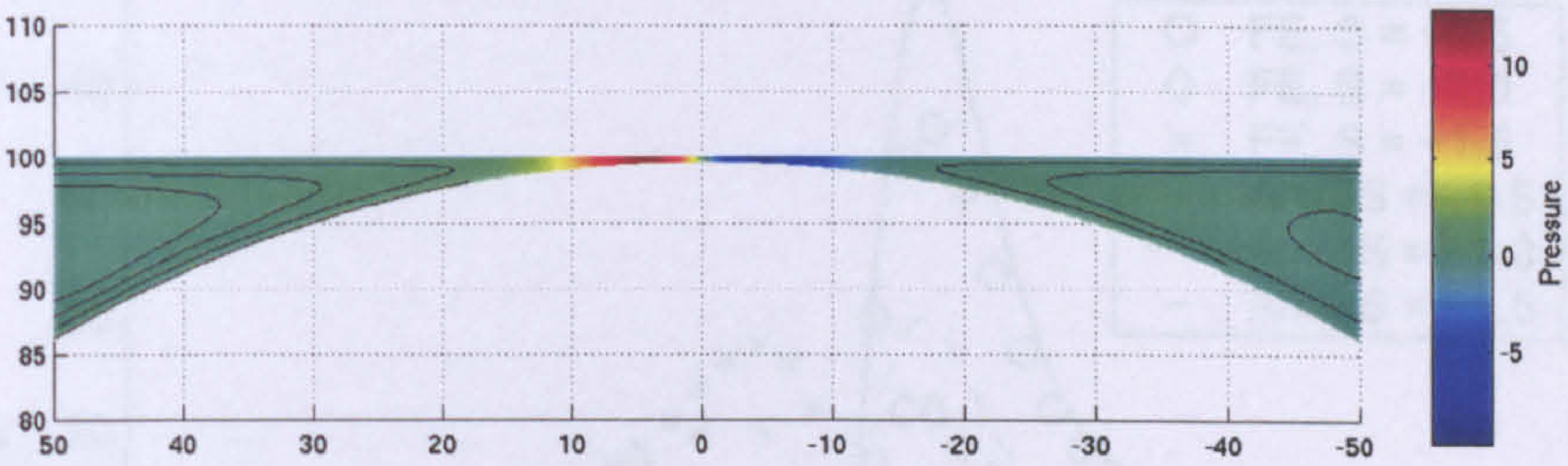

Figure E.3: Streamline and pressure plot of a typical result obtained from the finite element analysis of the flooded coating case.

E.2 Results

The parametric study of Reynolds numbers and speed ratios produced 120 results. The post processing interface within femlab and the femlab and general matlab functions available within matlab enabled pressure data to be extracted and volume flow data to be obtained. A typical pressure distribution and streamline plot obtained from the solution is shown in figure E.3. Flow topography is similar to that encountered in reverse mode meniscus roll coating [50, 47], with upstream and downstream eddies clearly visible. Similar eddies were experimentally observed as detailed in section 7.2.1. The pressure profiles are also in qualitative agreement with the pressure profiles encountered in smooth roll coating [8, 1]. The main difference between flooded smooth roll coating results and those for the tri-helical flow is that for a speed ratio of $S = 1$ a non-zero pressure profile is obtained, this can be attributed to the dominance of viscous forces due to the roll surface when compared to that of the web, due to the larger surface area of the roll exposed to the flow. When the roll and web are operating at equal but opposite velocities the pressure profile resembles that for smooth roll coating when the roll is moving at a greater speed than the web, i.e. there is a positive pressure on on the side at which the roll approaches the web to roll contact point and a corresponding negative pressure on the side that the roll leaves the web to roll contact point. This is shown in figure E.4. Two comparisons were made to ensure consistent results between the analytical model and the full finite element solution of the Navier–Stokes equations, these comparisons were the theoretical pickout from the groove and the other was the pressure distribution through the coating nip.

Comparison between pressure distribution and volume flow rate (or theoretical pickout) through

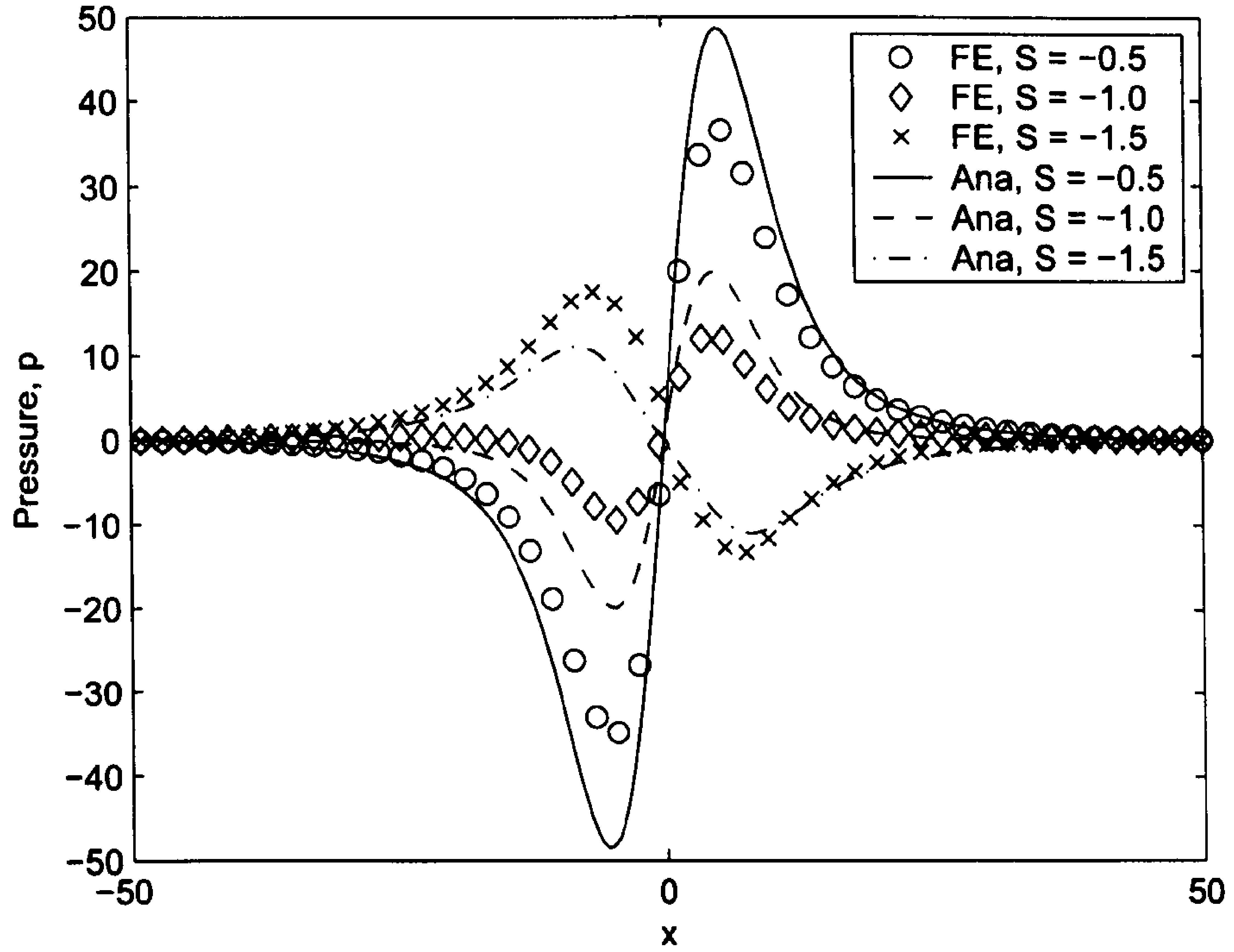

Figure E.4: Pressure distribution within the coating bead predicted by the finite element analysis and using the analytical model.

the coating nip can be made. The pressure distribution comparison was made between the one dimensional pressure field of the analytical model and that obtained from the finite element solution along the groove. As the pressure field from the finite element model is three dimensional the line chosen to plot the pressure distribution along had some effect on the results. The pressure within the groove was observed to be fairly constant at any cross section perpendicular to the x-direction. Using matlab's functions the averaged cross sectional pressure was determined. The pressure distributions for speed ratios of $S = -0.5$, $S = -1$ and $S = -1.5$ are shown in figure E.4. It can clearly be seen that while the pressures predicted by the two methods are in clear qualitative agreement the quantitative agreement is not perfect with the most likely source of the discrepancy being the small gap between the web and the roll surface artificially introduced in the FE analysis to ensure meshing was possible.

Appendix F

Consistent Meniscus Dimensional Scalings

The problem of ensuring consistent dimensional scalings throughout the coating models is complicated by the use of different non-dimensional scalings for the hydrodynamic equations and the film forming analyses.

Consistent Non-Dimensional Scalings The difference in scalings used in the cavitation models and those used to derive the hydrodynamic pressure equations are clearly different. This lead to potential problems implementing the meniscus models into the complete coating model. In the hydrodynamic pressure equations the following scalings and dimensionless parameters are used:

$$\left[1/\kappa, d, a'\right] = \frac{[1/\kappa, d, A']}{A} \tag{F.1}$$

$$u = \frac{U}{U_{\text{roll}}} \tag{F.2}$$

$$p = \frac{PA^n}{\lambda U_{\text{roll}}^n} \tag{F.3}$$

$$Ca = \frac{\lambda U_{\text{roll}}^n}{\sigma A^{n-1}}. \tag{F.4}$$

These parameters have been given for non-Newtonian fluids that obey the power law model but are also valid for Newtonian fluids, where $n = 1$ and $\lambda = \mu$. However the scalings and dimensionless parameters are used by the cavitation models are:

$$1/\kappa_{FF}, h_{FF}, a'_{FF} = \frac{1/\kappa, H, A'}{H_\infty} \tag{F.5}$$

$$u_{FF} = \frac{U}{U_{\text{substrate}}} \tag{F.6}$$

$$p_{FF} = \frac{PH_\infty^n}{\lambda U^n_{\text{substrate}}} \tag{F.7}$$

$$Ca_{FF} = \frac{\lambda U^n_{\text{substrate}}}{\sigma H_\infty^{n-1}}. \tag{F.8}$$

This results in the following definitions,

$$\left[1/\kappa_{FF}, c, a'_{FF}\right] = \left[1/\kappa, d, a'\right] \frac{A}{H_\infty} \tag{F.9}$$

$$u_{FF} = u\frac{U_{\text{roll}}}{U_{\text{substrate}}} \tag{F.10}$$

$$Ca_{FF} = Ca\frac{U^n_{\text{substrate}} A^{n-1}}{U^n_{\text{roll}} H_\infty^{n-1}} \tag{F.11}$$

$$p_{FF} = p\frac{U^n_{\text{roll}} H^n_\infty}{U^n_{\text{substrate}} A^n}. \tag{F.12}$$

From these definitions the equations describing the meniscus locations and pressures can be derived in terms of the dimensionless variables used to describe the coating problem rather than the parameters specific to the film forming equations.

$$c = \mathcal{F}\left(Ca_{FF}\right) \tag{F.13}$$

$$\kappa_{FF} = \mathcal{G}\left(Ca_{FF}\right) \tag{F.14}$$

Which in terms of the dimensionless variables used in the coating model are:

$$c = \mathcal{F}\left(Ca\frac{U^n_{\text{substrate}} A^{n-1}}{U^n_{\text{roll}} H_\infty^{n-1}}\right)\frac{H_\infty}{A} \tag{F.15}$$

$$\kappa = \mathcal{G}\left(Ca\frac{U^n_{\text{substrate}} A^{n-1}}{U^n_{\text{roll}} H_\infty^{n-1}}\right)\frac{A}{H_\infty} \tag{F.16}$$

At the downstream meniscus for a given coating flux the film thickness (h_w) was obtained from equation (4.46), as h_w is the non-dimensional form of the film thickness deposited on the web then clearly $h_w = \frac{H_\infty}{A}$. The following equations describe the film thickness and curvature as,

$$c = \mathcal{F}\left(Ca\frac{|S|^n}{h_w^{n-1}}\right)h_w \tag{F.17}$$

$$\kappa = \mathcal{G}\left(Ca\frac{|S|^n}{h_w^{n-1}}\right)\frac{1}{h_w} \tag{F.18}$$

The multiple surface presented at the upstream meniscus make the equations describing the upstream meniscus more complex than those describing the downstream meniscus, from the dimensions given in figure 5.10 and equation (5.29) the film thicknesses h_1, h_2 and h_3 are,

$$h_1 = \frac{r+d}{c_1} \quad , \quad h_2 = \frac{a}{2c_2} \quad \text{and} \quad h_3 = \frac{d}{c_3}, \tag{F.19}$$

where c_1, c_2 and c_3 are the gap to film thickness ratio corresponding to film thicknesses h_1, h_2 and h_3 respectively. The problem arose when determining the gap to film thickness ratios as the capillary numbers used to determine these values was based on the film thicknesses h_1, h_2 and h_3 unsolved variables. The process used to solve the problem was,

1. Using capillary numbers based on the groove width the gap to film thickness ratios c_1, c_2 and c_3 were determined.
2. From equation (5.37) the web to roll gap was determined (d).
3. The film thicknesses h_1, h_2 and h_3 were then determined using equations (F.19).
4. Using these new film thicknesses new capillary numbers were obtained and the gap to film thickness ratios (c_is) determined.
5. Stages 2 to 4 were repeated until the final capillary numbers for each coated surface of the roll remained constant.

The curvatures κ_{y1}, κ_{y2} and κ_z were then solved as

$$\kappa_{y1} = \mathcal{G}\left(\frac{Ca}{h_3^{n-1}}\right)\frac{1}{h_3} \tag{F.20}$$

$$\kappa_{y2} = \mathcal{G}\left(\frac{Ca}{h_1^{n-1}}\right)\frac{1}{h_1} \tag{F.21}$$

$$\kappa_z = \mathcal{G}\left(\frac{Ca}{h_2^{n-1}}\right)\frac{1}{h_2} \tag{F.22}$$

Appendix G

Raw Data

Below is the experimental pickout and film thickness data included in this thesis.

Roll	Fluid	Wrap Angle	Roll Speed	Web Speed	Pickout	Film Thickness (μm)
B1	A	5°	0.333	0.083	0.266	90.000
B1	A	5°	0.333	0.167	0.426	72.000
B1	A	5°	0.333	0.250	0.559	63.000
B1	A	5°	0.333	0.333	0.650	55.000
B1	A	5°	0.333	0.417	0.745	50.400
B1	A	5°	0.333	0.500	0.780	44.000
B1	A	5°	0.333	0.583	0.745	36.000
B1	A	5°	0.333	0.667	0.721	30.500
B1	A	5°	0.333	0.833	0.638	21.600
B1	A	5°	0.500	0.083	0.177	90.000
B1	A	5°	0.500	0.167	0.319	81.000
B1	A	5°	0.500	0.250	0.410	69.333
B1	A	5°	0.500	0.333	0.538	68.250
B1	A	5°	0.500	0.417	0.599	60.800
B1	A	5°	0.500	0.500	0.678	57.333
B1	A	5°	0.500	0.583	0.725	52.571
B1	A	5°	0.500	0.667	0.757	48.000

B1	A	5°	0.500	0.750	0.741	41.778
B1	A	5°	0.500	0.833	0.709	36.000
B1	A	5°	0.500	1.000	0.678	28.667
B1	A	5°	0.500	1.167	0.623	22.571
B1	B	5°	0.333	0.083	0.248	84.000
B1	B	5°	0.333	0.167	0.431	73.000
B1	B	5°	0.333	0.250	0.567	64.000
B1	B	5°	0.333	0.333	0.709	60.000
B1	B	5°	0.333	0.417	0.741	50.133
B1	B	5°	0.333	0.500	0.741	41.778
B1	B	5°	0.333	0.667	0.654	27.667
B1	B	5°	0.500	0.083	0.216	109.500
B1	B	5°	0.500	0.167	0.343	87.000
B1	B	5°	0.500	0.250	0.390	66.000
B1	B	5°	0.500	0.333	0.493	62.571
B1	B	5°	0.500	0.417	0.591	60.000
B1	B	5°	0.500	0.500	0.701	59.333
B1	B	5°	0.500	0.583	0.675	48.980
B1	B	5°	0.500	0.667	0.678	43.000
B1	B	5°	0.500	0.833	0.615	31.200
B1	B	5°	0.500	1.000	0.532	22.500
B1	B	5°	0.500	1.167	0.413	14.961
B1	B	5°	0.667	0.083	0.121	82.000
B1	B	5°	0.667	0.167	0.221	74.667
B1	B	5°	0.667	0.250	0.381	86.000
B1	B	5°	0.667	0.333	0.431	73.000
B1	B	5°	0.667	0.417	0.544	73.600
B1	B	5°	0.667	0.500	0.615	69.333
B1	B	5°	0.667	0.583	0.638	61.714
B1	B	5°	0.667	0.667	0.695	58.800
B1	B	5°	0.667	0.750	0.730	54.933
B1	B	5°	0.667	0.833	0.738	49.920
B1	B	5°	0.667	0.917	0.674	41.455

B1	B	5°	0.667	1.000	0.609	34.333
B1	B	5°	0.667	1.167	0.520	25.143
B3	A	5°	0.333	0.083	0.103	66.867
B3	A	5°	0.333	0.167	0.213	69.298
B3	A	5°	0.333	0.250	0.322	69.906
B3	A	5°	0.333	0.333	0.411	66.867
B3	A	5°	0.333	0.417	0.523	68.082
B3	A	5°	0.333	0.500	0.610	66.191
B3	A	5°	0.333	0.583	0.671	62.416
B3	A	5°	0.333	0.667	0.739	60.180
B3	A	5°	0.333	0.750	0.769	55.655
B3	A	5°	0.333	0.833	0.709	46.199
B3	A	5°	0.333	1.000	0.616	33.433
B3	A	5°	0.500	0.083	0.085	83.077
B3	A	5°	0.500	0.167	0.174	85.103
B3	A	5°	0.500	0.250	0.255	83.077
B3	A	5°	0.500	0.333	0.315	76.998
B3	A	5°	0.500	0.417	0.377	73.756
B3	A	5°	0.500	0.500	0.443	72.135
B3	A	5°	0.500	0.583	0.524	73.090
B3	A	5°	0.500	0.667	0.577	70.459
B3	A	5°	0.500	0.750	0.641	69.568
B3	A	5°	0.500	0.833	0.703	68.655
B3	A	5°	0.500	0.917	0.724	64.364
B3	A	5°	0.500	1.000	0.778	63.321
B3	A	5°	0.500	1.083	0.778	58.450
B3	A	5°	0.500	1.167	0.648	45.248
B3	B	0°	0.333	0.083	0.109	70.919
B3	B	0°	0.333	0.167	0.243	79.024
B3	B	0°	0.333	0.250	0.367	79.700
B3	B	0°	0.333	0.333	0.473	76.998
B3	B	0°	0.333	0.417	0.582	75.863
B3	B	0°	0.333	0.500	0.664	72.135

B3	B	0°	0.333	0.583	0.732	68.082
B3	B	0°	0.333	0.667	0.644	52.430
B3	B	0°	0.333	0.750	0.590	42.687
B3	B	0°	0.333	0.833	0.567	36.940
B3	B	0°	0.333	1.000	0.552	29.989
B3	B	0°	0.500	0.083	0.070	68.893
B3	B	0°	0.500	0.167	0.165	80.544
B3	B	0°	0.500	0.250	0.257	83.752
B3	B	0°	0.500	0.333	0.328	80.037
B3	B	0°	0.500	0.417	0.408	79.754
B3	B	0°	0.500	0.500	0.459	74.816
B3	B	0°	0.500	0.583	0.485	67.735
B3	B	0°	0.500	0.667	0.597	72.946
B3	B	0°	0.500	0.750	0.664	72.045
B3	B	0°	0.500	0.833	0.684	66.867
B3	B	0°	0.500	0.917	0.603	53.604
B3	B	0°	0.500	1.000	0.554	45.084
B3	B	5°	0.333	0.083	0.175	114.281
B3	B	5°	0.333	0.167	0.308	100.300
B3	B	5°	0.333	0.250	0.434	94.221
B3	B	5°	0.333	0.333	0.529	86.116
B3	B	5°	0.333	0.417	0.634	82.672
B3	B	5°	0.333	0.500	0.724	78.619
B3	B	5°	0.333	0.583	0.776	72.251
B3	B	5°	0.333	0.667	0.672	54.709
B3	B	5°	0.333	0.750	0.653	47.280
B3	B	5°	0.333	0.833	0.641	41.741
B3	B	5°	0.333	1.000	0.616	33.433
B3	B	5°	0.500	0.083	0.133	129.681
B3	B	5°	0.500	0.167	0.232	113.471
B3	B	5°	0.500	0.250	0.318	103.745
B3	B	5°	0.500	0.333	0.393	96.045
B3	B	5°	0.500	0.417	0.458	89.480

B3	B	5°	0.500	0.500	0.535	87.129
B3	B	5°	0.500	0.583	0.588	82.103
B3	B	5°	0.500	0.667	0.641	78.264
B3	B	5°	0.500	0.750	0.677	73.546
B3	B	5°	0.500	0.833	0.691	67.542
B3	B	5°	0.500	0.917	0.691	61.402
B3	B	5°	0.500	1.000	0.622	50.657
B4	A	5°	0.333	0.083	0.120	68.000
B4	A	5°	0.333	0.167	0.216	61.500
B4	A	5°	0.333	0.250	0.372	70.400
B4	A	5°	0.333	0.333	0.456	64.800
B4	A	5°	0.333	0.417	0.558	63.360
B4	A	5°	0.333	0.500	0.642	60.800
B4	A	5°	0.333	0.583	0.726	58.971
B4	A	5°	0.333	0.667	0.752	53.400
B4	A	5°	0.333	0.750	0.710	44.800
B4	A	5°	0.333	0.833	0.617	35.040
B4	A	5°	0.333	1.000	0.549	26.000
B4	A	5°	0.500	0.083	0.092	78.000
B4	A	5°	0.500	0.167	0.187	79.500
B4	A	5°	0.500	0.250	0.267	76.000
B4	A	5°	0.500	0.333	0.338	72.000
B4	A	5°	0.500	0.417	0.405	69.120
B4	A	5°	0.500	0.500	0.456	64.800
B4	A	5°	0.500	0.583	0.524	63.771
B4	A	5°	0.500	0.667	0.563	60.000
B4	A	5°	0.500	0.750	0.612	57.971
B4	A	5°	0.500	0.833	0.640	54.545
B4	A	5°	0.500	0.917	0.673	52.121
B4	A	5°	0.500	1.000	0.575	40.833
B4	A	5°	0.500	1.167	0.574	34.971
C2	C	5°	0.333	0.083	0.157	115.350
C2	C	5°	0.333	0.167	0.304	111.373

C2	C	5°	0.333	0.250	0.423	103.417
C2	C	5°	0.333	0.333	0.537	98.445
C2	C	5°	0.333	0.417	0.625	91.644
C2	C	5°	0.333	0.500	0.676	82.535
C2	C	5°	0.333	0.583	0.765	80.120
C2	C	5°	0.333	0.667	0.790	72.342
C2	C	5°	0.333	0.750	0.749	60.990
C2	C	5°	0.333	0.833	0.684	50.118
C2	C	5°	0.333	0.917	0.603	40.138
C2	C	5°	0.333	1.000	0.627	38.284
C2	C	5°	0.500	0.083	0.119	131.261
C2	C	5°	0.500	0.167	0.220	120.819
C2	C	5°	0.500	0.250	0.307	112.509
C2	C	5°	0.500	0.333	0.387	106.202
C2	C	5°	0.500	0.417	0.467	102.622
C2	C	5°	0.500	0.500	0.516	94.468
C2	C	5°	0.500	0.583	0.615	96.599
C2	C	5°	0.500	0.667	0.666	91.485
C2	C	5°	0.500	0.750	0.727	88.833
C2	C	5°	0.500	0.833	0.760	83.529
C2	C	5°	0.500	0.917	0.825	82.445
C2	C	5°	0.500	1.000	0.743	68.078
C2	C	5°	0.500	1.083	0.738	62.418
C3	D	0°	0.333	0.083	0.102	100.000
C3	D	0°	0.333	0.167	0.238	117.000
C3	D	0°	0.333	0.250	0.358	117.333
C3	D	0°	0.333	0.333	0.476	117.000
C3	D	0°	0.333	0.417	0.573	112.800
C3	D	0°	0.333	0.500	0.652	107.000
C3	D	0°	0.333	0.583	0.683	96.000
C3	D	0°	0.333	0.667	0.577	71.000
C3	D	0°	0.333	0.750	0.553	60.444
C3	D	0°	0.333	0.833	0.537	52.800

C3	D	0°	0.333	0.917	0.423	37.818
C3	D	0°	0.333	1.000	0.439	36.000
C3	D	0°	0.500	0.083	0.102	102.000
C3	D	0°	0.500	0.167	0.238	118.286
C3	D	0°	0.500	0.250	0.358	126.000
C3	D	0°	0.500	0.333	0.476	129.000
C3	D	0°	0.500	0.417	0.573	126.400
C3	D	0°	0.500	0.500	0.652	124.000
C3	D	0°	0.500	0.583	0.683	121.714
C3	D	0°	0.500	0.667	0.577	114.000
C3	D	0°	0.500	0.750	0.553	109.333
C3	D	0°	0.500	0.833	0.537	93.600
C3	D	0°	0.500	0.917	0.423	81.818
C3	D	0°	0.500	1.000	0.439	69.000
D1	D	5°	0.333	0.083	0.123	98.000
D1	D	5°	0.333	0.167	0.205	82.000
D1	D	5°	0.333	0.250	0.270	72.000
D1	D	5°	0.333	0.333	0.330	66.000
D1	D	5°	0.333	0.417	0.390	62.400
D1	D	5°	0.333	0.500	0.443	59.000
D1	D	5°	0.333	0.583	0.480	54.857
D1	D	5°	0.333	0.667	0.525	52.500
D1	D	5°	0.333	0.750	0.578	51.333
D1	D	5°	0.333	0.917	0.667	48.545
D1	D	5°	0.333	1.000	0.705	47.000
D1	D	5°	0.333	1.083	0.728	44.769
D1	D	5°	0.333	1.167	0.705	40.286
D1	D	5°	0.500	0.056	0.100	120.000
D1	D	5°	0.500	0.111	0.170	102.000
D1	D	5°	0.500	0.167	0.210	84.000
D1	D	5°	0.500	0.222	0.253	76.000
D1	D	5°	0.500	0.278	0.267	64.000
D1	D	5°	0.500	0.333	0.340	68.000

D1	D	5°	0.500	0.389	0.380	65.143
D1	D	5°	0.500	0.444	0.400	60.000
D1	D	5°	0.500	0.500	0.447	59.556
D1	D	5°	0.500	0.556	0.467	56.000
D1	D	5°	0.500	0.611	0.493	53.818
D1	D	5°	0.500	0.667	0.533	53.333
D1	D	5°	0.500	0.722	0.560	51.692
D1	D	5°	0.500	0.778	0.613	52.571
D1	D	5°	0.500	0.837	0.613	48.871
D2	D	5°	0.333	0.083	0.142	114.000
D2	D	5°	0.333	0.167	0.240	96.000
D2	D	5°	0.333	0.250	0.338	90.000
D2	D	5°	0.333	0.333	0.435	87.000
D2	D	5°	0.333	0.417	0.502	80.400
D2	D	5°	0.333	0.500	0.578	77.000
D2	D	5°	0.333	0.583	0.630	72.000
D2	D	5°	0.333	0.667	0.710	71.000
D2	D	5°	0.333	0.750	0.770	68.444
D2	D	5°	0.333	0.833	0.820	65.600
D2	D	5°	0.333	0.917	0.830	60.364
D2	D	5°	0.333	1.000	0.780	52.000
D2	D	5°	0.333	1.083	0.690	42.462
D2	D	5°	0.333	1.167	0.640	36.571
D2	D	5°	0.333	1.250	0.620	33.067
D2	D	5°	0.500	0.056	0.108	129.000
D2	D	5°	0.500	0.111	0.197	118.000
D2	D	5°	0.500	0.167	0.270	108.000
D2	D	5°	0.500	0.222	0.330	99.000
D2	D	5°	0.500	0.278	0.387	92.800
D2	D	5°	0.500	0.333	0.453	90.667
D2	D	5°	0.500	0.389	0.487	83.429
D2	D	5°	0.500	0.444	0.535	80.294
D2	D	5°	0.500	0.500	0.593	79.111

D2	D	5°	0.500	0.556	0.620	74.400
D2	D	5°	0.500	0.611	0.660	72.000
D2	D	5°	0.500	0.667	0.720	72.000
D2	D	5°	0.500	0.722	0.760	70.154
D2	D	5°	0.500	0.778	0.780	66.857
D2	D	5°	0.500	0.833	0.820	65.600
D3	D	5°	0.333	0.083	0.094	60.000
D3	D	5°	0.333	0.167	0.163	52.000
D3	D	5°	0.333	0.250	0.225	48.000
D3	D	5°	0.333	0.333	0.275	44.000
D3	D	5°	0.333	0.417	0.319	40.800
D3	D	5°	0.333	0.500	0.356	38.000
D3	D	5°	0.333	0.583	0.406	37.143
D3	D	5°	0.333	0.667	0.475	38.000
D3	D	5°	0.333	0.750	0.569	40.444
D3	D	5°	0.333	0.833	0.625	40.000
D3	D	5°	0.333	0.917	0.717	41.697
D3	D	5°	0.333	1.000	0.750	40.000
D3	D	5°	0.333	1.083	0.767	37.744
D3	D	5°	0.333	1.167	0.781	35.714
D3	D	5°	0.333	1.250	0.825	35.200
D3	D	5°	0.500	0.056	0.077	74.000
D3	D	5°	0.500	0.111	0.121	58.000
D3	D	5°	0.500	0.167	0.171	54.667
D3	D	5°	0.500	0.222	0.211	50.667
D3	D	5°	0.500	0.278	0.244	46.933
D3	D	5°	0.500	0.333	0.267	42.667
D3	D	5°	0.500	0.389	0.300	41.143
D3	D	5°	0.500	0.444	0.328	39.333
D3	D	5°	0.500	0.500	0.367	39.111
D3	D	5°	0.500	0.556	0.433	41.600
D3	D	5°	0.500	0.611	0.483	42.182
D3	D	5°	0.500	0.667	0.533	42.667

D3	D	5°	0.500	0.722	0.625	46.154
D3	D	5°	0.500	0.778	0.692	47.429
D3	D	5°	0.500	0.833	0.708	45.333
E2	D	0°	0.333	0.083	0.122	41.787
E2	D	0°	0.333	0.167	0.252	43.093
E2	D	0°	0.333	0.250	0.352	40.046
E2	D	0°	0.333	0.333	0.444	37.869
E2	D	0°	0.333	0.417	0.551	37.608
E2	D	0°	0.333	0.500	0.643	36.564
E2	D	0°	0.333	0.583	0.711	34.698
E2	D	0°	0.333	0.667	0.780	33.299
E2	D	0°	0.333	0.750	0.734	27.858
E2	D	0°	0.333	0.833	0.711	24.289
E2	D	0°	0.333	0.917	0.666	20.656
E2	D	0°	0.333	1.000	0.643	18.282
E2	D	0°	0.333	1.083	0.620	16.273
E2	D	0°	0.333	1.167	0.597	14.551
E2	D	0°	0.333	1.250	0.597	13.581
E2	D	0°	0.500	0.056	0.061	31.340
E2	D	0°	0.500	0.111	0.145	37.216
E2	D	0°	0.500	0.167	0.224	38.305
E2	D	0°	0.500	0.222	0.286	36.564
E2	D	0°	0.500	0.278	0.357	36.564
E2	D	0°	0.500	0.333	0.418	35.693
E2	D	0°	0.500	0.389	0.459	33.579
E2	D	0°	0.500	0.444	0.530	33.952
E2	D	0°	0.500	0.500	0.597	33.952
E2	D	0°	0.500	0.556	0.673	34.474
E2	D	0°	0.500	0.611	0.689	32.052
E2	D	0°	0.500	0.667	0.658	28.076
E2	D	0°	0.500	0.722	0.643	25.313
E2	D	0°	0.500	0.778	0.597	21.826
E2	D	0°	0.500	0.833	0.566	19.326

E3	D	5°	0.333	0.083	0.047	41.020
E3	D	5°	0.333	0.167	0.087	38.090
E3	D	5°	0.333	0.250	0.140	41.020
E3	D	5°	0.333	0.333	0.200	43.951
E3	D	5°	0.333	0.417	0.280	49.225
E3	D	5°	0.333	0.500	0.401	58.601
E3	D	5°	0.333	0.583	0.521	65.298
E3	D	5°	0.333	0.667	0.721	79.111
E3	D	5°	0.333	0.750	0.775	75.530
E3	D	5°	0.333	0.833	0.815	71.493
E3	D	5°	0.333	0.917	0.801	63.928
E3	D	5°	0.333	1.000	0.748	54.694
E3	D	5°	0.333	1.083	0.735	49.585
E3	D	5°	0.333	1.167	0.694	43.532
E3	D	5°	0.333	1.250	0.681	39.848
E3	D	5°	0.500	0.056	0.022	29.300
E3	D	5°	0.500	0.111	0.062	41.020
E3	D	5°	0.500	0.167	0.093	41.020
E3	D	5°	0.500	0.222	0.120	39.555
E3	D	5°	0.500	0.278	0.134	35.160
E3	D	5°	0.500	0.333	0.223	48.834
E3	D	5°	0.500	0.389	0.267	50.229
E3	D	5°	0.500	0.444	0.383	62.996
E3	D	5°	0.500	0.500	0.481	70.321
E3	D	5°	0.500	0.556	0.588	77.353
E3	D	5°	0.500	0.611	0.677	80.976
E3	D	5°	0.500	0.667	0.739	81.064
E3	D	5°	0.500	0.722	0.650	65.813
E3	D	5°	0.500	0.778	0.694	65.298
E3	D	5°	0.500	0.833	0.721	63.289
B4	E	5°	0.333	0.167	0.278	78.409
B4	E	5°	0.333	0.250	0.364	68.484
B4	E	5°	0.333	0.333	0.470	66.251

B4	E	5°	0.333	0.417	0.618	69.675
B4	E	5°	0.333	0.500	0.725	68.153
B4	E	5°	0.333	0.583	0.792	63.805
B4	E	5°	0.333	0.667	0.771	54.341
B4	E	5°	0.333	0.750	0.750	46.979
B4	E	5°	0.333	0.833	0.750	42.281
B4	E	5°	0.333	0.917	0.750	38.438
B4	E	5°	0.333	1.000	0.707	33.249
B4	E	5°	0.500	0.111	0.171	72.454
B4	E	5°	0.500	0.167	0.251	70.800
B4	E	5°	0.500	0.222	0.320	67.740
B4	E	5°	0.500	0.278	0.366	61.933
B4	E	5°	0.500	0.333	0.429	60.544
B4	E	5°	0.500	0.389	0.549	66.357
B4	E	5°	0.500	0.444	0.648	68.484
B4	E	5°	0.500	0.500	0.713	67.050
B4	E	5°	0.500	0.556	0.732	61.933
B4	E	5°	0.500	0.611	0.741	57.025
B4	E	5°	0.500	0.667	0.713	50.288
B4	E	5°	0.500	0.722	0.704	45.809
B4	E	5°	0.500	0.778	0.704	42.537
B4	E	5°	0.333	0.083	0.038	27.843
B4	E	5°	0.333	0.167	0.138	50.714
B4	E	5°	0.333	0.250	0.265	64.636
B4	E	5°	0.333	0.333	0.391	71.597
B4	E	5°	0.333	0.417	0.472	69.210
B4	E	5°	0.333	0.500	0.578	70.602
B4	E	5°	0.333	0.583	0.643	67.335
B4	E	5°	0.333	0.667	0.725	66.376
B4	E	5°	0.333	0.750	0.741	60.327
B4	E	5°	0.333	0.833	0.749	54.891
B4	E	5°	0.333	0.917	0.760	50.624
B4	E	5°	0.333	1.000	0.717	43.754

B4	E	5°	0.333	1.083	0.717	40.388
B4	E	5°	0.500	0.056	0.025	27.843
B4	E	5°	0.500	0.111	0.095	52.206
B4	E	5°	0.500	0.167	0.182	66.625
B4	E	5°	0.500	0.222	0.257	70.602
B4	E	5°	0.500	0.278	0.344	75.574
B4	E	5°	0.500	0.333	0.408	74.779
B4	E	5°	0.500	0.389	0.467	73.301
B4	E	5°	0.500	0.444	0.554	76.071
B4	E	5°	0.500	0.500	0.630	76.900
B4	E	5°	0.500	0.556	0.706	77.563
B4	E	5°	0.500	0.611	0.717	71.597
B4	E	5°	0.500	0.667	0.749	68.613
B4	E	5°	0.500	0.722	0.771	65.171
B4	E	5°	0.500	0.778	0.814	63.926
B4	E	5°	0.500	0.833	0.803	58.868

The rheology data for fluids A to E is given below.

Fluid	Shear rate (s^{-1}	Viscosity (Pas))
A	99.9000	0.00548
A	111.0000	0.00548
A	123.0000	0.00548
A	136.0000	0.00549
A	151.0000	0.00548
A	168.0000	0.00549
A	186.0000	0.00549
A	206.0000	0.00549
A	228.0000	0.00550
A	253.0000	0.00550
A	281.0000	0.00551
A	311.0000	0.00551
A	345.0000	0.00552

A	383.0000	0.00553
A	425.0000	0.00553
A	471.0000	0.00554
A	522.0000	0.00556
A	579.0000	0.00557
A	642.0000	0.00558
A	712.0000	0.00559
A	789.0000	0.00561
A	875.0000	0.00563
A	970.0000	0.00563
A	1080.0000	0.00565
A	1190.0000	0.00568
A	1320.0000	0.00554
A	1470.0000	0.00556
A	1630.0000	0.00562
A	1800.0000	0.00565
A	2000.0000	0.00569
B	9.9700	0.00754
B	26.9000	0.00755
B	43.8000	0.00757
B	60.6000	0.00757
B	77.5000	0.00757
B	94.4000	0.00758
B	111.0000	0.00757
B	128.0000	0.00757
B	145.0000	0.00757
B	162.0000	0.00758
B	179.0000	0.00758
B	196.0000	0.00759
B	213.0000	0.00758
B	230.0000	0.00759
B	246.0000	0.00759
B	263.0000	0.00760

B	280.0000	0.00759
B	297.0000	0.00760
B	314.0000	0.00761
B	331.0000	0.00761
B	348.0000	0.00761
B	365.0000	0.00762
B	382.0000	0.00763
B	399.0000	0.00763
B	415.0000	0.00764
B	432.0000	0.00764
B	449.0000	0.00764
B	466.0000	0.00764
B	483.0000	0.00765
B	500.0000	0.00766
C	9.9900	0.00748
C	11.9000	0.00748
C	14.2000	0.00747
C	17.0000	0.00747
C	20.3000	0.00748
C	24.2000	0.00748
C	28.9000	0.00748
C	34.5000	0.00748
C	41.2000	0.00748
C	49.2000	0.00747
C	58.7000	0.00747
C	70.1000	0.00745
C	83.7000	0.00746
C	99.9000	0.00746
C	119.0000	0.00745
C	142.0000	0.00745
C	170.0000	0.00746
C	203.0000	0.00746
C	242.0000	0.00750

C	289.0000	0.00752
C	345.0000	0.00753
C	412.0000	0.00753
C	492.0000	0.00755
C	588.0000	0.00757
C	702.0000	0.00759
C	838.0000	0.00762
C	1000.0000	0.00766
D	1.0500	0.00724
D	26.3000	0.00727
D	51.6000	0.00726
D	76.9000	0.00727
D	102.0000	0.00728
D	127.0000	0.00728
D	153.0000	0.00728
D	152.0000	0.00728
D	203.0000	0.00728
D	229.0000	0.00728
D	254.0000	0.00728
D	279.0000	0.00728
D	304.0000	0.00728
D	330.0000	0.00728
D	355.0000	0.00729
D	380.0000	0.00729
D	406.0000	0.00729
D	431.0000	0.00729
D	456.0000	0.00729
D	482.0000	0.00729
D	507.0000	0.00729
D	532.0000	0.00729
D	557.0000	0.00730
D	583.0000	0.00730
D	608.0000	0.00730

D	633.0000	0.00730
D	659.0000	0.00730
D	684.0000	0.00730
D	709.0000	0.00730
D	734.0000	0.00730
D	760.0000	0.00730
D	785.0000	0.00731
D	810.0000	0.00730
D	835.0000	0.00730
D	861.0000	0.00731
D	886.0000	0.00731
D	911.0000	0.00731
D	937.0000	0.00732
D	962.0000	0.00732
D	987.0000	0.00731
D	1010.0000	0.00732
D	1040.0000	0.00731
D	1060.0000	0.00731
D	1090.0000	0.00731
D	1110.0000	0.00732
D	1140.0000	0.00732
D	1160.0000	0.00732
D	1190.0000	0.00732
D	1210.0000	0.00732
D	1240.0000	0.00732
D	1270.0000	0.00732
D	1290.0000	0.00732
D	1320.0000	0.00732
D	1340.0000	0.00732
D	1370.0000	0.00732
D	1390.0000	0.00732
D	1420.0000	0.00732
D	1440.0000	0.00732

D	1470.0000	0.00732
D	1490.0000	0.00733
D	1520.0000	0.00733
D	1540.0000	0.00733
D	1570.0000	0.00733
D	1590.0000	0.00733
D	1620.0000	0.00733
D	1650.0000	0.00733
D	1670.0000	0.00733
D	1700.0000	0.00733
D	1720.0000	0.00734
D	1750.0000	0.00734
D	1770.0000	0.00734
D	1800.0000	0.00734
D	1820.0000	0.00734
D	1850.0000	0.00735
D	1870.0000	0.00735
D	1900.0000	0.00735
D	1920.0000	0.00735
D	1950.0000	0.00735
D	1970.0000	0.00735
D	2000.0000	0.00736
E	1.0000	0.03620
E	16.1000	0.02680
E	31.2000	0.02420
E	46.4000	0.02240
E	61.5000	0.02100
E	76.7000	0.01990
E	91.8000	0.01900
E	107.0000	0.01830
E	122.0000	0.01770
E	137.0000	0.01710
E	152.0000	0.01660

E	167.0000	0.01620
E	183.0000	0.01580
E	198.0000	0.01550
E	213.0000	0.01520
E	228.0000	0.01500
E	243.0000	0.01490
E	258.0000	0.01470
E	273.0000	0.01450
E	288.0000	0.01440
E	304.0000	0.01430
E	319.0000	0.01410
E	334.0000	0.01400
E	349.0000	0.01380
E	364.0000	0.01370
E	379.0000	0.01330
E	394.0000	0.01310
E	410.0000	0.01290
E	425.0000	0.01280
E	440.0000	0.01260
E	455.0000	0.01250
E	470.0000	0.01230
E	485.0000	0.01220
E	500.0000	0.01210
E	516.0000	0.01200
E	531.0000	0.01190
E	546.0000	0.01170
E	561.0000	0.01170
E	576.0000	0.01160
E	591.0000	0.01150
E	606.0000	0.01140
E	621.0000	0.01130
E	636.0000	0.01130
E	652.0000	0.01120

E	667.0000	0.01110
E	682.0000	0.01100
E	697.0000	0.01090
E	712.0000	0.01090
E	727.0000	0.01080
E	742.0000	0.01070
E	758.0000	0.01070
E	773.0000	0.01060
E	788.0000	0.01050
E	803.0000	0.01040
E	818.0000	0.01040
E	833.0000	0.01030
E	848.0000	0.01030
E	864.0000	0.01020
E	879.0000	0.01020
E	894.0000	0.01020
E	909.0000	0.01010
E	924.0000	0.01000
E	939.0000	0.00996
E	954.0000	0.00990
E	969.0000	0.00985
E	984.0000	0.00978
E	1000.0000	0.00972
E	1010.0000	0.00966
E	1020.0000	0.00967
E	1050.0000	0.00954
E	1060.0000	0.00950
E	1080.0000	0.00945
E	1090.0000	0.00939
E	1110.0000	0.00934
E	1120.0000	0.00930
E	1140.0000	0.00925
E	1150.0000	0.00919

E	1170.0000	0.00914
E	1180.0000	0.00910
E	1200.0000	0.00906
E	1210.0000	0.00903
E	1230.0000	0.00898
E	1240.0000	0.00895
E	1260.0000	0.00893
E	1260.0000	0.00892
E	1290.0000	0.00884
E	1300.0000	0.00881
E	1300.0000	0.00881
E	1330.0000	0.00873
E	1350.0000	0.00872
E	1360.0000	0.00872
E	1380.0000	0.00865
E	1390.0000	0.00861
E	1410.0000	0.00859
E	1420.0000	0.00852
E	1440.0000	0.00847
E	1450.0000	0.00844
E	1470.0000	0.00841
E	1480.0000	0.00838
E	1500.0000	0.00835
F	9.9900	0.00622
F	30.1000	0.00378
F	50.2000	0.00351
F	70.3000	0.00334
F	90.4000	0.00323
F	110.0000	0.00313
F	131.0000	0.00305
F	151.0000	0.00299
F	171.0000	0.00292
F	191.0000	0.00287

F	211.0000	0.00282
F	231.0000	0.00278
F	251.0000	0.00274
F	271.0000	0.00271
F	291.0000	0.00268
F	311.0000	0.00265
F	331.0000	0.00262
F	351.0000	0.00259
F	353.0000	0.00259
F	392.0000	0.00256
F	412.0000	0.00253
F	432.0000	0.00251
F	452.0000	0.00249
F	472.0000	0.00246
F	492.0000	0.00244
F	512.0000	0.00243
F	532.0000	0.00242
F	552.0000	0.00240
F	572.0000	0.00238
F	593.0000	0.00237
F	613.0000	0.00236
F	633.0000	0.00235
F	653.0000	0.00233
F	672.0000	0.00235
F	693.0000	0.00231
F	713.0000	0.00230
F	733.0000	0.00228
F	753.0000	0.00227
F	773.0000	0.00227
F	793.0000	0.00226
F	814.0000	0.00224
F	834.0000	0.00224
F	854.0000	0.00223

F	874.0000	0.00224
F	894.0000	0.00225
F	914.0000	0.00225
F	934.0000	0.00225
F	954.0000	0.00224
F	974.0000	0.00224
F	994.0000	0.00224
F	1010.0000	0.00224
F	1030.0000	0.00223
F	1050.0000	0.00222
F	1070.0000	0.00222
F	1090.0000	0.00221
F	1110.0000	0.00221
F	1140.0000	0.00221
F	1160.0000	0.00221
F	1180.0000	0.00220
F	1200.0000	0.00220
F	1220.0000	0.00219
F	1240.0000	0.00219
F	1260.0000	0.00219
F	1280.0000	0.00219
F	1300.0000	0.00218
F	1320.0000	0.00218
F	1340.0000	0.00217
F	1360.0000	0.00217
F	1380.0000	0.00217
F	1400.0000	0.00217
F	1420.0000	0.00216
F	1440.0000	0.00216
F	1460.0000	0.00215
F	1480.0000	0.00215
F	1500.0000	0.00215
F	1490.0000	0.00215

F	1540.0000	0.00214
F	1560.0000	0.00214
F	1580.0000	0.00213
F	1600.0000	0.00213
F	1620.0000	0.00213
F	1640.0000	0.00213
F	1660.0000	0.00212
F	1680.0000	0.00212
F	1700.0000	0.00212
F	1720.0000	0.00211
F	1740.0000	0.00211
F	1760.0000	0.00211
F	1780.0000	0.00211
F	1800.0000	0.00211
F	1820.0000	0.00210
F	1840.0000	0.00210
F	1860.0000	0.00210
F	1880.0000	0.00209
F	1900.0000	0.00209
F	1920.0000	0.00209
F	1940.0000	0.00209
F	1960.0000	0.00209
F	1980.0000	0.00208
F	2000.0000	0.00208

Bibliography

[1] W. H. Banks and C. C. Mill. Some observations on the behaviour of liquids between rotating rollers. *Proceedings of the Royal Society of London A*, 223:414, 1954.

[2] L. Landau and B. Levich. Dragging of a liquid by a moving plate. *ACTA Physicochimica URSS*, 17:42, 1942.

[3] F.P. Bretherton. The motion of long bubbles in tubes. *Journal of Fluid Mechanics*, 10:166, 1961.

[4] K. J. Ruschak. Boundary-conditions at a liquid air interface in lubrication flows. *Journal of Fluid Mechanics*, 119(JUN):107–120, 1982.

[5] J.C. Coyne. *Conditions for the rupture of a lubricating film*. Eng. sci. d. dissertation, Columbia, 1967.

[6] J.C. Coyne and H.G. Elrod. Conditions for the rupture of a lubricating film. part 1: Theoretical model. *Journal of Lubrication Technology*, 92:451, 1970.

[7] F. Kamisli and M. E. Ryan. Perturbation method in gas-assisted power-law fluid displacement in a circular tube and a rectangular channel. *Chemical Engineering Journal*, 75(3):167–176, 1999.

[8] S. F. Kistler and P. M. Schweizer. *Liquid film coating scientific principles and their technological implications*. Chapman and Hall, London, 1997.

[9] R. Westervelt. Polyester - dupont and teijin take a joint role in films. *Chemical Week*, 161(6):19–19, 1999.

[10] P. H. Sim. Polyester films - dupont teijin shuts us plants, plans closures in europe. *Chemical Week*, 163(43):14–14, 2001.

[11] E. Park, L. E. Scriven, and M. S. Carvalho. Physics of coatng tensioned web over slot die. In *12th International Coating Science and Technology Symposium*, page 173, Rochester, New York, USA, 2004. International Society of Coating Science and Technology.

[12] D. F. Benjamin and L. E. Scriven. Coaters analyzed by form and function. *Ind. Coating Res.*, 2:1–31, 1992.

[13] M. Priest, D. Dowson, and C. M. Taylor. Theoretical modelling of cavitation in piston ring lubrication. *Proceedings of the Institution of Mechanical Engineers Part C- Journal of Mechanical Engineering Science*, 214(3):435–447, 2000.

[14] R. I. Taylor. The inclusion of lubricant shear thinning in the short bearing approximation. *Proceedings of the Institution of Mechanical Engineers Part J- Journal of Engineering Tribology*, 213(J1):35–46, 1999.

[15] R. I. Taylor. Simplifications to the short bearing approximation. *Proceedings of the Institution of Mechanical Engineers Part J- Journal of Engineering Tribology*, 218(J6):569–573, 2004.

[16] S. J. Weinstein, K. J. Ruschak, and K. C. Ng. Developing flow of a power-law liquid film on an inclined plane. *Physics of Fluids*, 15(10):2973–2986, 2003.

[17] S. J. Weinstein and K. J. Ruschak. Coating rows. *Annual Review of Fluid Mechanics*, 36:29–53, 2004.

[18] P. H. Gaskell, P. K. Jimack, M. Sellier, H. M. Thompson, and M. C. T. Wilson. Gravity-driven flow of continuous thin liquid films on non- porous substrates with topography. *Journal of Fluid Mechanics*, 509:253–280, 2004.

[19] O. Reynolds. On the theory of lubrication and its application to mr beauchamp tower's experiment, including an experimental determination of the viscosity of olive oil. *Philosophical Transactions of the Royal Society of London*, 177:157–234, 1886.

[20] E.K. Gatcombe. Lubrication characteristics of involute spur gears. *Transactions of the ASME*, 67:177, 1945.

[21] M.R. Hopkins. Viscous flow between rotating cylinders and a sheet moving between them. *British Journal of Applied Physics*, 8:442–444, 1957.

[22] L. Prandtl. Motion of fluids with very little viscosity. Technical memorandum of the national advisory committee, NACA, March 1928 1928.

[23] J. Greener and S. Middleman. Reverse roll coating of viscous and viscoelastic liquids - response. *Industrial and Engineering Chemistry Fundamentals*, 22(4):507–507, 1983.

[24] M.D. Savage. Cavitation in lubrication. part1. on the boundary conditions and cavity-fluid interfaces. *Journal of Fluid Mechanics*, 80(4):763–755, 1977.

[25] E. Pitts and J. Greiller. The flow of thin liquid films between rollers. *Journal of Fluid Mechanics*, 11:33, 1961.

[26] G. B. Schneider. Analysis of forces causing flow in roll coaters. *Transactions of the Society of Rheology*, 6:209–221, 1962.

[27] H. W. Swift. The stability of lubricating films in journal bearings. *Proceedings of the institute of civil engineers*, 233:267–288, 1932.

[28] W. Stieber. *Das Scwimmlager*, 1933.

[29] J. C. Hintermaier and R. E. White. The splitting of a water film between rotating rolls. *Tappi Journal*, 48(11):617–625, 1965.

[30] H. Benkreira, M. F. Edwards, and W. L. Wilkinson. A semi-empirical model of the forward roll coating flow of Newtonian fluids. *Chemical Engineering Science*, 36(2):423–427, 1981.

[31] H. Benkreira, M. F. Edwards, and W. L. Wilkinson. Roll coating operations. *Journal of Non-Newtonian Fluid Mechanics*, 14:377–389, 1984.

[32] H. Benkreira, M. F. Edwards, and W. L. Wilkinson. Mathematical-modeling of the reverse and metering roll coating flow of Newtonian fluids. *Chemical Engineering Science*, 37(2):277–282, 1982.

[33] H. Benkreira, M. F. Edwards, and W. L. Wilkinson. Roll coating of purely viscous-liquids. *Chemical Engineering Science*, 36(2):429–434, 1981.

[34] M. D. Savage. Mathematical-models for coating processes. *Journal of Fluid Mechanics*, 117(APR):443–455, 1982.

[35] D. J. Coyle, C. W. Macosko, and L. E. Scriven. Film-splitting flows in forward roll coating. *Journal of Fluid Mechanics*, 171:183–207, 1986.

[36] R.I. Tanner. Full film lubrication theory for a maxwell liquid. *International Journal of Mechanical Science*, 1:206–215, 1960.

[37] C. A. Richardson. *A theoretical investigation of reverse roll coating*. Phd, University of Leeds, 1996.

[38] P. H. Gaskell, M. D. Savage, and H. M. Thompson. Stagnation-saddle points and flow patterns in stokes flow between contra-rotating cylinders. *Journal of Fluid Mechanics*, 370:221–247, 1998.

[39] D. J. Coyle, C. W. Macosko, and L. E. Scriven. Film-splitting flows of shear-thinning liquids in forward roll coating. *Aiche Journal*, 33(5):741–746, 1987.

[40] C. Munch. Process and apparatus for applying solutions, us patent us1847065, 23/02/1932 1932.

[41] W. S. Ho and F. M. Holland. Between-roll metering coating technique, a theoretical and experimental study. *Tappi Journal*, 61:53, 1978.

[42] J. Greener and S. Middleman. Reverse roll coating of viscous and viscoelastic liquids. *Industrial and Engineering Chemistry Fundamentals*, 20(1):63–66, 1981.

[43] D. J. Coyle, C. W. Macosko, and L. E. Scriven. A simple-model of reverse roll coating. *Industrial and Engineering Chemistry Research*, 29(7):1416–1419, 1990.

[44] D. J. Coyle, C. W. Macosko, and L. E. Scriven. The fluid-dynamics of reverse roll coating. *Aiche Journal*, 36(2):161–174, 1990.

[45] H. M. Thompson, N. Kapur, P. H. Gaskell, J. L. Summers, and S. J. Abbott. A theoretical and experimental investigation of reservoir-fed, rigid-roll coating. *Chemical Engineering Science*, 56(15):4627–4641, 2001.

[46] Y. D. Shikhmurzaev. The moving contact line on a smooth solid-surface. *International Journal of Multiphase Flow*, 19(4):589–610, 1993.

[47] D. J. Coyle, C. W. Macosko, and L. E. Scriven. Reverse roll coating of non-Newtonian liquids. *Journal of Rheology*, 34(5):615–636, 1990.

[48] P. H. Gaskell and Savage M.D. Meniscus roll coating. In S. F. Kistler and P. M. Schweizer, editors, *Liquid film coating*. Chapman and Hall, 1995.

[49] B. Malone. *An Experimental Investigation into Roll Coating Phenomena*. Phd thesis, University of Leeds, 1992.

[50] P. H. Gaskell, G. E. Innes, and M. D. Savage. An experimental investigation of meniscus roll coating. *Journal of Fluid Mechanics*, 355:17–44, 1998.

[51] P. H. Gaskell, M. D. Savage, J. L. Summers, and H. M. Thompson. Modeling and analysis of meniscus roll coating. *Journal of Fluid Mechanics*, 298:113–137, 1995.

[52] J. L. Summers, H. M. Thompson, and P. H. Gaskell. Flow structure and transfer jets in a contra-rotating rigid- roll coating system. *Theoretical and Computational Fluid Dynamics*, 17(3):189–212, 2004.

[53] W.E. Hoare. Variation in thickness of the tin coating of tinplate and its effects on porosity. *Journal of the Iron and Steel Institute*, (2):99–115, 1937.

[54] D. J. Coyle, C. W. Macosko, and L. E. Scriven. Stability of symmetrical film-splitting between counter- rotating cylinders. *Journal of Fluid Mechanics*, 216:437–458, 1990.

[55] B. Chalmers and W.E. Hoare. The longitudinal ridged structure in the tin coating of tinplate. *Journal of the Iron and Steel Institute*, (2):127–132, 1941.

[56] L. H. Sjodahl. Ink flow on rotating rollers. *American Ink Maker*, 29:31, 1951.

[57] J. C. Miller and R. R. Myers. A photographic study of liquid flow in a roll nip. *Transactions of the Society of Rheology*, 2:77–93, 1958.

[58] R. R. Myers, J. C. Miller, and A. C. Zettlemoyer. The splitting of thin films. kinematics. *Journal of Colloid Science*, 14:287–299, 1959.

[59] R. R. Myers and R. D. Hoffman. The distribution of pressures in the roll appliecation of Newtonian fluids. *Transactions of the Society of Rheology*, 5:317–328, 1961.

[60] R. D. Hoffman and R. R. Myers. The splitting of thin liquid films. cavitation dynamics. *Transactions of the Society of Rheology*, 6:197–207, 1962.

[61] C. C. Mill and G. R. South. Formation of ribs on rotating rollers. *Journal of Fluid Mechanics*, 28(3):523–529, 1967.

[62] J. Greener, T. Sullivan, B. Turner, and S. Middleman. Ribbing instability of a two roll coater- Newtonian fluids. *Chemical Engineering Communication*, 5:73–83, 1980.

[63] H. Benkreira, M. F. Edwards, and W. L. Wilkinson. Ribbing instability in the roll coating of Newtonian fluids. *Plastics and Rubber Processing and Applications*, 2:137–144, 1982.

[64] T. Hasegawa and K. Sorimachi. Wavelength and depth of ribbing in roll coating and its elimination. *Aiche Journal*, 39(6):935–945, 1993.

[65] N. Daniels. *Instabilities in roll and slot coating flows*. Phd, University of Leeds, 1998.

[66] N. Kapur. *Flow phenomena in fixed-gap and gravure roll coating systems*. PhD thesis, University of Leeds, 1999.

[67] P. H. Gaskell, N. Kapur, and M. D. Savage. Bead-break instability. *Physics of Fluids*, 13(5):1243–1253, 2001.

[68] D. J. Coyle. Roll coating. In E. D. Cohen and E. B. Gutoff, editors, *Modern coating and drying technology*, pages 63–116. Willey-VCH, New York, 1992.

[69] D. G. Higgins. Coating methods. In *Encyclopedia of Polymer Science and Technology*, volume 3, pages 765 – 807. John Wiley, 1965.

[70] S. C. Zink. Coatings processes. In J. I. Kroschwitz and M. Howe-Grant, editors, *Encyclopedia of Chemical Technology*, volume 6, pages 386–426. 3 edition, 1979.

[71] H. Benkreira and O. Cohu. Direct forward gravure coating on unsupported web. *Chemical Engineering Science*, 53(6):1223–1231, 1998.

[72] R. Patel and H. Benkreira. Gravure roll coating of Newtonian liquids. *Chemical Engineering Science*, 46(3):751–756, 1991.

[73] F. R. Pranckh and D. J. Coyle. *Liquid film coating scientific principles and their technological implications, Chapter 12b, Elastohydrodynamic Coating Systems*. Chapman & Hall, London, 1997.

[74] R. Hanumanthu. Variation of gravure coating thickness during early stages of doctor blade wear. *Aiche Journal*, 45(12):2487–2494, 1999.

[75] W. W. Pulkrabek and J. D. Munter. Knurl roll design for stable rotogravure coating. *Chemical Engineering Science*, 38(8):1309–1314, 1983.

[76] R. Hanumanthu and L. E. Scriven. Coating with patterned rolls and rods. *Tappi Journal*, 79(5):126–138, 1996.

[77] H. Benkreira and R. Patel. Direct gravure roll coating. *Chemical Engineering Science*, 48(12):2329–2335, 1993.

[78] N. Kapur. A parametric study of direct gravure coating. *Chemical Engineering Science*, 58(13):2875–2882, 2003.

[79] S. R. Rees. *An experimental and theoretical investigation of gravure roll coating*. PhD thesis, University of Leeds, 1995.

[80] L. W. Schwartz. Numerical modeling of liquid withdrawal from gravure cavities in coating operations; the effect of cell pattern. *Journal of Engineering Mathematics*, 42(3-4):243–253, 2002.

[81] C. A. Powell, M. D. Savage, and P. H. Gaskell. Modelling the meniscus evacuation problem in direct gravure coating. *Chemical Engineering Research and Design*, 78(A1):61–67, 2000.

[82] Y. Yin and S. Kumar. Elastohydrodynamics of gravure: Lubrication flow between a cavity and a flexible wall. In *The 12th International Coating Science and Technology*, Rochester, New York, USA, 2004.

[83] R. B. Bird, R. C. Armstrong, and O. Hassager. *Dynamics of Polymeric Liquids*, volume 1. Wiley, New York, 2 edition, 1987.

[84] F. H. Garner and A. H. Nissan. Rheological properties of high-viscosity solutions of long molecules. *Nature*, 158(4018):634–635, 1946.

[85] K. Weissenberg. A continuum theory of rheological phenomena. *Nature*, 159(4035):310–311, 1947.

[86] R.I. Tanner. Some methods for estimating the normal stress functions in viscometric flows. *Transactions of the Society of Rheology*, 14(4):483–507, 1970.

[87] J. G. Oldroyd. On the formulation of rheological equations of state. *Proceedings of the Royal Society of London Series a- Mathematical and Physical Sciences*, 200(1063):523–541, 1950.

[88] P. J. Carreau. *Rheological Equations for Molecular Network Theories*. Phd, University of Wisconsin, Madison, 1968.

[89] K Yasuda. *Investigation of the analogies between viscometric and linear viscometric properties of polystyrene fluids*. Phd, Massachusetts Institute of Technology, 1979.

[90] E. C. Bingham. *Fluidity and plasticity*. Internatinal Chemical Series. McGraw Hill, New York, 1 edition, 1922.

[91] M. Reiner. *Deformation, strain and flow*. H. K. Lewis & Co. Ltd., London, 2 edition, 1960.

[92] Matsuhis.S and R. B. Bird. Analytical and numerical solutions for laminar flow of non-newtonian ellis fluid. *Aiche Journal*, 11(4):588–595, 1965.

[93] M. M. Cross. Rheology of non-Newtonian fluids - a new flow equation for pseudoplastic systems. *Journal of Colloid Science*, 20(5):417–437, 1965.

[94] J. A. Tallmadge. A variable coefficient plate withdrawal theory for power-law fluids. *Chemical Engineering Science*, 24(3):471–480, 1966.

[95] The Song of Deborah and Barak, verse 5. In *The Book of Judges*.

[96] J. B. Grotberg and O. E. Jensen. Biofluid mechanics in flexible tubes. *Annual Review of Fluid Mechanics*, 36:121–147, 2004.

[97] J. Rosenzweig and O. E. Jensen. Capillary-elastic instabilities of liquid-lined lung airways. *Journal of Biomechanical Engineering-Transactions of the Asme*, 124(6):650–655, 2002.

[98] D. Quere. Fluid coating on a fiber. *Annual Review of Fluid Mechanics*, 31:347–384, 1999.

[99] D. Quere. Fluid coating. In *European Coating Symposium*, pages 11–32, Strasbourg, 1999.

[100] J. A. Tallmadge and R. Stella. Some properties of apparent water paradox in entrainment. *Aiche Journal*, 14(5):838, 1968.

[101] F. S. Goucher and H. Ward. The thickness of liquid films formed on solid surfaces under dynamic conditions. *Philosophical Magazine*, 44:1002–1014, 1922.

[102] J. Greener and S. Middleman. Theoretical and experimental studies of the fluid dynamics of a two-roll coater. *Industrial and Engineering Chemistry Fundamentals*, 18(1):35–41, 1979.

[103] C. Gutfinger and J. A. Tallmadge. Films of non-Newtonian fluids adhering to flat plates. *Aiche Journal*, 11:403–413, 1965.

[104] C. G. M. Marangoni. ber die ausbreitung der tropfen einer flssigkeit auf der oberflche einer anderen. *Annals of Physical Chemistry*, 143:337–354, 1871.

[105] A. R. Williams. *Two dimensional surfactant driven flows in thin liquid filmds*. Phd, University of Cambridge, 1998.

[106] B. J. Carroll and J. Lucassen. Capillarity-controlled entrainment of liquid by a thin cylindrical filament moving through an interface. *Chemical Engineering Science*, 28(1):23–30, 1973.

[107] J. Ratulowski and H. C. Chang. Marangoni effects of trace impurities on the motion of long gas-bubbles in capillaries. *Journal of Fluid Mechanics*, 210:303–328, 1990.

[108] C. W. Park. Effects of insoluble surfactants on dip coating. *Journal of Colloid and Interface Science*, 146(2):382–394, 1991.

[109] T. D. Blake and K. J. Ruschak. Wetting: Static and dynamic contact lines. In S. F. Kistler and P. M. Schweizer, editors, *Liquid Film Coating*. Chapman & Hall, London, 1997.

[110] R. Ablett. An investigation of the angle of contact between parafin wax and water. *Philosophical Magazine*, 46:244–256, 1923.

[111] T. D. Blake and J. M. Haynes. Kinetics of liquid/liquid displacement. *Journal of Colloid and Interface Science*, 30(3):421–423, 1969.

[112] L.H. Tanner. The spreading of silicone oil drops on horizontal surfaces. *Journal of Physics D: Applied Physics*, 12(9):1473–1484, 1979.

[113] P. G. Degennes. Wetting - statics and dynamics. *Reviews of Modern Physics*, 57(3):827–863, 1985.

[114] S. Kalliadasis and H. C. Chang. Apparent dynamic contact-angle of an advancing gas-liquid meniscus. *Physics of Fluids*, 6(1):12–23, 1994.

[115] R. L. Hoffman. Study of advancing interface .1. interface shape in liquid-gas systems. *Journal of Colloid and Interface Science*, 50(2):228–241, 1975.

[116] K.M. Jiang, S. Oh, and J.C. Slattery. Correlation for dynamic contact angle. *Journal of Colloid and Interface Science*, 69(1):74–77, 1979.

[117] J. E. Seebergh and J. C. Berg. Dynamic wetting in the low capillary number regime. *Chemical Engineering Science*, 47(17-18):4455–4464, 1992.

[118] A. Bates. Private communication, 2005.

[119] M. Abraham-Thomas. Private communication, 2005.

[120] G. E. Innes. *An Experimental and Theoretical Study of Viscous Lifting inTribology*. Phd thesis, University of Leeds, 1993.

[121] G. I. Taylor. Deposition of a viscous fluid on the wall of a tube. *Journal of Fluid Mechanics*, 10(2):161–165, 1961.

[122] B. G. Cox. On driving a viscous fluid out of a tube. *Journal of Fluid Mechanics*, 14(1):81–96, 1962.

[123] J.C. Coyne and H. G. Elrod. Conditions for the rupture of a lubricating film. part 2: New boundary conditions for reynolds equation. *Journal of Lubrication Technology*, 93:156–167, 1971.

[124] E. H. Smith. *A study of film rupture in hydrodynamic lubrication*. Phd, University of Leeds, 1975.

[125] H. I. You and S. S. Lu. Inertia effect in hydrodynamic lubrication with film rupture. *Journal of Tribology-Transactions of the Asme*, 109(1):86–90, 1987.

[126] W. H. Press, S. A. Teukolsky, W. T. Vetterling, and B. P. Flannery. *Numerical Recipes in C++*. Numerical Recipes. Cambridge University Press, Cambridge, 2 edition, 2002.

[127] J.C. Coyne and H. G. Elrod. An exact asymptotic solution for a seperating film. *Journal of Lubrication Technology*, 91:651–652, 1969.

[128] L. F. Shampine, J. Kierzenka, and M. W. Reichelt. Solving boundary value problems for ordinary differential equations in matlab with bvp4c, 2000.

[129] P. V. O'Neil. *Advanced Engineering Mathematics*. Wadsworth, 2003.

[130] P. H. Gaskell, S. R. Rees, M. D. Savage, and S. P. Storey. A mathematical model of roll-to-web kiss coating. *Chemical Engineering Research and Design*, 76(A1):29–37, 1998.

[131] N. Kapur, P. H. Gaskell, and A. Bates. A parametric study of offset gravure coating. *Chemical Engineering Research and Design*, 79(A1):41–50, 2001.

[132] H. Versteeg and W. Malalasekra. *An Introduction to Computational Fluid Dynamics : The Finite Volume Method Approach*. Prentice Hall, 1996.

[133] G. E. Forsythe and W. R. Wasow. *Finite-difference methods for partial differential equations*. J. Wiley, 1960.

[134] M. J. Fagan. *Finite element analysis : theory and practice*. Harlow : Longman Scientific & Technical, 1992.

[135] G. E. Karniadakis and S. J. Sherwin. *Spectral/hp element methods for CFD*. Oxford University Press, 1999.

[136] L. N. Trefethen. *Spectral methods in matlab*. Society for Industrial and Applied Mathematics, c2000., Philadelphia, PA :, 2000.

[137] S. F. Kistler and L. E. Scriven. Coating flow theory by finite-element and asymptotic analysis of the navier-stokes system. *International Journal for Numerical Methods in Fluids*, 4(3):207–229, 1984.

[138] G. Fairweather. *Finite Element Galerkin Methods for Differential Equations*, volume 34 of *Lecture Notes in Pure and Applied Mathematics*. Marcel Dekker, Inc., New York, 1978.

[139] Y. W. Kwon and Hyochoong Bang. *The finite element method using matlab*. CRC Mechanical engineering series. CRC Press LLC, 2 edition, 2000.

[140] S. Syrjala. Finite-element analysis of fully-developed laminar-flow of power-law non-Newtonian fluid in a rectangular duct. *International Communications in Heat and Mass Transfer*, 22(4):549–557, 1995.

[141] S. Syrjala. Numerical study of fully developed non-Newtonian fluid flow and heat transfer in a rectangular channel with a moving wall. *International Communications in Heat and Mass Transfer*, 24(1):11–25, 1997.

[142] S. H. Hashemabadi, S. G. Etemad, M. R. G. Naranji, and J. Thibault. Laminar flow of non-Newtonian fluid in right triangular ducts. *International Communications in Heat and Mass Transfer*, 30(1):53–60, 2003.

[143] D. M. Wei and H. B. Luo. Finite element solutions of heat transfer in molten polymer flow in tubes with viscous dissipation. *International Journal of Heat and Mass Transfer*, 46(16):3097–3108, 2003.

[144] J. Kepner. Matlabmpi, MIT Lincoln laboratory, MIT, Massachusetts., 2001.

[145] J. Kepner. Parallel programming with matlabmpi. In *Proceedings of the High Performance Embedded Computing (HPEC 2001) workshop*, MIT Lincoln Laboratory, Lexington, MA., 2001.

[146] X. Y. Yin and S. Kumar. Lubrication flow between a cavity and a flexible wall. *Physics of Fluids*, 17(6), 2005.